Surfactant and Polyelectrolytes Templated Mesostructured inorganic Materials

Yang, Bin

Award date:
2010

Awarding institution:
University of Bath

Surfactant and Polyelectrolytes Templated Mesostructured inorganic Materials

Bin Yang
A thesis submitted for the degree of Doctor of Philosophy
University of Bath
Department of Chemistry
Sep. 2010

Acknowledgements

Foremost I would like to thank my supervisor Dr. Karen Edler for her enthusiastic and consistent support throughout the application process prior to my arrival in the UK and for continued support and supervision that has been invaluable over the past three year.

I would also like to thank previous and continuing members of staff in the Department of Chemistry who have helped me learn new experimental methods and developed my theoretical understanding over the past three years. I am grateful to all the members of the Edler Research group who have made working in the group enjoyable socially and have helped develop a harmonious environment in which to work.

The financial supports, for fees and subsistence, generously provided by the University of Bath and the Overseas Research Student Award Scheme have also been vital. I am deeply grateful for this assistance, without which I would have been unable to undertake postgraduate research in the UK. Furthermore, I would like to both acknowledge the ISIS, ESRF and Diamond research facilities, and the tireless and ever dependable beamline scientists employed therein, who have helped facilitate much of the key research involved in my PhD.

Personally, I would like to thank my friends and family both in China and in England who have been supportive ever since my initial application. Such support has made relocation half a world away much easier to adjust and has been of great importance in helping me stay focused during the more trying times of my research. Last, but by no means least, I would like to thank my boyfriend, Chunyu Jin, for his patience, care, motivation, love and encouragement both past and present to make me a very happy person.

Table of Contents

TABLE OF CONTENTS

Abstract

Surfactant and polyelectrolyte templated mesostructured inorganic materials

In this work we have explored the possibility of using surfactant/polyelectrolyte complexes as templates to synthesize inorganic mesostructured materials mainly with a film morphology. Inorganic species deposit in those regions of the films which are filled with a polymer hydrogel, surrounding the arrays of ordered surfactant micelles. This method produced thick robust films where the inorganic regions are reinforced and functionalized by the polymer, thus these materials are expected to have potential applications in separation, absorption, catalysis and chemical sensing.

Initial work involved mixing silicate precursors directly into CTAB/PEI solutions to form highly ordered 2D hexagonal silica films at the air/water interface. Time resolved synchrotron SAXS allowed investigation of processes occurring in solution during the reaction, from which a film growth mechanism was proposed. Films had good thermal properties and after post-synthesis TMOS vapour treatment, retained structure upon template removal. Silica gel monoliths with various mesostructures were also rapidly fabricated in one minute with surfactant/LPEI complexes.

Cat-ionic surfactant mixtures with polymers were also employed to template silica films with different cubic mesostructures at the air/water interface. The mesophases of the interfacial films were enriched due to more complicated interactions between the polymers and two surfactants. Polymer molecular weight, total composite concentration, chemical nature of the polymer as well as the cationic-anionic surfactant molar ratio was used to systematically control the silica film mesophase.

Robust titania films were also prepared with cat-anionic surfactant mixtures and polymers at the air/water interface. Although the film mesostructure was lost after calcination, the *in-situ* and dry free-standing films display ordered cubic mesostructures and the films are stable to calcination after post-synthesis treatment. Ordered lamellar iron oxide films templated by SDS/LPEI complexes were also prepared at the air/water interface.

Chapter 1 Introduction

The combination of soft matter physical chemistry, inorganic and hybrid sol-gel chemistry has opened new avenues for advanced materials research. Since the late 1990s, micellar and lyotropic liquid-crystal phases have been used as templated for the design of periodically organized mesoporous materials and this field is experiencing explosive growth. In this work, by thoroughly characterising and gaining an understanding of the interactions between surfactants and polyelectrolytes as well as their interactions with inorganic species, functionalised inorganic materials with ordered mesostructure, mainly with a film geometry, were prepared at the air/water interface.

1.1 Surfactants and Polyelectrolytes

In recent years, self-assembled surfactant/polyelectrolyte complexes which result in solid precipitates with periodically ordered nanostructures have become of great interests to chemists and material scientists. These materials combine the properties of polymers (mechanical stability) and surfactants (formation of highly ordered mesophases), which allows a great variety in designing structural as well as functional properties of mesostructured materials.

1.1.1 Surfactants and Self Assembly

Surfactants, which contain both hydrophobic groups (generally a long-chain hydrocarbon) and hydrophilic groups (generally an ionic or highly polar group that can impart some water solubility to the molecule), can reduce the surface tension of water by adsorbing at the air/water interface and the interfacial tension between oil and water by adsorbing at the liquid-liquid interface, thus leading to self-assemble into aggregates known as micelles in the bulk solution.

There are four basic types of surfactants which are chemically classified by the nature of the hydrophile:

Anionic surfactants

Anionic surfactant have a hydrophile which is negatively charged, such as carboxyl ($RCOO^-M^+$), sulfate ($ROSO_3^-M^+$), sulfonate ($RSO_3^-M^+$) or phosphate ($ROPO_3^-M^+$). They are mainly used for directing the structure of positively charged inorganic species, and are widely applied for many industrial applications because of their low cost of manufacturing, rapid biodegradability and low toxicity.

Cationic surfactants

Their hydrophile bears a positive charge, such as the quaternary ammonium halides ($R_4N^+X^-$) and the four R^- groups may or may not be the same, such as cetyltrimethylammonium bromide (CTAB), other alkyltrimethylammonium salts as well as cetylpyridinium chloride. CTAB was the surfactant employed to make the first mesoporous material from Mobil[1] and it is also the main commercially available cationic surfactant used for the synthesis of mesoporous materials. Gemini surfactants,[2, 3] bolaform surfactants,[4] multi-headgroup surfactants and recently reported cationic fluorinated surfactants can also be used as the templates for the synthesis of mesoporous materials.[5] These surfactants have excellent solubility, high critical micelle temperature (CMT) and can be used either in acid or basic media, however, they are relatively expensive, toxic and don't degrade in the environment.

Nonionic surfactants

The hydrophile in non-ionic surfactants has no charges. They are widely used in industry due to their attractive properties such as low price, non-toxicity and biodegradability. The self-assembly of nonionic surfactants, especially block copolymers, produce mesophases with different geometries and packing symmetries.[6, 7] The main types of non-ionic surfactants for synthesizing ordered mesostructures are oligomeric alkyl poly(ethylene oxides) (e.g. Brij), alkylphenol poly(ethylene oxides) (e.g. Triton), sorbitan ester surfactants (e.g. Tween, Span) and poly(alkylene oxide) block copolymers (e.g. PEO-PPO-PEO).

Amphoteric (and zwitterionic)

The molecule contains both a negative charge and a positive charge, for example the sulfobetaines ($RN^{+}(CH_3)_2CH_2CH_2SO_3^{-}$). But reports on the preparation of mesoporous materials using this type of surfactant are rare.

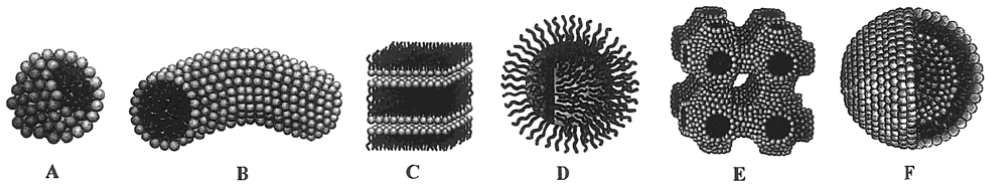

Figure 1.1 *micellar structures (A=sphere, B=cylinder, C=bilayer, D=reverse micelles, E=bicontimuous phase, F=liposomes.)*[8] *used with permission from Ref.8.*

Amphiphilic surfactant molecules display a polar head and non-polar tail and are likely to aggregate in solvents if one of these parts is insoluble. Above the critical micellar concentration (CMC), the amphiphilic molecules form micelles. Driven by entropic interactions, such as coulombic force and H-bonding, these micelles self-assemble into colloids with different microstructures. Upon progressive increase of surfactant concentration in the aqueous solution, a number of phases appear, presenting different packing ordering which always follow a similar order: sphere, cylinder, lamella, inverse cylinder and inverse sphere. This order corresponds to variations of the interfacial curvature. Some typical micellar structures are presented in **Figure 1.1**.

Until now, different parameters have been taken into account to predict the geometry of micelles, such as the hydrophobic interactions between the organic chains, geometric restrictions due to molecular packing, molecular exchange between aggregates and electronic repulsion between polar heads.

The model suggested by Israechvili[9] is widely accepted to explain and predict the resulting self-assembled mesostructures. It is explained from geometrical considerations which rely on the ratio of the polar head surface area to the hydrophobic volume. In this model, amphiphilic molecules are considered as a conical

hydrophobic fragments attached to a spherical hydrophilic head. The packing parameter is described as follows:

$$g = V / La$$

where V is the volume of the hydrocarbon chain, a is the effective head group area and L is the maximum effective chain length. For single chain surfactants where the chain is linear L and V can be calculated as $V= (27.4+26.9n)\ Å^3$ per hydrocarbon chain; $L= (1.5+1.265n)\ Å$ per hydrocarbon chain. Here n is the number of carbon atoms. g links the molecular structure of the amphiphilic molecule to the architecture of the aggregates. The limited values of g can be easily calculated for an aggregate of known geometry by using an estimation of the aggregation number, as shown in **Table 1.1.**

Table 1.1 *Summary of the different micellar structures compatible with a given packing parameter g.*[9]

Micelle packing parameter	Structure
g<1/3	Spherical micelles
1/3<g<1/2	Cylinder micelles
1/2<g<1	Bilayer (vesicles)
1<g<2	Bilayer (membrane)
2<g<3	Inverse cylindrical micelles
g>3	Inverse spherical micelles

1.1.2 Polyelectrolytes

Polyelectrolytes are polymers either bearing positively or negatively charged ionisable groups, typical examples are polystyrene sulfonate, polyacrylic and polymethacrylic acids, and DNA. In polar solvents such as water, these groups can dissociate, releasing counterions in solution and leaving charges on the polymer chains.

Commercial polyethyleneimine (PEI) is a hyper branched polyelectrolyte with amine groups. The structure has each nitrogen atom joined to at least one other via an ethylene group linkage. It is highly charged at low pH and its charge density decreases as the pH is increased.[10] Static light scattering studies indicate that the pair interaction

between the polyelectrolyte molecules is repulsive.[8] Charge density and the radius of gyration increase with decreased pH due to the increased electrostatic repulsion between the polyelectrolytes. Molecular weight is found to be slightly higher at low pH values because an increasing number of chloride ions are associated with the polyelectrolytes at low pH values.[11] Dynamic light scattering measurements shows PEI forms essentially monomodal rather large aggregates with a broad size distribution.[11] Polyacrylamide (PAAm) and polyethylene oxide (PEO) are also used in this work and the molecular structures of these polymers are shown in **Figure 1.2**.

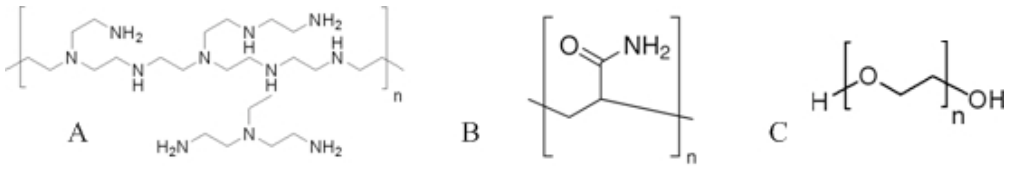

Figure 1.2 *Molecular structures of polyelectrolytes (A) polyethyleneinine (PEI) (B) polyacrylamide (PAAm) and (c) poly(ethylene oxide) (PEO)*

1.1.3 Mixed Surfactant and Polyelectrolyte Complexes

Polyelectrolyte and surfactant interactions have been extensively investigated and reviewed in both bulk solution and at the interface,[12-15] since they are widely used in biochemical, pharmaceutical products, paint and cosmetics industries.

In bulk solution, most of the studies have been focused on either neutral polymers with ionic surfactants or charged polymers with oppositely charged surfactants. Work by Goddard et al[16, 17] demonstrated that there were two extremes: either surfactant micellization occurred prior to polymer/surfactant aggregation (weakly interacting) or surfactant binding to the polymer occurred below the CMC, with the polymer becoming saturated with surfactant before micellization took place (strongly interacting). Precipitation is usually observed at intermediate surfactant to polyelectrolyte ratios, whereas at higher or lower polyelectrolyte to surfactant ratios transparent systems may be formed. Different structures of polyelectrolyte/surfactant complexes have been reported, the structure of the complex depends on the different

types of interactions, including pure electrostatic forces, chemical nature, rigidity, molecular architecture and polymer conformation.[10] Mixture of SDS and polyelectrolytes, such as SDS/PEG[18], SDS/PEI[10, 19, 20], SDS/Polyacrylamide[21], DTAB/DNA[22] are particular interesting. Winnik[23] has used fluorescence labelling and microcalorimetry to probe both monomer and micelle binding in SDS and PEI solutions. Electrostatic and hydrophobic interactions were thought to be the main interactions between the SDS and PEI complexes. Li[24] also confirmed the significant role of the hydrophobic interactions. Meszaros[10] indicated the interaction between SDS and PEI can be divided into different SDS concentration ranges. At low surfactant concentrations, the surfactant/polymer complex is a thermodynamically stable solution. Above this critical concentration, system becomes an unstable colloid dispersion of complex particles. At even higher surfactant concentrations, the system may be a stable dispersion of the SDS/PEI particles. Impact of electrolytes has also been investigated by Mezei[19].

The development of instrumentation, such as surface tensiometer, neutron reflectivity and ellipsometry, offers the opportunity to make a systematic exploration of the behaviour of surfactant/polymer mixture at the interface.[15] Here we can also take the SDS/polyelectrolyte system as an example. Penfold reported the pH dependence of the surface tension and adsorption of SDS/PEI mixtures; the strong surface interaction between the SDS and PEI gives rise to significantly enhanced SDS adsorption down to very low surfactant concentrations. The surface adsorption of the linear PEI/SDS complex resulted in a monolayer in which the amount of PEI/SDS complex adsorbed is independent of pH. For branched PEI, a similar pattern of adsorption was observed at low pH, the adsorbed layer also forms multilayer depending on the pH and SDS concentration.[25] An impact of salt (NaCl) on the SDS/PEI adsorption was also observed[26], where at high pH a more extended region of surface multilayer formation is observed, reinforcing the importance of this non-electrostatic interaction. Similar observations of multilayer formation at high pH for PEI/SDS/dodecyl hexaethylene glycol mixtures have also been reported.[27]

Concerning my work, interactions between the cationic surfactant CTAB and

neutral PEI complexes are of particular interest. CTAB and PEI interactions in bulk solution was first observed by Kudryavtsev,[28] who proposed that it is due to hydrophobic interaction between the surfactant and polymer[29] as well as a charge-dipole interaction[30] which enhances the building of surfactant/polymer aggregates. Based on these interactions, we discovered that CTAB/PEI can assemble at the air-solution interface into 2D assembly hexagonal arrays of rod-like surfactant micelles encased in polymer and forming films with up to 3 μm thickness.[31] The surfactant alkyl chain length, concentration of polymer, pH value and polymer molecular weights have a great influence towards the ordering and thickness of the film.[30, 32, 33]

1.2 Templated Mesoporous Materials

1.2.1 Evolution of Mesoporous Materials Research

Technical advances in various fields, such as adsorption, catalysis, drug delivery, and sensors, require the development of ordered porous materials with controllable structure and systematically tailored pore architecture.[34] However, zeolite and microporous materials whose pore size is less then 20 Å are far away from the application demands. As early as the 1990s, Mobil scientists reported the synthesis of highly ordered mesostructured M41S molecular sieves templated by quaternary ammonium cationic surfactants such as CTAB in basic conditions.[35] From then on, periodically ordered materials with mesostructures have experienced an explosive growth, and the concept of “template” was also postulated in the synthesis of mesoporous materials.

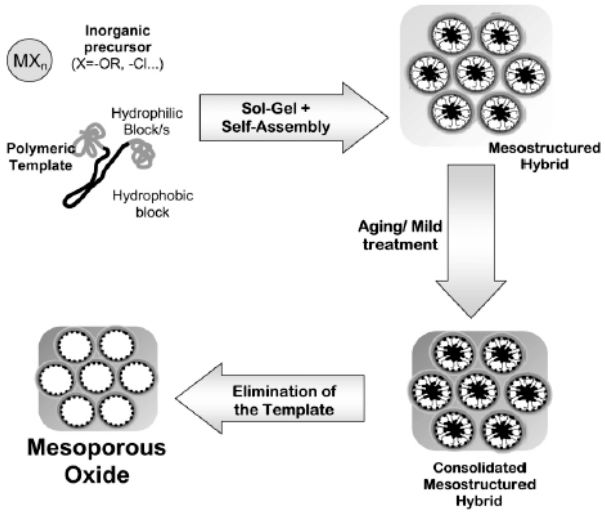

Figure 1.3 *Synthesis process for mesoporous materials templated by surfactants.*[36] *used with permission from Ref.36.*

Driven by the weak non-covalent bonds such as hydrogen bonds, Van de Waals forces and electrovalent bonds between each other, the organic surfactant and inorganic precursor species can cooperatively assemble into mesostructured hybrid. Mesopores can then be obtained by the removal of the organic template, as shown in **Figure 1.3**.

These pioneering findings were followed by development of various kinds of mesoporous materials. For example, hexagonal mesoporous silica (HMS) templated by neutral amines possess a slightly disordered hexagonal structure and thicker walls, giving superior thermal stability upon calcination.[37] Michigan State University synthesized the MSU type of mesoporous material using polyethylene oxide (PEO) as a template, this material also has a disordered channel structure.[38,40] In 1998, the highly ordered large pore mesoporous silica, Santa Barbara Amorphous-15 (SBA-15) with thick pore walls and two dimensional hexagonal structure was prepared using triblock copolymers as the structure directing reagent in strong acidic media.[7, 39, 40] These novel materials not only have large uniform pore sizes (2-30nm), highly ordered nanochannels but also large surface area which is extremely important in fields like catalysis,[41, 42] sensors,[43] photovoltaics,[44] etc.

Silica-based materials have consistently remained at the forefront of developments in mesoporous materials due to the early success of such materials and the relatively easy use of silica precursor chemicals. In the past decades, an increasing quantity of mesostructured materials with diverse chemical compositions (oxides, metals, carbons and semiconductor etc) shaped as powders, monolith, and films have appeared.[45, 46] Template assisted synthesis methodologies to prepare mesoporous silica have been extended to various mesoporous metal oxides.[47-49] The first study concerning non-silica mesostructured materials was reported by researchers of the University of Santa Barbara.[50-52] Nowadays, a great variety of oxide-based materials containing surfactant templates and metal cations have been synthesized, such as TiO_2,[53, 54] Ta_2O_5, Nb_2O_5,[55, 56] ZnO_2,[57] Al_2O_3,[58] SnO_2,[59] CeO_2[60, 61], Fe_3O_4[62, 63] and V_2O_5[64] as well as mesoporous aluminophosphate.[65] One of the most exciting approaches relies upon the modification of silica sources to synthesise periodic mesoporous organosilicates (PMO).[66, 67] The invention of PMO materials were reported firstly by Fowler[68] and then independently by three groups, Inagaki's group,[69] Ozin's group[70] and Stein's group[71] in 1999. Organic molecules with multiple alkoxysilane groups were used as the silica source, introducing various organic components into the framework. Synthetically designed surfactants other than conventional surfactants were also used to fabricate mesoporous materials. Using chiral organic compounds as the template, chiral structured mesoporous material was first prepared[72, 73]. Ordered mesoporous carbon materials (CMK-X) were first reported by Ryoo et al using sucrose as a carbon source and mesoporous silicate (such as MCM-48, SBA-1 and SBA-15) as secondary templates.[74-76] The structure of the mesoporous silica template has a crucial role that the carbon replica must have a continuous phase to keep its structure. For example, mesoporous MCM-48 has a cubic phase with a bicontinuous pore geometry, which makes it an appropriate template for the mesoporous carbon CMK-1.

As briefly summarized above, mesoporous material area is experiencing an explosive growth in the last decades, and various approaches have been extensively investigated to prepare mesoporous materials. The potential of these structures have been recognised in various applications such as catalysis, separation techniques,

controlled delivery, adsorption and sensors.[77, 78]

1.2.2 Formation Mechanism

Until now, much work has been done on the synthesis of highly ordered mesoporous materials with various pore structures and morphologies through varying the synthesis parameters and post-synthetic treatments. The resulting materials are composites containing an organized surfactant micelle array embedded in an inorganic matrix. Scientists are still trying to understand how the inorganic species interact with the surfactant during the self-assembly process, which could help to control the material structures and improve material properties required for specific applications, such as films, sensors, encapsulation of drugs and photoelectro-chemical applications.

Mesoporous materials templated by surfactant are mainly prepared in three ways: For the first route, the mesophase is directed by a concentrated surfactant solution,[6] the inorganic species polymerizes around the surfactant structure and copies the initial lyotropic phase. This way normally uses high viscosity reaction solutions, but helps to predict the final structure.

The second way is most common for synthesis of mesoporous powders with lyotropic liquid-crystalline phases templated by surfactant whose concentration is much lower than the concentration normally required to create these phases. Small amount of dilute surfactant and inorganic precursors are mixed together. During the self-assembly process, interaction between the inorganic species and surfactant cause the formation of solid phase that has a different surfactant structure than the initial solution, the solid phase can form as either precipitate with uniform morphologies or thin films at different interfaces.[79]

The third way is to form films though chemical solution deposition, such as spin coating or dip-coating. The templating agent and inorganic precursors are mixed into a highly dilute homogeneous dispersed solution, which is then cast onto the substrate either by spinning, dipping or spraying. Self-assembly is triggered during the evaporation of the deposition solution just after deposition of the layer on the

substrate. The whole process is complex and mainly involves four factors: the fast evaporation of the solvent, the film water content equilibration with the atmosphere, the formation and stabilization of the template/inorganic homogenous phases and the consolidation of the inorganic network. It has been shown that the final film structure is sensitive to conditions such as the ratio of template to inorganic precursor, the pH, the aging time, the evaporation speed etc.[80-83]

Detailed studies on the mechanism of formation of mesoporous materials have been conducted through several in-situ methods such as FTIR spectroscopy,[84] NMR,[85] and neutron scattering[86]. Beck et al first proposed two mechanisms: the first suggests that the organic liquid crystalline structure has already formed before the silicate species were added. However, this mechanism has its limitations and can not explain the mesophase formed in the dilute reaction solution, it just fits the first synthesis route mentioned above (**Figure 1.4**).[35] Another mechanism is that the inorganic materials coat the micelles in the solution and the silicate-coated micelles then aggregate together to form the ordered mesophase composite. This mechanism seems more likely to be suitable for the dilute solutions and provides an explanation for the growth of the spectacular curved and crystal-like large scale morphologies observed in some syntheses (**Figure 1.5**).[87] Later on, people paid more attention to the charge interaction between the inorganic species and organic headgroup in alkaline solutions. They suggested that the drying and further condensation of the silica framework surround the micelles decreased the framework charge, which increased the apparent surfactant headgroup size which finally caused an increase in curvature of the micelle's surface. This leads to a transformation from a lamellar phase mesostructure to hexagonal or cubic phase (**Figure 1.6**).[88] This mechanism is mainly relevant to the synthesis of mesoporous materials from silicate precursors with an existing sheet-like structure, such as the mineral kanemite.

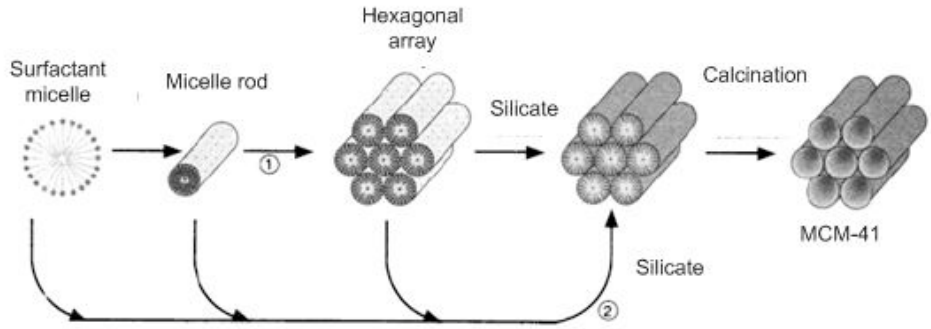

Figure 1.4 *Liquid crystalline mechanism.*[35] *used with permission from Ref. 35.*

Until now, the charge-matching cooperative templating mechanism (**Figure 1.7**),[50, 89] which is based on the observation of the interaction between the silica polyion species S and the alkyltrimethylammonium surfactants I, has been widely accepted. The polyion-surfactant pair (S^+I^-) assembles into a molecular inorganic liquid crystal which undergoes further condensation causing the rearrangement of the encapsulated surfactant phase, until eventually, the mesophase structures solidified.

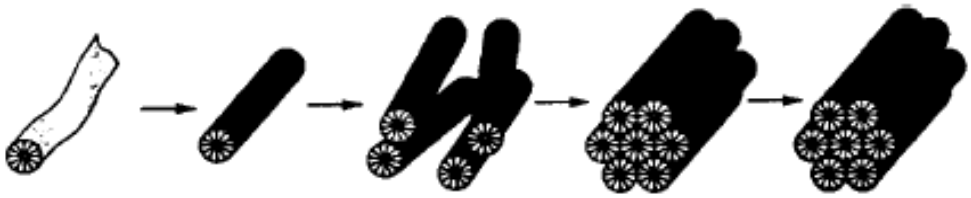

Figure 1.5 *Rod Assembly Mechanism.*[87] *used with permission from Ref. 87.*

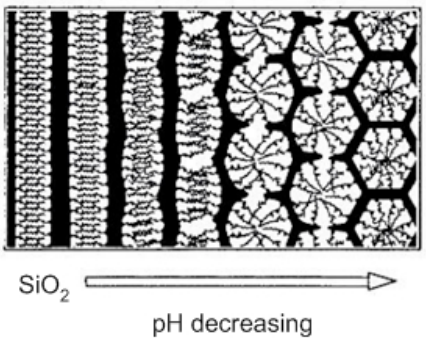

Figure 1.6 *Folded Sheets Mechanism.*[88] *used with permission from Ref.88.*

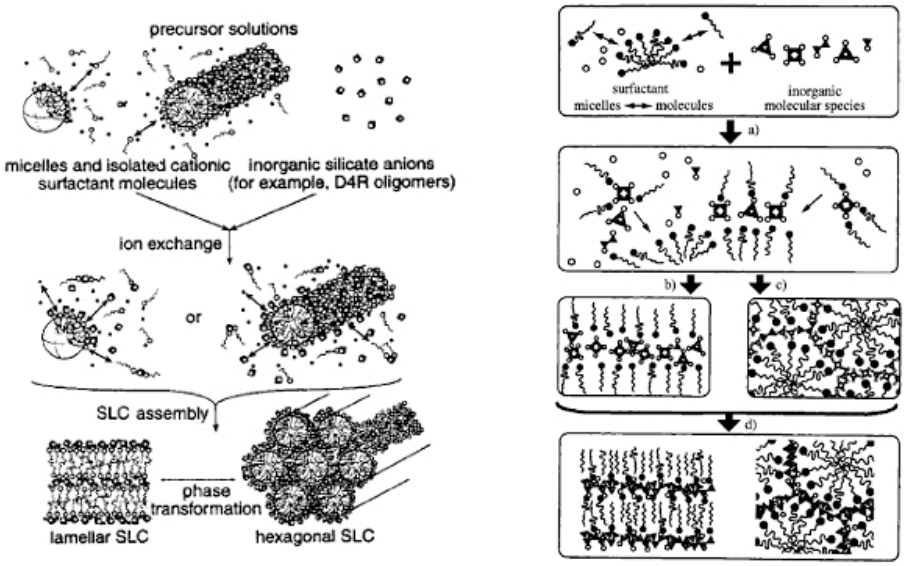

Figure 1.7 *Cooperative Formation Mechanism.*[50, 89] *used with permission from Ref.50, 89.*

More recently, the newer inorganic-driven phase separation mechanism has been proposed.[90] In this mechanism, interacting inorganic-organic species aggregated into large liquid-crystal particles where microphase separation of the inorganic and surfactant under high concentration conditions resulted in the final mesostructure. A phase separation resulting from this binding of surfactant to silica oligomers was first put forward by Chan et al,[91] who observed a liquid-liquid phase separation which formed droplets of concentrated silica oligomers and surfactant. These droplets

rearranged and further silica condensation caused microphase separation within the droplets, producing the organized mesostructure. This inorganic-driven phase-separation mechanism has gained further experimental support, suggesting that generally, inorganic and organic species aggregate into larger liquid-like particles, where microphase separation of the inorganic and surfactant under high concentration conditions results in the formation of the final mesostructure.[92, 93]

Recently, Linton et al developed the SBA-15 formation mechanism using in-situ X-ray scattering.[94] After addition of the silica sources, the siliceous species attach to the PEO part of micelles and continuously increase the density in the PEO layer,[95, 96] and this eventually leads to phase separation of flocs,[97, 98] consisting of siliceous species and Pluronic molecules in a dilute aqueous solution. Later a mixed system is formed after nucleation, having spherical micelles in solution and in the floc or a mixture of spherical and differently sized elongated micelles in the floc. As a consequence of the higher local concentration of polymer and silicate in the flocs, the micelles coalesce to cylinders,[97] which arrange in a nematic-like phase followed, by eventually , the hexagonal phase appearing.

Specifically concerning silica films synthesized at the air/water interface in acid solutions, until now most of the in-situ studies have been done in acid solution since silica polymerization is relatively slower in acid solution than in alkaline solution and because film formation had only been observed in acidic solutions, while only precipitates were found in alkaline solutions. In situ X-ray and neutron scattering studies initially showed that silica species and surfactant associate to produce micelles with a diffuse silica coating. These micelles can migrate to the solution interface where an ultra-thin inorganic layer already exists[99] or form particles by coacervation in the subphase which then are responsible for film formation. More recent studies show that the film formation process is concentration dependent. When the silicate-to-surfactant molar ratio is at a high or low ratio, highly elongated silicate coated micelles were mainly observed in bulk solutions while between these ratios, highly ordered phase-separated mesostructured silica particles dominate in the solution. Surface-driven and particle driven film formation has been reported by our

group.[86, 100-102]

Mesoporous films have developed a lot over the past few years. Manipulation of the surfactant and inorganic species concentration, pH values and addition of other solvent have allowed great flexibility in tuning the film structure, large scale morphologies and pore sizes; However, further investigations are still needed to explain the mechanism which will supply efficient control over the synthesis of mesoporous materials and thus facilitate specific applications.

1.2.3 Precursor Reactivity

Compared to transition metal precursors, silicate precursors have been more frequently used as the starting point for the formation of ordered mesoporous materials templated by surfactants. It has been extensively studied because silicon is comparatively less susceptible to nucleophilic attack since it is electropositive, therefore the kinetics of hydrolysis and condensation is considerably slower than observation for transition metal system, making the studies easier.[103]

The most commonly used precursors are tetramethoxysilane (TMOS) and tetraetholxysilane (TEOS), as shown in **Figure 1.8**. however because these materials are expensive and generate alcohols during hydrolysis, which are environmentally unfavourable and also can change surfactant packing parameter resulting in different structures, so cheaper precursors such as sodium silicate solutions are also used.

Figure 1.8 *Molecular structure of most commonly used silicate precursors.*

The silica isoelectric point is pH = 2, which appears as a boundary for the polymerization of silicate precursors. When the pH is above 2, it is generally assumed that the condensation rate is proportional to $[OH^-]$, and the silicate reactions are as follows:

$$\equiv Si-OH + OH^- \rightarrow \equiv Si-O^- + H_2O$$
$$\equiv Si-O^- + HO-Si \equiv \rightarrow \equiv Si-O-Si \equiv + OH^-$$

When pH is below 2, the polymerization rate is proportional to $[H^+]$,

$$\equiv Si-OH + H_3O^+ \rightarrow \equiv Si^+ + 2H_2O$$
$$\equiv Si^+ + HO-Si \equiv \rightarrow \equiv Si-O-Si \equiv + H^+$$

The silica sol can be synthesized by hydrolysis of tetrafunctional alkoxide precursors either under acid or base conditions. The whole process can be described as follows:

Hydrolysis

$$\equiv Si-OR + H_2O \rightarrow \equiv Si-OH + ROH$$

Water condensation

$$\equiv Si-OH + HO-Si \equiv \rightarrow \equiv Si-O-Si \equiv + H_2O$$

Alcohol condensation

$$\equiv Si-OR + HO-Si \equiv \rightarrow \equiv Si-O-Si \equiv + ROH$$

In the hydrolysis reaction, hydroxyl groups replace alkoxide groups and subsequent condensation reactions produce siloxane bonds, forming linkage networks $-Si-O-Si-$ with the by-products, alcohol and water.

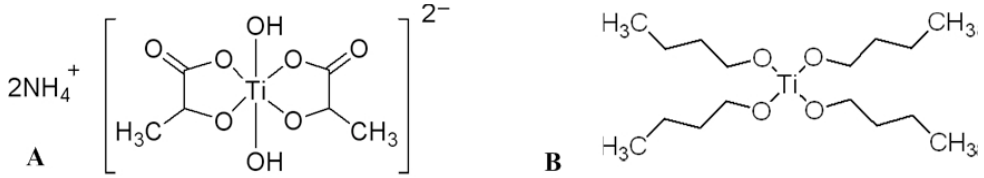

Figure 1.9 *Molecular structure of Titanium (IV) bis (ammonium lactato dihydroxide (TiBALD, A) and Titanium butoxide (TiB, B).*

Transition metal precursors are frequently highly reactive in the presence of water thus it is necessary to control moisture when used. The reactivity of these materials is partially derived from a low electro-negativity and a desire to fill the metal coordination sphere as titanium (IV) and other transition metal reactants, such as alkoxides, $M(OR)_z$, have four ligands rather than the desired six.[104, 105] The most

commonly used transition metal precursors in our research are titanium (IV) bis (ammonium lactato)dihydroxide and titanium butoxide (**Figure 1.9**). While the titanium alkoxides hydrolyze rapidly, Titanium (IV) bis(ammonium lactato) dihydroxide (TiBALD) is stable at ambient temperature in neutral solution which may be a good candidate to synthesize titania oxide films under aqueous conditions.

Alkoxides represent a common reactant in the production of mesoporous materials and in aqueous conditions promptly undergo hydrolysis and condensation through alcoxolation and oxolation reactions. These reactions lead to the formation of inorganic polymers that may precipitate from solution, as shown in **Figure 1.10**.

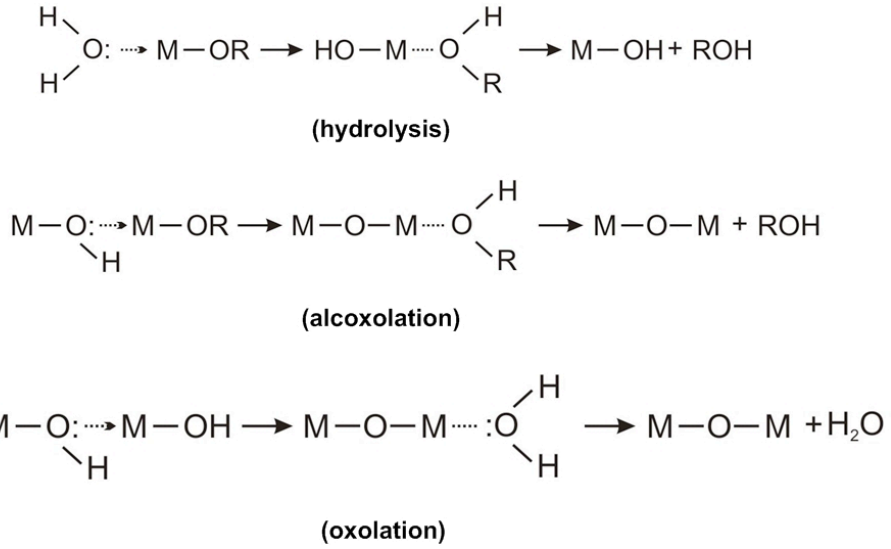

Figure 1.10 *hydrolysis, alcoxidation and oxolation reactions of metal alkoxides.*[104]

Control of hydrolysis and condensation reactions is a key issue for generation of ordered, crystalline transition metal oxide materials. Inorganic hydrolysis and condensation have to be controlled to avoid the instantaneous formation of an inorganic network, which would irreversibly freeze an ill-organized structure. The reactivity of precursors is known to be efficiently controlled in different ways, such as adjusting pH; using nonaqueous solvents and limited quantities of water, resorting to evaporation induced self assembly, modifying the redox state and using preformed nano-objects to build the walls of the mesoporous material.

Generally two ways are employed to control the hydrolysis and condensation

processes of reactive alkoxides or chloroalkoxides. First is to complex the alkoxide precursors $M(OR)_n$ (M= Ti, Al, Zr,..) using acetylacetone, ethylene glycol or other chelating agents. These strong chelating agents also restrain the condensation reactions, leading to the presence of low-weight oligomeric species. The high surface to volume ratio of these oligomeric species makes them ideal to interact with surfactant molecules in the self assembly process but can disrupt the surfactant self-organisation into micelles. For example, acetylacetone was used as an inhibitor to control alumina oxide mesostructures in the presence of alkyl phosphate templates.[53, 106] Tris(ethylene glycolate)Ti and Zr complexes have been used to as starting species to create mesoporous titania and zirconia in alkaline media using alkylammonium templates.[107]

The other way is to add acid, strongly acidic conditions (pH<1) also help to control the reactivity of alkoxide $M(OR)_n$ (M= Ti, Al, Zr etc). Under strongly acidic conditions, condensation is hindered by protonation of M-OH nucleophilic species present in the medium, and the depolymerisation processes are promoted. Two dimensional hexagonal mesostructured TiO_2 was prepared in ethanol under high acid conditions using EISA method.[108]

Alternately, nonaqueous solvents and controlled amounts of water were also used to avoid massive precipitation of nonstructured phases. A typical example is the first synthesis of mesostructured alumina phases, reported by Bagshaw et al using non-ionic surfactants as template in alcohol/water mixture.[58] A great number of mesostructured metal oxides have been successfully obtained using ethanolic solutions of MCl_n and PEO based triblock copolymers, ordered hexagonal and cubic mesostructures were obtained using EISA method (see **Section 1.3.1.1** below).[109]

1.3 Templated Mesoporous Thin Films

1.3.1 Processing of Mesoporous Thin Films

Thin solid films can be prepared through a great number of different techniques, chemical solution deposition techniques, such as dip-, spin-, meniscus-, and

spray-coating, compatible with evaporation-induced self-assembly approach (EISA, where inorganic precursors and the organic template are cooperatively self-assembled at the surface of the substrate through the evaporation of solvent.)are the most employed.[110] Films have also been prepared by electrochemical techniques, by impregnation in vapour phase or in solution, by pulsed laser deposition techniques, and grown at the air/water or substrate-solution interface.

1.3.1.1 Chemical Solution Deposition

Chemical solution deposition is widely employed to synthesize thin porous film because it is cheap, easy to be use, and it is convenient to control the chemical state of both volatile and non-volatile parts in solution before self-assembly in chemical solution deposition. The solution is deposited on the substrate surface and is allowed to evaporate under specific conditions so as to control the evaporation speed of each volatile constituent. While the template and inorganic precursor solution becomes concentrated through evaporation, the self-assembly thus begins until a quasi equilibrium state is reached. Consolidation of the inorganic networks around the micelles and further anchoring of the film at the substrate surface are completed by further poly-condensation.

The initial solution deposition can be achieved by dip-coating technique, in which substrates withdraw from the solution at a constant rate. Reaction solution drains away to a particular thickness, which dependant upon evaporation, viscosity and dipping speed during the withdrawal process. Subsequent heating generates preferential evaporation of alcohol from the remaining solution leading to the development of a liquid crystal phase as the relative surfactant concentration increases. However, the rate of evaporation and structure formation are highly dependant upon both temperature and humidity.

Alternatively, spin coating was also widely used to prepare films. A small amount of solution is dropped onto the centre of a spinning substrate and spread by the centrifugal force. Spin coating is usually performed with partially hydrolysed precursors, utilises heating to evaporate solvent and allows formation of a liquid

crystal phase as a template. Use of evaporation makes the spin coating technique sensitive to both temperature and humidity, requiring attention to both factors. The film thickness is possible to be controlled by both the spinning rate and the viscosity of the precursor solution. The first report of highly ordered mesoporous films was published by Ogawa in 1994.[111] TMOS and acidic solutions containing CTAB were mixed and spin coated on to a substrate and dried at 100°C resulting in films with thickness of 1 μm.

Until now, a lot of thin films were synthesized by dip-coating and spin-coating techniques, and the films display different mesostructures such as lamellar, 2D hexagonal or cubic on the variation of surfactant/inorganic precursor molar ratio.[79, 112]

1.3.1.2 Spontaneous Film Growth at Different Interfaces

In addition to such solvent evaporation methods at a substrate, film formation may be performed at either a solid-liquid, liquid-liquid or air-liquid interface. Normally, the surfactant micelles and inorganic precursor condensation takes place forming a highly ordered inorganic-organic nano-composite at the interface.

Spontaneous growth of silicate film on a mica substrate was first reported almost simultaneously by Yang et al,[113] and Aksay et al[114]. An acid solution containing surfactant CTACl and the inorganic precursor TEOS were poured over a mica substrate which was laid horizontally. Thin ordered mesoporous films with thickness between 0.2 and 1.0 μm grew on the solid interface. Most of the mesoporous silicate films grown at the solid-liquid surface have been prepared under acidic conditions using CTAB or CTACl as the structure directing agents and TEOS as the inorganic precursor. These films can be grown on different substrates, such as gold, borosilicate glass, silicon, graphite etc [114, 115] and the nature of the substrate affects the structure of the film formed on its surface.

Ordered mesostructured porous films can also be made at the liquid-liquid interface. Schacht reported the formation of mesoporous silicate fibers, spheres and thin sheets at the oil-water interface in 1996.[116] Also in 1996, the first surfactant/silicate films grown at the air/solution interface were reported almost simultaneously by Yang et

al[117] and Aksay et al,[114] these films form from quiescent dilute acidic solutions containing a silica precursor and the surfactant template. Further studies suggested that the mesoporous thin films were formed by self-assembling surfactant micelles in solution which templated the polymerised silica. The micelles were suggested to pack at the air-liquid interface to from highly ordered arrays, to give the final structure of a 2D hexagonal mesophase with the cylindrical micelles aligned parallel to the surface. More recently the formation of these films was shown to be concentration dependant, growing either from silica-coated micelles or phase-separated inorganic-surfactant composite particles, behaviour which was identified as similar to that of soluble polymers interacting with micelles in solution.[31, 100] In recent years, therefore by substituting the silicate precursors for a polymer, highly ordered free standing solid polyelectrolyte films have also been prepared at the air/solution interface using solutions of positive surfactants and neutral polyelectrolytes.[31] These polymer films are much more flexible and robust allowing them to be removed easily from the air-water surface and resulting in free-standing films.

Compared to the solution deposition techniques for a single layer, for growth at interfaces, the processing time is generally longer but it provides free-standing and self-supporting films potentially useful as membranes for separation or catalysis as well as a system which is very useful to understand the formation mechanism of silica-surfactant materials.[86, 118, 119] Another advantage is that the nanostructure in films produced by evaporation methods is extremely sensitive to preparation conditions, particularly relative humidity, while structures grown from solution are far more reproducible and the mesostructure produced is insensitive to large variations in temperature and humidity.[120] Moreover, films grown at the interface are relatively much thicker than dip and spin coated films.

In recent years, the inorganic precursor used for syntheses of mesoporous films has extended to metal oxide films, which are required for application such as dye sensitised solar cells and batteries. Films produced by evaporation routes have a limited thickness determined by the deposition conditions and the concentration of the dipping solution, therefore multiple coatings are required to build up sufficiently thick

layers for the films to be used in these applications.[121] Thus the ability to grow thicker films of transition metal oxides using surfactant and polyelectrolyte complexes in a one-step manner is a real advantage of the solution self-assembly method. Based on all of these, formation of films at the air/liquid interface is a highly successful technique for production of highly ordered films and continues to be developed.

1.3.2 Development of Mesoporous Thin Films

1.3.2.1 Silica Thin Films

Beyond the relevant chemical and self-assembly phenomena, the shaping and geometry of ordered mesoporous materials is also extremely important for the practical application and gain wide interests of chemists and material scientists. Until now the majority of research studies concern ordered mesoporous materials as powders and monoliths, however, for many exciting application such as chemical sensing, solar cells, catalysis and separation,[42, 78, 122] it is advantageous to develop mesoporous materials in the form of thin films.

Silica films evolution was generally described in the previous section. Following a similar procedure, Sanchez and co-workers were able to identify the different parameters influencing the final structure of the mesoporous films prepared by EISA process. These films present various structures such as 2D-hexagonal, lamellar, wormlike or cubic, as shown in **Figure 1.11**.[111, 115, 123] It appears that during the dip-coating step, the relative humidity in the chamber for film deposition has a strong influence on the final structure of the film.[124] Porosity, pore shape and inorganic wall size are also governed by the dimension of the micelles, the surfactant/Si molar ratio and the water content in the film.[83]

Growth of silica films at the air/water interface has been extensively investigated in our group. CTAB templated mesostructured films were prepared in acidic solution at the air/water interface as a function of the CTAB/TMOS molar ratio, GIXD measurements showed that the films were composed of hexagonally packed cylindrical micelles aligned parallel to the surface.[125] High humidity slows down the growth process due to lack of evaporation and increased temperatures decrease the

film formation time.[120] Using non-ionic surfactant $C_{16}EO_8$, distorted 2D-hexagonal phase and the cubic phases $Pm\bar{3}n$ and $Im\bar{3}m$ were obtained at different TMOS-$C_{16}EO_8$ molar ratios. However, these films are brittle and lack mechanical strength and they are difficult to take off the interface, limiting their practical applications.

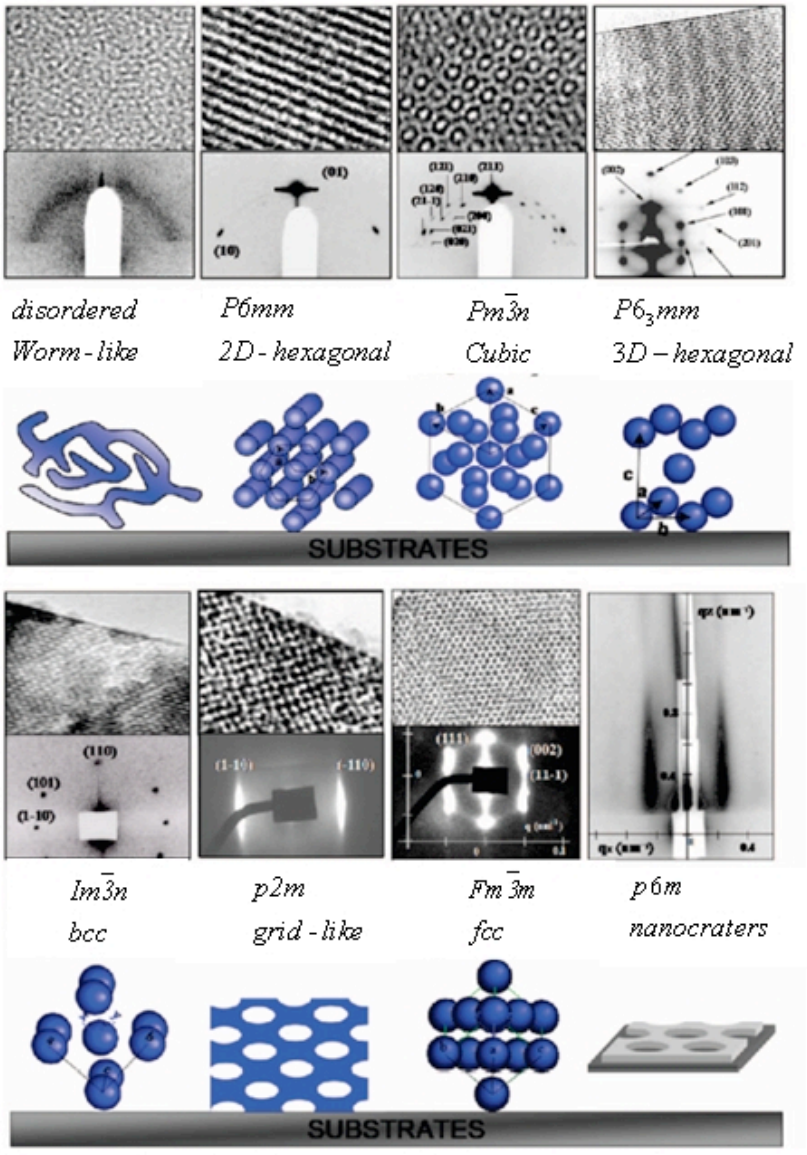

Figure 1.11 *Two dimensional SAXS patterns corresponding to the various types of mesostructures obtained for silica films prepared using the EISA process.[83, 126] Used with permission from Ref. 83, 126.*

1.3.2.2 Non Silica Transition Metal Oxide Films

Mixed transition metal silicon oxide thin films have now also been created by coating method or growing at the solution interface. These impose a chemical challenge, because of the marked difference in hydrolysis condensation behaviour of transition metal and silicate cations. Homogeneous Ti-Si mixed mesoporous films were reported in 2002.[127]

Though the first non-silica oxide materials shaped as powders were reported as early as 1995 by Antonelli & Ying[53], Ying et al[55] and later by Yang et al[109], the first stable non-silicate based mesoporous ordered thin film was invented by Grosso et al[128]. It was made by mixing pluronic type copolymers and $TiCl_4$ deposited from a mixed water and ethanol solution under a very high acidity. By a careful control over the sol-gel chemistry, the nature of the template, the deposition process, a wide family of high quality, reproducible mesoporous thin films with nano-crystalline metal oxide wall have been obtained. Recently, the development of templates, such as poly (ethylene-co-butylene)-b-(poly(ethylene oxide) (KLE) allow the synthesis of TiO_2 thin films in less drastic experimental conditions.[129] Al_2O_3[130], CeO_2[61, 131], WO_3[132] and SnO_2 [133-135] thin films with periodically ordered mesostructure have also been reported. However, the EISA process is difficult and is highly dependant on strict control of variables such as temperature, humidity, substrate roughness etc during synthesis, so we seek alternate more reproducible methods for film production. The generation of these transition metal-based materials which would be widely used in sensors, decomposition of pollutants, solar cell technology etc, holds additional challenges in comparison to silica-based materials.

1.3.2.3 Polyelectrolytes Films

Polymerizing silica has been found to act as a neutral polyelectrolyte during the formation of nanostructured silica/surfactant films,[31] thus substituting the silicate precursor with a carbon polyelectrolyte, also results in formation of a film with an ordered liquid crystalline phase at the air-water surface. Compared to inorganic films, polyelectrolyte/surfactant films are much more flexible and robust allowing them to

be removed easily from the air-water surface and resulting in free-standing films.[30] These free-standing films have great potential to act as a delivery system for hydrophobic compounds, such as hydrophobic drugs[136], which could be released through the break down of films or slow diffusion out from the polymer/surfactant film.

The Edler group first reported that mixing polyethylenimine (PEI) and cationic alkyltrimethylammonium bromide (CTAB) surfactant results in a solid film with well organized 2D hexagonal structure composed of cylindrical micelles aligned to the air-solution interface.[31,135] Vaknin et al also later reported a 2D hexagonal phase composed of closely packed cylindrical micelles aligned parallel to the interface using mixture solution of poly (diallyl-dimethylammonium chloride) and sodium dodecyl sulfate (SDS) at the gas-water interface, similar to that observed in inorganic/surfactant films.[137] Different parameters, such as polymer molecular weight, pH, ionic strength, cross linker and temperature, play important roles in defining the film structure.[30, 32, 33] Small angle neutron scattering results indicate there is no liquid crystalline ordering in the bulk solution under these films. With the aid of small angle neutron reflectivity and X-ray reflectivity measurements, an evaporation driven steady state formation mechanism has been proposed. Dehydration of the upper layer of the solution via evaporation prompts aggregation in the bulk solution close to the interface, and as the distance from the interface increases the dehydration degree obtained will decrease until the enthalpic benefit becomes too small to promote further aggregation. Both phase separation and mesophase ordering only occur within the film.[33]

Mixing cationic surfactant and anionic surfactant results in cat-anionic surfactant solutions, in which two oppositely charged groups are distributed within mixed micelles. The micellar properties can be tailored by adjusting the competition of various molecular interactions (Van der waals, hydrophobic, electrostatic force etc), resulting in a variety of structures, such as cat-anionic vesicles, salts and micelles.[138-141] Cat-anionic complexes are reported to interact with hydrophobically modified biocompatible polymers,[142] DNA or charged polymers[143] and salts. The Edler

group have also prepared polymer films with highly ordered mesophases at the air/water interface using water soluble polymers and cat-anionic surfactant mixtures.[144-146]

1.4 Surfactant/Polyelectrolyte Complex Templated Inorganic Materials

The formation of these films and structures are an interesting outcome of fundamental studies on the interactions between soluble polymers and surfactants and they may have potential applications. Our self-assembled membranes are a rapid and straightforward method to prepare ordered solid-state materials containing surfactant micelles and thus present a potential template for synthesis of robust inorganic mesostructured films. This use of these polymer/surfactant membranes to synthesis mesostructured inorganic oxide films is the central aim of this thesis.

Surfactant/polyelectrolyte complexes have been known for quite a while as a highly ordered organic solids with mesomorphous structures.[147] Such complexes generally form because of the coulombic interaction between the charged functional groups of the polyelectrolyte and an oppositely charged surfactant. Complexes of oppositely charged polyelectrolytes and surfactants were used in the presence of a silica source to prepare a series of mesoporous powders with different pore structures and morphology. Pantazis and Pomonis reported SBA-1 mesoporous silica particles templated by a poly(acrylic acid)-CTAB complex under acidic conditions, while addition of alkaline earths resulted in different morphologies.[148] Silicas synthesized using CTAB and Poly(4-styrenesulfonate sodium) (PSS) were without ordered mesostructures.[149] In the work of Pantazis and Pomonis, the pores were templated on the entire polymer/surfactant complex, not just the surfactant micelles, since the pore size varied with the size of the complex, controlled by the ionization degree of the polymer. Pang also studied mesoporous silica templated by CTAB and two ionic polymers, the anionic sulphonated aromatic poly(ether ether ketone) (SPEEK) or cationic poly(allylamine hydrochloride) (PAACl).[150] Using the anionic polymer with

CTAB produced bimodal pores, templated either on the CTAB micelles (2 nm) or the nanophase separated polymer particles (20 - 50 nm), while the cationic polymer used with CTAB produced unimodal pores (2 - 3 nm) with increasing disorder as the concentration of polymer increased. Highly ordered mesoporous materials constructed using mixtures of CTAB with poly(acrylic acid) having an integrated polymer/silica hybrid framework templated on the CTAB micelles were also reported by Kang et al.[151] Recently, polyelectrolyte/surfactant/aminosilanol complexes were processed into mesostructured silica hybrids.[152] However, these studies of mesoporous materials synthesized with polyelectrolyte/surfactant complexes are mainly concerned with powders, and in general they lack long range ordering of the mesostructure, regular morphology, or thermal stability.

In this work, employing the surfactant/polyelectrolytes complexes as co-templates we present the spontaneous formation of thick robust inorganic films at the air/solution interface. After an explanation of theories, techniques and experimental methods in Chapter Two, Chapter Three will describe ordered 2D hexagonal robust silica films synthesized using cationic surfactant CTAB and PEI, investigate the film forming solution and elaborate the film formation mechanism. Rapid synthesis of silica gel monoliths using surfactant and LPEI will also be discussed in Chapter three. Chapter Four will present silica films with a range of mesostructures synthesized with cat-anionic surfactant mixtures and several water soluble polymers. The different parameters which determine the final film mesostructure will also be included. In Chapter Five, this surfactant and polyelectrolyte complex mineralization work will be extended to growth of titania and iron oxide based mesostructured films at the air/water interface.

1.5 References

(1) J. S. Beck, J. C. Vartuli, W. J. Roth, M. E. Leonowicz, C. T. Kresge, K. D. Schmitt, C. T. W. Chu, D. H. Olson, E. W. Sheppard, S. B. Mccullen, J. B. Higgins, and J. L. Schlenker, *Journal of the American Chemical Society* **114**(27), 10834 (1992).

(2) J. M. Kim, Y. Y. Lyu, S. H. Yi, S. Y. Lee, L. S. Pu, J. E. Yie, K. Char, and S. Chang, *Abstracts of Papers of the American Chemical Society* **226**, U695 (2003).

(3) Y. Sakamoto, M. Kaneda, O. Terasaki, D. Y. Zhao, J. M. Kim, G. Stucky, H. J. Shim, and R. Ryoo, *Nature* **408**(6811), 449 (2000).

(4) D. Y. Zhao, Q. S. Huo, J. L. Feng, J. M. Kim, Y. J. Han, and G. D. Stucky, *Chemistry of Materials* **11**(10), 2668 (1999).

(5) S. D. Shen, A. E. Garcia-Bennett, Z. Liu, Q. Y. Lu, Y. F. Shi, Y. Yan, C. Z. Yu, W. C. Liu, Y. Cai, O. Terasaki, and D. Y. Zhao, *Journal of the American Chemical Society* **127**(18), 6780 (2005).

(6) G. S. Attard, J. C. Glyde, and C. G. Goltner, *Nature* **378**(6555), 366 (1995).

(7) D. Y. Zhao, J. L. Feng, Q. S. Huo, N. Melosh, G. H. Fredrickson, B. F. Chmelka, and G. D. Stucky, *Science* **279**(5350), 548 (1998).

(8) D. F. Evans, and H. Wennerström, *The colloidal domain : where physics, chemistry, biology, and technology meet*. Wiley-VCH: New York, 1999.

(9) J. N. Israelachvili, D. J. Mitchell, and B. W. Ninham, *Journal of the Chemical Society-Faraday Transactions Ii* **72**, 1525 (1976).

(10) R. Meszaros, L. Thompson, M. Bos, I. Varga, and T. Gilanyi, *Langmuir* **19**(3), 609 (2003).

(11) L. A. Bastardo, V. M. Garamus, M. Bergstrom, and P. M. Claesson, *Journal of Physical Chemistry B* **109**(1), 167 (2005).

(12) A. F. Thunemann, *Progress in Polymer Science* **27**(8), 1473 (2002).

(13) M. A. C. Stuart, B. Hofs, I. K. Voets, and A. de Keizer, *Current Opinion in Colloid & Interface Science* **10**(1-2), 30 (2005).

(14) J. Penfold, R. K. Thomas, and D. J. F. Taylor, *Current Opinion in Colloid & Interface Science* **11**(6), 337 (2006).

(15) D. J. F. Taylor, R. K. Thomas, and J. Penfold, *Advances in Colloid and Interface Science* **132**(2), 69 (2007).

(16) E. D. Goddard, *Colloids and Surfaces* **19**(2-3), 255 (1986).

(17) E. D. Goddard, *Colloids and Surfaces* **19**(2-3), 301 (1986).

(18) H. J. Liu, and M. T. Hai, *Journal of Chemical and Engineering Data* **55**(1), 354 (2010).

(19) A. Mezei, A. Abraham, K. Pojjak, and R. Meszaros, *Langmuir* **25**(13), 7304 (2009).

(20) M. A. Winnik, S. M. Bystryak, C. Chassenieux, V. Strashko, P. M. Macdonald, and J. Siddiqui, *Langmuir* **16**(10), 4495 (2000).

(21) M. T. Hai, and B. X. Han, *Journal of Chemical and Engineering Data* **51**(5), 1498 (2006).

(22) D. McLoughlin, M. Delsanti, P. A. Albouy, and D. Langevin, *Molecular Physics* **103**(21-23), 3125 (2005).

(23) M. A. Winnik, S. M. Bystryak, and J. Siddiqui, *Macromolecules* **32**(3), 624 (1999).

(24) Y. Li, R. Xu, S. Couderc, D. M. Bloor, J. Warr, J. Penfold, J. F. Holzwarth, and E. Wyn-Jones, *Langmuir* **17**(18), 5657 (2001).

(25) J. Penfold, I. Tucker, R. K. Thomas, and J. Zhang, *Langmuir* **21**(22), 10061 (2005).

(26) J. Penfold, I. Tucker, R. K. Thomas, D. J. F. Taylor, J. Zhang, and X. L. Zhang, *Langmuir* **23**(7), 3690 (2007).

(27) J. Penfold, I. Tucker, R. K. Thomas, D. J. F. Taylor, J. Zhang, and C. Bell, *Langmuir* **22**(21), 8840 (2006).

(28) D. B. Kudryavtsev, R. F. Bakeeva, L. A. Kudryavtseva, L. Y. Zakharova, and V. F. Sopin, *Russian Chemical Bulletin* **49**(9), 1501 (2000).

(29) R. von Klitzing, B. Kolaric, W. Jaeger, and A. Brandt, *Physical Chemistry Chemical Physics* **4**(10), 1907 (2002).

(30) B. M. D. O'Driscoll, E. Milsom, C. Fernandez-Martin, L. White, S. J. Roser, and K. J. Edler, *Macromolecules* **38**(21), 8785 (2005).

(31) K. J. Edler, A. Goldar, T. Brennan, and S. J. Roser, *Chemical Communications* (14), 1724 (2003).

(32) B. M. D. O'Driscoll, C. Fernandez-Martin, R. D. Wilson, S. J. Roser, and K. J. Edler, *Journal of Physical Chemistry B* **110**(11), 5330 (2006).

(33) B. M. D. O'Driscoll, C. Fernandez-Martin, R. D. Wilson, J. Knott, S. J. Roser, and K. J. Edler, *Langmuir* **23**(8), 4589 (2007).

(34) G. J. D. Soler-illia, C. Sanchez, B. Lebeau, and J. Patarin, *Chemical Reviews* **102**(11), 4093 (2002).

(35) C. T. Kresge, M. E. Leonowicz, W. J. Roth, J. C. Vartuli, and J. S. Beck, *Nature* **359**(6397), 710 (1992).

(36) G. J. D. A. Soler-Illia, E. L. Crepaldi, D. Grosso, and C. Sanchez, *Current Opinion in Colloid &*

Interface Science **8**(1), 109 (2003).

(37) P. T. Tanev, and T. J. Pinnavaia, *Science* **267**(5199), 865 (1995).

(38) S. A. Bagshaw, E. Prouzet, and T. J. Pinnavaia, *Science* **269**(5228), 1242 (1995).

(39) M. Antonietti, B. Berton, C. Goltner, and H. P. Hentze, *Advanced Materials* **10**(2), 154 (1998).

(40) D. Y. Zhao, Q. S. Huo, J. L. Feng, B. F. Chmelka, and G. D. Stucky, *Journal of the American Chemical Society* **120**(24), 6024 (1998).

(41) N. S. Ramgir, Y. K. Hwang, S. H. Jhung, H. K. Kim, J. S. Hwang, I. S. Mulla, and J. S. Chang, *Applied Surface Science* **252**(12), 4298 (2006).

(42) A. Corma, *Chemical Reviews* **97**(6), 2373 (1997).

(43) L. Nicole, C. Boissiere, D. Grosso, P. Hesemann, J. Moreau, and C. M. Sanchez, *Chemical Communications* (20), 2312 (2004).

(44) A. Corma, P. Atienzar, H. Garcia, and J. Y. Chane-Ching, *Nature Materials* **3**(6), 394 (2004).

(45) P. Y. Feng, X. H. Bu, G. D. Stucky, and D. J. Pine, *Journal of the American Chemical Society* **122**(5), 994 (2000).

(46) D. Y. Zhao, J. Y. Sun, Q. Z. Li, and G. D. Stucky, *Chemistry of Materials* **12**(2), 275 (2000).

(47) M. Tiemann, and M. Froba, *Chemistry of Materials* **13**(10), 3211 (2001).

(48) P. Behrens, *Angewandte Chemie-International Edition in English* **35**(5), 515 (1996).

(49) A. Sayari, and P. Liu, *Microporous Materials* **12**(4-6), 149 (1997).

(50) Q. S. Huo, D. I. Margolese, U. Ciesla, D. G. Demuth, P. Y. Feng, T. E. Gier, P. Sieger, A. Firouzi, B. F. Chmelka, F. Schuth, and G. D. Stucky, *Chemistry of Materials* **6**(8), 1176 (1994).

(51) Q. S. Huo, D. I. Margolese, U. Ciesla, P. Y. Feng, T. E. Gier, P. Sieger, R. Leon, P. M. Petroff, F. Schuth, and G. D. Stucky, *Nature* **368**(6469), 317 (1994).

(52) U. Ciesla, S. Schacht, G. D. Stucky, K. K. Unger, and F. Schuth, *Angewandte Chemie-International Edition in English* **35**(5), 541 (1996).

(53) D. M. Antonelli, and J. Y. Ying, *Angewandte Chemie-International Edition in English* **34**(18), 2014 (1995).

(54) U. Bach, D. Lupo, P. Comte, J. E. Moser, F. Weissortel, J. Salbeck, H. Spreitzer, and M. Gratzel, *Nature* **395**(6702), 583 (1998).

(55) D. M. Antonelli, and J. Y. Ying, *Angewandte Chemie-International Edition in English* **35**(4), 426 (1996).

(56) D. M. Antonelli, A. Nakahira, and J. Y. Ying, *Inorganic Chemistry* **35**(11), 3126 (1996).

(57) F. Schuth, U. Ciesla, S. Schacht, M. Thieme, Q. Huo, and G. Stucky, *Materials Research Bulletin* **34**(3), 483 (1999).

(58) S. A. Bagshaw, and T. J. Pinnavaia, *Angewandte Chemie-International Edition in English* **35**(10), 1102 (1996).

(59) V. Subramanian, J. C. Jiang, P. H. Smith, and B. Rambabu, *Journal of Nanoscience and Nanotechnology* **4**(1-2), 125 (2004).

(60) T. Brezesinski, M. Antonietti, M. Groenewolt, N. Pinna, and B. Smarsly, *New Journal of Chemistry* **29**(1), 237 (2005).

(61) T. Brezesinski, B. Smarsly, M. Groenewolt, M. Antonietti, D. Grosso, C. Boissiere, and C. Sanchez, *Nanoporous Materials Iv* **156**, 243 (2005).

(62) T. Brezesinski, M. Groenewolt, M. Antonietti, and B. Smarsly, *Angewandte Chemie-International Edition* **45**(5), 781 (2006).

(63) F. Jiao, J. C. Jumas, M. Womes, A. V. Chadwick, A. Harrison, and P. G. Bruce, *Journal of the American Chemical Society* **128**(39), 12905 (2006).

(64) P. Liu, I. L. Moudrakovski, J. Liu, and A. Sayari, *Chemistry of Materials* **9**(11), 2513 (1997).

(65) A. Mazaj, S. Costacurta, N. Z. Logar, G. Mali, N. N. Tusar, P. Innocenzi, L. Malfatti, F. Thibault-Starzyk, H. Amenitsch, V. Kaucic, and G. J. A. A. Soler-Illia, *Langmuir* **24**(12), 6220 (2008).

(66) W. J. Hunks, and G. A. Ozin, *Journal of Materials Chemistry* **15**(35-36), 3716 (2005).

(67) B. Hatton, K. Landskron, W. Whitnall, D. Perovic, and G. A. Ozin, *Accounts of Chemical Research* **38**(4), 305 (2005).

(68) C. E. Fowler, S. L. Burkett, and S. Mann, *Chemical Communications* (18), 1769 (1997).

(69) S. Inagaki, S. Guan, Y. Fukushima, T. Ohsuna, and O. Terasaki, *Journal of the American Chemical Society* **121**(41), 9611 (1999).

(70) T. Asefa, M. J. MacLachlan, N. Coombs, and G. A. Ozin, *Nature* **402**(6764), 867 (1999).

(71) B. J. Melde, B. T. Holland, C. F. Blanford, and A. Stein, *Chemistry of Materials* **11**(11), 3302 (1999).

(72) S. Che, Z. Liu, T. Ohsuna, K. Sakamoto, O. Terasaki, and T. Tatsumi, *Nature* **429**(6989), 281 (2004).

(73) H. Y. Jin, Z. Liu, T. Ohsuna, O. Terasaki, Y. Inoue, K. Sakamoto, T. Nakanishi, K. Ariga, and S. N. Che, *Advanced Materials* **18**(5), 593 (2006).

(74) R. Ryoo, S. H. Joo, and S. Jun, *Journal of Physical Chemistry B* **103**(37), 7743 (1999).

(75) S. H. Joo, S. Jun, and R. Ryoo, *Microporous and Mesoporous Materials* **44**, 153 (2001).

(76) S. Jun, S. H. Joo, R. Ryoo, M. Kruk, M. Jaroniec, Z. Liu, T. Ohsuna, and O. Terasaki, *Journal of the American Chemical Society* **122**(43), 10712 (2000).

(77) M. S. Morey, A. Davidson, and G. D. Stucky, *Journal of Porous Materials* **5**(3-4), 195 (1998).

(78) A. Taguchi, and F. Schuth, *Microporous and Mesoporous Materials* **77**(1), 1 (2005).

(79) Y. F. Lu, R. Ganguli, C. A. Drewien, M. T. Anderson, C. J. Brinker, W. L. Gong, Y. X. Guo, H. Soyez, B. Dunn, M. H. Huang, and J. I. Zink, *Nature* **389**(6649), 364 (1997).

(80) M. H. Huang, F. Kartono, B. Dunn, and J. I. Zink, *Chemistry of Materials* **14**(12), 5153 (2002).

(81) D. Grosso, F. Babonneau, P. A. Albouy, H. Amenitsch, A. R. Balkenende, A. Brunet-Bruneau, and J. Rivory, *Chemistry of Materials* **14**(2), 931 (2002).

(82) D. Grosso, F. Babonneau, C. Sanchez, G. J. D. A. Soler-Illia, E. L. Crepaldi, P. A. Albouy, H. Amenitsch, A. R. Balkenende, and A. Brunet-Bruneau, *Journal of Sol-Gel Science and Technology* **26**(1-3), 561 (2003).

(83) D. Grosso, F. Cagnol, G. J. D. A. Soler-Illia, E. L. Crepaldi, H. Amenitsch, A. Brunet-Bruneau, A. Bourgeois, and C. Sanchez, *Advanced Functional Materials* **14**(4), 309 (2004).

(84) A. Brunet-Bruneau, A. Bourgeois, F. Cagnol, D. Grosso, C. Sanchez, and J. Rivory, *Thin Solid Films* **455-56**, 656 (2004).

(85) N. Baccile, G. Laurent, C. Bonhomme, P. Innocenzi, and F. Babonneau, *Chemistry of Materials* **19**(6), 1343 (2007).

(86) T. Brennan, S. J. Roser, S. Mann, and K. J. Edler, *Chemistry of Materials* **14**(10), 4292 (2002).

(87) C.-Y. Chen, S. L. Burkett, H.-X. Li, and M. E. Davis, *Microporous Materials* **2**(1), 27 (1993).

(88) A. Monnier, F. Schuth, Q. Huo, D. Kumar, D. Margolese, R. S. Maxwell, G. D. Stucky, M. Krishnamurty, P. Petroff, A. Firouzi, M. Janicke, and B. F. Chmelka, *Science* **261**(5126), 1299 (1993).

(89) A. Firouzi, D. Kumar, L. M. Bull, T. Besier, P. Sieger, Q. Huo, S. A. Walker, J. A. Zasadzinski, C. Glinka, J. Nicol, D. Margolese, G. D. Stucky, and B. F. Chmelka, *Science* **267**(5201), 1138 (1995).

(90) W. Z. Zhou, and J. Klinowski, *Chemical Physics Letters* **292**(1-2), 207 (1998).

(91) H. B. S. Chan, P. M. Budd, and T. D. Naylor, *Journal of Materials Chemistry* **11**(3), 951 (2001).

(92) S. Sadasivan, C. E. Fowler, D. Khushalani, and S. Mann, *Angewandte Chemie-International Edition* **41**(12), 2151 (2002).

(93) R. I. Nooney, D. Thirunavukkarasu, Y. M. Chen, R. Josephs, and A. E. Ostafin, *Chemistry of Materials* **14**(11), 4721 (2002).

(94) P. Linton, A. R. Rennie, M. Zackrisson, and V. Alfredsson, *Langmuir* **25**(8), 4685 (2009).

(95) V. L. Zholobenko, A. Y. Khodakov, M. Imperor-Clerc, D. Durand, and I. Grillo, *Advances in Colloid and Interface Science* **142**(1-2), 67 (2008).

(96) C. Boissiere, A. Larbot, C. Bourgaux, E. Prouzet, and C. A. Bunton, *Chemistry of Materials* **13**(10), 3580 (2001).

(97) K. Flodstrom, C. V. Teixeira, H. Amenitsch, V. Alfredsson, and M. Linden, *Langmuir* **20**(12), 4885 (2004).

(98) V. Alfredsson, H. Amenitsch, K. Flodstrom, M. Linden, C. V. Teixeira, and H. Wennerstrom, *Nanoporous Materials Iv* **156**, 69 (2005).

(99) A. S. Brown, S. A. Holt, T. Dam, M. Trau, and J. W. White, *Langmuir* **13**(24), 6363 (1997).

(100) T. Brennan, A. V. Hughes, S. J. Roser, S. Mann, and K. J. Edler, *Langmuir* **18**(25), 9838 (2002).

(101) K. J. Edler, T. Brennan, S. J. Roser, S. Mann, and R. M. Richardson, *Microporous and Mesoporous Materials* **62**(3), 165 (2003).

(102) K. J. Edler, A. Goldar, A. V. Hughes, S. J. Roser, and S. Mann, *Microporous and Mesoporous Materials* **44**, 661 (2001).

(103) C. J. Brinker, Scherer, G. W., *Sol-Gel Science*, (1990).

(104) F. Facca, G. Puccetti, and R. M. Leblanc, *Colloids and Surfaces a-Physicochemical and Engineering Aspects* **149**(1-3), 89 (1999).

(105) C. Sanchez, and J. Livage, *New Journal of Chemistry* **14**(6-7), 513 (1990).

(106) R. L. Putnam, N. Nakagawa, K. M. McGrath, N. Yao, I. A. Aksay, S. M. Gruner, and A. Navrotsky, *Chemistry of Materials* **9**(12), 2690 (1997).

(107) D. Khushalani, O. Dag, G. A. Ozin, and A. Kuperman, *Journal of Materials Chemistry* **9**(7), 1491 (1999).

(108) G. J. D. A. Soler-Illia, A. Louis, and C. Sanchez, *Chemistry of Materials* **14**(2), 750 (2002).

(109) P. D. Yang, D. Y. Zhao, D. I. Margolese, B. F. Chmelka, and G. D. Stucky, *Nature* **396**(6707), 152 (1998).

(110) G. J. A. A. Soler-Illia, E. L. Crepaldi, D. Grosso, D. Durand, and C. Sanchez, *Chemical Communications* (20), 2298 (2002).

(111) M. Ogawa, *Journal of the American Chemical Society* **116**(17), 7941 (1994).

(112) N. Petkov, S. Mintova, B. Jean, T. H. Metzger, and T. Bein, *Chemistry of Materials* **15**(11), 2240 (2003).

(113) H. Yang, A. Kuperman, N. Coombs, S. MamicheAfara, and G. A. Ozin, *Nature* **379**(6567), 703 (1996).

(114) I. A. Aksay, M. Trau, S. Manne, I. Honma, N. Yao, L. Zhou, P. Fenter, P. M. Eisenberger, and S. M. Gruner, *Science* **273**(5277), 892 (1996).

(115) M. Ogawa, *Chemical Communications* (10), 1149 (1996).

(116) S. Schacht, Q. Huo, I. G. VoigtMartin, G. D. Stucky, and F. Schüth, *Science* **273**(5276), 768 (1996).

(117) H. Yang, N. Coombs, I. Sokolov, and G. A. Ozin, *Nature* **381**(6583), 589 (1996).

(118) K. J. Edler, *Australian Journal of Chemistry* **58**(9), 627 (2005).

(119) K. J. Edler, *Soft Matter* **2**(4), 284 (2006).

(120) S. J. R. C. Fernandez-Martin, K.J. Edler, *Langmuir* **20**(24), 10679 (2004).

(121) K. Hou, B. Z. Tian, F. Y. Li, Z. Q. Bian, D. Y. Zhao, and C. H. Huang, *Journal of Materials Chemistry* **15**(24), 2414 (2005).

(122) F. Schuth, and W. Schmidt, *Advanced Materials* **14**(9), 629 (2002).

(123) C. J. Brinker, Y. F. Lu, A. Sellinger, and H. Y. Fan, *Advanced Materials* **11**(7), 579 (1999).

(124) F. Cagnol, D. Grosso, G. J. D. A. S. Soler-Illia, E. L. Crepaldi, F. Babonneau, H. Amenitsch, and C. Sanchez, *Journal of Materials Chemistry* **13**(1), 61 (2003).

(125) T. Brennan, S. J. Roser, S. Mann, and K. J. Edler, *Langmuir* **19**(7), 2639 (2003).

(126) C. Sanchez, C. Boissiere, D. Grosso, C. Laberty, and L. Nicole, *Chemistry of Materials* **20**(3), 682 (2008).

(127) N. Husing, B. Launay, D. Doshi, and G. Kickelbick, *Chemistry of Materials* **14**(6), 2429 (2002).

(128) D. Grosso, G. J. D. A. A. Soler-Illia, F. Babonneau, C. Sanchez, P. A. Albouy, A. Brunet-Bruneau, and A. R. Balkenende, *Advanced Materials* **13**(14), 1085 (2001).

(129) B. Smarsly, D. Grosso, T. Brezesinski, N. Pinna, C. Boissiere, M. Antonietti, and C. Sanchez, *Chemistry of Materials* **16**(15), 2948 (2004).

(130) M. Kuemmel, D. Grosso, U. Boissiere, B. Smarsly, T. Brezesinski, P. A. Albouy, H. Amenitsch, and C. Sanchez, *Angewandte Chemie-International Edition* **44**(29), 4589 (2005).

(131) T. Brezesinski, C. Erpen, K. Iimura, and B. Smarsly, *Chemistry of Materials* **17**(7), 1683 (2005).

(132) W. H. Lai, J. Shieh, L. G. Teoh, I. M. Hung, C. S. Liao, and M. H. Hon, *Journal of Alloys and Compounds* **396**(1-2), 295 (2005).

(133) T. Brezesinski, A. Fischer, K. Iimura, C. Sanchez, D. Grosso, M. Antonietti, and B. M. Smarsly, *Advanced Functional Materials* **16**(11), 1433 (2006).

(134) C. Velasquez, F. Rojas, J. M. Esparza, A. Ortiz, and A. Campero, *Journal of Physical Chemistry B* **110**(24), 11832 (2006).

(135) C. Velasquez, M. Luisa Ojeda, A. Campero, J. Marcos Esparza, and F. Rojas, *Nanotechnology* **17**(14), 3347 (2006).

(136) B. M. D. O'Driscoll, A. M. Hawley, and K. J. Edler, *Journal of Colloid and Interface Science* **317**(2), 585 (2008).

(137) D. Vaknin, S. Dahlke, A. Travesset, G. Nizri, and S. Magdassi, *Physical Review Letters* **93**(21), 218302 (2004).

(138) E. W. Kaler, A. K. Murthy, B. E. Rodriguez, and J. A. N. Zasadzinski, *Science* **245**(4924), 1371 (1989).

(139) E. W. Kaler, K. L. Herrington, A. K. Murthy, and J. A. N. Zasadzinski, *Journal of Physical Chemistry* **96**(16), 6698 (1992).

(140) L. L. Brasher, K. L. Herrington, and E. W. Kaler, *Langmuir* **11**(11), 4267 (1995).

(141) L. L. Brasher, and E. W. Kaler, *Langmuir* **12**(26), 6270 (1996).

(142) J. H. Lee, J. P. Gustin, T. H. Chen, G. F. Payne, and S. R. Raghavan, *Langmuir* **21**(1), 26 (2005).

(143) F. E. Antunes, E. F. Marques, R. Gomes, K. Thuresson, B. Lindman, and M. G. Miguel, *Langmuir* **20**(11), 4647 (2004).

(144) H. Chakraborty, and M. Sarkar, *Langmuir* **20**(9), 3551 (2004).

(145) K. J. Edler, M. J. Wasbrough, J. A. Holdaway, and B. M. D. O'Driscoll, *Langmuir* **25**(7), 4047 (2009).

(146) B. M. D. O'Driscoll, E. A. Nickels, and K. J. Edler, *Chemical Communications* (10), 1068 (2007).

(147) M. Antonietti, J. Conrad, and A. Thunemann, *Macromolecules* **27**(21), 6007 (1994).

(148) C. C. Pantazis, and P. J. Pomonis, *Chemistry of Materials* **15**(12), 2299 (2003).

(149) C. C. Pantazis, A. P. Katsoulidis, and P. J. Pomonis, *Chemistry of Materials* **18**(1), 149 (2006).

(150) J. B. Pang, H. Na, and Y. F. Lu, *Microporous and Mesoporous Materials* **86**(1-3), 89 (2005).

(151) Y. S. Kang, H. I. Lee, Y. Zhang, Y. J. Han, J. E. Yie, G. D. Stucky, and J. M. Kim, *Chemical Communications* (13), 1524 (2004).

(152) S. Koga, and S. Mann, *Journal of Materials Chemistry* **20**(27), 5736 (2010).

Chapter 2 Experimental

2.1 Principles of Analysis

Various techniques have been used to investigate the surfactant and polyelectrolyte templated inorganic films. In situ interfacial film development was investigated using Brewster angle microscopy (BAM), time-resolved reflectivity; and the interfacial film structure was clarified by grazing incidence diffraction. To understand the film forming process, the subphase solution phase evolution was examined by the time-resolved small angle X-ray scattering (SAXS). Neutron reflectivity and SAXS data were modeled with programs that run in the IGOR PRO software. Dry film textural properties were studied by SAXS, nitrogen adsorption and TGA. The theories and techniques are explained in this Chapter.

2.1.1 Neutron and X-ray scattering

2.1.1.1 Neutron

Since Bertram Brockhouse and Clifford Shull used neutrons to develop neutron diffraction and neutron spectroscopy techniques, neutrons (an uncharged subatomic particles with mass 1839 times that of the electron ($m=1.67\times10^{-27}$ kg)) have been used to study condensed matter.

Neutrons scatter from materials by interacting with the nucleus of an atom rather than the electron cloud. Unlike X-rays where the scattering power increases in proportion to the number of electrons in the atom, the scattering power (cross-section) of an atom is not strongly related to its atomic number, thus it is easier to sense light atoms, to distinguish neighbouring elements in the periodic table as well as isotopes of the same element.

Neutron is a powerful technique to investigate the structure of materials since (1) The interaction of neutron with the nucleus of an atom is weak, making them a highly penetrating probe into the interior of materials. (2) Neutron energies are similar to the energy of atomic and electronic process, allowing energy scales from the μeV to eV

transitions within the electronic structure of materials. (3) Neutrons can be used for diffraction measurements since they have a wavelength similar to atomic spacing. (4) Neutrons have a magnetic moment that can couple directly to the magnetisation of materials on the atomic scale.

Neutron cross section (σ) is used to describe the amount of neutrons scattered by atoms. The cross section is the quantity that is actually measured in a scattering experiment. Suppose we measure the number of neutron scattered in a given direction as function of their energy E', as shown in **Figure 2.1**, the *differential cross section* $d\sigma$ is described as the number of neutrons scattered per second into $d\Omega$ in the direction θ (angle between the incident and scattered beams) and ϕ (a second azimuthal angle). Thus the *total cross section* is defined as:

$$\sigma_{tot} = \int_{all-directions} (\frac{d\sigma}{d\Omega}) d\Omega \qquad \textbf{(2.1)}$$

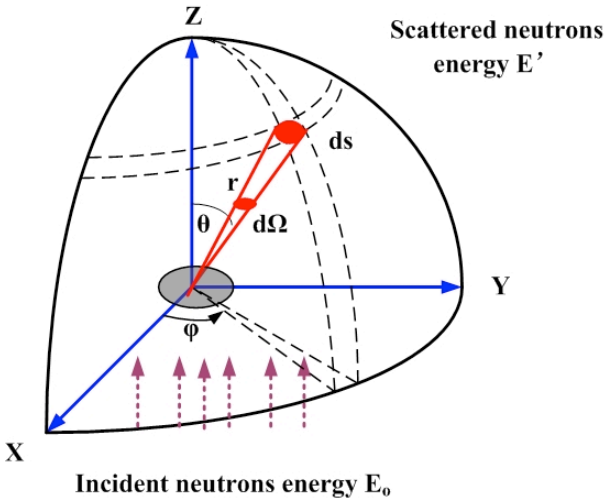

Figure 2.1 *Geometry for scattering experiment*[1]

Assuming it is an elastic scattering and indicating the velocity of the neutrons as v, the number of scattered neutrons passing through an area ds per second is

$$vds\left|\varphi_s\right|^2 = vds\frac{b^2}{r^2} = vb^2 d\Omega \qquad \textbf{(2.2)}$$

where φ_s is the wave-function of the scattered neutrons at the point r.

Φ is incident flux which is described as the number of incident neutrons per unit area per second:

$$\Phi = v|\varphi_i|^2 = v \tag{2.3}$$

so

$$\frac{d\sigma}{d\Omega} = \frac{vb^2 d\Omega}{\Phi d\Omega} = b^2 \tag{2.4}$$

and then integrating over all space (4π steradians), we obtain

$$\sigma_{tot} = 4\pi b^2 \tag{2.5}$$

The *differential cross section* is

$$\frac{d\sigma}{d\Omega}(q) = \frac{1}{N}\left|\sum_i^N b_i e^{iqr}\right|^2 \tag{2.6}$$

The discussion above focus on atomic properties, but there are many problems where the length scales in questions are much larger than atomic dimensions therefore we define a quantity called the *scattering length density*.

$$\rho = \sum_{i=1}^{N} b_i \times \frac{dN_A}{MW} \tag{2.7}$$

where d is the physical density, N_A is Avogadro's number, MW is molecular weight and b_i is the neutron scattering length of the element. The variation of b_i for different elements and isotopes is random.

2.1.1.2 X-ray

X-ray is electromagnetic radiation with wavelength from 10^{-2} to 10^2 Å, but only a narrow wavelength range (of 0.5-2.5 Å) is used for the study of the material structure. The Kα characteristic radiation from a copper target tube (wavelength of 1.15418 Å) is generally used for laboratory studies on materials. This wavelength is the same order of magnitude as most inter-atomic distances of interest in condensed matter, thus it can be utilized to probe the structure.

A monochromator is utilized to select the X-rays of a similar wavelength from a broad spectrum emitted by a synchrotron radiation source. X-rays propagate with the

speed of light $c = 2.998 \times 10^8 (\text{m/s})$, and the wavelength λ and the frequency v are related as

$$\lambda = \frac{c}{v} \tag{2.8}$$

The scattering is catalougued into two types: one is *compton scattering* (incoherent scattering)[2] and the other is *rayleigh scattering* (coherent scattering)[3]. Compton scattering is produced when a photon hits an electron and is bounced away, this process will lose energy which results in a different wavelength than the incident radiation. Rayleigh scattering happens when photons colloide with strongly bound electrons. The eletrons start oscillating at the same frequency as that of the incoming radiation. The electrons emit radiation with the same frequency due to the oscillation. Compton scattering can not carry structural information while coherent scattering contains the particle structure information since the emitted waves of neighbouring atoms oscillate strictly synchronously to each other.

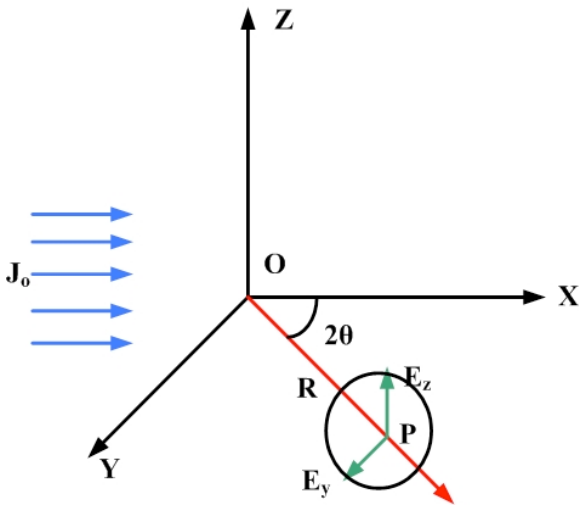

Figure 2.2 *Scattering of an unpolarized X-ray by a single free electron at the origin.*[4]

Taking a single electron as an example as shown in **Figure 2.2**. Assume a free electron is placed at position O and is irradiated with a beam of X-rays of flux J_o propagating in the direction of the X axis. The detector is placed at point P which is in the XY plane at a large distance R from O. The scattering angle between OX and OP

is 2θ. Since the electromagnetic wave is a transverse wave, its electric field vector E_o is in the plane YZ perpendicular to the propagation direction X.

The flux of energy reaching a unit area per second at P is given by

$$J_O(\frac{e^2}{mc^2})^2 \frac{1}{R^2}\frac{1+\cos^2 2\theta}{2} \tag{2.9}$$

where $J_O = E_O^2$. This unit area at P subtends a solid angle $1/R^2$ at O, and therefore the energy scattered in the direction OP per unit solid angle per second, i.e., the flux J_e of the scattered X-ray is

$$J_e = J_O(\frac{e^2}{mc^2})^2 \frac{1+\cos^2 2\theta}{2} \tag{2.10}$$

This is called the *Thomson Formula* for the scattering of X-rays by a single electron. and e and m are the electronic charge and mass, respectively.

The factor e^2/mc^2 has dimension of length and is called the classical radius of the electron(r_e). Its numerical value is 2.818 x 10^{-15} m. thus, the *differential scattering cross section of an electron* for unpolarized X-rays is

$$(\frac{d\sigma}{d\Omega})_e = r_e^2 \frac{1+\cos^2 2\theta}{2} \tag{2.11}$$

the *scattering length of an electron* for unpolarized X-ray is

$$b_e = r_e(\frac{1+\cos^2 2\theta}{2})^{1/2} \tag{2.12}$$

By integrating throughout the solid angle Ω, we find the *total scattering cross section of an electron* to be

$$\sigma_e = \frac{8}{3}\pi r_e^2 \tag{2.13}$$

The numerical value of which is 6.65 x 10^{-2} m^2 = 0.665 barn (1 barn = 10 x 10^{-28} m^2), the cross section σ_e given in (**Equation 2.13**) is independent of the state of polarization of the incident X-rays. The scattering of X-rays from matter results entirely from the electrons in an atom.

The X-ray atomic scattering factor increases smoothly with atomic number (as shown in **Figure 2.3**). Therefore, with X-rays, scattering from heavy atoms, such as metal atoms, present in an organic molecule can often overwhelm the scattering from the rest of the molecule. However, neutron scattering plays a complementary role to X-ray scattering in the study of the structure of materials because the neutron cross section varies seemingly randomly among elements.

The large difference in the scattering cross section between hydrogen and deuterium plays a crucial role in neutron scattering. The deuterium labelling technique, where hydrogens are substituted with deuterium in some of the molecules, can effectively make the molecules selectively "visible" to neutron beams (**Figure 2.4**). A summary of the neutron and X-ray scattering length densities (SLD) of the materials used in this work is shown in **Table 2.1.**

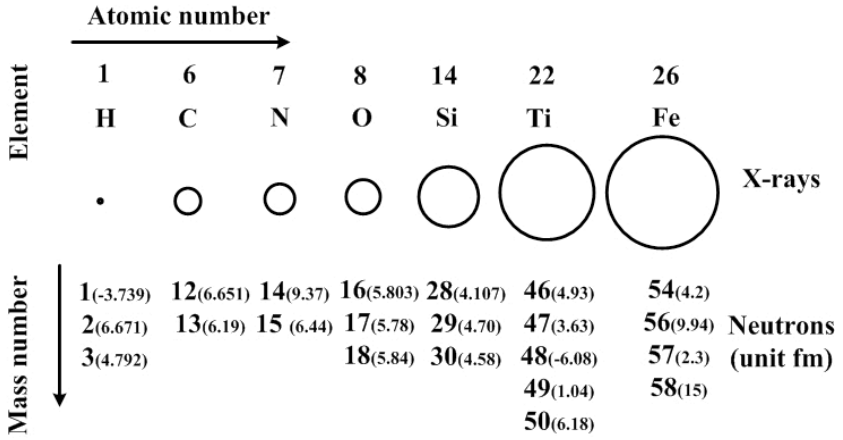

Figure 2.3 *Schematic representation of neutron and x ray scattering length variation with selected element, more information can be obtained at website* http://www.ncnr.nist.gov/resources/n-lengths/.

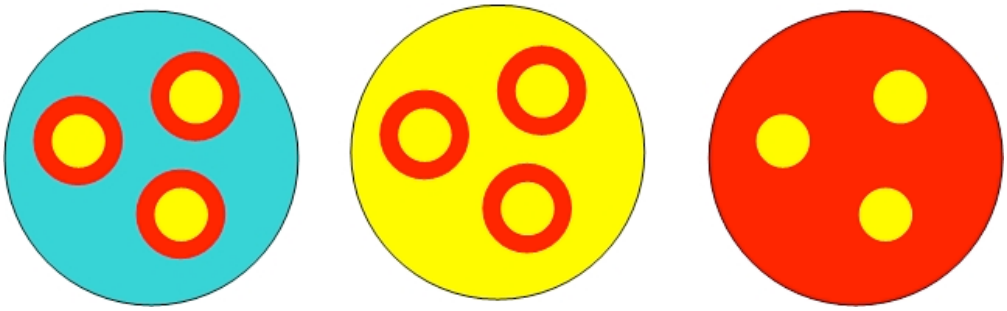

Figure 2.4 *An example of deuterium labeling showing the effect of contrast variation on the measurable structure of a core-shell particle.*[5]

Table 2.1 *Summary of X-ray and neutron scattering length densities of materials used, which are calculated using* ***Equation 2.7 and 2.13.***

Compound	Chemical structure	Density (g/ml)	Neutron SLD	X-ray SLD
Silicon oxide	SiO_2	2.160[6]	3.41 x10^{-6} Å^{-2}	1.82x10^{-5} Å^{-2}
TMOS	$Si(OCH_3)_4$	1.023[a]	3.67 x10^{-7} Å^{-2}	9.32 x10^{-6} Å^{-2}
CTAB head group	$N(CH_3)_3$	0.926	-4.1 x10^{-7} Å^{-2}	9.01 x10^{-6} Å^{-2}
CTAB tail	$CH_3(CH_2)_{15}$	0.820[6]	-3.73 x10^{-7} Å^{-2}	7.94x10^{-6} Å^{-2}
SDS head group	OSO_3	0.702	1.14 x10^{-6} Å^{-2}	5.93 x10^{-6} Å^{-2}
SDS tail	$CH_3(CH_2)_{11}$	0.802[7]	-3.91 x10^{-7} Å^{-2}	7.77 x10^{-6} Å^{-2}
PEI	(CH_2CH_2NH)	1.080[a]	5.98 x10^{-7} Å^{-2}	1.02 x10^{-5} Å^{-2}
Deuterated water	D_2O	1.107[a]	6.37 x10^{-6} Å^{-2}	9.35 x10^{-6} Å^{-2}
Water	H_2O	0.997[a]	-5.58 x 10^{-7} Å^{-2}	9.37 x10^{-6} Å^{-2}

a, density obtained from MSDS form on the Aldrich website.

2.1.2 X-ray and Neutron Sources

2.1.2.1 X-ray Sources

X-rays were first generated by Coolidge in 1913. Electrons, which are released from a hot tungsten filament, are accelerated toward a metal target in an evacuated tube, and X-rays are generated on the impact of the electrons at the target.

Synchrotron radiation sources are huge facilities, which are designed to provide intense X-ray beams and ultraviolet light. In a synchrotron, a closed orbit is designed

with a series of bending magnets placed along the ring circumference whose size ranges from about 50 to 1000 m. A charged particle that is accelerated emits electromagnetic radiation, and bending is a form of acceleration. A beam of electrons is made to circulate on this closed orbit under high vacuum in a storage ring until it is accelerated to an energy on the order of Gigaelectron Volts (GeV). The flux of X-rays emitted is many orders of magnitude greater than that obtainable with conventional X-ray tubes, making a single measurement very rapid and therefore is suitable for rapid time series measurements with samples undergoing dynamic evolution.[4]

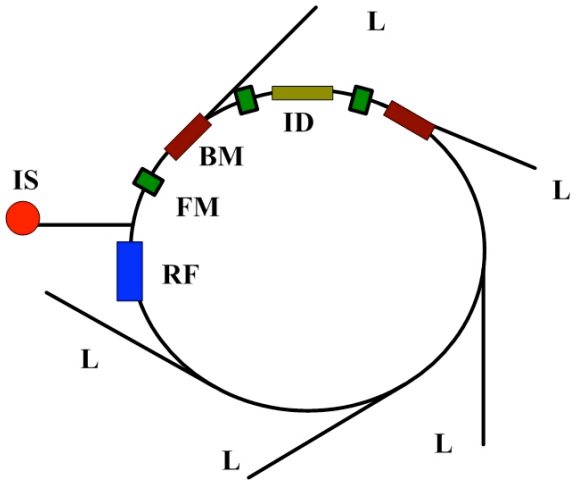

Figure 2.5 *Schematics of a synchrotron radiation facility.*[4]

Figure 2.5 illustrate the components of the storage ring. In this graph, **IS** is the injection system, which generates electrons, accelerates them and injects them into the vacuum chamber. **RF** is the radiofrequency cavity system, which restores the energy the circulating electrons lose through the emission of electromagnetic radiation. **BM** are bending magnets which bend the trajectory of the electrons and force them to circulate in a closed orbit. **FM** represent the focusing magnets which fine tune the electron beam trajectory to keep the electrons within a narrow range of defined path. **L** are beam lines through which the electromagnetic radiation exits into the user's experimental chambers. **ID** are insertion devices, such as wigglers and undulators, inserted into straight sections of the ring. They further modify the electron trajectories from a straight line, and thereby induce emission of additional synchrotron radiation.

There are about 50 synchrotrons in the world. The most powerful ones are such as the Diamond in Oxfordshire, UK; Advance Photon Source in Illinois, USA, Spring-8 in Nashi Harima, Japan and the European Synchrotron Radiation Facility (ESRF) in Grenoble, France.

Our X-ray experiments were conducted on beamline I22 at Diamond, Oxfordshire, UK. Diamond is a new X-ray source and it went into operation in 2007 (**Figure 2.6**). In Diamond synchrotron source, low energy electrons are generated by an electron gun and then are fed into the first accelerator linac. Then it enters the booster synchrotron when the energy is increased to around 100 MeV. After that it is injected into the massive storage ring when the electrons energy is boosted to final energy of 3 GeV. More information could be found on their Diamond light sources website.[8]

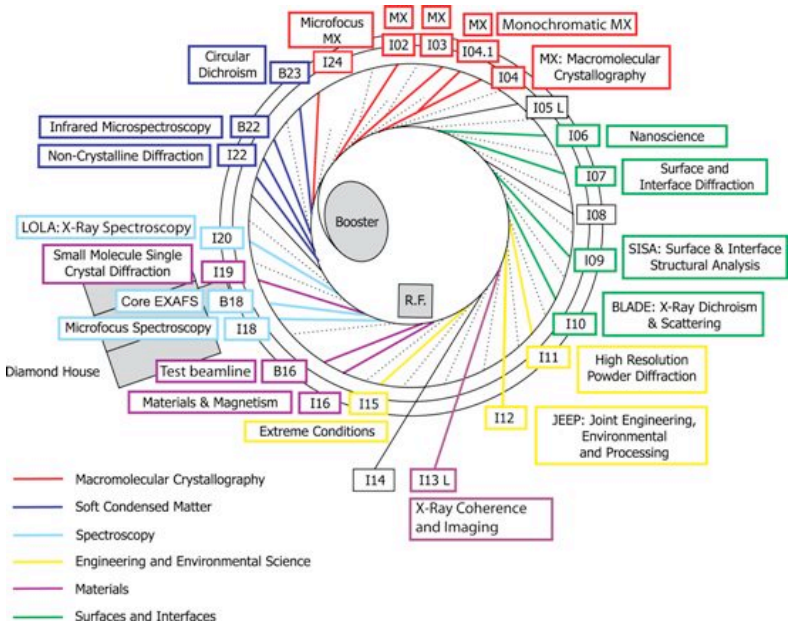

Figure 2.6 *Scheme showing the layout of the beamlines on Diamond, Oxfordshire, UK.*[9]

2.1.2.2 Neutron Sources

Conventionally, the neutron flux produced by the fission of ^{235}U nuclei is unchanging with time and covers a wide range of neutron wavelengths. Therefore, it is necessary to monochromate the neutron beam so that it covers a narrow range of

neutron wavelengths to perform neutron experiments. The most powerful reactor neutron source is the Institute Laue-Langevin (ILL) in Grenoble, France.

Alternatively neutrons can be produced by spallation where a proton beam is fired at a heavy metal target and neutrons are produced by a violent interaction between the proton and the target nucleus, leading to the emission of neutrons and a variety of light nuclear fragments. Each proton produces 15 neutrons from the target. More recent accelerator-based neutron sources include a linear accelerator and a synchrotron to accelerate a beam of protons to a high energy. Accelerator-based sources are usually pulsed (typically with a pulse repetition rate of order 50 Hz) and so they produced a pulsed neutron flux. These neutrons are detected according to their speed, since measuring the time-of-flight taken for a neutron to travel from the moderator to the detector can determine the neutron wavelength. This so called time-of-flight technique removes the need to monochromate the neutron beam and thus even though the raw flux produced by an accelerator-based source is much less than that produced by a reactor source, the final flux available is of a comparable order of magnitude.[10] **Figure 2.7** is a scheme of the instruments at ISIS spallation neutron source with the instruments used in this work circled in red.

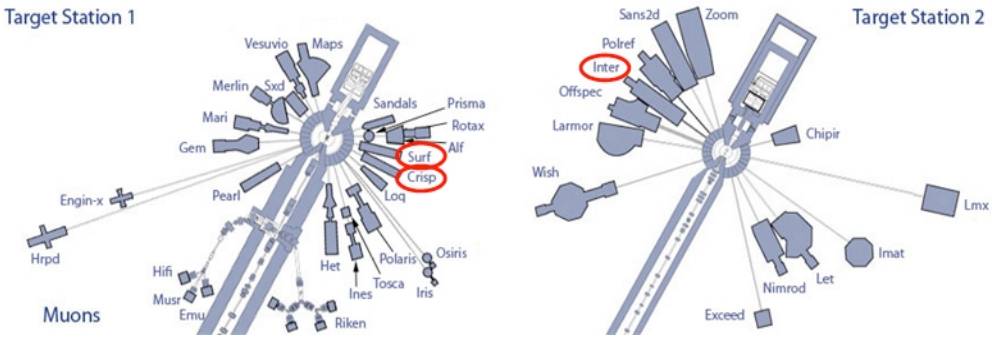

Figure 2.7 *Scheme of the layout neutron instruments at ISIS spallation neutron source*[11]

2.1.3 Specular Reflection and Off-specular Reflection

2.1.3.1 Specular Reflection

Specular neutron reflection provides information about inhomogeneities normal to

an interface or surface.[12] The basis of reflectivity is measuring the intensity, or reflectivity, of radiation from an interface during specular reflection, at which the angles of incidence and reflection are equal. At a planar boundary between two homogeneous media of refractive indices n_o and n_1, both the reflected and refracted rays are in the plane of incidence (**Figure 2.8**). The refractive index can be described as:

$$n = \frac{n_1}{n_o} \tag{2.14}$$

That is, the ratio of the wave vectors in the two media at the interface.

The refractive index can also be expressed as:

$$n = 1 - \lambda^2 A - i\lambda B \tag{2.15}$$

where for neutrons $A = N\,b/2\pi$ and $B = N(\sigma_a + \sigma_i)/4\pi$, N is number of atoms per volume unit, b is the neutron coherent scattering length, and σ_a, σ_i are the absorption and incoherent scattering cross sections. For neutrons, the absorption cross section density is usually small and can be neglected except when the material contains isotopes of Li or B which have high absorption cross-sections.

For X-rays, $A = NZr_e/2\pi$ and $B = \mu/4\pi$, where Z is the atomic number and μ the linear absorption coefficient. B for most organic materials is about 10^{-2} and 10^{-3} times of A, therefore can also be ignored without causing significant errors.[4]

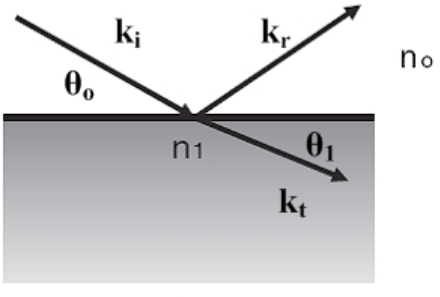

Figure 2.8 *Reflection geometry for an interface.*

For most materials, we consider the first medium is air or vacuum, therefore n_0 is equal to 1, while b is normally positive and so the refractive n_1 is usually smaller than 1, thus total external reflection is usually observed. From *Snell's Law* we can write:

$$n_1 \sin\theta_1 = (n_1^2 - n_0^2 \cos\theta_0^2)^{1/2} \quad \textbf{(2.16)}$$

At total reflection $\theta_0 = \theta_c$ and $\theta_1 = 0$ and so:

$$\cos\theta_c \approx 1 - \rho\lambda^2 / 2\pi \quad \textbf{(2.17)}$$

where θ_c is the critical glancing angle, ρ is material scattering length density.

The basis of a neutron reflection experiment is the variation of specular reflectivity with q_z (the wave vector transfer), perpendicular to the surface or interface. This can be achieved in two ways: either by using a single monochromatic wavelength and varying the grazing angle of incidence, or by using a fixed angle of incidence and a range of wavelengths which are sorted by time-of-flight.

The magnitude of the propagation number of the wave vectors, k_i, k_r and k_t shown in **Figure 2.8** are defined such that $k_i = 2\pi / \lambda$. It is horizontal interfaces at various depths through the sample that cause the reflection. The information gained from a specular reflectivity scattering curve corresponds to depth profile perpendicular to the interface, along the z-axis, Thus it is the z component (k_{iz}) of the wave vectors incident to and reflected from the surface, which are able to be calculated as $k_{iz} = 2\pi \sin\theta_o / \lambda$.

Interfacial structures are probed by specular reflectivity via plotting reflectivity against the scattering vector q, q is defined as the difference between the incident and reflected wave vectors (**Figure 2.9**).

$$q = k_r - k_i \text{ and } q_z = k_{rz} - k_{iz} \quad \textbf{(2.18)}$$

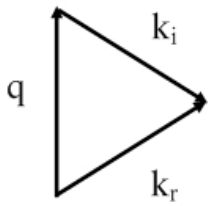

Figure 2.9 *Derivation of the scattering vector q .*

As only the sign of the z component has changed between the incident and reflected wave vectors, and it is already found that the wave vector of the incident and reflected wave vector are equal as well, thus

$$q_z = \frac{4\pi \sin\theta_o}{\lambda} \tag{2.19}$$

Although reflection from a single, smooth interface is relatively straightforward, the reflectivity profile of an interface becomes more complex if a sample has multiple layers of different scattering length density. If long range order with a periodic structure, such as a hexagonal, cubic or lamellar phase, exists there may be further changes to a specular reflection profile. Constructive interference of radiation from subsequent layers can give rise to Bragg peaks in the scattering profile, as illustrated in **Figure 2.10.**

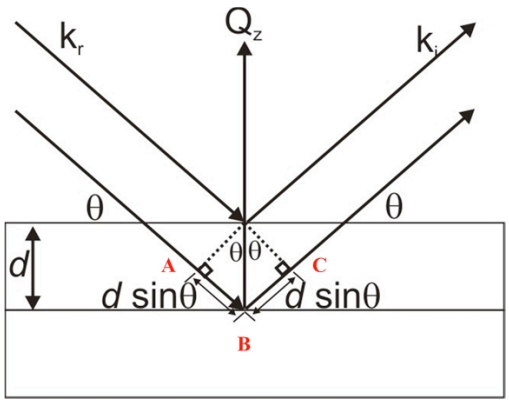

Figure 2.10 *The conventional derivation of Bragg's law treats each lattice plane as a reflecting the incident radiation. The path length differ by AB+BC, which depends on the glancing angle θ. Constructive interference occurs when AB=BC is equal to an integer number of wavelength* $n\lambda$.

As the path length differs between the layers, rays reflected from subsequent layers become out of phase by *2dsinθ* which gives the requirement for constructive interference as *Braggs' law*:

$$n\lambda = 2d\sin\theta_o \tag{2.20}$$

where n is the order of diffraction (an integer) with $n = 2,3...$ are called second order, third order and so on. They correspond to path length differences of $2,3...$ wavelengths. λ is the radiation wavelength in Ångströms, θ_o is the angle of incidence and *d* is the repeat layer spacing (d-spacing) in Ångströms.

Such interference gives rise to peaks in a reflectivity profile. For a single layer, fringes are visible in a reflectivity pattern, and peaks develop with increasing numbers of layers and long range order. By combining **Equations 2.19 and 2.20**, it is possible to calculate interlayer distances or d-spacing directly from a reflectivity profile as

$$q_z = \frac{2\pi}{d} \tag{2.21}$$

The specular reflectivity from a simple interface can be expressed in terms of scattering theory or from thin film optics(*Fresnel's Law*) by approximation:

$$R(q_z) = \frac{16\pi^2}{(q_z)^4}\Delta\rho^2 \tag{2.22}$$

where q_z is the wave-vector transfer in the perpendicular direction (z), and $\Delta\rho$ is the change in scattering length density normal to the interface.

From thin film optics,[13] *Fresnel's law* can also be written exactly as:

$$R = \left|\frac{n_0\sin\theta_0 - n_1\sin\theta_1}{n_0\sin\theta_0 + n_1\sin\theta_1}\right|^2 \tag{2.23}$$

Modelling of reflectivity data is discussed in **Section § 2.1.5.1** below.

2.1.3.2 Off-specular Reflectivity

Off specular reflectivity is the reflectivity obtained when the incident angle is different to the reflected angle ($\theta_i \neq \theta_r$). Depending on the angle chosen, the linear detector is able to collect different peaks at different channel positions, which will be

transferred into q_z (Å^{-1}) afterwards. The data collection takes 60 seconds which is much faster than the specular data collection.

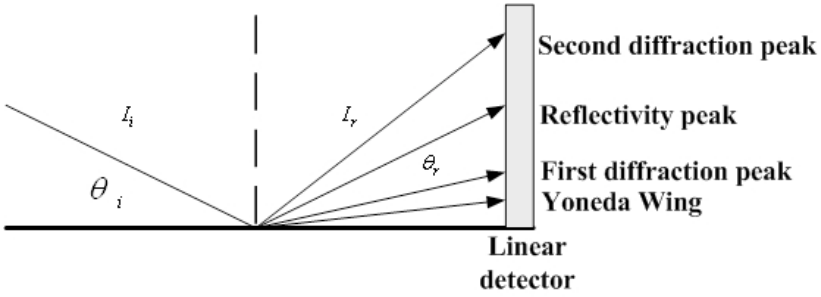

Figure 2.11 *Off specular X-ray reflectivity indicating the characteristic peak positions in the linear detector.*

In this geometry, both the specularly reflected beam and diffuse scattering at angles other than the specular are seen. As shown in **Figure 2.11, t**he most characteristic peaks are described as the yoneda wing, specular reflectivity and diffration peak. Yoneda wing which is a doubling of intensity at the critical angle of the surface is related to mesoscale surface roughness; The specular reflectivity peak is the specular reflectance occuring when the incident angle is equal to the scattered angle; Diffraction peak are an indication of the thin film mesostructure. The incident angle was chosen so that the specular peak won't cover the diffraction peak. Variation of the peak intensities and positions with time indicates how the surface structure varies as the film developes

2.1.4 Small Angle Scattering

The technique of small angle scattering is used to study structures whose size is on the order of 10 Å or larger. Information on such relatively large scale structures is contained at small angle (2θ <2°) for scattered X-rays or neutrons. A full derivation of the small angle scattering principles is beyond the scope of this brief overview, however detailed descriptions of scattering theory are available in the literature.[4, 14-16]

By taking the integral of the scattering length density (**Equation 2.7**) distribution across the whole sample and normalized by sample volume,

$$\frac{d\Sigma}{d\Omega}(q) = \frac{N}{V}\frac{d\sigma}{d\Omega}(q) = \frac{1}{V}\left|\int_V \rho(r)e^{iqr}dr\right|^2 \qquad \textbf{(2.24)}$$

This result is known as the "*Rayleigh-Gans Equation*". The differential cross section $d\sigma/d\Omega$ is the directly measured quantity in a scattering experiment. In the case of small angle scattering the results are usually normalized by the sample volume to obtain the result in an "absolute" scale as this permits straightforwards comparision of scattering from different samples.

The macroscopic cross section generally contains three components: coherent component, incoherent component and an absorption component. Information about the distribution of matter in the sample is contained in the coherent component, whilst the incoherent component is not q-dependent and contributions only to the noise level. The absorption component is usually small and simply reduces the overall signal.

$$\frac{d\Sigma}{d\Omega}(q) = \frac{d\Sigma_{coh}}{d\Omega}(q) + \frac{d\Sigma_{inc}}{d\Omega} + \frac{d\Sigma_{abs}}{d\Omega} \qquad \textbf{(2.25)}$$

The scattering can be averaged to give the macroscopic cross section as a function of magnitude of q (the one-dimensional small angle scattering pattern), unless there is some specific orientation of scattering objects within the sample. Then it is necessary to perform some analysis on the scattering to ($d\Sigma/d\Omega(q)$) extract useful information. There are essentially two classes of analysis: model-dependent and model-independent. The former consists of building a mathematical model of the scattering length density distribution, while the latter includes direct manipulations of the scattering data to yield useful information.

In dilute particulate systems, the matrix is simply presents a uniform, homogeneous background assuming there is no internal structure. In a practical system, there is always a granularity because of the presence of atoms as its basic building blocks. The effect does not manifest itself in the small q range as long as such inhomogeneity is of a size scale much smaller than 1/q.

The important assumption of the dilute particulate model is that the positions of the particles in it are uncorrelated, so that the waves scattered by different particles lack a

phase of coherence and the total intensity is then simply the sum of the intensities. Another assumption is the system is isotropic and takes all different orientations with equal probabilities.

2.1.4.1 Guinier Analysis

Regardless of whether it is geometrically ordered or ill-defined in shape, the size of a particle, can be conveniently characterized by its radius of gyration R_g. If the particle is of a constant scattering length density in its entirety, it can be given as:

$$R_g^2 = \frac{1}{v}\int r^2 \sigma(r) dr \qquad \textbf{(2.26)}$$

where v is the volume of the particle and $\sigma(r)$ is its shape function. The radius of gyration is the average root-mean-square distance of all points in the particle from its center of mass.

The low Q limit scattering can be described as *Guinier Law*:

$$I(q) = I(0)e^{-\frac{(qR_g)^2}{3}} \qquad \textbf{(2.27)}$$

$$\ln(I(q)) = \ln(I(0)) - \frac{R_g^2}{3}q^2 \qquad \textbf{(2.28)}$$

where $I(q)$ is the intensity of independent scattering by spherical particles. Thus the radius of gyration of the scattering object can be extracted from the slope of a plot of $\ln(I(q))$ vs q^2, allowing determination of the radius of gyration R_g from small-angle scattering measurement. The Guinier law is valid provided that $qR_g << 1$, the system is dilute (particles in the system scatter independently), isotropic (random orientations) and the particles are dispersed at constant density and are devoid of any internal structure that can by itself give scattering in the interested range of q.

The radius of gyration of a sphere is given by: [5]

$$R_g^2 = \frac{3}{5}r^2 \qquad \textbf{(2.29)}$$

Spherical shell with radii $r_1 > r_2$:

$$R_g^2 = \frac{3}{5}\frac{r_1^5 - r_2^5}{r_1^3 - r_2^3} \qquad \textbf{(2.30)}$$

Ellipse with semi-axes a, b and c:

$$R_g^2 = \frac{a^2 + b^2 + c^2}{4} \tag{2.31}$$

Cylinder with radius r and length l:

$$R_g^2 = \frac{r^2}{4} + \frac{l^2}{12} \tag{2.32}$$

Elliptical cylinder with semiaxes a and b and height h:

$$R_g^2 = \frac{a^2 + b^2}{4} + \frac{h^2}{12} \tag{2.33}$$

2.1.4.2 Porod Analysis

The ideal two-phase system is generally thought to contain only two different regions, each of the region has constant scattering length density, ρ_1 and ρ_2, and the boundary between these two regions is sharp with no measurable thickness. The most important theoretical result for this ideal two-phase model is *Porod's law* (**Equation 2.34**), in which $I(q)$ is supposed to decrease as q^{-4} for large q limit, and this law should be related to the total area S of the boundaries between the two phases in the scattering volume.

$$I(q) \to \frac{2\pi(\Delta\rho)^2 S}{q^4} \tag{2.34}$$

After consideration of fractal surfaces, where the scale of the measurement may change the result, the equation becomes:

$$I(q) \to \frac{2\pi(\Delta\rho)^2 S}{q^{-(6-D)}} \tag{2.35}$$

where D is a measure of how fractal the surface is.

Surface roughness can be gained from the slope of the plot of $\ln I(q)$ vs $\ln q$. The slopes of -2 and -4 are indicatives of the smooth two-dimensional and three-dimensional surfaces respectively; while a slope in the range -3 to -4 suggests a rough surface.

2.1.4.3 Model-dependent Analysis

The macroscopic scattering cross section for a two-phase system can be divided

into a contrast factor (describing the difference in scattering length density between two phases), and an integral term (describing the spatial arrangement of the material in the phases). This latter function must be modeled, which can provide information on size, shape and interactions of the species or particles in solution.

It is possible to describe the distribution of material in terms of a form factor $F(q)$ and structure factor $S(q)$.

$$I(q) = N_p V_P^2 (\rho_P - \rho_S)^2 F(q) S(q) + B_{inc} \tag{2.36}$$

where N_p is the number of scattering species, V_p is the sample volume, ρ_P and ρ_S are the scattering length densities of the scattering species and solvent, $F(q)$ is the form factor representing scattering from single particle, $S(q)$ is the structure factor arising from structure in the sample due to inter-particle interactions and B_{inc} is the incoherent background.

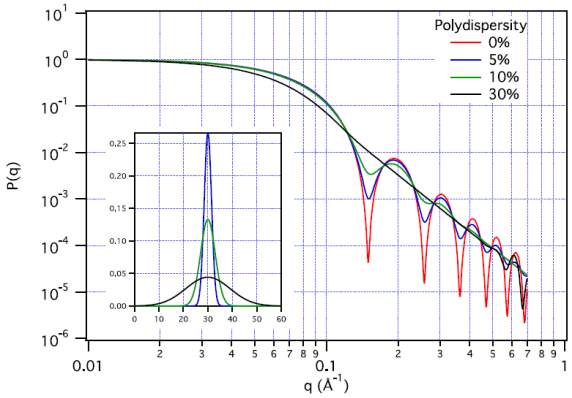

Figure 2.12 *Form factor of spheres of radius 30 Å with a distribution of radii. Size distributions for the non-zero polydispersities are inset.*[5]

If there is no inter-particle correlations, $S(q) = 1$. In the case of an isotropic solution the structure factor is presented as:

$$S(q) = 1 + 4\pi N_P \int_0^\infty [g(r) - 1] \frac{\sin(qr)}{qr} r^2 dr \quad \textbf{(2.37)}$$

where g(r) is the pair correlation function for the scattering objects and $\ln g(r)$ is directly related to the potential energy function that describes the inter-particle interaction.

The form factor describes the size and shape of the scattering objects. Analytical expressions have been derived for many common shapes such as spheres and cylinders. More specifically, taken the form factor for spheres as an example:

$$F(q) = \left[\frac{3(\sin(qr) - qr\cos(qr)}{(qr)^3} \right]^2 \quad \textbf{(2.38)}$$

In a real system, the sizes distribution of scattering objects has the effect of damping the high q oscillations or "smearing" the scattering curve (as shown in **Figure 2.12**). This effect can be evaluated by performing an integral over the appropriate size distribution. Especially when the particle is anisotropically shaped and the polydispersity of multiple dimensions is required, models that already have multiple integrals can become very complicated.[5]

2.1.5 Small Angle Scattering and Reflectivity Data Modeling

Generally, detailed information about the system is possible to be obtained via the modeling of reflectivity and small angle scattering data. However, physical realistic of the values obtained from a model should be carefully considered. Therefore, it is necessary to fix as many variables as possible before data modeling, or to place limitations on the fitting values to ensure the values are physically realistic. In the case of small angle scattering and reflectivity data, further confirmation may be achieved by keeping the physical structure of the samples the same, and simultaneously fitting multiple experiment data sets where the scattering length densities of layers or part of the particle are varied.

2.1.5.1 Small Angle Scattering Data Fitting

Small angle scattering measures the absolute scattering cross section $I(q)$ (cm^{-1})

of a sample as a function of the modulus of momentum transfer q, where $q = (4\pi \sin\theta)/\lambda$, 2θ is the scattering angle and λ is the wavelength.

For small angle scattering data, data modeling includes two parts, the form factor that describes a particle shape and structure factor that indicates the interparticle interactions, as described above.

In this work, considering the surfactant/polyelectrolyte/silica film formation mechanisms, three models, the Debye model, charged prolate core-shell ellipse and charged uniform ellipse were used and will be described in detail here.

The SAXS data was analyzed using a method of a simultaneous nonlinear least-squares fitting using models within the SANS analysis software developed by the SANS group at NIST Centre for Neutron Research, run within the IGOR PRO version 6.20 platform (available from WaveMetrics).[17] Since beam intensity collected on the detector was in arbitrary X-ray counts, the structural models were modified with an "X-ray scale" parameter before they were used to fit the data. This parameter is an arbitrary multiplying factor to account for the fact that the X-ray data is not on an absolute scale.

The particles are assumed to have a homogeneous scattering length, the form factor and structure factor are the sample-dependent parameter that gives us information on particle size, shape and interactions. The form factor describes how the intensity if modified by the radiation scattered by different parts of the same scattering body.

In the fitting of surfactant CTAB and high molecule LPEI complex, similar SAXS patterns were obtained at the initiate stage after adding inorganic precursor since silica precursor just begin to hydrolyze. Attempts to fit this data to a single prolate_core_shell model did not give physically realistic results, although a range of possible micelle models from spherical to cylindrical and lamellar were tried. Thus debye and prolate_core_shell_structure combined model were employed, it is used to describe ellipse with core and shell structure dispersed in the PEI network.[18] The macroscopic scattering cross section for the debye model includes the debye function, scale factor as well as a constant background term.

$$d\Sigma / d\Omega = scale * D(x) + bkg \quad \textbf{(2.39)}$$

where $scale = \phi(\Delta\rho)^2 Z V_m$, ϕ is polymer volume fraction, $\Delta\rho$ is scattering contrast, Z is number of monomers per chain and V_m is volume of a monomer. The Debye function $D(x)$ represents the form factor for a polymer chain with Gaussian coil in dilute solution, giving a radius of gyration R_g.

$$D(x) = 2(e^{-x} + x - 1)/x^2 \quad \textbf{(2.40)}$$

in which $x = (qR_g)^2$.

The prolate_core_shell_structure model is used to describe the form factor for polydispersed prolate ellipsoid particles with a core and uniform shell thickness. The prolate ellipsoid particles have a long and short axis with a constant shell thickness. [19,20] The form factor is normalized by the total particle volume such that

$$F(q) = scale* < f * f > /Vol + bkg \quad \textbf{(2.41)}$$

where f is the single particle scattering amplitude, the <> represent the orientation average.

When the silicate species hydrolyze and condense and the silicate species coated the surfactant began to aggregate, the debye and prolate_core_shell_structure combined model is difficult to get a proper fit, therefore fractal and prolate_core_shell_structure combined model was employed to fit. The fractal model is used to describe the scattering from fractal-like aggregates built from silica species coating micelles.[21] The form factor $F(q)$ is the scattering from randomly distributed "building block" particles, having radius R_0, volume fraction ϕ, scattering length density difference $\Delta\rho$.

$$F(q) = \phi V_p \Delta\rho^2 F(qR_o)^2 \quad \textbf{(2.42)}$$

and the interference from building blocks of fractal-like cluster can be calculated as

$$S(q) = 1 + \frac{\sin[(D_f - 1)\tan^{-1}(q\xi)]}{(qR_o)^{D_f}} \frac{D_f \Gamma(D_f - 1)}{[1 + 1/(q^2\xi^2)]^{(D_f - 1)/2}} \quad \textbf{(2.43)}$$

where ξ is their overall size and D_f is self-similarity dimension.

In the fitting of surfactant CTAB and low molecule SPEI complex and the initiate stage after adding inorganic precursor, uniform_ellipse_structure_factor_model was employed.[22] This model is used to describe the form factor for a polydispersed ellipsoid with uniform scattering length density.

2.1.5.2 Reflectivity Data Fitting

Reflectivity is a useful technique to study layered film structures on the surfaces; The measured reflectivity depends on the variation in the contrast between layers perpendicular to the interface. Especially, neutron reflectivity offers the ability to characterize surface layers because isotopic substitution between hydrogen and deuterium provides different contrast between the interfacial layers and subphase.

Although the scattering length density profile is normally a continuous changing function, the interfacial structure can often be well approximated by a model where layers with a certain thickness, scattering length density and roughness are sandwiched between the super and subphase. It is necessary to fit these parameters in order to minimize the difference between the theoretical and measured reflectivity files. The general principle is to fit a single structural model using the minimum number of layers required for a satisfactory fit.

The reflectivity fitting program MOTOFIT, which runs in the IGOR PRO software, has been used in this work.[17] MOTOFIT perform nonlinear least-square regression on the experimental reflectivity curves using a slab model approach with the Abeles matrix method,[23] and extensions for surface roughness.

In this description, the interface is split into n layers, since the incident beam is refracted by each of the layers, the value of the wave vector (k_n) in layer n, is given as:

$$k_n = \sqrt{k_0^2 - 4\pi(\rho_n - \rho_{o)}} \quad \textbf{(2.44)}$$

where $k_o = q_z / 2$.

The Fresnel reflection coefficient between layer n and layer $n+1$ is then given as:

$$r_{n,n+1} = \frac{k_n - k_{n+1}}{k_n + k_{n+1}} \tag{2.45}$$

considering the roughness and diffuseness of each interface, the Fresnel coefficient was modified and accounted for by an error function:

$$r_{n,n+1} = \frac{k_n - k_{n+1}}{k_n + k_{n+1}} \exp(-2k_n k_{n+1} \sigma_{n,n+1}^2) \tag{2.46}$$

A phase factor β which accounts for the thickness of each layer (d_n) is introduced.

$$\beta_n = k_n d_n \tag{2.47}$$

A characteristic matrix c_n is then calculated for each layer:

$$c_n = \begin{bmatrix} \exp\beta_n & r_n \exp(\beta_n) \\ r_n \exp(-\beta_n) & \exp(-\beta_n) \end{bmatrix} \tag{2.48}$$

The resultant matrix is defined as the product of these characteristic matrices:

$$M = \prod_{n=0}^{n} c_n \tag{2.49}$$

from which the reflectivity is calculated:

$$R = \left| \frac{M_{11}}{M_{21}} \right|^2 \tag{2.50}$$

A minimum of five parameters were included in fitting each reflectivity curve: the instrumental scale factor, which is used in case the reflectivity below the critical angle, is not equal to 1; the SLDs of the superphase and the subphase; the sample background and the roughness of the subphase. To give best agreements between the theoretical data and the experimental data, four parameters are required for each layer: the layer thickness, scattering length density, solvent penetration and roughness.

2.1.6 Indexing Crystals and Liquid Crystalline Mesostructures

An electron in an alternating electromagnetic field will oscillate with the same frequency as the field. In other words, the electrons around the atom start to oscillate with the same frequency as the incoming beam when X-rays hit an atom. Destructive interference occurs almost in all directions since the combined waves are out of phase and there is no resultant energy leaving the solid sample. However, constructive interference can be obtained in a very few directions when the atoms in a crystal are arranged in a regular pattern. Constructive interference causes bright spots at the detector, while destructive interference produces dark regions at the detector. The 2D interference pattern, in which the intensity varies from position to position in the detection plane, is characteristic of the internal structure of the materials and is the basis of diffraction analysis. A similar process occurs upon scattering neutron waves from the nuclei, thus since both neutron and X-ray wavelengths are comparable with inter-atomic distance, resulting in an excellent probe for this structure length scale.

The arrangement of atoms within a given type of crystal structure can be described in terms of its unit cell. The unit cell is given by its lattice parameters, the length of the cell edges are denoted as a, b, c and the angles between them are denoted as α, β and γ. Vector and lattice planes can be given using the Miller index notation, which are written as (hkl) to describe the individual plane. To specify a set of parallel planes we use $\{hkl\}$. *Bragg's law* is an approach to model a crystal as stacks of reflecting lattice planes of separation d (**Figure 2.10 and Equation 2.20**).[24]

For SAXS patterns, Bragg's law is also written as:

$$q = 4\pi \sin\theta / \lambda \qquad \textbf{(2.51)}$$

where q (nm^{-1} or $Å^{-1}$) is the length of the scattering vector or momentum transfer. **Table 2.2** lists the relationship between d value and lattice index (hkl) of six crystal systems.

In a densely packed particle system, the position and orientations of these particles can be aligned with respect to each other due to the particle-particle repulsion. The peaks in the diffraction pattern become more and more pronounced if the particle

positions become increasingly ordered while the peaks become narrow and intense if the domain size of ordered particles increases.

The degree of orientation can be easily detected in a 2D scattering pattern. When the sample is randomly oriented, the scattering pattern of concentric circles around the incident beam with equal intensities can be seen. When the sample is partially oriented, it shows intensity modulations. When the sample is a single crystal in a specific orientation with respect to the incident beam, then the scattering pattern will appear as intense spots.

Table 2.2 *The relationship between d value and lattice index hkl of six crystal systems.*[25]

System	Essential symmetries	d value
cubic	a=b=c, α=β=γ=90°	$\frac{1}{d^2}=\frac{h^2+k^2+l^2}{a^2}$
tetragonal	a=b≠c, α=β=γ=90°	$\frac{1}{d^2}=\frac{h^2+k^2}{a^2}+\frac{l^2}{c^2}$
orthogonal	a≠b≠c, α=β=γ=90°	$\frac{1}{d^2}=\frac{h^2}{a^2}+\frac{k^2}{b^2}+\frac{l^2}{c^2}$
hexagonal	a=b≠c, α=β=90°	$\frac{1}{d^2}=\frac{4}{3}\frac{h^2+hk+k^2}{a^2}+\frac{l^2}{c^2}$
trigonal	a=b=c, α=β=γ≠90°	$\frac{1}{d^2}=\frac{(h^2+k^2+l^2)\sin^2\alpha+2(hk+kl+hl)(\cos^2\alpha-\cos\alpha)}{a^2(1-3\cos^2\alpha+2\cos^3\alpha)}$
monoclinic	a≠b≠c, α=β=90°≠γ	$\frac{1}{d^2}=\frac{h^2}{a^2\sin^2\beta}+\frac{k^2}{b^2}+\frac{l^2}{c^2\sin^2\beta}-\frac{2h\cos\beta}{ac\sin^2\beta}$

Until now, many mesostructures have been assigned according to the diffraction peaks, which are indicative of the periodicity and packing geometry of mesoporous networks. Reflections are due to the ordered arrangement of micelles or (after calcination) material pore channels. Since the materials are not crystalline at the atomic level, these reflections are only observed in the small angle range. **Table 2.3** summarizes some reported surfactant-templated silica mesostructures and their

diffraction properties. Some typical ratios of q values relative to the fundamental reflection at q* are also given in **Table 2.3** for various symmetries.

Table 2.3 *Summary of the reported mesostructures and their diffraction properties.*

Crystal system	Space group	Mesoporous materials	Diffraction property (Ratio q/q*)
Wormlike		MSU, HMS, KIT-1	One or two broad diffraction peaks
Lamellar		MCM-50	$\frac{1}{d} = \frac{l}{a}$ 1(001): 2(002): 3(003): 4(004): 5(005)….
Hexagonal	$p6mm$ (No.183)	MCM-41, SBA-3,SBA15, FSM-16, TMS-1	$\frac{1}{d_{hk0}^2} = \frac{4}{3}\frac{h^2+hk+k^2}{a^2}$ 1(100) : $\sqrt{3}$ (110):2(200) : $\sqrt{7}$ (210):3(300)…
Orthogonal	$c2mm$ (No.38)	SBA-8, KSW-2	$\frac{1}{d_{hk}^2} = \frac{h^2}{a^2} + \frac{k^2}{b^2}$ $\sqrt{2}$ (110), $\sqrt{4}$ (200), $\sqrt{8}$ (220), $\sqrt{10}$ (310), $\sqrt{16}$ (400)…
Cubic	$Pm\bar{3}n$ (NO.223)	SBA-1, SBA-6	$\frac{1}{d_{hkl}^2} = \frac{h^2+k^2+l^2}{a^2}$ $\sqrt{2}$ (110): $\sqrt{4}$ (200): $\sqrt{5}$ (210): $\sqrt{6}$ (211): $\sqrt{8}$ (220): $\sqrt{10}$ (31 0: $\sqrt{12}$ (222): $\sqrt{13}$ (320): $\sqrt{14}$ (321): $\sqrt{16}$ (400)…
	$Im\bar{3}m$ (No.229)	SBA-16	$\sqrt{2}$ (110): $\sqrt{4}$ (200): $\sqrt{6}$ (211): $\sqrt{8}$ (220): $\sqrt{10}$ (310): $\sqrt{12}$ (222): $\sqrt{14}$ (321): $\sqrt{16}$ (400)…
	$Fd\bar{3}m$ (No.227)	FDU-2	$\sqrt{3}$ (111): $\sqrt{8}$ (220): $\sqrt{11}$ (311): $\sqrt{12}$ (222): $\sqrt{16}$ (400): $\sqrt{19}$ (331): $\sqrt{24}$ (422)…
	$Fm\bar{3}m$ (No.225)	FDU-12	$\sqrt{3}$ (111): $\sqrt{4}$ (200): $\sqrt{8}$ (220): $\sqrt{11}$ (311): $\sqrt{12}$ (222): $\sqrt{16}$ (400): $\sqrt{19}$ (331): $\sqrt{20}$ (420): $\sqrt{24}$ (422)…
	$Pm\bar{3}m$ (No.221)	SBA-11	No space group extinction; 1(100): $\sqrt{2}$ (110): $\sqrt{3}$ (111): 2(200): $\sqrt{5}$ (210): $\sqrt{6}$ (211): $\sqrt{8}$ (220): $\sqrt{9}$ (300): $\sqrt{10}$ (310) : $\sqrt{11}$ (311): $\sqrt{12}$ (222): $\sqrt{13}$ (320): $\sqrt{14}$ (321): $\sqrt{16}$ (400)…

$Ia\bar{3}d$ (No.230)	MCM-48, FDU-5	$\sqrt{6}$ (211): $\sqrt{8}$ (220): $\sqrt{14}$ (321): $\sqrt{16}$ (400): $\sqrt{20}$ (420): $\sqrt{22}$ (332): $\sqrt{24}$ (422): $\sqrt{26}$ (431): $\sqrt{32}$ (440): $\sqrt{38}$ (532)…
$Pn\bar{3}m$ (No.224)	HOM-7	$\sqrt{2}$ (110): $\sqrt{3}$ (111): $\sqrt{4}$ (200): $\sqrt{6}$ (211): $\sqrt{8}$ (220): $\sqrt{9}$ (221): $\sqrt{10}$ (310): $\sqrt{11}$ (311): $\sqrt{12}$ (222): $\sqrt{14}$ (321): $\sqrt{16}$ (400)…

Numbers below the space group symbols are space group numbers (refer to website: http://it.iucr.org/A/).

2.1.7 Grazing Incidence X-ray Diffraction (GIXD)

Introduced by Marra et al,[26] grazing incidence X-ray diffraction (GIXD) is a scattering geometry based on the diffraction and the X-ray total external reflection from crystal surfaces. This provides superior technique in the studies of thin surface layers, since the penetration depth of X-ray can range from 1 nm to 10 μm inside the film.

Two-dimensional GIXD patterns provide structural information about both out-of-plane and in-plane lattices, as well as periodicities that are neither normal nor parallel to the film. In the GIXD setup, both the angle of the incoming and outgoing beam are kept at very small constant values. The incidence and exit angle are now denoted as α_i and α_f, as shown in **Figure 2.13**. The recording of the diffraction pattern proceeds by continuously increasing the scattering angle $2\theta_{xy}$, but in this scanning mode, the X-ray tube and the detector operate very close to the plane of the sample surface. Accordingly, the incident and the diffracted wave vectors K_0 and K are almost confined to the surface plane and so is the vector of momentum transfer $Q = K - K_0$ that is nearly perpendicular to the substrate normal, $Q \perp s_3$. Since the structure of the sample is always probed in direction of Q in diffraction, GIXD probes the interplanar spacing of vertically inclined lattice planes.[27]

The diffracted intensity as a function of both the vertical (Q_z) and the horizontal scattering vector components (Q_{xy}) were recorded by rotating the detector through the

angle $\delta = 2\theta_{xy}$. The horizontal component (in-plane) of the scattering vector is given by $Q_{xy} = (4\pi/\lambda)\sin(\theta_{xy})$ and the vertical component is presented as $Q_z = (2\pi/\lambda)\sin(\alpha_f)$ where λ is the X-ray wavelength. GIXD patterns showing diffraction spots were indexed using the rules for identifying ordered mesostructures outlined above in **Section § 2.1.6**. The instruments will be described in **Section 2.2.3** below.

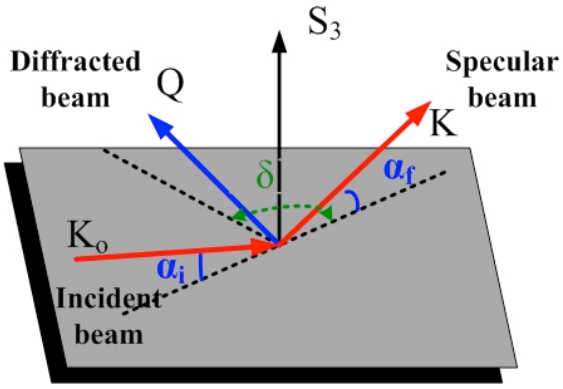

Figure 2.13 *Geometrical representation of GIXD.*[27]

2.1.8 Brewster Angle Microscopy

Brewster angle microscopy (BAM) is an in situ optical technique which allows the direct observation of films gown at the gas/liquid or solid/gas interfaces. The basis of this method is illustrated in **Figure 2.14.**

It is based on the theory that no reflection occurs from a clean surface when the polarised incoming light is at the Brewster angle θ_B, which is also referred to as the polarisation angle, the angle at which only light with an electric vector perpendicular to the plane of incidence is reflected.[28, 29]

Using *Snell's law*,

$$n_1 \sin(\theta_1) = n_2 \sin(\theta_2) \qquad \textbf{(2.52)}$$

we can calculate the incident angle $\theta_1=\theta_B$ at which no light is reflected:

$$n_1 \sin(\theta_B) = n_2 \sin(90 - \theta_B) = n_2 \cos(\theta_B) \qquad \textbf{(2.53)}$$

Rearranging, we get *Brewster's Law*:

$$\tan(\theta_B) = \frac{n_2}{n_1} \quad \textbf{(2.54)}$$

where n_1 and n_2 are the refractive indices of the two media.

No reflection occurs if plane polarized light is incident upon a sample at the Brewster angle. A change in the refractive index of the sample leads to a change in the polarization angle, therefore, reflection begins to occur as the incident angle and polarization angles diverge. Thus changes in the sample media or the development of an interfacial layer can be observed and it is possible to distinguish between different areas of a sample with micrometer resolution. The reflected light can be easily captured by a detector such as a CCD camera and in that way the surface can be visualised.

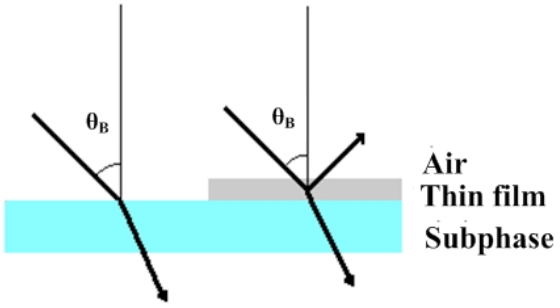

Figure 2.14 *Brewster angle microscopy (BAM) techniques. θ_B is the Brewster angle.*

2.1.9 Nitrogen Adsorption and Desorption

2.1.9.1 Porosity and Adsorption Isotherms

According to IUPAC, pores are classified into three main types according to their sizes: micropores (size less than 2 nm), mesopores (size between 2 nm and 50 nm) and macropores (size exceeding 50 nm).

Since 1777, when Fontana[30] found that cooled calcined charcoal was able to take up several times of its own volume of gases, the measurement of adsorption of gas and vapor has been used to yield information about material surface area and pore structure. The term adsorption was introduced by Kayser in 1881, and now has been

internationally defined as the enrichment of one or more components in an interfacial layer.[31]

Physical forces (van der Waals) and chemical forces are suggested to be the main absorption interactions between the solid and molecules of gas. The quantity of gas taken up by a sample of solid, which can be expressed in **Equation 2.55**,

$$N = f(p, T, \text{gas}, \text{solid}) \quad \textbf{(2.55)}$$

It is affected by the mass of the sample, temperature, vapor pressure and the nature of both solid and gas. At a certain temperature, an adsorption isotherm can be plotted by taking measurements of the amount of gas absorbed as a function of a range of partial pressures. Depending on the type of adsorbent and adsorbate, and intermolecular interactions between them, these isotherms display very different shapes.

The first systematic attempt to interpret adsorption isotherms for gas-solid equilibria was introduced by Brunauer, Deming, Deming and Teller (BDDT) in 1940.[32] Six types isotherms, including the one introduced by Sing, has become the core of the modern IUPAC classification of adsorption isotherms.[31] as shown in **Figure 2.15**.

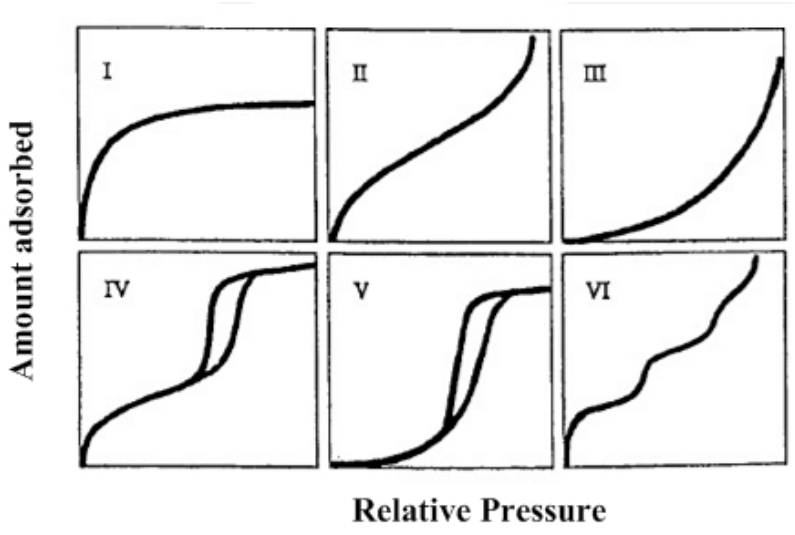

Figure 2.15 *The IUPAC classification for adsorption isotherms*[33, 34]

In this graph, Type I isotherms describe microporous adsorbents having smaller

external surfaces, such as activated carbons, molecular sieve zeolites. Type II and III characterize the adsorption on non-porous or macroporous adsorbents with strong and weak adsorbate-adsorbent interactions, respectively. Type IV represents adsorption isotherms with hysteresis, which is associated with capillary condensation taking place in mesopores and is given as the characteristic of mesoporous materials. Although Type V also has hysteresis in the adsorption isotherms, it represents porous materials with particularly weak interactions between the adsorbate and adsorbent. Finally, Type VI has steps, which is rare but is of particular theoretical interest. The sharpness of the steps, which depends on the system and the temperature, indicates stepwise multilayer adsorption on a uniform non-porous surface. The step-height is associated with the monolayer capacity for each adsorbed layer. Practically, there are considerable numbers of isotherms that are difficult to assign to a single type rather than another.

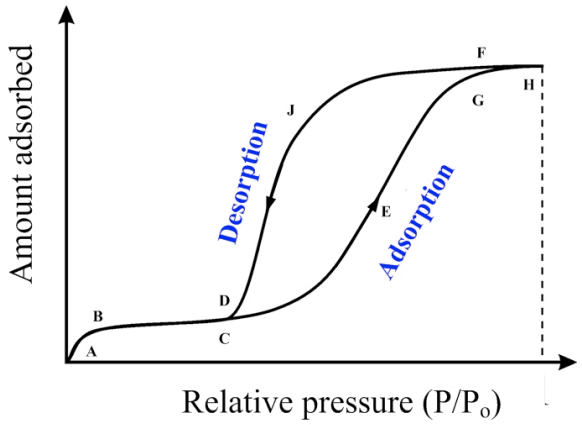

Figure 2.16 *Typical adsorption isotherm of mesoporous material.*

Figure 2.16 is a typical adsorption isotherm (type IV) for mesoporous materials. It follows the same path as the corresponding Type II isotherm (ABC) in the lower relative pressure region. In the relative pressure region between 0.05-0.3 the adsorption isotherm shows a point of inflection (Point B), corresponding to the completion of the adsorbed monolayer. This adsorption is limited to a thin layer on the wall until point D, which is the inception of the hysteresis loop. Significant

adsorption in the ABC region indicates the presence of micropores in the sample. After point D it begins to deviate upwards (CDE) until higher pressures, then its slope increases (EFG). Capillary condensation commences in the finest pores, and as the pressure is progressively increased, wider and wider pores are filled until the saturation pressure is approached (FGH). The amount adsorbed along the desorption branch (FJD) is always greater than along the adsorption branch (DEF) at any given relative pressure, thus a hysteresis loop appear, this is a characteristic feature of type IV isotherm although the exact shape of the loop changes from one adsorption system to another.

2.1.9.2 BET model, T-plot and Pore Size Distribution

The most influential theory for the calculation of surface area from adsorption is Brunauer, Emmett and Teller (BET) model which is based on a kinetic model brought forward by Langmuir[35]. This model is based on a dynamic equilibrium state: the rate at which molecules arrive from the gas phase and condense onto bare sites is the similar to the rate at which molecules evaporate from occupied sites.

Langmuir only confined his analysis to monolayer adsorption,

$$\frac{n}{n_m} = \frac{Bp}{1 + Bp} \tag{2.56}$$

where n is the amount adsorbed (in moles) on 1g of adsorbent, n_m is the monolayer capacity, B is an empirical constant and can be evaluated as:

$$B = \frac{a_1 k}{z_m v_1} e^{q_1 / RT} \tag{2.57}$$

in which, a_1 is the fraction of incident molecules which condense on a surface, k is a constant given by kinetic theory, z_m is the number of sites per unit area, and v_1 is the frequency of oscillation of the molecule in a direction normal to the surface.

BET theory extended the Langmuir equation to multilayer adsorption and can be written as follows: [32, 36]

$$\frac{p / p_o}{V(1 - p / p_o)} = \frac{1}{V_m c} + \frac{c - 1}{V_m c} \frac{p}{p^o} \tag{2.58}$$

where P/P^0 is the relative pressure, V_m is the amount adsorbed in a statistical monolayer coverage, c is a constant relating to the strength of the interaction between the adsorbate and adsorbent, the parameter c is related to the heat of adsorption and given as:

$$c = \frac{a_1 v_2}{a_2 v_1} e^{(q_1 - qL)/RT} \tag{2.59}$$

It is possible to calculate both V_m and c by plotting the absorbed amount and relative pressure as in **Equation 2.58**, from which the surface area can be calculated*:*

$$A = \frac{V_m a_m L}{22414} \tag{2.60}$$

where A is the surface area, a_m is the area of a single molecule of the adsorbate, the value of a_m for nitrogen at 77 K is 16.2 Å^2, and L is Avogadro's number. 22414 is the volume of one mole of an idea gas under STP conditions in ml. Division by the sample mass yield the surface area per gram for the material, typically expressed in square meters per gram.

The t-plot is also employed to show capillary condensation in mesopores, the presence of micropores and evaluate their volume. A t-plot is constructed by plotting the volume of adsorbate against the average layer thickness that could be obtained from the *Halsey equation*[37, 38]:

$$t(nm) = \frac{V}{V_m}\sigma = 0.35\left[\frac{5}{2.303\log_{10}(p_0/p)}\right]^{(1/3)} \tag{2.61}$$

The t-plot is supposed pass through the origin if surface is not microporous (as shown in **Figure 2.17 A a and c, Figure 2.17 B a**). If the adsorbent contains mesopores, capillary condensation will occur when the relative pressure reaches a value which is related to the radius of the pore by the Kelvin Equation. The uptake of gas will be enhanced by the amount of adsorbate condensing in the pores, the t-plot will therefore show an upward deviation beginning at the relative pressure at which

the finest pores are just being filled (as shown in **Figure 2.17 A c, (i)** is the mesoporous isotherm adsorption branch, and (ii) is the mesoporous isotherm desorption branch)).

If the surface is microporous then it will have additional adsorption at low pressure, and the t-plot then does not pass through the origin (as shown in **Figure 2.17 B b**), The micropore volume is about the volume which is equivalent to the amount of nitrogen (77K) corresponding to the intercept. The slope of the linear branch is proportional to the external solid surface area .

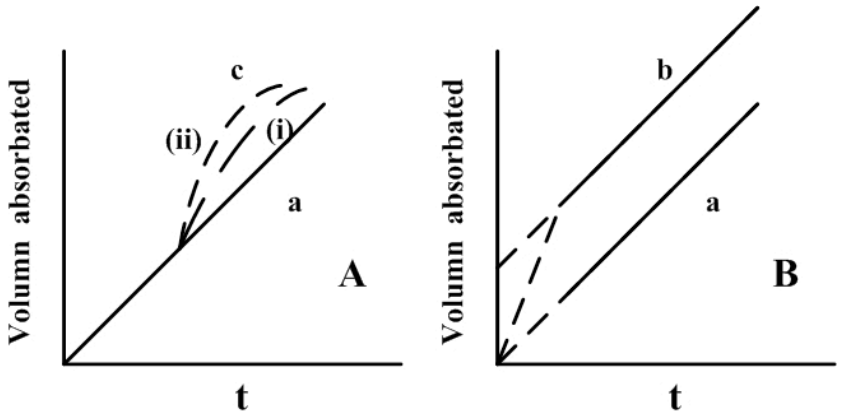

Figure 2.17 *Effect of mesoporosity and microporosity on the t-plot. A (a) and B (a) are the t-plot for a nonporous absorbent sample. A (b) is the t-plot for the same solid where mesopores have been introduced, with (i) being the adsorption, and (ii) the desorption branch. B (b) is the t-plot for a sample with micropores.*[31]

Liquid nitrogen fills in the whole pore when the relative pressure is increased sufficiently. For an isolated cylindrical pore, the pressure where condensation occurs is presented by the *Kelvin Equation*:

$$In\frac{p}{p^0} = \frac{k\gamma V_L}{RT}\frac{1}{r_c}\cos\theta \qquad \textbf{(2.62)}$$

in which γ and V_L are the surface tension and molar volume of the condensed liquid phase respectively, r_c is the pore (core) radius, and θ is the contact angle with which the liquid meets the wall. The pore core radius is the pore radius minus

any multi-layer film thickness. k is a geometric parameter and depends on the pore type: for a cylinder pore open at both ends $k = 1$ and for a pore with one dead end or for desorption, $k = 2$.

Generally, the Kelvin Equation is valid for pore sizes in the range of 10 – 250 Å although these limits are largely experimental limits. Few pores which is less than 10 Å may be considered as mesoporous. Measurements of the pressure differences for pore sizes greater than 250 Å are difficult to be trusted with a sufficient accuracy. Thus the Kelvin equation is subject to considerable inaccuracies and must be used with its limitations.

The Kelvin Equation and the Barrett-Joyner-Halenda (BJH) algorithm are conventionally used to evaluate the full pore size distribution of a porous solid in the capillary condensation region of an isotherm. Using BJH theory it is difficult to tell anything about the other dimensions of pores, such as their length, since the BJH algorithm generates a density function for pore diameter weighted by void volume. Additionally, it is always observed experimentally that pore size distributions calculated from the adsorption branch are different to that evaluated from the desorption branch on an isotherm. In fact the use of the desorption branch is likely to suffer errors due to pore blocking and tensile strength effects. Thus it is recommended to use the adsorption branch of an isotherm for the calculation of a pore size distribution.

2.1.10 Thermogravimetric Analysis

The Thermogravimetric Analysis (TGA) is a technique which is used to measure weight changes in sample as a function of temperature. Detailed descriptions of TGA measurement are readily available from research publications.[39, 40]

A furnace heats the sample at a constant heating rate or holds it at a constant temperature while a sensitive balance monitors record sample weight changes due to chemical reactions etc. The atmosphere used in the TGA experiment plays an important role and can be reactive, oxidising or inert. The results of a TGA measurement are usually displayed as a TGA curve in which mass or percent mass is

plotted against temperature. This shows the rate at which the mass changes and is known as the differential thermogravimetric curve. Different effects can cause a sample to lose, or even gain, mass and thus generate steps in the TGA curve. These effects may include:

(1) Evaporation of volatile constituents; drying, desorption and adsorption of gases, moisture and other volatile substances; loss of crystallisation.

(2) Oxidation of metals in air or oxygen.

(3) Oxidative decomposition of organic substances in air or oxygen.

(4) Thermal decompositon in an inert atmosphere with the formation of gas products.

Potentially, TGA coupled with Mass Spectrometry (MS) and FT-Infrared Spectroscopy (FT-IR) provides elemental analysis of decomposition products. Applications include asessment of moisture and volatiles, asessment of composition, thermal stability, oxidative stability and decomposition kinetics.

2.2 Methods of Analysis

2.2.1 Neutron Reflectivity

Neutron reflectivity measurements of the films grown at the air/water interface were performed on SURF, CRISP (Target Station I), and INTER instruments (Target Station II, detailed schematic diagram in **Figure 2.18**) at the ISIS Pulsed Neutron Source facility within the Rutherford Appleton Laboratories.[41] All three instruments have been established for the study of surfaces using specular neutron reflectivity. For Target station 1, Neutrons of wavelengths 0.55 - 6.8 Å in pulses at 50 Hz are utilized to give a q range of 0.048 - 1.1 $Å^{-1}$. A hydrogen moderator at 25 K is used to cool the neutrons in each pulse prior to travel down a flight path with a series of four slits, two before and two after the sample. An optical laser is used to aid alignment of the sample height that is controlled on a sample stage with 0.05 mm accuracy. The incident angle for the reflectivity experiment was 1.5^{o} and 0.5^{o}. The detector is a He^{3} gas detector.

For the INTER instrument (Target Station II), it operated at lower frequency of

10Hz by taking 1 in 5 pulses from the existing ISIS synchrotron. The INTER reflectivity views the grooved surface of the cold coupled methane moderator giving the best possible flux gains without compromising resolution or signal to noise. Incident angle used for the reflectivity experiment was 2.3°, with data being collected between 0.035 and 0.326 $Å^{-1}$ in D_2O at room temperature.

In neutron reflectivity experiments, the solution is prepared by pouring a film formation solution into a 4 x 15 cm PTFE trough to provide a meniscus above the edge of the trough, then the scattering was collected on this air/solution interface. Reflection experiments from the interface were performed at 25 °C. In order to clarify the surfactant templated film structure, some deuterated surfactants were used. Some samples were run using first deuterated and then hydrogenated versions of the templating surfactant to provide a second contrast to constrain the fitting parameters.

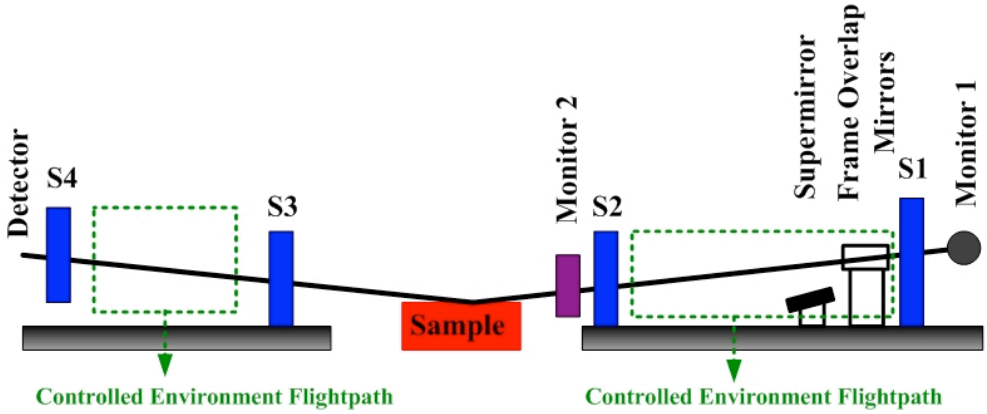

Figure 2.18 *Schematic diagram of the INTER reflectivity on Target II at ISIS.*

2.2.2 Small Angle X-ray Scattering

Synchrotron small angle X-ray scattering experiments were performed using non-crystalline diffraction beamline (I22) instrument at the Diamond, ISIS, UK (**Figure 2.19 A**). **Table 2.4** gives the I22 beamline specifications.[42]

A purpose built flow system consisting of a reservoir containing the surfactant/polymer/silica solution under continuous stirring, tubing connecting the reservoir to the sample capillary and a peristaltic pump to circulate the solution was utilized on the beamline (**Figure 2.19 B and C**). An X-ray wavelength of 0.0827 nm

and a 3.2 m flight tube was used with the RAPID 2D SAXS detector, giving a Q range of 0.7 nm^{-1} to 8 nm^{-1}.

Two-dimensional data are processed into linear data by integrating a certain angular area of the two dimensional data using DREAM software. Water background was also subtracted from the sample data in DREAM. In the linear profile, the scattering intensity was plotted as a function of detector channel that can be calibrated into Q using the standard rat-tail collagen sample, which has a lamellar pattern with a known d-spacing of 670 Å.

Table 2.4 *I22 beamline specifications.*

Specifications	Parameter
Energy range	3.7 - 20 keV
d-spacing range	1 - 5000 Å
Photon beam size at sample	320 (H) x 70 (V) µm
Beam divergence at 12 keV	50 (H) x 20 (V) µrad

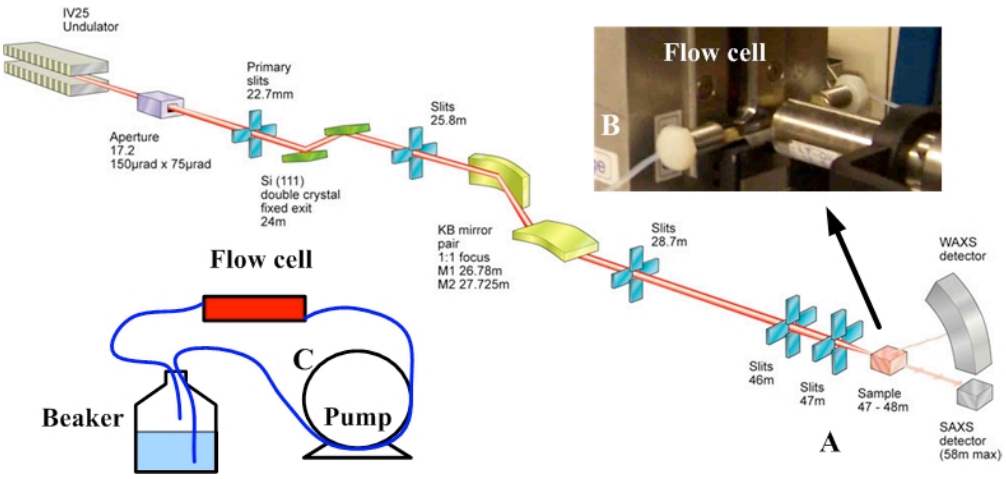

Figure 2.19 *(A)Beamline layout (I22) at Diamond, Oxford[43] (B) photograph of the home designed flow cell. (C) Drawing of the flow system.*

An Anton Paar SAXSess small and wide angle X-ray scattering instrument with a measurable q range of 0.077 – 27.0 nm^{-1} was used to perform small angle X-ray

scattering measurements at the University of Bath (as seen in **Figure 2.20**). Line and pin-hole X-ray sources operated at 40 kV and 50 mA are used. An elliptical focusing mirror is utilized to further enhance the flux. Collimation is achieved using a block collimator with a roughness of less than 0.14 μm/cm and the flight path from source to detector is in a chamber evacuated to below 5 mbar. X-rays are detected by a reusable Europium excitation based image plate (size: 66 x 200 mm) with a 42.3 μm^2 pixel size, after that, the image plate is read by a Perkin Elmer cyclone reader using OptiQuant software.

SAXSquant program was used to generate SAXS profiles. Data processing, such as background subtraction, was performed using the Primary Data Handling (PDH) program. Desmearing from a line to a point source was performed with a custom program provided by Anton Paar using the Lake method of desmearing.

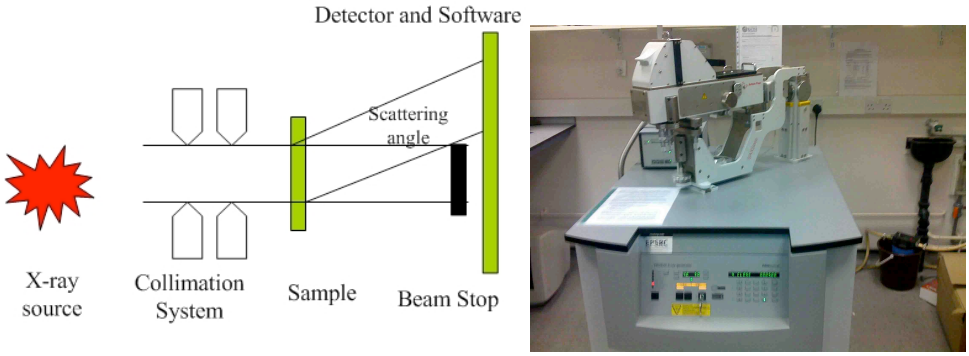

Figure 2.20 *The components of a SAXS instrument.*[44] *and SAXS machine in Bath University.*

Films produced at the air-solution interface were removed using a plastic mesh and were dried in the air. Then pieces of film materials (normally two or three pieces) which were cut from the mesh voids were mounted in a sample holder between two pieces of sellotape™ and held in place by two copper plates.

Liquid samples of surfactants in solution have been examined by filling a 100 μL quartz capillary after the capillary was flushed briefly with the sample solution. The capillary was then mounted in the temperature controlled sample holder provided. In

both cases the temperature was maintained at 25°C.

2.2.3 X-ray Reflectivity

X-ray reflectivity experiments were performed on the ID10B Tröika II beamline at the European Synchrotron Radiation Facility in Grenoble, France.[45] The ID10B beamline is a high-brilliance undulator beamline at the ESRF designed for high resolution X-ray scattering and surface diffraction.[46] ID10B uses photons with the energys 8 keV or 22.2 keV provided by a diamond double-crystal monochromator. Studies of thin film formation at the air-liquid interface were performed using time-resolved off-specular X-ray reflectivity because the flux of the synchrotron radiation was sufficient to allow short scans to be collected. Time-resolved experiments with a time – resolution of 1 minute, were able to cover a Q_z range of 0.085 - 0.25 $Å^{-1}$ by using a linear detector with a vertical orientation to collect data over a range of reflected angles as described in the literature.[47]

X-ray reflectivity and grazing-incidence diffraction experiments were performed on developed mature films. X-ray reflectivity patterns were collected over a Q_z range of 0.0014 - 0.3535 $Å^{-1}$. Grazing-incidence diffraction patterns were collected with two Q_z ranges: 0.0014 - 0.89 $Å^{-1}$ (energy 8.06 keV) and 0 - 2.0 $Å^{-1}$ (energy 21.85 keV). The Q_{xy} range is 0 - 0.2 $Å^{-1}$. A 1024-channel linear detector with a vertical alignment was used to collect data during GIXD experiments and it was rotated incrementally in *xy* plane, as shown in **Figure 2.21**.

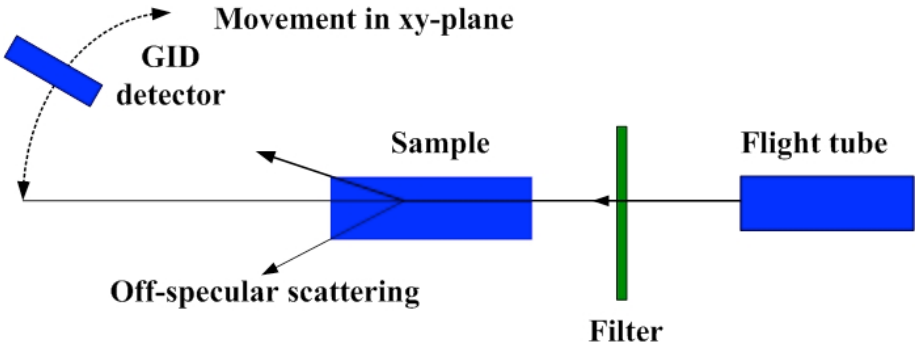

Figure 2.21 *Diagram of how grazing incidence diffraction is collected on the ID10B beamline.*

Experiments at the air/solution interface were performed on the ID10B beamline by pouring a film preparation solution into a 4 x 15 cm PTFE trough identical to those used for neutron reflectivity experiments. X-ray reflection experiments from the interface were performed at 28°C, controlled by a water bath, and at 34 - 49% measured relative humidity.

Angle dispersive X-ray reflectivity and GIXD experiments were performed on fully developed films at the air-solution interface to observe the final film structure, at two different incident angles, corresponding to a true grazing incidence angle () and the angle of the first order peak observed in an initial reflectivity profile. The true grazing incidence angle was normally 0.13 ° with an energy of 8.06 KeV and 0.045° when an energy of 21.85 KeV was applied. At low incidence angles the depth penetration of the X-rays is much smaller and the structure observed corresponds only to that which is present very close to the surface. When the incidence angle increases above the grazing incidence conditions the X-rays begin to observe the sample structures further into the film.

2.2.4 Brewster Angle Microscopy Measurements

Brewster angle microscopy experiments were performed at the Department of Chemistry, University of Bath utilizing a Nanofilm Technologies (NFT) I-Elli 2000 Imaging Ellipsometer used as a Brewster angle microscope, as shown in **Figure 2.22**. A frequency doubled NdYAG diode laser with a wavelength of 532 nm was used in

the I-Elli 2000.[48] The incidence angle and reflection angle can be changed with an angular range of 45º to 80º and with an accuracy of 0.01º. The BAM image is viewed on a computer using a digital CCD camera with a high grade 768 x 572 pixel sensor featuring a lateral resolution of 2 μm. An automated system is utilized for image collection to remove the complication that a limited strip of the image is in focus that arises from the use of an inclined observation angle.

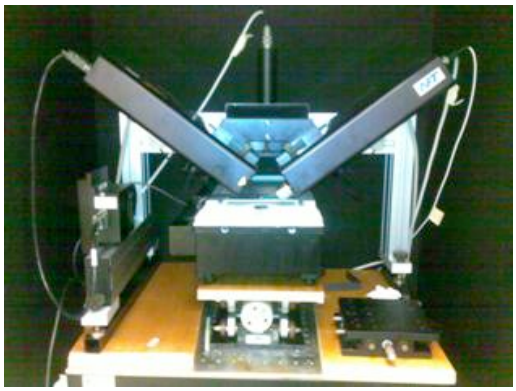

Figure 2.22 *Photograph of the Brewster Angle Microscope at Bath University.*

Samples for BAM imaging were prepared by pouring a reaction solution into a 6 cm diameter polyethylene Petri dish which was placed on an anti-vibration stage. Solutions were left *in situ* to continue development undisturbed; however, the sample stage was adjusted horizontally in order to confirm that the appearance of the interface was uniform over the whole sample.

Film preparation solutions were observed in a live image as the film developed and records of the time of film formation were taken manually using the live image to observe the point of film formation. Additionally, images of the reaction solutions were collected until no further change was observed at the interface.

2.2.5 Nitrogen Adsorption Measurements

Measurements of the nitrogen adsorption isotherms for powdered film material were conducted in the Department of Chemical Engineering at the University of Bath. A Micromeritics Accelerated Surface Area and Porosimetry Analyzer (ASAP) 2010 instrument was utilized for the automated measurement of nitrogen adsorption and

desorption from powdered film material at 77 K. The instrument records the amount of gas absorbed by measuring a change in pressure and converting this to a volume of gas adsorbed per gram of sample, then an isotherm was generated by plotting the gas volume absorbed against the relative pressure.

Film samples were prepared by cutting out the film material from holes in a piece of mesh and removing the film template either by calcination or by washing with ethanol, approximately 0.1 g of the powder was used. Material from approximately 30 film samples, made with identical reagent concentrations, was required to provide sufficient material for examination. Samples were degassed under vacuum overnight about 200°C for calcined sample and 75°C for 48 hour for washed samples before measurement. Measurement was performed over a partial pressure cycle of 0-1-0 in 0.03 increments with an equilibration period of 45 seconds at each partial pressure.

2.2.6 Thermogravimetric Analysis Measurements

Analysis of the solvent content and organic content of film materials, which were recovered from the air/solution interface and dried in air, was undertaken using a Perkin Elmer TGA 7 thermogravimetric analyser. The instrument uses a vertical balance accurate to ± 0.005 mg to measure the change in the sample mass during heating. A Perkin Elmer TAC 7/DX thermal analysis controller and Puris software was used for instrument control and data collection in terms of percentage mass and sample temperature.

For surfactant/polyelectrolyte templated film material a sample of 1.5 - 3 mg of film material, within the 1 - 5 mg recommend sample size, was used for TGA experiments. Film material was taken off the air/water interface using a plastic mesh and allowed to dry in air prior to measurement. Dry free standing films were cut out of the mesh holes and measured under nitrogen flow in the temperature range from room temperature to 1000°C at a heating rate of 5°C /min.

2.3 Film Preparation

2.3.1 Materials

2.3.1.1 Surfactants

The cationic surfactant cetyltrimethylammonium bromide (CTAB), didodecyldimethylammonium bromide (DDAB has two 12-carbon tails) were purchased from Sigma-Aldrich. Anionic surfactant sodium dodecylsulphate (SDS) was purchased from Acros Organic; The Pluronic surfactant P-123 with structure $H(C_2H_4O)_{20}(C_3H_6O)_{70}(C_2H_4O)_{20}H$, average molecular weight 5750 g/mol, was generously supplied by BASF as a sample and the Pluronic surfactant F-127, $H(C_2H_4O)_{106}(C_3H_6O)_{70}(C_2H_4O)_{106}H$, average molecular weight 12600 g/mol, as well as Cetylpyridinium chloride monohydrate (CpCl· H_2O, $C_{16}H_{33}N(C_5H_5)$· H_2O) with average molecular weight of 358 g/mol were purchased from Sigma. All the chemicals were used without further purification. The partially fluorinated surfactant Zonyl FSO–100 with the structure $F(C_2F_4)_4(C_2H_4O)_9H$, average molecular weight 725 g/mol, was generously supplied by DuPont as free samples and all bottles supplied were from the same synthesis batch. The surfactant molecular structures are shown in **Figure 2.23**.

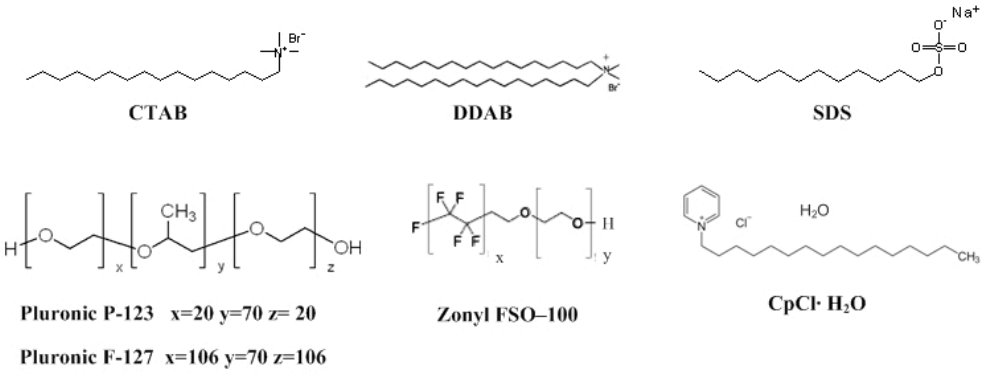

Figure 2.23 *Molecular structures of surfactants used in this work.*

2.3.1.2 Polyelectrolytes

Branched PEI (MW=750,000 (denoted as LPEI); 2000Da (denoted as SPEI)) as 50% weight solutions in water, ethylene glycol diglycidyl ether (EGDGE, 75% pure),

poly(ethylene oxide) with average molecular weight of 10,000, polyacrylamide (PAAm) with average molecular weight of 1500 as 50% weight solution in water were purchased from Sigma-Aldrich; Polymer molecular structures were shown in **Section 1.1.2, Figure 1.2**. All the chemicals were used without further purification.

2.3.1.3 Inorganic Precursors

Silica precursor tetramethoxysilane (TMOS, 98% pure), the titania precursor titanium (IV) bis(ammonium lactato)dihydroxide (TiBALDD, 50% solution in water), titanium butoxide (TiB, 97% pure), titanium tetrachloride ($TiCl_4$, 99.9% pure), titanium(IV) ethoxide (TiE, 80% pure), titanium propoxide (TiP, 98%) and the inorganic precursor for iron oxide based film synthesis, ferric chloride ($FeCl_2$) were purchased from Sigma-Aldrich. All the chemicals were used as supplied and inorganic precursor molecular structure is displayed in **Section 1.2.3 Figure 1.8 and Figure 1.9**.

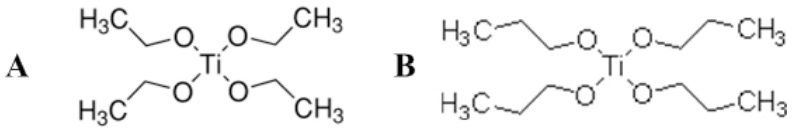

Figure 2.24 *Molecular structures of titanium precursor (A) Titanium ethoxide (B) titanium propoxide.*

2.3.1.4 Other Reagents

Ultra pure Milli-Q water (18.2 MΩ cm resistance) was used for all preparations other than those used in neutron reflectivity techniques. D_2O (Sigma-Aldrich, 99.99%) was used as the solvent for neutron reflectivity experiments. Deuterated cationic surfactant d-CTAB ($C_{16}D_{33}NBr$) was purchased from CDN-Isotopes or supplied by the Oxford Isotope Facility. Sodium hydroxide (NaOH) was purchased from Sigma-Aldrich, hydrochloric acid (HCl, 37wt%. in H_2O), was purchased from Fisher Scientific.

2.3.2 Surfactant and Polyelectrolyte Films

To prepare the CTAB/PEI films, a 0.074 M CTAB solution in ultrapure water was mixed with an equal volume of 80 g/l polymer solution in ultrapure water, which was poured into a polystyrene dish over a piece of plastic mesh after a short period of stirring. Film was removed from the solution surface by drawing the open plastic mesh up through the interface lifting the film with it and films were dried in air at room temperature. A range of PEI concentrations from 10g/l to 50g/l were investigated and are discussed in **Section § 3.2.1**. In order to successfully remove film synthesized with low MW PEI (SPEI) and PAAm, EGDGE was added to the CTAB/SPEI mixture to cross-link the polymer.[49] For LPEI, 0 - 0.04 M EGDGE was used while 0 - 0.1 M EGDGE was used for film synthesized with SPEI.

DDAB/PEI films were synthesized using the same procedures. In the final film forming solutions, DDAB concentrations were varied from 0.0045 M to 0.018 M, PEI with two molecular weights (LPEI and SPEI) were used, the polymer concentration was changed from 10 g/l - 30 g/l.

CTAB/SDS/polymer films were also synthesized using a cat-anionic surfactant mixture with four different polymers: high molecular PEI, low molecular PEI, polyacrylamide and poly(ethylene oxide). Stock solutions were prepared as follows: the concentration of CTAB was fixed at 0.074 M, the concentration of SDS solution was fixed at 0.0925 M, while the PEI, PAAm and PEO concentration was fixed at 100 g/l. To prepare films in which the final concentration ratio of CTAB:SDS = 2:1 (the final CTAB concentration is 0.037M and SDS concentration is 0.0185M), with a LPEI concentration of 20 g/l, the stock solutions were used as follows: 4ml 0.0925 M SDS solution was added into 10 ml 0.074 M CTAB solution and stirred for five minutes. 4ml 100 g/l LEI solution was diluted into 6 ml solution with water and this solution was then added to the co-surfactant mixed solution. CTAB/SDS molar ratios were varied from 2:1 to 8:1 (for all the ratios, the final CTAB concentration was kept as 0.037M), PEI concentration ranged from 10 g/l to 40 g/l. PAAm concentration changed from 12.5 g/l to 37.5 g/l; PEO concentrations varied from 25 g/l to 75 g/l. The concentration variations will be detailed in the experiments results.

2.3.3 Silica Materials Templated by Surfactant and Polyelectrolytes

Silica films were prepared by the same procedure as above by mixing the surfactant and polymer and then adding silicate precursor (TMOS, 2.5 ml / 20 ml solution) into the surfactant/polyelectrolyte mixture before pouring the solution into the dish. For the preparation of CTAB/PEI templated films, the concentration of CTAB was fixed at 0.037 M, which is above the CMC but below the sphere-rod micelle transition for this surfactant. The polymer concentration is given in grams of polymer per liter, and the polymer concentration varied from 10 g/l to 50 g/l. The concentration of cross-linker (EGDGE) was varied from 0.02 M to 0.1 M. The final concentration of TMOS varied from 0.0335 to 0.402 M. No pH adjustment was made to the solution except where NaOH was added (as noted below), so the solution pH was 9 - 10. The solution pH increased to around 12 when NaOH was added.

In order to see how co-surfactants (such as anionic surfactant and copolymer surfactant) changed the framework structure, experiments were carried out using mixed surfactants. We used CTAB/SDS as a cationic-anionic surfactant pair. Preparation of a silicate film templated by CTAB/SDS/LPEI, which had a final concentration ratio of CTAB:SDS = 2:1, and a LPEI concentration of 20 g/l is as follows: 4 ml 0.0925 M SDS solution was added into 10 ml 0.037 M CTAB solution and stirred for five minites. 4 ml 100 g/l LEI solution was diluted into 6 ml solution with ultra-pure water and then was added to the co-surfactant mixed solution. This solution was poured into the dish after the silicate precusor TMOS (0.25 ml / 20 ml total solution) was added into the solution. CTAB/SDS molar ratios were varied from 2:1 to 8:1, PEI concentration ranged from 10 g/l to 40 g/l. PAAm concentration changed from 12.5 g/l to 37.5 g/l; The experimental procedure remained the same and the concentration variations are detailed with the results of these experiments. In each case the concentration of only one reagent was varied at a time.

In order to improve the mesostructure retention after removing the template, a dried silica film was exposed in a TMOS atmosphere in an oven at 40°C for one day, and then the film was calcined under 600°C for 6 hours or washed by ethanol in order to remove the surfactant template while retaining the polymer in the silicate walls.

2.3.4 Investigation of Film Forming Solutions using Synchrotron Time-resolved Small Angle X-ray Scattering

During the SAXS measurements, the CTAB/PEI mixture (total volume 30 ml) was first circulated continuously through the 1.5 mm radius quartz capillary and measured for 5 minutes, and then the interval of data collection in each frame was decreased to 20 seconds and SAXS data collection restarted. Tetramethoxysilane (0.375 ml) was added to the solution reservoir (total solution volume used is 30 ml) at the fourth frame, and this mixed CTAB/PEI/TMOS solution continued to circulate while SAXS patterns were collected for 30 frames of 20 seconds. At this point the solution had become cloudy and the interval of data collection in each frame was increased to 100 seconds and data collected until no further changes were observed in the SAXS patterns.

2.3.5 Silica Monoliths synthesized with Surfactants and Polyelectrolytes

Using surfactant and polyelectrolyte LPEI, silica monoliths were also synthesized. A typical method to synthesize silica monoliths was: mix 0.5 ml TMOS with high molecular weight LPEI solution and shake well before adding 10 ml 0.074 M CTAB surfactant. Silica gel monoliths formed within 1 min and only formed when the LPEI concentration was less than 20 g/L. The silica gel monolith took a longer time to form as the LPEI concentration increased. Surfactant concentrations used were as follows: CTAB (from 0.0375 M to 0.1 M), F-127 (from 0.001 M to 0.015 M), P-123 (from 0.001 M to 0.015 M), and Zonyl-FSO (from 0.025 M to 0.15 M).

For small angle scattering experiments, silica monoliths were aged at a temperature of 60 ^{o}C for a day to ensure a complete hydrolysis and condensation of silicate precursors, then the bottle cap was loosened and the composite dried at 40°C for several days to get a transparent silica/PEI/CTAB monolith. Small pieces of these materials were grilled and mounted as appropriate for X-ray scattering measurements.

2.3.6 Titania Films Templated by Surfactants and Polymers

Following the formation of silica films at the air/water interface, titania films templated using CTAB/SDS/polymer mixture were studied. In this case, all the procedures are similar to those for silicate films templated by CTAB/SDS/PEI complexes. Polyacrylamide and poly(ethylene oxide) were also used to template the titania films, and two titanium precusors were used and compared with each other: titanium butoxide (TiB) and Titanium (IV) bis(Ammonium lactato) Dihydroxide (TiBALD) which is stable at ambient temperature in aqueous solution. Those titania oxide films are not thermally strong since they fell apart after calcination at 450°C which probably is because not enough titania existed inside the film. Variation of the molar ratio of reagents was used to observe the effects of different reagent concentrations on film formation and structure. In each case the concentration of only one reagent was varied at any time. Precise details of the reaction conditions used are given with the results of these experiments. In all other respects the film preparation method remained the same throughout the experiments.

Titania films were also synthesized by impregnating the titanium precursors into the dry surfactant/polymer membranes using two methods: either evaporating the titania precursors onto the dry template in an evacuated, sealed container which was put in an oven at 40°C or by soaking the dry polymer-surfactant film template directly in the titania precursors. CTAB templated PEI films are too thin and melt or break up under both these methods. CTAB/SDS templated films were used in this study since they are thicker. Titania precursors were also initially introduced into some of the polymer-surfactant films during their formation to enhance the mechanical strength of the films. Thus two types of film were used as dry templates: dried CTAB/SDS/polymer films and CTAB/SDS/polymer/TiO_2 films containing some initial TiO_2.

In the evaporation experiments, five titania precursors were used: TiB, TiBALD, titanium(IV) ethoxide, titanium propoxide, and titanium tetrachloride. however, only titanium tetrachloride was able to be evaporated into the films. The calcined films fell apart probably because titanium tetrachloride hydrolyses very fast and only deposited

in a thin layer on top of the dry template, stopping the continuously accumulation into the deeper layers of the dry template films.

If the films were soaked into the titanium precursors (TiB or TiBALD), films were likely to melt in the TiBALD since 50% of this precursor solution is water, thus these films were strengthened by cross-linker (EGDGE) before soaking. These cross-linked polymer films swelled and became a block rather than a film if left in the solutions too long, so the soaking time was fixed as 1 hour. The physical strength of these titanium oxide films templated by soaking the dry polymer/surfactant template in the titanium precursor was improved. The films were either calcined at 450°C or washed with ethanol to remove the template, these films were still intact and did not fall apart.

2.3.7 Iron Oxide Films Templated by Surfactant and Polyelectrolyte

Templating by mixed surfactants and polyelectrolytes in interfacial films was also extended to iron oxide precursors. The CTAB stock solution concentration and the SDS stock concentration were constant as 0.2 M, while the polyelectrolyte solution was kept at 100g/L. Two polyelectrolytes LPEI and SPEI were used. The iron oxide film was templated by CTAB/PEI, CTAB/SDS/PEI, LPEI itself, SDS/PEI, Hydrogen chloride and sodium hydroxide were used to adjust the pH values of the film forming solutions.

The procedure to prepare iron oxide films templated by surfactant and polyelectrolyte is similar to that of preparation of silica films. To take SDS/PEI templated iron oxide as an example, 2 ml 0.2 M SDS solution was mixed with 4ml 100 g/L LPEI. $FeCl_2$ was dissolved into 14ml water and mixed with the SDS/LPEI solution and stirred for five minutes. For some samples, the pH value of the solution was adjusted by either adding NaOH solution or HCl solution. This solution was poured into a dish and left to form films. The experimental procedure remained the same and the concentration variations will be detailed with the experiments results. In each case, the concentration of only one reagent was varied at a time. Template was removed either by washing with ethanol or calcined at 450°C.

2.4 References

(1) S. W. Lovesey, *Theory of neutron scattering from condensed matter. Vol 1, Nuclear scattering*. Clarendon Press: Oxford, 1984.

(2) J. H. Hubbell, *Journal of Physical and Chemical Reference Data* **6**(2), 615 (1977).

(3) J. H. Hubbell, and I. Overbo, *Journal of Physical and Chemical Reference Data* **8**(1), 69 (1979).

(4) R. J. Roe, *Methods of X-ray and neutron scattering in polymer science*. Oxford University Press: New York, 2000.

(5) A. J. Jackson, *Introduction to Small-Angle Neutron Scattering and Neutron Reflectometr [online]: NIST Center for Neutron Research.* **Available from: http://www.ncnr.nist.gov/summerschool/ss10/pdf/SANS_NR_Intro.pdf** (2008).

(6) G. Fragneto, R. K. Thomas, A. R. Rennie, and J. Penfold, *Langmuir* **12**(25), 6036 (1996).

(7) D. Stigter, *Journal of Colloid and Interface Science* **23**(3), 379 (1967).

(8) *Diamond light source technology website [Online] Oxfordshire UK* **Available from: http://www.diamond.ac.uk/Home/Technology/Parameter.html**,

(9) *Layout of beamlines, Diamond light website [Online] Oxfordshire UK* **Available from: http://www.diamond.ac.uk/Home/Beamlines/plan.html**,

(10) S. A.C.Hannon, M,Bennington, S.Langridge, *Neutron Training Course Manual, Science and Technology Facilities Council, ISIS*, (2007).

(11) *Layout neutron instruments at ISIS spallation neutron source[Online] oxfordshire UK* **Available from: http://www.isis.stfc.ac.uk/instruments/instruments2105.html**,

(12) J. Penfold, and R. K. Thomas, *Journal of Physics-Condensed Matter* **2**(6), 1369 (1990).

(13) M. Born, and E. Wolf, *Principles of optics. Electromagnetic theory of propagation, interference and diffraction of light. 4.ed*. Pergamon press: Oxford, 1970.

(14) O. Glatter, and O. Kratky, *Small angle x-ray scattering*. Academic Press: London; New York, 1982.

(15) S. M. King, *Small Angle Neutron Scattering [online]; Rutherford Appleton Laboratory, Oxfordshire, UK* **Available from: www.small-angle.ac.uk/dms/small-angle/Intro_to_SANS_Web.pdf**, (1995).

(16) A. Guinier, G. Fournet, C. B. Walker, and K. L. Yudowitch, *Small-angle scattering of X-rays*. Wiley ; Chapman and Hall: New York; London, 1955.

(17) A. Nelson, *Journal of Applied Crystallography* **39**, 273 (2006).

(18) R.-J. Roe, *Methods of X-ray and Neutron Scattering in Polymer Science, Oxford University Press. Inc*, (2000).

(19) M. Kotlarchyk, and S. H. Chen, *Journal of Chemical Physics* **79**(5), 2461 (1983).

(20) S. S. Berr, *Journal of Physical Chemistry* **91**(18), 4760 (1987).

(21) J. Teixeira, *Journal of Applied Crystallography* **21**, 781 (1988).

(22) L. A. a. S. Feigin, *Structure and Analysis by Small-Angle X-Ray and Neutron Scattering,Plenum Press, NewYork*,

(23) O. S. Heavens, *Optical properties of thin solid films*. Butterworths Scientific Publ.: London, 1955.

(24) P. W. Atkins, and J. De Paula, *Atkins' Physical chemistry*. Oxford University Press: Oxford; New York, 2006.

(25) 徐如人, and 庞文琴, *分子筛与多孔材料化学，北京:科学出版社*, (2004).

(26) W. C. Marra, P. Eisenberger, and A. Y. Cho, *Journal of Applied Physics* **50**(11), 6927 (1979).

(27) M. Birkholz, W. John, Sons, and I. Wiley, *Thin film analysis by x-ray scattering*. Wiley-VCH Verlag GmbH & Co. KGaA: Weinheim, 2006.

(28) A. Lakhtakia, *Optik* **90**(4), 184 (1992).

(29) E. Hecht, and A. Zajac, *Optics, 4th Edition*. Addison-Wesley Publishing Company: Reading, MA, 2002.

(30) F.Fontana, *Memorie Mat. Fis. Soc. Ital Sci. I* **679**, (1777).

(31) S. J. Gregg, and K. S. W. Sing, *Adsorption, surface area, and porosity*. Academic Press: London, 1982.

(32) S. D. Brunauer, L.;Deming,W.; Teller,E., *Journal of the American Chemical Society* **62**, 1723 (1940).

(33) K. S. W. Sing, D. H. Everett, R. A. W. Haul, L. Moscou, R. A. Pierotti, J. Rouquerol, and T. Siemieniewska, *Pure and Applied Chemistry* **57**(4), 603 (1985).

(34) J. Rouquerol, D. Avnir, C. W. Fairbridge, D. H. Everett, J. H. Haynes, N. Pernicone, J. D. F. Ramsay, K. S. W. Sing, and K. K. Unger, *Pure and Applied Chemistry* **66**(8), 1739 (1994).

(35) I. Langmuir, *Journal of the American Ceramic Society* **38**, (1916).

(36) S. E. Brunauer, P.H.; Teller,E., *Journal of the American Chemical Society* **60**, 309 (1938).

(37) G. Halsey, J., *J. Chem. Phys.* **16**, 931 (1948).

(38) J. G. Harkins W.D., *J. Chem. Phys.* **11**, 431 (1943).

(39) C. Duval, *Inorganic Thermogravimetric Analysis*. Elsevier Publishing: London, 1963.

(40) P. Gabbott, *Principles and applications of thermal analysis*. Blackwell Pub.: Oxford, 2008.

(41) W. Schmatz, T. Springer, J. Schelten, and K. Ibel, *Journal of Applied Crystallography* **7**(4), 96 (1974).

(42) *Beamline I22 instrument specifications[online], Diamond light source, oxfordshire, UK* **Available from: http://www.diamond.ac.uk/Home/Beamlines/I22/status.html**,

(43) *Beamline layout I22 instrument [online], Diamond light source, oxfordshire, UK* **Available from: http://www.diamond.ac.uk/Home/Beamlines/I22/tech/specs.html**,

(44) H. Schnablegger, and Y. Singh, *A practical guide to SAXS*. Anton Parr: Austria, 2006.

(45) D.-M. Smilgies, N. Boudet, B. Struth, and O. Konovalov, *Journal of Synchrotron Radiation* **12**, 329 (2005).

(46) *O. Konovalov, J. Novak, A. Singh, A. Vorobiev, P. Feder, and K. Lhost, ID10B [online]. ESRF: 2008;* **Available from: http://www.esrf.eu/UsersAndScience/Experiments/SoftMatter/ID10B/id10b_manual.pdf**,

(47) K. Edler, A. Goldar, A. V. Hughes, S. J. Roser, and S. Mann, *Microporous and Mesoporous Materials* **44-45**, 661 (2001).

(48) R. Thiruvengadathan, Y. Levi-Kalisman, and O. Regev, *Current Opinion in Colloid & Interface Science* **10**(5-6), 280 (2005).

(49) E. Kokufuta, H. Suzuki, R. Yoshida, K. Yamada, M. Hirata, and F. Kaneko, *Langmuir* **14**(4), 788 (1998).

Chapter 3 Cationic Surfactant/Polyelectrolytes Complex Templated Silica Materials

3.1 Introduction

Free-standing nanostructured surfactant and polyelectrolytes films at the air/water surface have now been extensively studied by our group and have been summarized in **Section § 1.3.2.3**; [1-3] however, using the surfactant and polyelectrolytes complexes to generate films in the presence of silicate precursors had not previously been attempted.

In this chapter, the robust dried surfactant and polyelectrolyte films without silica were first prepared; these films were able to retain mesostructural order to some extent after removal from the solution surface. Studies of DDAB with PEI are also discussed. This is followed by an account of studies of the spontaneously formed silica films at the air/water interface. These films were synthesized using the CTAB/PEI solutions in the presence of silica precursors. Neutron reflectivity and GIXD were utilized to study the interfacial *in-situ* film structure; The real time evolution of the CTAB/PEI/silica film forming solutions were observed using synchrotron based small angle X-ray scattering (SAXS) and a film formation mechanism was proposed. All these films were removed from the surface to produce dried free-standing silica films. Most films displayed long-range 2D hexagonal mesostructures and retained their mesostructures even after the removal of template. Notably these films form at high pH, whereas previous work on film formation, including dip and spin coating as well as spontaneous growth of films at the solution surface, has required acidic solutions. Normally in alkaline solutions only precipitates are formed.

These stronger, thicker mesoporous silica films have improved mechanical strength over thinner, brittle silica/surfactant-only films and retain the polymer in the silica walls, providing a simple method of introducing polymer functionality into the pore

walls. These advantages open up potential applications in a variety of fields such as catalysis, molecular separation, and drug delivery. Preliminary studies on molecular separation will be reported in the **Appendices Section § 7.1**. To the best of our knowledge, this is the first report of a one step process to synthesize a mesoporous silica film with long range order and high hydrothermal stability templated by the surfactant/polyelectrolyte complex at the air/water surface.

Furthermore, I also report an instant preparation of silica monolith (less than one minute) by adding polyelectrolytes with amine groups into TMOS/CTAB solutions. Variation of surfactant types and concentrations led to monoliths with different mesostructures.

3.2 Dried Cationic Surfactant/Polyelectrolyte Films Removed from Air/water Interface

3.2.1 Dried CTAB/PEI Films

In previous papers, surfactant/polyelectrolyte films formed at the air/water surface were extensively studied *in situ*.[1] Films formed from low MW PEI (SPEI) are thin and contain a more highly ordered mesostructure than those formed from high MW PEI (LPEI) polymer.[1] The ordering, however, is maintained down to extremely low polymer and surfactant concentrations, even below the surfactant CMC.[4] Cross-linking causes little change in the mesostructure in *in situ* films but helps to freeze the metastable mesostructure and makes films strong enough to be removed from the solution surface.[3] Increasing the pH of the solution causes formation of thicker films and improves the ordering in low MW films, while high MW films can lose some order, although this occurs only at high polymer concentration.[3] Films are robust enough to be removed from the surface on an open mesh, as shown in **Figure 3.1**. The film is continuous, rubbery and slightly tacky due to the hydrophilic nature of the polymer.

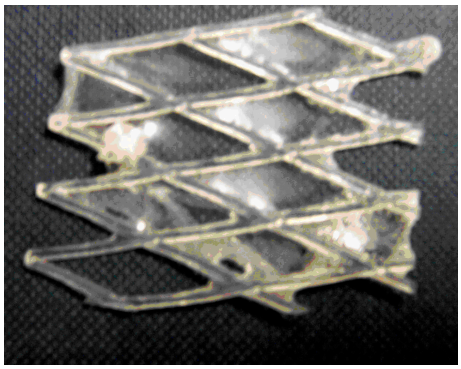

Figure 3.1 *Picture of dried film on an open plastic mesh synthesized with CTAB/PEI complexes, Mesh length is 3.5 cm.*

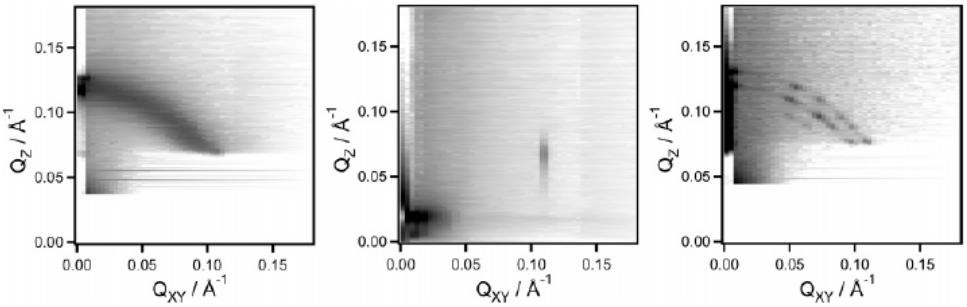

Figure 3.2 *GIXD patterns of CTAB/PEI films (left to right): CTAB:3.75 g/l LPEI, CTAB:15 g/l SPEI and CTAB: 60 g/l SPEI,*[3] *used with permission from Ref.3.*

Small-angle X-ray scattering patterns of the dried polymer films synthesized with CTAB and different concentrations of LPEI (from 10 g/l to 50 g/l), but without silica, are given in **Figure 3.3**. All of these patterns show a wide peak at 0.15 Å^{-1}, indicating that the mesostructure is retained but overall has relatively poor long-range order. The intensity and shape of the peak do not change with increasing LPEI concentration which shows that the solution concentration of LPEI makes little difference to the dried polymer film mesostructure. A second sharper peak at 0.24 Å^{-1} is from excess crystalline CTAB, which is assumed to be formed on the film surface where droplets of the subphase have dried. Compared to grazing incidence diffraction and neutron reflectivity data from CTAB/LPEI films at the air/water surface, which also shows partially ordered structures and broad diffraction peaks (as shown in **Figure 3.2**),[3] the dried films preserve their mesoscale structure during the drying process. The

d-spacing decreases from 54 Å in the interfacial film to 40 Å in the dried film, which indicates shrinkage of the lattice spacing due to loss of water from the polymer hydrogel between micelles during the drying process.

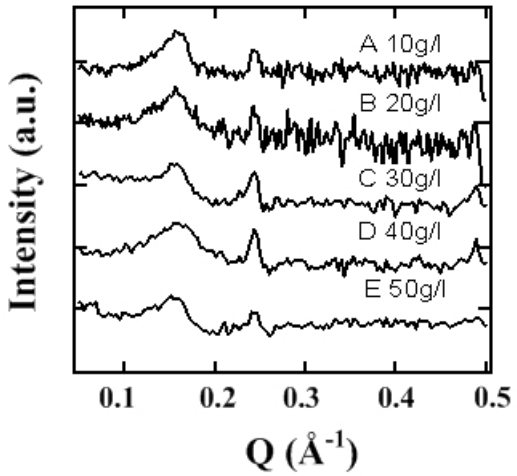

Figure 3.3 *SAXS patterns of dried polymer film synthesized with 0.037M CTAB, (top to bottom) with 10 g/l LPEI, 20 g/l LPEI, 30 g/l LPEI, 40 g/l LPEI, 50 g/l LPEI. No cross-linker (EGDGE) was used to prepare these films.*

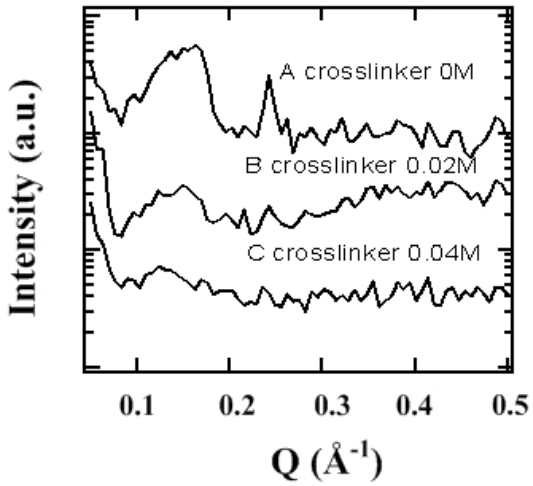

Figure 3.4 *SAXS patterns of dried polymer films synthesized using cross-linker at concentrations of (top to bottom) 0 M, 0.02 M, and 0.04 M EGDGE. The films were all prepared at concentrations of 0.037 M CTAB, 30 g/l LPEI.*

Cross-linker plays an important role in preparing the dried CTAB/PEI films. By cross-linking the polymer, permanent covalent bonds are formed between adjacent polymer strands, creating a stronger and more permanent linkage than the hydrogen bonding and polymer entanglement which holds the films together in the absence of cross-linker. Ethylene glycol diglycidyl ether (EGDGE) is a commonly used cross-linking agent for PEI, and the reaction occurs at room temperature in ambient conditions (Refer to **Section § 2.3.2** for synthesis conditions using EGDGE).[5] Cross-linking in the films was observed to proceed much faster than in the subphase solutions, as a result of the higher concentration at the interface. This allows cross-linked films to be removed from the liquid surface, since subphase gelation by the cross-linker does not occur for several hours after the cross-linking of the film is complete.

However, for films synthesized with LPEI (**Figure 3.4**), the first diffraction peak in SAXS patterns becomes less distinct when the concentration of EGDGE increases, which indicates that the cross-linking reaction reduces the ordering of the dried films synthesized with LPEI.

For SPEI without cross-linker, all the films were either difficult to remove intact from the air/water interface or displayed a disordered structure after drying. Higher pH is known to improve film ordering on the solution surface and increases the film thickness because the charge on PEI decreases at higher pH, so the polymer can interact more effectively with CTAB micelles through ion-dipole interactions[5]. Thus to improve the structure of the dried SPEI films, the pH was increased to 12 by adding sodium hydroxide to the CTAB/SPEI system. Similarly the effect of cross-linker has also been studied, since cross-linked films are stronger than those without cross-linking and are more easily removed from the solution surface without breaking. In contrast to films synthesized with LPEI, cross-linking was found to improve the mesostructure, as shown in **Figure 3.5**. The first peak around 0.16 $Å^{-1}$ becomes more distinct with increasing cross-linker concentration which shows that cross-linker helps to improve the structural ordering in the SPEI films.

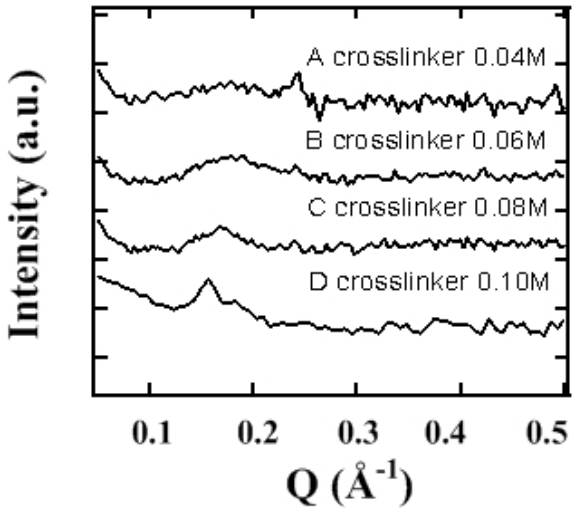

Figure 3.5 *SAXS pattern of dried polymer film synthesized with (top to bottom) 0.04 M, 0.06 M, 0.08 M EGDGE at pH 12, and solution concentrations of 0.037 M CTAB, 15 g/l SPEI.*

3.2.2 DDAB/PEI Films

3.2.2.1 Interfacial DDAB/PEI Films

Films synthesized with DDAB/PEI complexes have also been studied. Mixing surfactant DDAB and polyelectrolyte PEI also results in the formation of thick films at the air/water interface, which can be easily seen with the naked eye. These films are much thicker than films synthesized with CTAB/PEI, probably due to the higher hydrophobicity of the double alkyl chains.

GIXD patterns of films formed by DDAB with LPEI and SPEI are given in **Figure 3.6** and **Figure 3.8** respectively. Generally for each sample, an X-ray reflectivity profile was measured first, followed by the two GIXD patterns at two incidence angles, 0.045º and second angle that corresponded to the position of the first diffraction peak in the X-ray reflectivity.

GIXD patterns of DDAB/LPEI interfacial film synthesized with 0.045M DDAB and 20 g/l LPEI are shown in **Figure 3.6**. **Figure 3.6 A** shows GIXD patterns taken at 0.045º, which correspond to the film structure closest to the interface. **Figure 3.6 B**

was taken at an incident angle of 0.39° and shows the structure deeper in the film. The common features in these two patterns is a broad diffraction peak which indicates a partially ordered mesophase The line profiles which were taken from the GIXD patterns at Q_{xy}=0.007 $Å^{-1}$ only display a broad peak around 0.14 $Å^{-1}$(as shown in **Figure 3.6 C**), indicating a d-spacing of 45 Å. The film structure and d-spacing values are similar for the film top layers and layers deeper in the film. However, there is one spot on **Figure 3.6 B** corresponding to one peak at 0.75 $Å^{-1}$ in **Figure 3.6 Cb**, it may be from detector artifact or may come from the dry surfactant crystal at the surface since 8 Å spacing is as small as the distance between the surfactant tails.

Surfactant DDAB and polyelectrolyte LPEI concentration variations do not improve ordering of the mesophase, only a broad peak could be observed in all the GIXD patterns. However, variation of the surfactant and the LPEI concentrations result in changes in the first peak position. As shown in **Figure 3.7 A, B and C, D**, when the relative surfactant concentrations increased from 0.0045 M to 0.018 M and the LPEI concentration was kept at 20 g/l, the first peak position moves from 0.145$Å^{-1}$ to 0.12 $Å^{-1}$, corresponding to increase in d-spacing value from 45 Å to 52 Å. A similar trend was also observed when the surfactant concentration was kept at 0.0045 M while the LPEI concentrations decreased from 30 g/l to 20 g/l, as shown in **Figure 3.7 E, F and C, D**. This is probably due to the effects of charge screening by PEI towards the surfactant. When the PEI concentration decreases or the surfactant concentration increases, the PEI screens the charge on the surfactant molecules less effectively, causing adjacent micelles to move further apart.

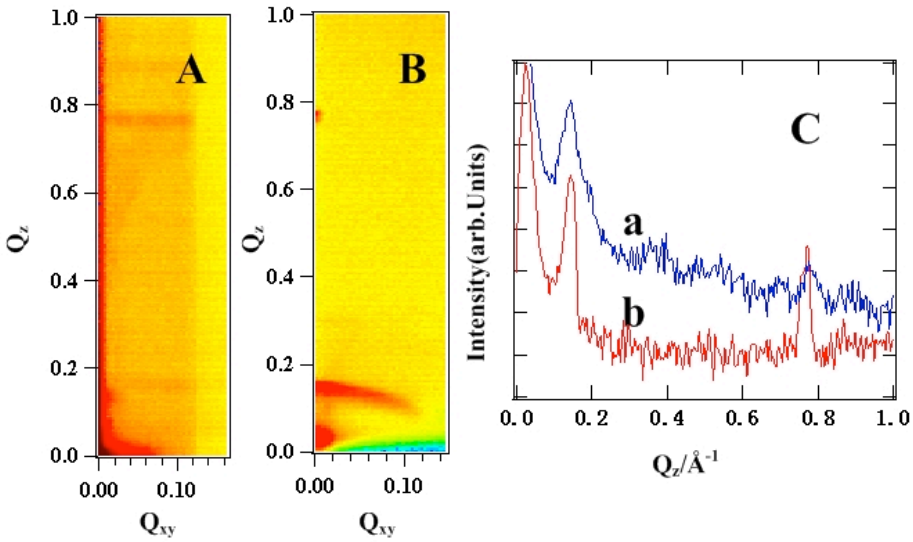

Figure 3.6 *GIXD patterns of interfacial DDAB/LPEI films templated by 0.045 M DDAB and 20 g/l LPEI complexes. (A) Pattern taken at an incident angle of 0.045° showing the structure of the top layers of interfacial DDAB/LPEI films. (B) Pattern taken at an incident angle of 0.39° showing the structure of relatively deeper layers of the interfacial DDAB/LPEI films. (C) Line profiles at* Q_{xy}*=0.007* $Å^{-1}$ *from the GIXD patterns in A & B.*

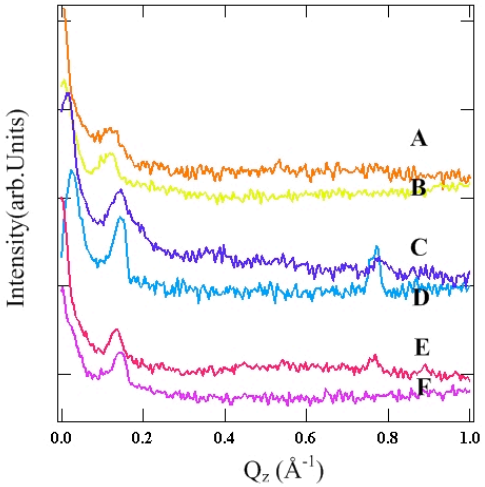

Figure 3.7 *Line profiles at* Q_{xy}*=0.007* $Å^{-1}$ *from GIXD patterns collected from interfacial DDAB/LPEI films. DDAB 0.018 M 20g/l LPEI, incident angles (A) 0.045° and (B) 0.385°. DDAB 0.0045 M 20 g/l LPEI incident angles (C) 0.045° and (D) 0.390°. DDAB 0.0045 M 30 g/l LPEI incident angles (E) 0.0045° and (F) 0.390°.*

For DDAB films made with short SPEI, more diffraction peaks were observed in their GIXD patterns and GIXD patterns collected on different component concentrations are similar. Typical GIXD patterns of the interfacial DDAB/SPEI film which is prepared from 0.0045 M DDAB and 20 g/l SPEI complexes was shown in **Figure 3.8 A and B**. Both the top layer and deeper interfacial film structure show two distinct diffraction peaks at Q_z of 0.15 Å^{-1} and 0.29 Å^{-1}, which were indexed as the (001) and (002) reflections, corresponding to a lamellar mesophase with a d-spacing of 42 Å, as shown in **Figure 3.8 C**.

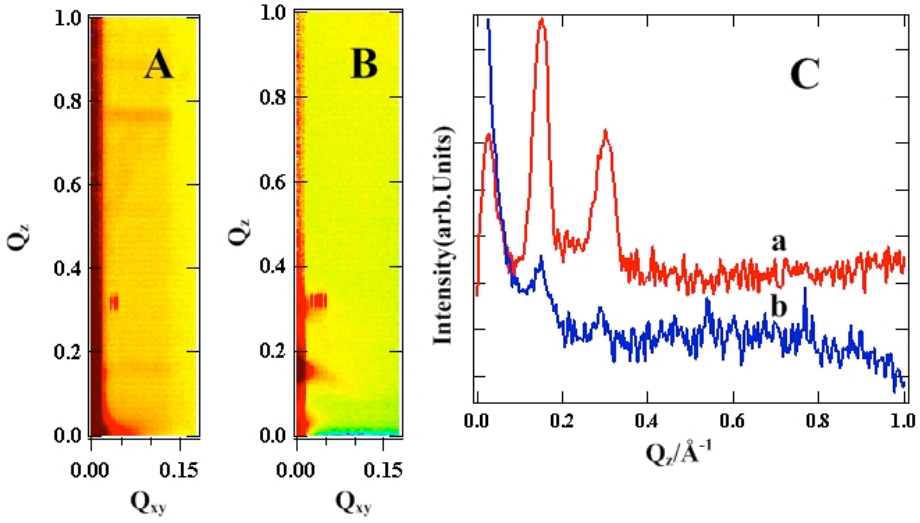

Figure 3.8 *GIXD patterns of interfacial DDAB/SPEI films prepared from 0.0045 M DDAB and 20 g/l SPEI. (A) Pattern taken at an incident angle of 0.045° showing the structure of the top layers of interfacial DDAB/SPEI films (B) Pattern taken at an incident angle of 0.399° showing the structure of relatively deeper layers of the interfacial DDAB/SPEI films. (C)Line profiles at Q_{xy}=0.007 Å^{-1} from GIXD patterns in (a) A & (b) B*

3.2.2.2 Dried DDAB/PEI Films

SAXS patterns of the dried polymer films synthesized with DDAB and different concentrations of PEI are given in **Figure 3.9**. All the peak positions are listed in **Table 3.1**.

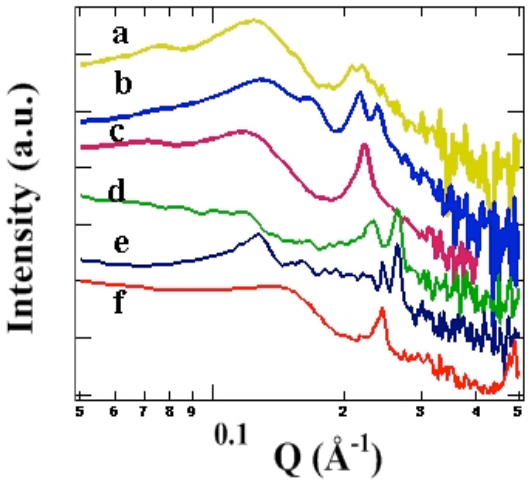

Figure 3.9 *SAXS patterns of dried DDAB/PEI polymer films. (a ,b, c). The DDAB concentration was fixed at 0.0045 M and LPEI concentrations are 10 g/l, 20 g/l, 30 g/l (d) DDAB 0.009 M 20 g/l LPEI. (e) DDAB 0.018 M 20 g/l LPEI. (f) DDAB 0.045 M 20 g/l SPEI.*

Table 3.1 *Peak position and d-spacing taken from the SAXS patterns of the dry films synthesized with DDAB/PEI*

Sample	DDAB	LPEI	Q[a] (Å^{-1})				Distance[a] (Å)
a	0.0045M	10 g/l	0.12	0.21	—	—	50
b	0.0045 M	20 g/l	0.12	0.17	0.21	0.23	51
c	0.0045 M	30 g/l	0.12	0.22	—	—	52
d	0.009 M	20 g/l	0.12	0.23	0.26	—	52
e	0.018 M	20 g/l	0.13	0.24	0.26		49
f	0.0045 M	20 g/l SPEI	0.15	0.24	—	—	43

a – errors in the Q values are ±0.01 Å^{-1} While errors in the d-spacings are ±1 Å.

The dried films show some degree of ordering, as shown in **Figure 3.9 A**. The SAXS patterns of the films show one broad peak in different positions at lower Q values and sharp peaks at relatively higher Q values, as shown in **Table 3.1**, these peak positions are difficult to assign to a single mesophase. The broad peak indicates a less ordered film structure in the dried film. Films synthesized with DDAB/PEI

appear to be less reproducible than films synthesized with CTAB/PEI probably because the phase diagram of DDAB is very sensitive to the environment and sample history, such as temperature and mixed phases can co-exist under room temperature.[6] However, it seems that film structures are relatively more stable and reproducible as the DDAB concentration is increased.

3.2.3 Discussion - Cationic Surfactant/Polyelectrolyte Films

Previously, polymer/surfactant films at the air/water surface have been extensively studied in our group and we have suggested a possible mechanism for the formation of the polymer films at the air/water interface.[3] Upon mixing the solutions of cationic surfactant and polyethylenimine, there is some association in the solution forming aggregates with the micelles loosely wrapped by polyelectrolyte chains. Evaporation and the slightly increased hydrophobicity of the micelle/polymer complex drives phase separation into a concentrated surfactant/polymer layer at the interface.[7] Continuing evaporation causes the dehydration of the upper layers of the film, and thus promotes the ordering of the film at the interface and helps assist further aggregation below it. Ordered films are therefore found over the entire concentration range where stable films are observed to form, even at very low polymer concentration, and surfactant concentrations below the CMC for sufficiently high molecular weight polymers.[4] For low molecular weight polymers where the polymer itself is more hydrophilic, unstable initially ordered films are observed to lose order with time by thinning, if there is insufficient material in the phase separated layer at the interface to completely cover that interface with a substantial mesostructured layer.

Using cross-linker in the reaction solution, polymer films synthesized with SPEI were able to be taken off of the surface and dried, and the dried films synthesized both with LPEI and SPEI are shown here to preserve the nanoscale structure observed at the solution surface in our previous work. The cross-linker (EGDGE) has a great effect on the structural ordering of the dried films. Cross-linking caused disordering in the films synthesized with LPEI but enhances the ordering of the films synthesized

with SPEI. EGDGE contains two epoxides that are susceptible to nucleophilic addition reactions involving the amine groups on the polymer. The cross-linking results indicate that there is probably an optimum polymer length for ordered mesostructured film formation. In the case of the hyper-branched LPEI, it is already longer than the optimal length for mesostructural ordering, so increasing the concentration of EGDGE will not only decrease the number of primary amine groups on the polymer, decreasing the dipole-cation bond formed between the polymer and surfactant micelles, but will also distort the PEI chain, which induces disorder in the arrangement of the surfactant micelles. For the SPEI, the polymer is shorter than the optimum polymer length for film formation, so in this case increasing the concentration of the EGDGE will bridge between SPEI chains and brings the cross-linked polymer closer to the optimum length, helping to improve both film thickness and also mesostructural ordering.

3.3 Silica Films Synthesized with Cationic Surfactant and Polyelectrolyte Complexes at the Air/Water Interface

Having established that the polymer/surfactant films contain well ordered structures at the solution interface but less well ordered structures after recovery from the surface and drying, it was decided to attempt to mineralize the *in situ* films at the air solution interface. Thus here, silica films have been synthesized using the surfactant/polyelectrolyte complex at the air/water surface by adding silica precursor to the surfactant/polymer mixture rather than to the simple surfactant templates used in the previous studies. The method is given in **Section § 2.3.3**. Free-standing solid films form readily from the mixed PEI/CTAB/TMOS solutions and can be clearly seen at the air/water interface. Film synthesized with LPEI develop rapidly and are clear, transparent and initially smooth but developed wrinkles upon aging. The film formation process for the film synthesized with SPEI, in contrast, is relatively slow, the film is white and smooth, and precipitation in the subphase solution could also be seen (**Figure 3.10**).

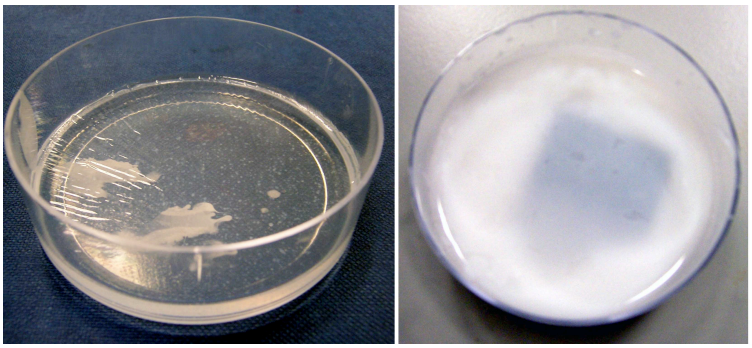

Figure 3.10 *Pictures of silica films at the air/water surface in a 62mm wide polystyrene dish synthesized with (left) CTAB: LPEI and (right) CTAB: SPEI.*

3.3.1 Brewster Angle Microscopy

BAM pictures of silica films, shown in **Figure 3.11**, were taken immediately after the mixture of the silicate precursor and surfactant/polymer solution was poured into a plastic dish and at intervals until film formation had occurred. The surfaces of silica/CTAB/LEPI solutions were mobile during the first 10 minutes and became still thereafter, indicating the formation of more continuous and less mobile films. The films became thick and rough at about 20 minutes. These images look similar to those of CTAB/PEI films prepared without silicate species[8-10]. Silica films synthesized with CTAB/SPEI initially looked similar to CTAB/LPEI in the BAM images but keep growing for longer, and after 5 h the film was much thicker and smoother than the CTAB/LPEI film. The overall times for formation of silica films synthesized with SPEI were much longer than the times for films synthesized with LPEI, but films synthesized with SPEI were much smoother on the micrometer length scale than films synthesized with LPEI.

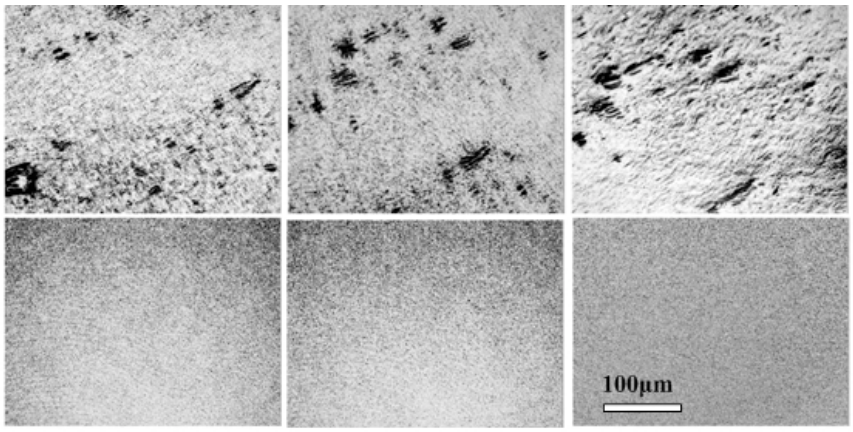

Figure 3.11 *BAM pictures of silica films grown at the air/water interface. At the top are films synthesized with 0.037 M CTAB: 30 g/l LPEI at (Left - Right) 0 min, 10 min, and 20 min, and at the bottom are films synthesized with 0.037 M CTAB: 30 g/l SPEI at (Left - Right) 0 min, 30 min, and 5 h, respectively. The images are all 340 µm along the bottom edge.*

3.3.2 Time-resolved Neutron Reflectivity

The neutron reflectivity patterns for the silica films synthesized with CTAB/LPEI are shown in **Figure 3.12**. In general the LPEI films show little evidence of long range mesostructural ordering as they grow. **Figure 3.12a** shows examples of data for films whose neutron reflectivity patterns have no distinct diffraction peaks, with lines showing the best fit to a layer model described in **Table 3.2**. The scattering length density (SLD) data from the fit suggests that these silica films synthesized with CTAB: LPEI contain about four layers; the first layer is a single CTAB monolayer lying close to the surface with a disordered silicate/PEI layer beneath. The SLD of the third layer decreases because of the CTAB micelles incorporated into this layer but this layer also contains PEI and silica. The SLD of the last layer is almost equal to the SLD of the sub-phase of the solution. As the film continues to grow at the air/water surface, the SLD of second layer increases as a result of the condensation of TMOS, and the SLD of last layer decreases to around 2×10^{-6} Å^{-2}, suggesting there is another layer of micelle-containing adsorbed material present. The film layer structure does

not seem to change much with the variation of LPEI and TMOS concentration. In **Figure 3.12b**, an *in situ* CTAB/LPEI/silica film (40 g/l LPEI: 0.134 M TMOS) with two broad diffraction peaks was observed, they are difficult to fit but give a spacing between adjacent repeat units of 65 Å, and again the structure does not change during the film growth process.

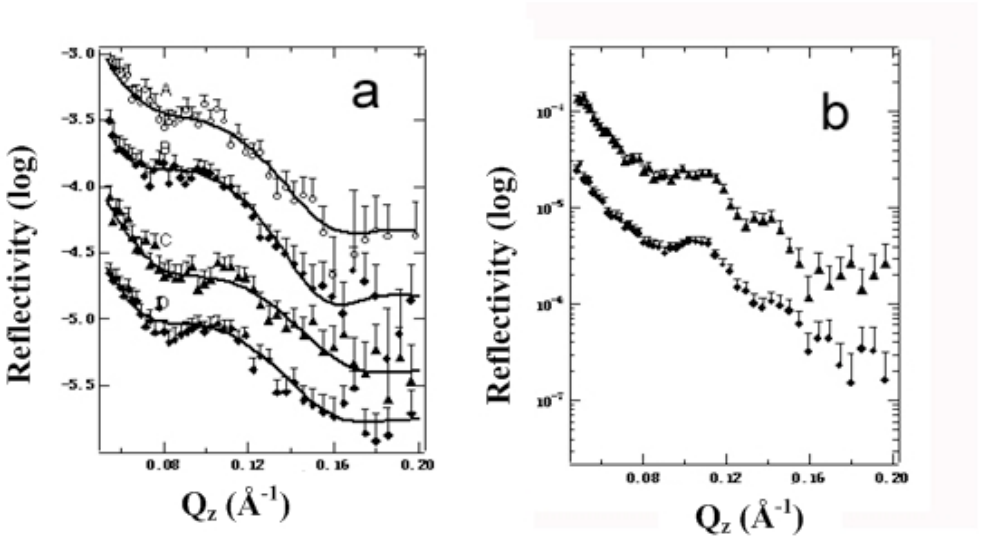

Figure 3.12 *Neutron reflectivity patterns of silica films without long range liquid crystalline order grown at the air/water interface with TMOS and LPEI. (a) A, B are 30 g/l LPEI:0.335 M TMOS film at 15 min & 45 min, respectively; C, 30 g/l LPEI:0.167 M TMOS film at 45 min; D, 20 g/l LPEI:0.167 M TMOS film at 45 min. A line of best fit to the data is also shown (see* ***Table 3.2****). (b) 40 g/l LPEI: 0.134 M TMOS film at 15 min and 45 min (from top to bottom). CTAB concentration was constant at 0.037 M.*

Neutron reflectivity patterns for the silica films synthesized with TMOS, SPEI and CTAB (shown in **Figure 3.13**) show a greater range of mesostructural order. **Figure 3.13 a** is a film synthesized with 0.037 M CTAB:20 g/l SPEI:0.134 M TMOS:0.04 M EGDGE, where no distinct peaks were observed. Fitting results, also in **Table 3.2**, shows this film has a similar layer structure to films synthesized with LPEI. **Figure 3.13 b** is a film synthesized with the same SPEI/CTAB/EGDGE concentrations but

more TMOS. Here the intensity of the diffraction peaks decreased with time, which is normal for SPEI/CTAB films without silica, synthesized at a low concentration of SPEI.[3] The disappearing peak is due to the redistribution or reorientation of the inorganic polymer/surfactant aggregates into thinner layers with time, and these thinner layers do not give rise to diffraction peaks, only fringes in the reflectivity. **Figure 3.13 c-f** show films with several distinct diffraction peaks. For all those films, two distinct peaks at about 0.12 $Å^{-1}$ and 0.14 $Å^{-1}$ (corresponding to d-spacings of 52 Å and 45 Å) were observed at the beginning of the reaction, which can be indexed to a cubic phase, although more peaks are needed to unambiguously confirm its structure. The position of these two peaks does not change as the SPEI concentration is varied. However, the intensity of the first peak decreases, and that of the second peak increases with time, which indicates that the silica film structure is changing.

The film synthesized with EGDGE changed structure faster, with the transition occurring at about one hour after mixing while the film synthesized without EGDGE underwent a similar transition at about two hours after mixing. Given that the position of the second peak which increases in intensity in the neutron reflectivity is similar to that of the first diffraction peak in SAXS data of dry films which have a 2D hexagonal mesostructure, as shown in **Figure 3.19**, we deduce that films at the air/water surface change from an initial cubic structure to a final 2D hexagonal structure while still on the solution surface. Thus the structural transition is not caused by the drying of the film after it is removed from the surface but by the continuing silica condensation and surface dehydration while the film is still on the solution surface. Comparing **Figure 3.13 c and d, e and f**, we can see that the addition of cross-linker speeds up the formation of films but has little effect on the silica film structure.

Table 3.2 *Fitting results for the neutron reflectivity patterns of disordered silica films synthesized with CTAB/PEI at the air/water surface.*

Sample	Layers	SLD of subphase[a] ($\times 10^{-6}$) Å^{-2}	Thickness[a] (Å)	SLD[a] ($\times 10^{-6}$) Å^{-2}
30 g/l LPEI / 0.335 M TMOS	4	3.30	15	-0.44
			11	0.98
			46	0.03
			17	3.05
		3.31	15	-0.35
			11	1.14
			46	0.02
			18	2.41
30 g/l LPEI / 0.167 M TMOS	4	4.34	15	-0.35
			16	0.65
			39	0.05
			19	2.24
20 g/l LPEI / 0.167 M TMOS	4	4.37	15	-0.35
			16	0.52
			40	0.05
			16	2.61
20 g/l SPEI / 0.134 M TMOS / 0.04 M EGDGE	4	4.66	16	-0.48
			8	0.20
			46	0.01
			25	4.39
		4.67	16	-0.35
			3	0.79
			37	0.01
			38	2.80

a – errors in the fitted layer thickness are ±2Å, and in the SLD values ±0.05×10^{-6}Å^{-2}

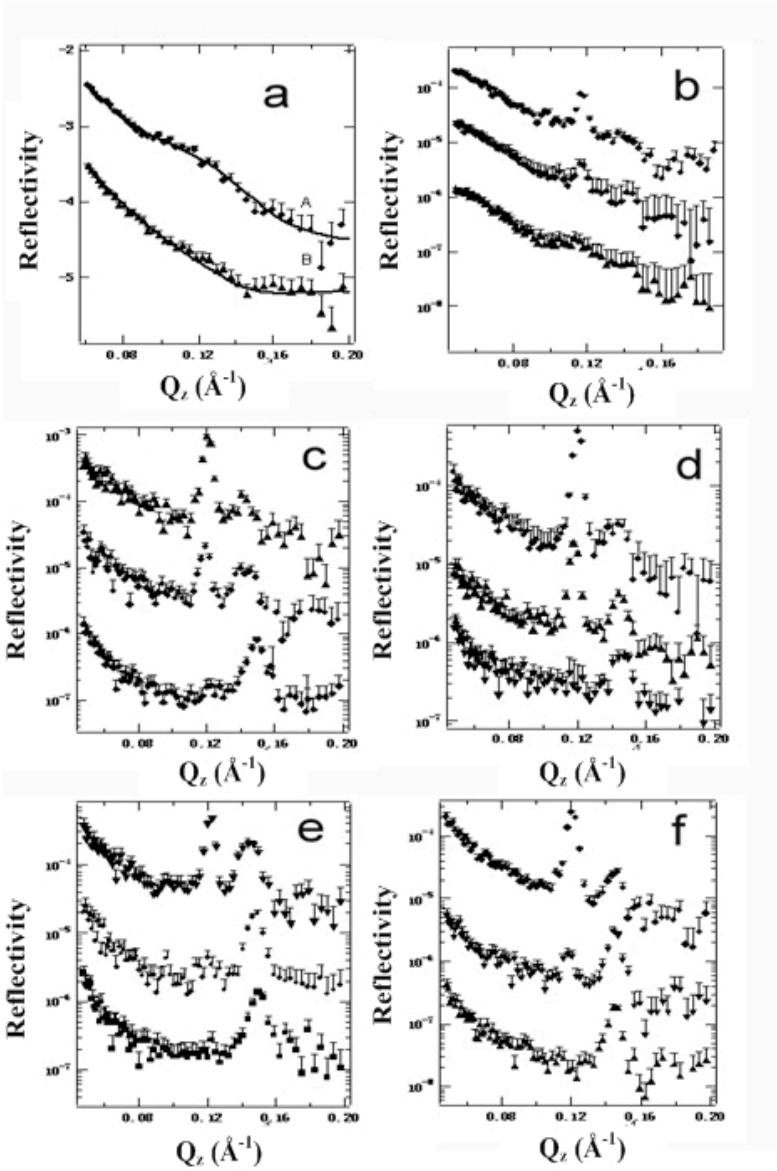

Figure 3.13 *Neutron reflectivity patterns of silica films grown at the air/water surface synthesized with TMOS and SPEI. (a) 20 g/l SPEI: 0.134 M TMOS: 0.04 M EGDGE, a best fit line to the data is also shown. (b) 20 g/l SPEI: 0.08375 M TMOS: 0.04 M CL film at 15 min to 1h (from top to bottom). (c) 30 g/l SPEI: 0.08375 M TMOS film at 15 min to 2 h (from top to bottom). (d) 30 g/l SPEI: 0.08375 M TMOS: 0.04 M CL at 30 min to 1 h (from top to bottom). (e) 40 g/l SPEI: 0.08375 M TMOS at 30 min to 2 h (from top to bottom). (f) is 40 g/l SPEI: 0.08375 M TMOS: 0.04 M CL at 30 min to 1 h (from top to bottom).*

Time-resolved neutron reflectivity data has also been collected on INTER, at ISIS. This instrument gives a faster time resolution of 30 seconds per pattern, as shown in **Figure 3.14**. Two peaks at 0.12 $Å^{-1}$ and 0.14 $Å^{-1}$ appeared around 10 minutes after mixing, which is identical with the data collected from SURF. Again, the intermediate structure of the film is difficult to assign, however, these two diffraction peaks evolved into one sharp peak at about one hour, indicating the phase transformation occurring within the interfacial film. GIXD patterns confirm the formation of the final 2D hexagonal mesostructure (as shown in **Figure 3.15**).

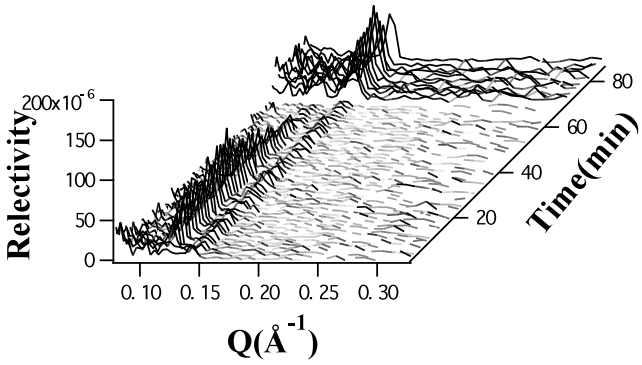

Figure 3.14 *Neutron reflectivity patterns of silica films grown at the air/water interface synthesized with 0.037 M CTAB and 40 g/L SPEI, collected on INTER, ISIS.*

3.3.3 Grazing Incidence X-ray Diffraction

Grazing incidence diffraction patterns were also collected on the mature interfacial CTAB/PEI/silica films at two incident angles: 0.13° and the first angle of the first diffraction peak which was generally around 1.1°. For silica films templated by CTAB/SPEI, GIXD patterns collected at low and high incident angles on the interfacial CTAB/SPEI/silica films were different. As shown in **Figure 3.15**, only a diffraction ring at 0.16 $Å^{-1}$ was observed for the low incident angles, corresponding to the top ~200 Å of the film structure, indicating the presence of an ordered mesophase with d-pacing of 40 Å, as shown in **Figure 3.15 A and C a**. The volume measured contains only three or four repeat units of the structure so higher order peaks are not

observed, however the peak width is narrow and similar to that measured at the higher incident angle. At the higher incident angle, which measures to a greater depth in the interfacial films, four sharp diffraction rings at 0.15 $Å^{-1}$, 0.26 $Å^{-1}$, 0.30 $Å^{-1}$, 0.40 $Å^{-1}$ could be observed from the GIXD patterns (**Figure 3.15 B and C b**). These four sharp diffraction peaks can be indexed as the (100), (110), (200), (210) reflections, suggesting a highly ordered 2D hexagonal mesophase with a d-spacing of 41 Å.

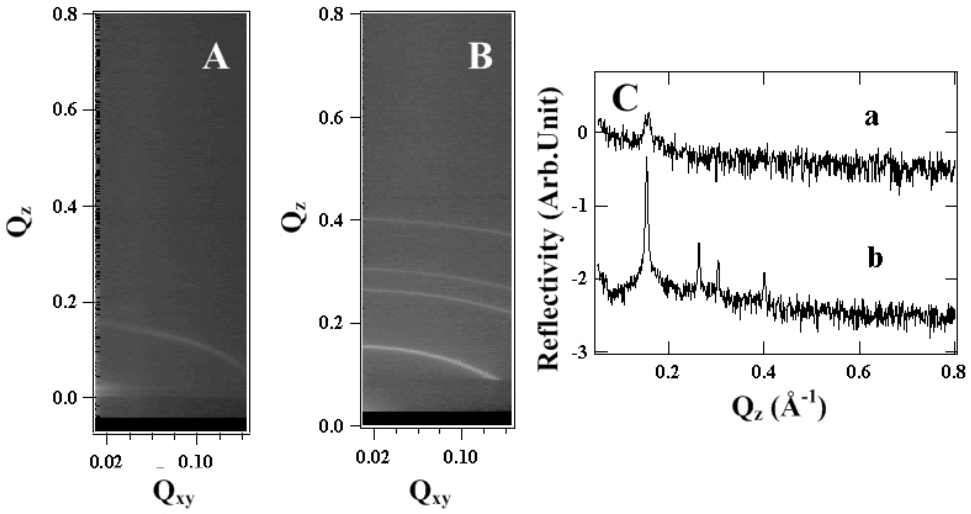

Figure 3.15 *GIXD patterns of interfacial silica films templated by 0.037 M CTAB, 30 g/l SPEI. Structure of (A) top layers and (B) relatively deeper layers of the film. (C) Line profiles at Qxy=0.007 $Å^{-1}$ from GIXD patterns (a) A and (b) B.*

GIXD has also been used to identify the mesostructure of the mature CTAB/LPEI/silica interfacial films, as shown in **Figure 3.16**. When GIXD patterns were taken at 0.13°, incident angle, two diffraction rings, corresponding to the two peaks at 0.10 Å and 0.13 Å in the linear profile at Q_{xy}=0.007 $Å^{-1}$ were observed. These two peaks can be indexed to a cubic mesophase, which corresponds well with the results from neutron reflectivity data. GIXD patterns at higher incident angles displayed four diffraction rings corresponding to four distinct peaks observed in the line profiles (**Figure 3.16 C b**),0.15 $Å^{-1}$, 0.26 $Å^{-1}$, 0.30 $Å^{-1}$, 0.39 $Å^{-1}$. These peaks can also be indexed as (100), (110), (200), (210) reflections, indicating a highly ordered 2D hexagonal mesophase with a d-spacing of 43 Å.

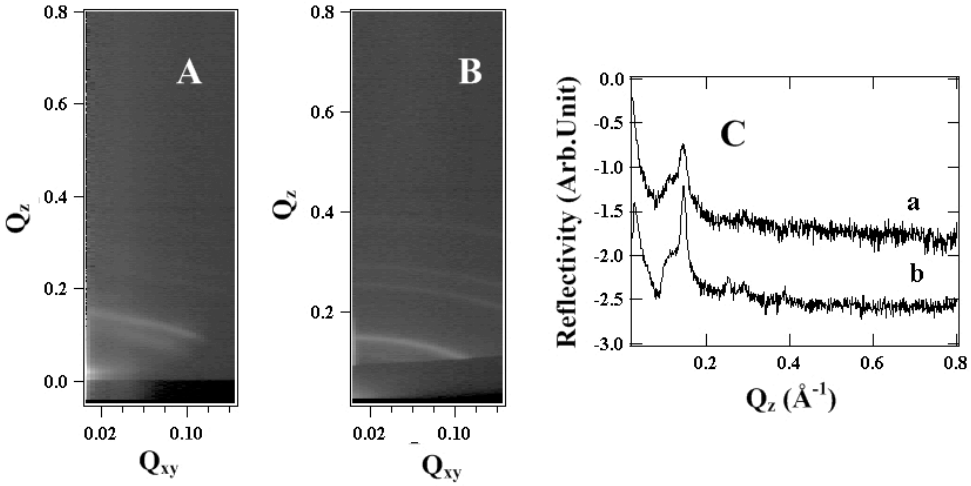

Figure 3.16 *GIXD patterns of interfacial silica films templated by CTAB/LPEI Structure of (A) top about 200 Å of interfacial silica films measured at low incident angle and (B) deeper layers of interfacial silica films measured at higher incident angles. (C) Line profiles at* Q_{xy}*=0.007* $Å^{-1}$ *from GIXD patterns (a) A and (b) B.*

3.3.4 Evolution of Film Forming Solutions

General mechanisms for the formation of surfactant templated silica, especially for the materials with film geometry, was introduced in **Section § 1.2.2**. Nowadays, many research groups are also interested in the preparation of silica materials with surfactant and polyelectrolytes, as seen in **Section § 1.4**. In the previous section **(Section § 3.3)**, we reported the first example of spontaneously formed silica films synthesized using alkaline CTAB/PEI complexes at the air/water interface. Thus investigation of the formation mechanism of this robust CTAB/PEI/silica film is of great interest.

Self assembly processes between inorganic and organic species and the formation of mesostructure have been followed by many *in situ* techniques, such as TEM,[11, 12] SEM,[13, 14], EPR,[15-17] NMR,[18, 19] small angle X-ray diffraction,[20, 21] and small angle neutron scattering (SANS).[22, 23] In addition, small angle X-ray scattering (SAXS)[23-27] has also been utilized as a very powerful means to obtain kinetic details of the formation and structural features as well as phase transformations in these materials

even after a precipitate forms.[27-29] However, there are no previous time-resolved studies on the evolution of CTAB micelles in the presence of PEI and silica precursors.

The aim of this work was to observe the real time evolution of the CTAB/PEI/silica film forming solutions using synchrotron based small angle X-ray scattering (SAXS). We studied PEI with two molecular weights, and different CTAB and PEI concentrations with a fixed silica precursor concentration, as for the work on the films discussed above. SAXS patterns showing the growth of the surfactant micelle/polyelectrolyte complexes in the presence of the silica precursor was continuously collected as a function of time. With the aid of the previous neutron reflectivity data from films grown at the air/water interface under similar conditions (**Section § 3.3.2**), a formation mechanism of these CTAB/PEI/silica films at the air/water interface is proposed.

3.3.4.1 Introduction of the Data Collection Procedure and Fitting Models

SAXS has been established as highly effective technique for *in situ* structural characterization of the mesoporous materials.[23, 25, 26] In the current study, the high brilliance of a synchrotron source and a capillary flow cell (**Section § 2.2.2**) have been used to generate good quality X-ray data for solutions where precipitate is formed, with a temporal resolution as fast as 20 seconds. SAXS profiles for CTAB/PEI/silica film forming solutions with different CTAB and PEI concentration as a function of time are shown in **Figure 3.17** and **Figure 3.19**. The time-resolved data collection process was explained in **Section § 2.3.4**. TMOS was added to the solution reservoir at the fourth frame, and this mixed CTAB/PEI/TMOS solution continued to circulate while SAXS data were collected for 30 frames of 20 seconds. At this point the solution had become cloudy and the interval of data collection in each frame was increased to 100 seconds and data collected until no further changes were observed in the SAXS patterns.

Figure 3.17 and **Figure 3.19** show that immediately after the addition of TMOS there is little change in the scattering pattern, and this lasts for a few 20 second frames

of data taken on the circulating solutions. After this a diffraction peak grows rapidly and this peak continues to evolve for some time in the solution. The evolution of the subphase species will be discussed in two sections, during the induction period before the appearance of the diffraction peak, and in the period after the appearance of mesoscale structure in the solutions.

The SAXS data was analyzed using a method of a simultaneous nonlinear least-squares fitting using models within the SANS analysis software developed by the SANS group at NIST Centre for Neutron Research, run within the IGOR PRO platform (available from WaveMetrics).[30] Given the X-ray scattering length densities for CTAB and PEI (scattering length density for CTAB tails is 7.45×10^{-6} $Å^{-2}$ CTAB head group is 9.01×10^{-6} $Å^{-2}$ while for PEI is 1.08×10^{-5} $Å^{-2}$), both species contribute significantly to the scattering and thus we must account for contributions from both species in analyzing the scattering curves. Our earlier work using neutron scattering shows that CTAB micelles are present in solution at the concentrations used here, but that they are not greatly altered by the presence of LPEI which does not bind strongly to the outside of the micelles. Thus the polymer will retain its largely random coil configuration in solution. Therefore, as discussed in **Chapter 2** SAXS patterns of the CTAB/LPEI/TMOS solutions were fitted using Debye and prolate core shell ellipse model, which describes the prolate CTAB micelles dispersed in the hyper branched LPEI and water mixture network.

Surfactant volume fractions have been calculated from the surfactant concentration and total solution volume, and they are summarized in **Table 3.3**, all these calculated surfactant volume fractions were fixed in the fitting. Moreover, the scattering length density of the micelle core was held at 7.45×10^{-6} $Å^{-2}$ since it was assumed that only CTAB tail groups were present in the micelle core. The solvent used in this work is considered as water and PEI mixed solution, whose scattering length density was calculated as 9.41×10^{-6} $Å^{-2}$. However, it is reasonable to consider the effects of methanol generated by continuous TMOS hydrolysis, 0.336 M methanol will be generated assuming the TMOS in the solution hydrolyzed completely, thus the

scattering length density of the solution would change to 9.02×10^{-6} Å^{-2} after TMOS hydrolysis.

For both LPEI and SPEI solutions, interactions between micelles were accounted for using the Hayter-Penfold mean spherical approximation (MSA) structure factor.[31, 32] The MSA is used to describe a system of charged spherical objects in dielectric medium; it allows for the inclusion of interparticle interference effects due to screened coulomb repulsion between charged particles. For all the models the dielectric constant of the solution was approximated to be that close to water (78), the temperature (298K), charge on the micelle (20) and sample backgrounds were also held during fitting. The movalent salt concentrations were calculated according to the PEI concentration utilized and the pH (since the PEI is only 3% charged at the pH used in the synthesis), as seen in **Table 3.3**. These values were held in the fitting as well.

Table 3.3 *Surfactant volume fractions and movalent salt concentrations used for fitting.*

	CTAB (M)	Polymer (g/l)	Surfactant volume fraction	Movalent salt (M)
	0.009	40	0.003	0.035
	0.0185	40	0.006	0.035
SPEI	0.037	40	0.012	0.035
	0.037	30	0.012	0.026
	0.037	15	0.012	0.013
	0.037	20	0.012	0.014
	0.037	30	0.012	0.021
LPEI	0.037	40	0.012	0.028
	0.0185	40	0.006	0.028
	0.009	40	0.003	0.028

3.3.4.2 Induction Period of CTAB/PEI/Silica Film Forming Solutions

In the induction period which is the period after addition of TMOS but before any precipitate was observed (the flow tubes were transparent) the X-ray patterns do not show any presence of Bragg diffraction peaks but do show significant structural evolution (**Figure 3.17**).

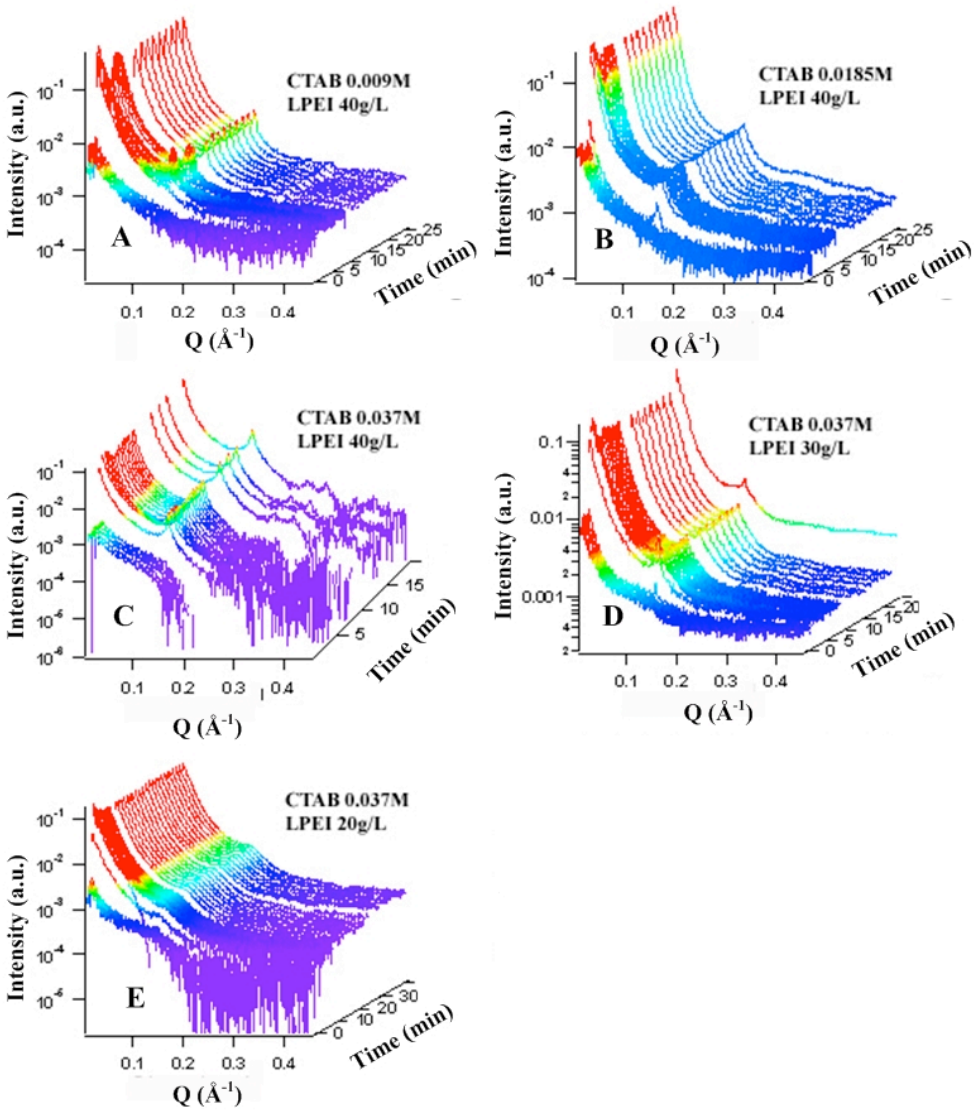

Figure 3.17 *Evolution of the CTAB/LPEI/silica film forming solutions investigated by time-resolved SAXS. CTAB and LPEI concentrations are indicated on each graph.*

Fitting results for LPEI/CTAB/TMOS solutions during the induction period are shown in **Table 3.4**. The micelle dimensions, the polymer R_g, the shell scattering length density, and a scale factor which determined the relative amounts of Debye and prolate ellipse summed in each model were fitted. Other variables were held as described above.

The Debye function represents the form factor for a polymer chain with Gaussian coil in dilute solution, giving a radius of gyration R_g.[33] The form factor for prolate particles with a core shell structure was used to describe the CTAB micelles.[34,35] It is suggested that PEI wraps around the CTAB micelles headgroup because of a dipole-cationic interaction between the surfactant and polyelectrolytes, where the dipoles on the polymer amine groups interact with charged CTAB quaternary ammonium group.[1] In the present study, the radius of gyration values for the polymer R_g decreased from 152 Å to 80 Å with an increase of CTAB concentration from 0.009 M to 0.037 M, (**Table 3.4 A-C**), which indicates that the CTAB molecules pull the LPEI chains into a more compact configuration. A similar shrinking of hyperbranched PEI in solution as CTAB is added has been found previously.[4] The prolate ellipsoid micelles have a minor core radius of about 14-18 Å and the micelle length (major core radius × 2) is in the range of 154-194 Å, increasing with an increasing CTAB concentration. The shell thickness is between 7 and 15 Å. This micelle length diameter is about twice of the length reported by O'Driscoll et al using the uniform ellipsoid model to fit SANS solutions of CTAB and PEI at similar concentrations.[1] The elongate of the micelles is probably due to the effects of shear since the micelles were pumped around the flow cell. The micelle shell is thought to contain a mixture of water, CTAB headgroup, with some PEI. When CTAB is 0.009 M and the LPEI is 40 g/l, the SLD of the shell is as low as 9.44×10^{-6} Å^{-2}, indicating the presence of a significant amount of water within the shell. When the LPEI concentration is 40 g/l, an increase of CTAB concentration leads to an increase of the aggregation number and the shell volume (**Table 3.4 A-C**)

The first SAXS profiles of the CTAB/LPEI/TMOS solution after TMOS addition (20s after TMOS was added) are similar to those of the CTAB/LPEI solutions since the silica precursors were only beginning to hydrolyze and the SLD of TMOS is very close to the solvent. SAXS patterns of the initial CTAB/LPEI mixtures and the CTAB/LEI/TMOS film forming solution in the induction period have been modeled, as shown in **Figure 3.18 A**. The fitting parameters are shown in **Table 3.5**. The micelle core and the shell thickness does not change very much, although the micelle

becomes a little more elongated although it is not obvious. The main changes which can be observed is in the SLD of the micelle shell, which increases because the silica precursor hydrolysed and partially condensed around the micelle headgroup.

Table 3.4 *Results of fitting CTAB/LPEI solutions (before TMOS addition) at different concentrations using Debye and prolate core shell ellipse models. Micelle aggregation number, shell volume, and the volume of PEI monomer and water in the micelle shell region were calculated from the fitting results using values for the volume of CTAB molecule components from the literature.*[36]

	A	B	C	D	E
LPEI (g/l)	40	40	40	30	20
CTAB(M)	0.009	0.0185	0.037	0.037	0.037
scale	0.006	0.017	0.002	0.014	0.012
Rg (Å)	152	152	80	146	134
major core radius (Å)	77	86	87	96	89
minor core radius (Å)	15	15	19	15	17
shell thickness (Å)	7	11	15	12.	13
SLD shell ($Å^{-2}$)	9.44×10^{-6}	9.59×10^{-6}	9.64×10^{-6}	9.71×10^{-6}	9.84×10^{-6}
Aggregation number	152	175	274	210	235
Shell volume (nm^3)	96	188	341	256	265
PEI monomer volume (nm^3)	15	67	145	128	159
Water volume (nm^3)	66	103	168	107	82

Errors in the scale is ±0.005， the fitted radius of gyration is ±5 Å, in the core radii and shell thickness are ±2 Å, in the shell SLD values are $\pm 0.5 \times 10^{-7}$ $Å^{-2}$. The errors in the calculated values are ±5.

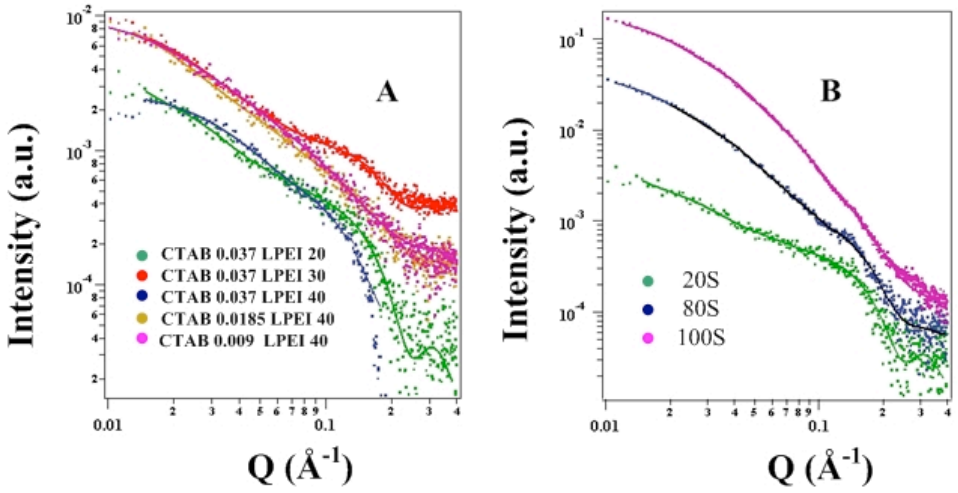

Figure 3.18 *(A) SAXS patterns for the CTAB/LPEI/TMOS mixtures during the induction period (20s after adding TMOS); (B) Time-resolved SAXS patterns for the film forming solution with 0.037M CTAB and 20 g/l LPEI, (80s and 100s after adding silica precursor TMOS). the lines of best fit were modeled as described in the text*

Table 3.5 *Fitting results of the initial stage of CTAB/LEPI/TMOS mixtures using Debye and prolate core shell ellipse combined models.*

	A	B	C	D	E
LPEI (g/l)	40	40	40	30	20
CTAB (M)	0.009	0.0185	0.037	0.037	0.037
scale	0.008	0.019	0.002	0.008	0.004
Rg (Å)	90	169	61	77	119
major core radius (Å)	64	87	88	179	115
minor core radius (Å)	16	15	19	15	17
shell thickness (Å)	6	7	17	17	12
SLD shell ($Å^{-2}$)	9.76×10^{-6}	9.89×10^{-6}	9.63×10^{-6}	9.72×10^{-6}	9.84×10^{-6}

Errors in the scale is ±0.0005, the fitted radius of gyration is ±5 Å, errors in the core radius and shell thickness are ±2 Å, the shell SLD values are $\pm0.5\times10^{-7}$ $Å^{-2}$.

At most concentrations studied, a diffraction peak appears in the SAXS patterns at about one minute after the addition of TMOS, indicating that the silicate precursor has

begun to condense and drives the formation of particles in the subphase solution. At this stage, the simple fitting model becomes less appropriate since it is difficult to describe the interparticle interference and the correct structure factor for charged particles is also extremely complicated.

Table 3.6 *Fitting results of time-resolved 0.037M CTAB/20 g/l LEPI/0.084M TMOS mixtures using Fractal and prolate core shell ellipse combined model.*

Debye and prolate_core_shell_ structure combined Model	**40s**	**Fractal and prolate_core_shell_ structure combined Model**	**80s**	**100s**
scale	0.004	**scale**	0.002533	0.004847
Rg (Å)	119	**Block Radius (Å)**	27	24
major core radius (Å)	115	**fractal dimension**	2	2
minor core radius (Å)	17	**correlation length (Å)**	70	47
shell thickness (Å)	12	**SLD block ($Å^{-2}$)**	9.39×10^{-6}	9.62×10^{-6}
SLD shell ($Å^{-2}$)	9.84×10^{-6}	**volume fraction**	0.012	0.022
		shell thickness (Å)	17	13
		SLD shell ($Å^{-2}$)	1.01×10^{-5}	1.24×10^{-5}

Error in the scale is ±0.0005, in the fitted block radius is ±2 Å, in the correlation length is 4 and in the shell SLD values is ± 0.5×10^{-7} $Å^{-2}$.

However, when CTAB was 0.037 M and the LPEI concentration was decreased to 20 g/l (**Figure 3.18 B**), the whole micelle evolution process becomes slower. SAXS patterns of the induction period (especially 100s after TMOS addition) were difficult to fit with Debye and prolate core shell ellipse combined model since the silica species coating micelles began to aggregate with each other, thus Fractal and Prolate-core shell ellipse combined model was used, fitting parameters are shown in **Table 3.6**. Assuming the TMOS is completely hydrolyzed after 80 second of adding TMOS, the scattering length density of the water decreased from 9.41×10^{-6} $Å^{-2}$ to $9.03\times10^{-6}Å^{-2}$ considering 0.336 M methanol released from 0.084 M TMOS hydrolysis. The micelle radii were held at the values determined for the same solution immediately after TMOS addition to reduce the number of fitted parameters. The SLD for the micelle

core and solution were also held, as were the sample background, temperature, charge on the micelle and dielectric constant (see values given above).

The shell thickness around the micelles increased from 12 Å (20 second) to 17 Å (80 second) probably due to the hydrolyzed silicate species accumulating around the micelle headgroup, however, it decreased to 12 Å at 100 second after the addition of TMOS, which indicates the silica species in the micelle wall is condensing and became more compact, a similar micelle-silica condensation phenomena has been observed by Boissiere[37] and Alfredsson[38]. The SLD of the shell increased from 9.84×10^{-6} $Å^{-2}$ to $1.01e\times10^{-5}$ $Å^{-2}$, suggesting the penetration, hydrolysis and condensation of silica species within the shell network. Additionally, the fractal parameters come out with a radius similar in size to the cross section of a surfactant-silica micelle in both the 80 and 100 second patterns, however, the correlation distance is more than twice of the surfactant-silica micelle in 80 second sample, while it is much smaller in the 100s sample, and the overall SLD of the fractal object increases which suggests that the micelles began to pack close together into particles and the particles became more condensed as silica polymerization continues. The macro "Number Density Fractal" was used to calculated the number density of building blocks, the aggregation number (the mean number of blocks per cluster) and Guinier radius of the cluster.[39] For the 80 second pattern, the Guinier radius is 125 Å and the aggregation number is 16 while for the 100 second pattern, the Guinier radius is 100 Å and the aggregation number is 19, suggesting the number of micelles aggregating together gets bigger and the cluster itself gets smaller with time as the silica polymerisation proceeds.

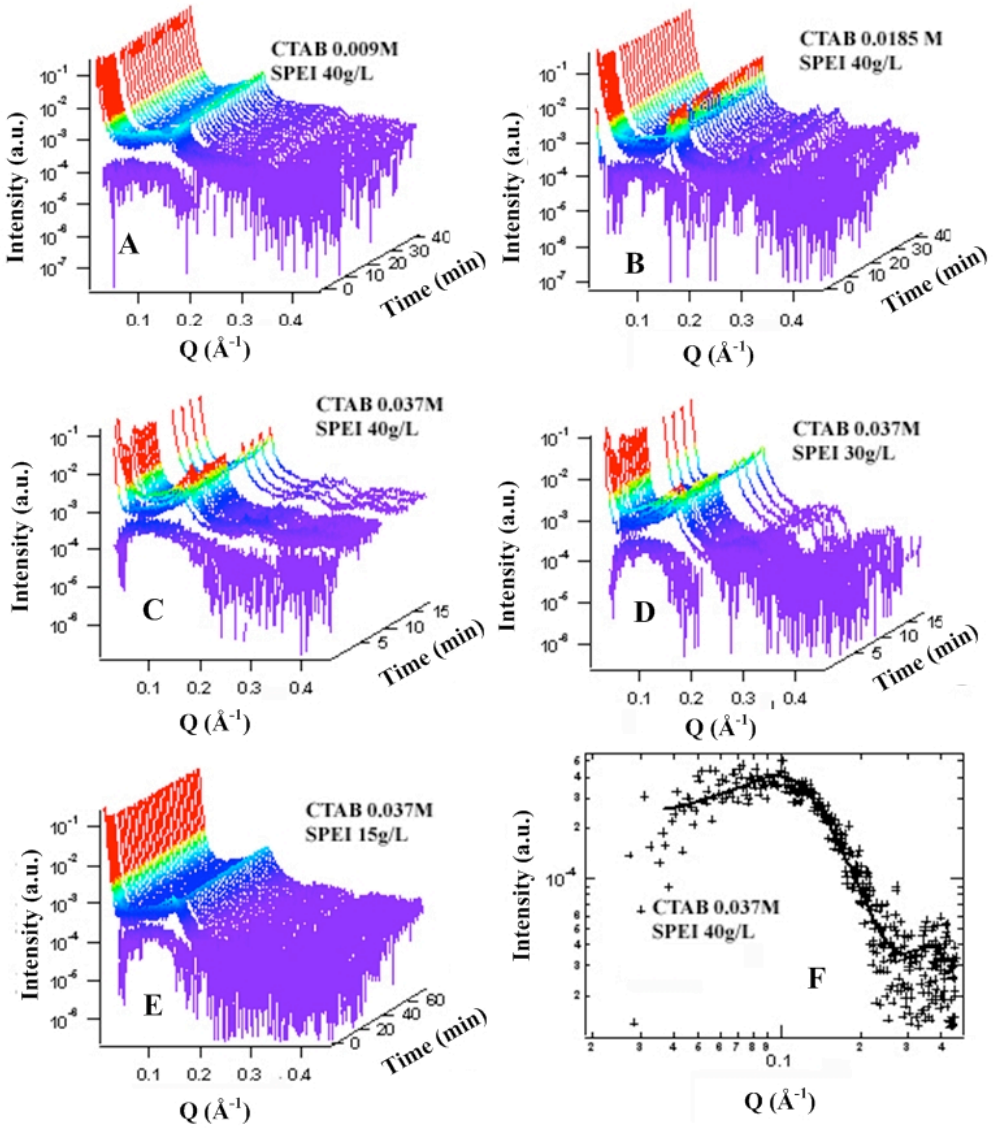

Figure 3.19 *(A-E) Evolution of CTAB/SPEI/silica film forming solutions investigated by time-resolved SAXS. CTAB and SPEI concentrations are indicated in each graph. (F)The induction period of SAXS patterns of CTAB/SPEI/TMOS mixture solution, the line of best fit was modeled using a charged uniform ellipse model.*

Evolution of CTAB/SPEI/silica film forming solutions was investigated by time-resolved SAXS, as shown in **Figure 3.19 A-E**. The scattering patterns during the induction period differ from those of LPEI/CTAB solutions since they show only a broad bump due to micelle-micelle correlation distances, but no upturn in the

scattering at lower Q due to the scattering from large polymer coils in solution. In the case of film forming solutions with SPEI, SPEI is physically thought to be dispersed small molecular chains, so it does not contribute to the small angle scattering signal like LPEI did, since SPEI has low molecular weight and is less branched than LPEI. Therefore the induction period of SAXS profiles for CTAB/SPEI solutions has been fitted to a charged uniform ellipse model, as shown in **Figure 3.19 F** and **Table 3.7**. The charged uniform ellipse model has a form factor describing the scattering for an ellipsoid particle with uniform scattering length density and a structure factor for charged ellipses using the Hayter-Penfold MSA formalism. The volume fraction was calculated from the CTAB concentration and held during fitting and as above the sample background, charge on the micelle, temperature and dielectric constant were held during fitting. The fitting results suggest these micelles are almost spherical in shape with their major radius and the minor radius both around 12 Å. These radii are smaller than that of CTAB micelles reported by Berr et al.[35] Considering the scattering length densities, the major change is between the tail region of the micelle, and the headgroup/water/PEI at the micelle surface, since in the shell region the mixture of headgroup, PEI and water will have a combined SLD which is fairly close to that of the SPEI/water solution surrounding the micelles. Thus the uniform ellipse measured in this fitting is largely the area occupied by the surfactant tails. The small dimensions indicate that some of the PEI chains and water have partly penetrated around the surfactant headgroups reducing the region solely filled by the surfactant hydrocarbon chain. When the silicate precursor was introduced to the CTAB/SPEI solution, the SAXS patterns again do not change immediately after TMOS addition, probably as for the case of LPEI above, because silica precursor has not started to accumulate in the shell within less than one minute. After this point the evolution of the scattering was too rapid to observe intermediate scattering patterns prior to the appearance of the diffraction peak, so the accumulation of silica around the micelles could not be modeled for these systems.

Table 3.7 *Fitting results of CTAB/SEPI/TMOS mixtures during the induction period at different concentrations of CTAB and SPEI (20s after addition of TMOS) using a charged uniform ellipse model. TMOS is 0.084M.*

	A	B	C	D	E
CTAB(M)	0.009	0.0185	0.037	0.037	0.037
SPEI (g/l)	40	40	40	30	15
Volume fraction	0.003	0.006	0.012	0.012	0.012
R(a) rotation axis (Å)	11	13	13	14	14
R(b) (Å)	11	10	13	13	12
Contrast ($Å^{-2}$)	1.97×10^{-6}	1.93×10^{-6}	1.93×10^{-6}	1.93×10^{-6}	1.93×10^{-6}

Errors in the fitted core radius and shell thickness are ±2 Å, and in the contrast values $\pm0.5\times10^{-7}$ $Å^{-2}$ the error in the monovalent salt concentration is 0.005.

3.3.4.3 Formation and Evolution of Mesostructured Particles in the CTAB/PEI/Silica Film Forming Solutions

Time-resolved SAXS was also used to observe the formation and evolution of the mesostructure after particle formation. Following the addition of TMOS and its hydrolysis and partial condensation, the solution quickly becomes opaque and a white solid precipitate was observed around one minute after the addition of TMOS. As soon as the precipitate has formed, the X-ray profiles obtained show the presence of a diffraction peak. The whole process is fast, similar to the formation of CTAB/silica precipitates in alkaline preparations where films do not form;[40] and is much shorter than the time required for films or precipitate to form in CTAB/silica solutions at low pH (without the addition of PEI).[29] The time required to observe the formation of particles has no dependence on the molecular weight or concentration of PEI used.

However, the process of mesostructure ordering within the particle differs at different PEI concentrations (**Figure 3.17** and **Figure 3.19**). For a constant CTAB concentration of 0.037 M, when the PEI is at a very low concentration (eg 20 g/l for LPEI **Figure 3.17 E**; 15 g/l for SPEI **Figure 3.19 E**), a relatively wide diffraction peak was observed 80s after addition of TMOS in both cases and this peak does not change with time, indicating there is a lack of long range of mesostructural ordering

in these particles. In other words, the PEI concentration should be above these concentrations to obtain good mesostructure ordering. A lack of order was also observed in the films grown at these PEI concentrations (see Figure 3.28 below).

For increased LPEI concentrations above 20 g/L, this initial diffraction peak continuously becomes sharper and other peaks grow in, so that finally the SAXS patterns demonstrate three intense reflections, which are characteristic of a 2D hexagonal mesostructure. However, when the SPEI concentration is increased, the SAXS patterns change abruptly from a broad bump to three diffraction peaks, suggesting that the micelles which initially in the solution were loosely wrapped by polyelectrolyte chains and hydrolyzed silicate networks, self assemble very rapidly and directly into particles with a highly ordered 2D hexagonal structure.

For SAXS patterns of subphase particles synthesized with LEPI and SPEI, both the peak area and full width at half maximum of the first diffraction peak have been measured using a peak fitting routine in the IGOR Pro software package. These are plotted in **Figure 3.20** and **Figure 3.21**. Noticeably, for all the patterns, there is a distinct jump in the peak area and peak width between 2 to 4 min after the addition of TMOS. This change is suggested to be due to a rearrangement within the liquid crystalline particles although the mesophase transition cannot be specified due to the lack of more than one distinct diffraction peak before this point.

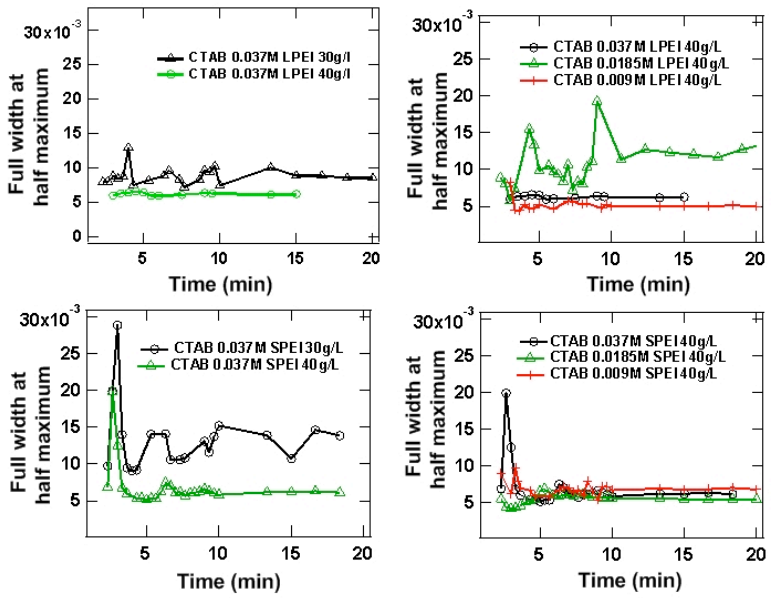

Figure 3.20 *Full width at half maximum of the first diffraction peak of all the time-resolved SAXS patterns for CTAB/SPEI/TMOS mixtures. TMOS concentration is 0.084 M. Errors are very small and within the markers.*

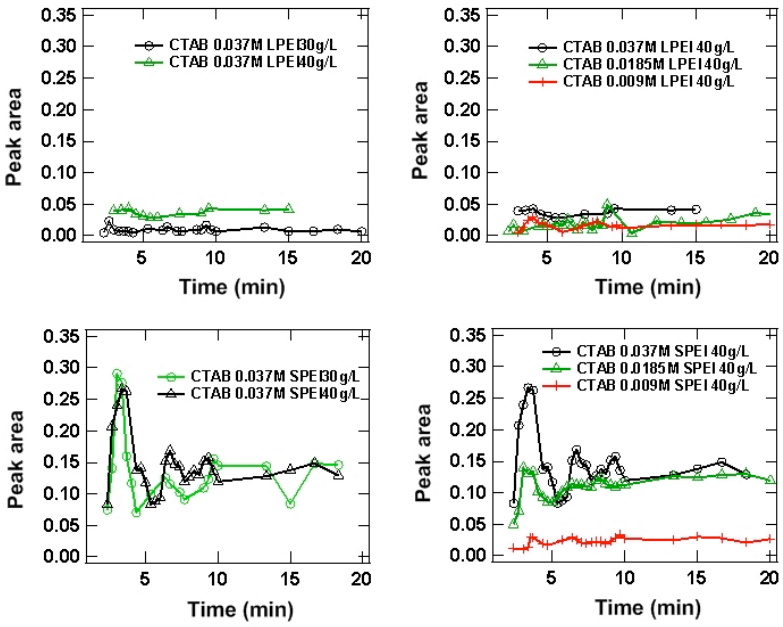

Figure 3.21 *Peak area of the first diffraction peak of all the time-resolved SAXS patterns for CTAB/SPEI/TMOS mixtures. TMOS concentration is 0.084 M. Errors are very small and within the markers.*

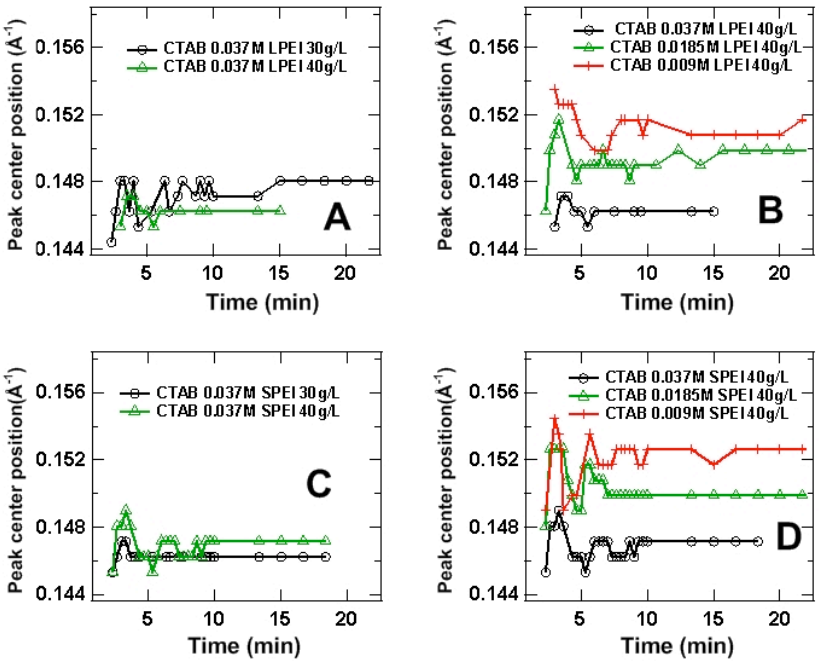

Figure 3.22 *Peak centre position of the first diffraction peak of the time-resolved SAXS patterns for CTAB/PEI/TMOS mixtures.*

The peak centre position of the first diffraction peak with function of time has also been plotted in **Figure 3.22**. At the beginning just after peak appearance, the peak centre positions vary a lot during this period of particle formation from the micellar solution. Most samples show a rapid increase in the peak position followed by a decrease again ending at about one min after the initial addition of TMOS and immediately after precipitation was observed. During this period other peaks appear at higher Q values and the ratio of the peak intensities for these reflections is changing. As the reaction proceeds, the peak positions stabilize generally at a higher Q than the initial Q value observed for that sample. For example for a CTAB concentration of 0.037 M with SPEI at 40g/l (**Figure 3.22 C**), the first peak position increases from 0.14 $Å^{-1}$ to 0.15 $Å^{-1}$, corresponding to a decrease of the d-spacing from 45 Å to 42 Å. This contraction of the hexagonal d-spacing can be linked to the condensation reaction taking place within the silicate wall leading to a relatively dense structure, which is normal for surfactant templated materials from alkaline preparations.[41] Ten

minutes after the addition of TMOS, most of the patterns from these solutions show highly ordered 2D hexagonal mesostructures, and the mesophases within the particles are stable under the conditions in the subphase solution.

When the CTAB concentration is decreased from the standard value of 0.037 M to 0.0185 M or 0.009 M, different trends are observed. At lower CTAB concentrations, a greater amount of PEI is needed to maintain mesostructural ordering, for example at 0.009 M CTAB and a SPEI concentration of 40 g/l (**Figure 3.19 A**) the particles are less well ordered than those at the same SPEI concentration but higher CTAB content.. Variation of the concentration of CTAB also altered the peak positions for the SAXS pattern of the film forming solution with PEI (**Figure 3.22 B and D**). When the particle evolution in the subphase solution becomes stable, at a SPEI concentration of 40 g/l and CTAB concentration is decreased from 0.037 M to 0.0185 M or 0.009 M, the d-spacings decrease by 0.35 Å and 1.40 Å, respectively. (**Figure 3.22 D**). This is probably due to the enhanced polymer binding to the micelles at relatively higher PEI concentration. This polymer binding will screen the charge on the micelles and allow closer packing between micelles, resulting in a smaller spacing between repeat units.

Interestingly, neutron reflectivity of films *in situ* at the solution interface and SAXS data on dry films show the same 2D hexagonal mesoscale ordering as seen here in the particles in the subphase solution,[42] which suggests that these particles are closely related to the films at the interface. The structure in the films is also oriented with respect to the interface, while that of the particles in solution is powder-like, indicating that if the films formed directly from the particles, that some orientation process or restructuring must occur as the film forms at the solution surface. Since silica condensation is likely to remain incomplete in these particles grown at room temperature it is possible that any particles which come in contact with the film remain soft enough to re-structure to a low energy configuration at the interface. However the 2D hexagonal mesostructure in the films forms much more slowly than that observed in the subphase, suggesting that these two processes are not directly coupled. This means that film formation occurs separately to particle formation in the subphase. This is the opposite observation to that made previously for acidic

silica/surfactant film forming systems where particle formation (or coated micelle formation) in the subphase occurred just before film formation and where the films formed from particles packing at the solution interface. The formation mechanism of the films in PEI/CTAB systems is discussed in more detail in **Section 3.3.9.2** below.

3.3.5 Small Angle X-ray Scattering on Dried Silica Films

Silica films templated by surfactant and both types of PEI are robust to removal from the air/water interface to form free-standing films (**Figure 3.23**). The films synthesized with LPEI remain continuous without cracking after drying; however films synthesized with SPEI are white, smooth and crack near the mesh strands. The film morphology is still retained even after calcination, suggesting the polymer in the template improves the film strength, possibly by increasing film thickness over surfactant-only templated silica films, which are extremely fragile and tend to fracture into powders after calcination.

Figure 3.23 *Picture of dried silica films synthesized with (left) CTAB:LPEI and (right) CTAB:SPEI.*

The SAXS patterns of dried films synthesized with CTAB/LPEI are shown in **Figure 3.24** and the peak position and d-spacings are shown in **Table 3.8**. SAXS patterns are shown for all samples where films were observed (see phase diagram in **Figure 3.24**). **Figure 3.24 A-E, G, H,** show one broad peak around 0.14 $Å^{-1}$, indicating a low degree of long range order, the peak at 0.24 $Å^{-1}$ is from excess crystalline CTAB. However, the SAXS patterns of samples of **Figure 3.24 F, I-K** show three low angle Bragg peaks indexed as (100), (110), (200), corresponding to well ordered 2D-hexagonal structures, with d-spacings between 46 Å and 48 Å

Variation of the concentrations of LPEI and TMOS does not significantly alter the peak positions. Compared with neutron reflectivity data in **Figure 3.12**, the drying process appears to improve the ordering of the micelles within these films, possibly since film shrinkage forces the charged micelles closer together so the electrostatic interactions between adjacent micelles forces greater ordering in the films.

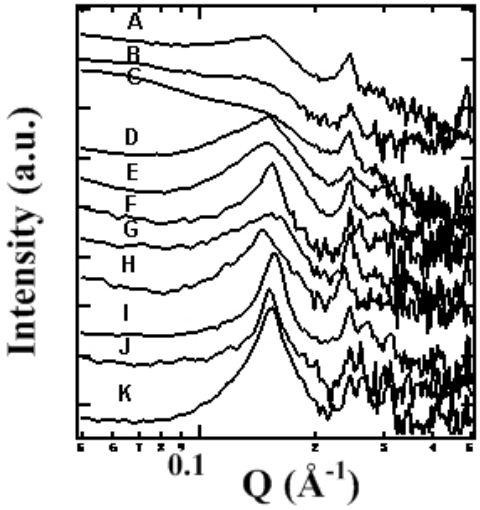

Figure 3.24 *SAXS patterns of dry silica films synthesized with: A 30 g/l LPEI:0.1675 M TMOS, B 10 g/l LPEI: 0.08375 M TMOS, C 20 g/l LPEI: 0.1675 M TMOS, D 10 g/l LPEI: 0.0335 M TMOS, E 20 g/l LPEI: 0.08375 M TMOS, F 40 g/l LPEI: 0.1675 M TMOS, G 30 g/l LPEI: 0.0335 M TMOS, H 20 g/l LPEI: 0.0335 M TMOS, I 40 g/l LPEI: 0.08375 M TMOS, J 40 g/l LPEI: 0.0335 M TMOS, K 30 g/l LPEI: 0.08375 M TMOS. CTAB is constant at 0.037M.*

The SAXS pattern of dried films synthesized with CTAB: SPEI are shown in **Figure 3.25** and the peak positions and d-spacings in **Table 3.9**. All of these samples show three low angle Bragg peaks indexed as the (100), (110), (200) peaks corresponding to well ordered 2D-hexagonal structures, with d-spacings around 46 Å. Again, variation of SPEI and TMOS concentrations do not have a great effect on the film structure. The effect of cross-linker has also been studied, as shown in **Figure 3.26**. The concentration of cross-linker has been changed from 0.02 M to 0.06 M for CTAB concentrations of 0.037 M, 30 g/l SPEI and 0.1 M TMOS. The peak positions

are unchanged, suggesting cross-linker also has little influence on the final structure of silica film synthesized with CTAB/SPEI, which corresponds well with neutron reflectivity data on the *in situ* films above.

Table 3.8 *Peak positions and d-spacings from SAXS patterns in* ***Figure 3.24***.

Sample	LPEI	TMOS (M)		Q^a ($Å^{-1}$)		Distance[a] (Å)
A	30 g/l	0.1675	0.15	—	—	49
B	10 g/l	0.08375	0.14	—	—	50
C	20 g/l	0.1675	0.15	—	—	49
D	10 g/l	0.0335	0.15	—	—	48
E	20g/l	0.08375	0.15	—	—	48
F	40 g/l	0.1675	0.15	0.267	—	46
G	30 g/l	0.0335	0.15	—	—	46
H	20 g/l	0.0335	0.15	—	—	48
I	40 g/l	0.08375	0.16	0.270	0.310	46
J	40 g/l	0.0335	0.15	0.260		48
K	30 g/l	0.08375	0.15	0.267	0.310	46

a – errors in the Q values are ±0.01 $Å^{-1}$ and in the d-spacings are ±1 Å.

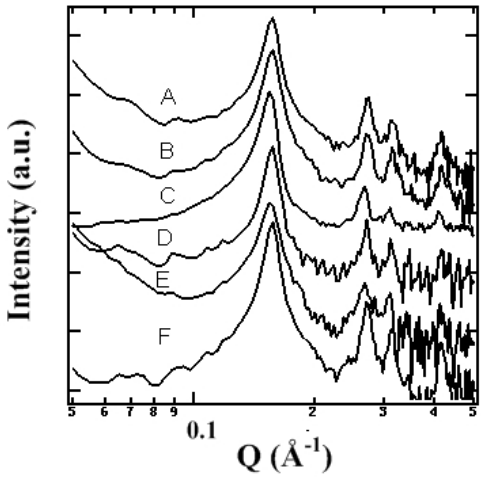

Figure 3.25 *SAXS patterns of dry silica films synthesized with CTAB: SPEI. A (30 g/l SPEI: 0.1675 M TMOS), B (30 g/l SPEI: 0.08375 M TMOS), C (40 g/l SPEI: 0.08375 M TMOS), D (20 g/l SPEI: 0.0335 M TMOS), E (30 g/l SPEI: 0.0335 M*

TMOS), F (20 g/l SPEI: 0.08375 M TMOS). The CTAB concentration was 0.037 M and cross-linker concentration was 0.04 M.

The organic material in the films was removed either by calcination or by washing with ethanol. A SAXS pattern from a sample calcined in air at 600°C for six hours is shown in **Figure 3.27 B**. The first peak becomes less distinct, the higher orders disappear and the peak position shifts to a higher Q value, suggesting a decrease of the long-range order and unit cell spacing. However, when the samples were exposed to TMOS vapor at 40°C for one day before calcination, the three distinct peaks in **Figure 3.27 D** show that the 2D hexagonal pore ordering is retained after calcination. This indicates the high thermal stability of these films, although the d-spacing still decreased by 3 Å, The SAXS pattern for a sample where surfactant removal was carried out by washing in ethanol after exposure to TMOS vapor for one day is also shown in **Figure 3.27**. In these films, not only is the 2D hexagonal pore order well retained, but also the d-spacing is constant, indicating no shrinkage of unit cell during template removal.

Table 3.9 *Peak position and d-spacing from SAXS patterns in* ***Figure 3.25***.

Sample	SPEI (g/l)	TMOS (M)	Q^a ($Å^{-1}$)			Distance[a] (Å)
A	30	0.1675	0.16	0.27	0.31	46
B	30	0.08375	0.16	0.27	0.31	46
C	40	0.08375	0.15	0.27	0.31	46
D	20	0.0335	0.16	0.27	0.31	46
E	30	0.0335	0.15	0.27	0.31	46
F	20	0.08375	0.16	0.27	0.31	46

a – errors in the Q values are $\pm 0.01 Å^{-1}$ and in the d-spacings are ±1 Å.

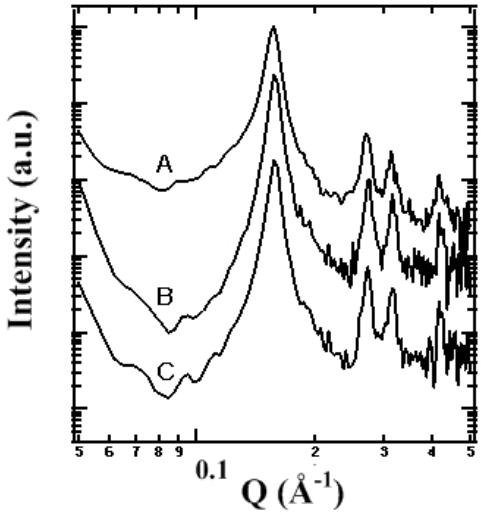

Figure 3.26 *SAXS pattern of silica films synthesized at CTAB 0.037 M, SPEI 30 g/l and 0.1 M TMOS with different concentrations of EGDGE: (A) 0.04 M, (B) 0.06 M and (C) has 0.02 M cross-linker.*

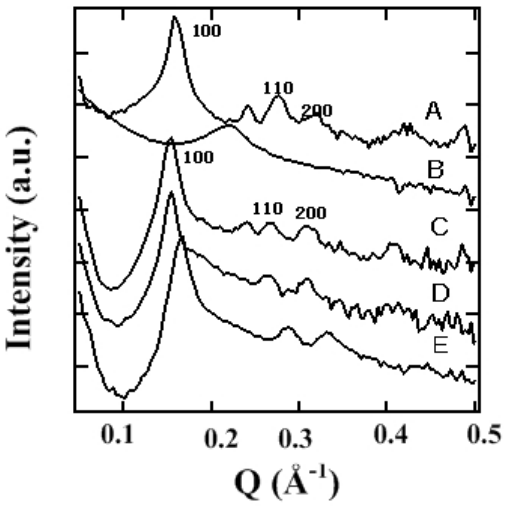

Figure 3.27 *SAXS pattern of as-synthesized (A) and calcined (B) silica film synthesized with CTAB: 30 g/l SPEI. C is the as-synthesized film after exposure to TMOS vapour for a day. D and E are SAXS patterns of C films with the surfactant template removed by calcination and washing by ethanol respectively.*

3.3.6 Phase Diagram for CTAB/PEI/TMOS Film Forming Systems

On the basis of these experimental results, both from neutron reflectivity measurements of film growth at the air/water surface and from SAXS studies of the dried free-standing films, the phase diagrams of the CTAB/TMOS/LPEI and CTAB/TMOS/SPEI film forming systems are presented in **Figure 3.28**, in which the concentration regions where different film phases exist are depicted. In the CTAB/TMOS/LPEI system, the region for gel formation (where no films form as the entire solution gels), ordered films and disordered films have been examined. Silica gelation was observed at high TMOS concentration and low LPEI concentration. With an increase of LPEI concentration and decrease of TMOS concentration, films formed and the film structure became more ordered. Neutron reflectivity data on the films at the air/water surface shows some order at low TMOS concentration and high LPEI concentration. When taken off the surface and dried, those films present a highly ordered 2D hexagonal structure, indicating the drying process improved the ordering of the film. However, for intermediate concentrations where the neutron reflectivity measurements showed no ordering of the film on the solution surface, dried films also contained no long-range mesostructural ordering.

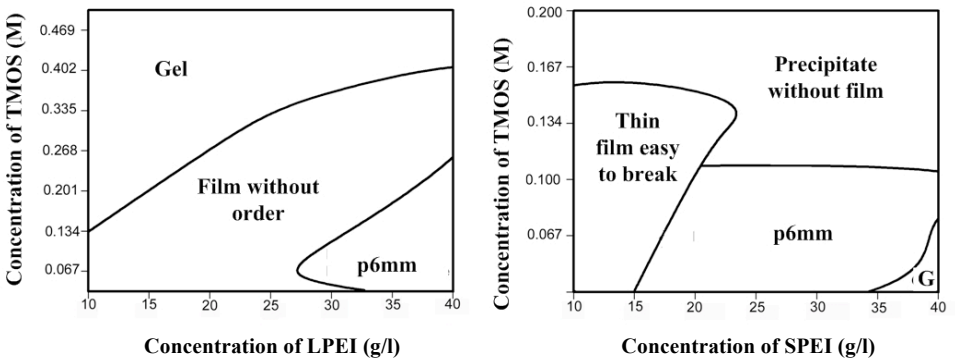

Figure 3.28 *Phase diagrams for CTAB/PEI/TMOS film forming systems. (Left: CTAB/LPEI/TMOS and right: CTAB/SPEI/TMOS). G represents gel.*

In the CTAB/TMOS/SPEI system, 0.04 M EGDGE was used in all these preparations to cross-link the film. The film at the air/water surface is too thin to be removed from the surface at low concentrations of TMOS and low concentrations of

SPEI, only one broad bump can be seen on neutron reflectivity, as shown in **Figure 3.13**. However, with an increase of concentration of SPEI, the system separated into two phases, precipitation of a composite without film was found at high concentrations of TMOS and this precipitated powder also contains ordered 2D hexagonal mesostructures. At low concentrations of TMOS, films at the air/water interface present initially a cubic phase and change into 2D hexagonal with time, and this ordered 2D hexagonal structure was retained when the films were dried. Again the regions where neutron reflectivity indicated ordered film formation at the solution surface correspond with the concentrations where films that retained order after drying could be recovered from the solution surface. Gelation of the entire solution was also observed, at even higher concentration of SPEI and lower TMOS.

3.3.7 Thermogravimetric Analysis

The most elementary proof for the composite nature of the film is its thermal weight-loss behavior, TGA patterns of silica films synthesized with CTAB: 30 g/l LPEI, or CTAB: 30 g/l SPEI are given in **Figure 3.29**. These indicate that the films have a composition of about 35% silica and 45% organics for films synthesized with LPEI, and 25% silica and 60% organics for films synthesized with SPEI, respectively. These two samples showed a similar decomposition pattern of three degradation weight-loss steps. The first drop in weight (up to 150°C) is due to water loss. The next step 150°C -250°C is the range of polymer and surfactant loss by combustion. Weight loss at temperatures between 250°C and 500°C is due to the further condensation of silicate. Silica films synthesized with LPEI contained more inorganic species than films synthesized with SPEI. SAXS patterns show that the d-spacing of dry films synthesized with LPEI is bigger than that of dry films templated by SPEI (refer to **Table 3.8 and Table 3.9**), which indicating that there are more spacing to incorporate polymer and silica between micelle layers for films prepared with LPEI. It happens not only because of the strong interaction between LPEI and silica, but also because the fact that LPEI molecules are bigger which limits the CTAB micelles to pack closely,

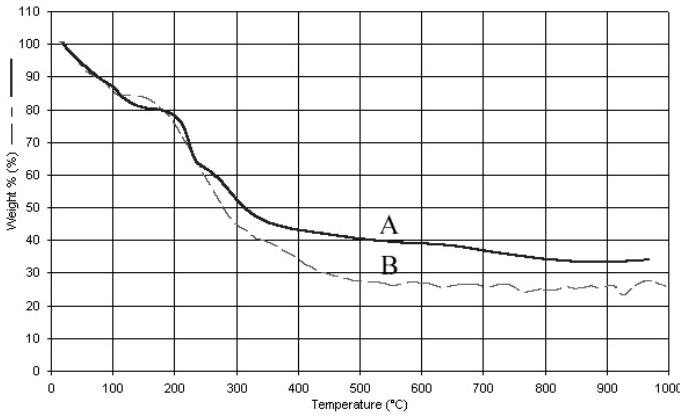

Figure 3.29 *TGA of silica films synthesized with (A) CTAB: 30 g/l LPEI, (B) CTAB: 30 g/l SPEI*

3.3.8 Nitrogen Adsorption and Desorption

A N_2 absorption and desorption experiment was conducted on the sample prepared with 0.037 M CTAB and 40g/l SPEI. The ordered 2D hexagonal mesostructure in the tested material was confirmed with SAXS and it was retained even after calcination.

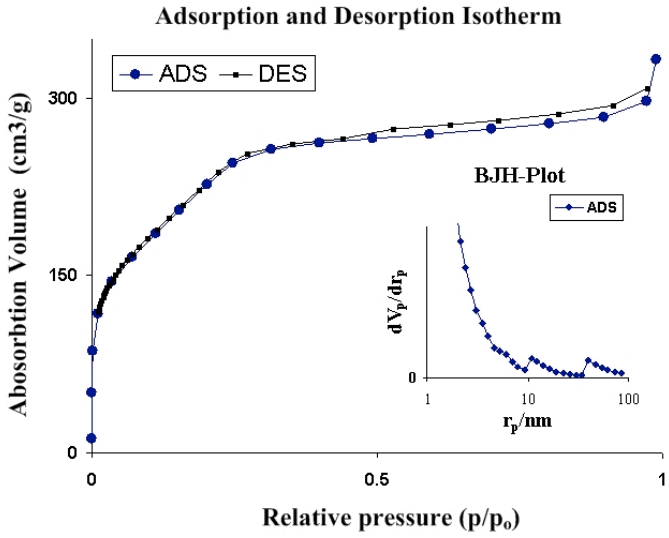

Figure 3.30 *Nitrogen adsorption isotherms for silica films templated by 0.037M CTAB and 40 g/l SPEI. Pore size distribution calculated from BJH method is inset.*

At very low pressure, generally considered as the micropore absorption range, the adsorption isotherm shows a big step, suggesting a large amount of microporosity

exists in this silica film. This is sensible since micelles are dispersed inside the PEI polymer-silica network, so calcination of the polymer will generate a large amount of micropores in the film. A hysteresis loop, which is characteristic of mesoporous materials due to capillary condensation, appears from the relative pressure of 0.45. The hysteresis loop does not close in the high relatively pressure range, indicating the existance of macropores. The silica film has a BET specific surface area of about 796.7 m^2/g and a pore volume of 185.2 cm^3/g. The BJH method was used to calculate the pore size distribution, which is shown as an insert graph in **Figure 3.30**. It was calculated according to the absorption branch of the isotherm. From the graph, we can not only see that there are a large number of micropores in the material, but also see the coexistance of 100 Å mesopores and 500 Å macropores. The average pore diameter is about 34 Å. The macropores may come from the gaps between sheets of close packed film materials forming slit-shaped pores, since many films were prepared in order to have sufficient material to measure the adsorption isotherm.

3.3.9 Discussion

3.3.9.1 Cationic Surfactant/Polyelectrolyte/Silica films

In this Chapter, it was demonstrated that robust highly ordered silica films can be templated by CTAB/PEI complexes at the air/water interface. In the pH range used for these experiments (between 9 to 12), PEI has a very small net positive charge, but the dominant interaction between the polymer and surfactant is a dipole-cationic interaction, where the dipoles on the polymer amine groups interact with charged CTAB quaternary ammonium group.[1] Thus the polymer chains surround the CTAB micelles in solution in a loose hydrogel. Silicate species are negatively charged under basic conditions, so they are electrostatically attracted to the cationic surfactant upon mixing with the surfactant/polymer solution. There is also a strong interaction between the uncharged amine groups on the polymer and the negatively charged silica species. Similar interactions are seen between silica anions and amines in the proteins responsible for biosilicification.[43] The silica therefore infiltrates the surfactant/polymer complex, interacting either with the nitrogens in the

polyelectrolyte chains or directly with the CTAB micelles. The collective electrostatic interactions and the dipole-cation interaction allow co-assembly resulting in the homogenous dispersion of the polymer and silicate species around the CTAB micelles.

Silica films synthesized with LPEI form very rapidly with relatively low internal ordering. In a typical preparation, the PEI concentration is 30 g/l, giving a concentration of monomer units of the polymer of 0.6975 M, about 19 times the concentration of the surfactant, and the polymer is long enough to completely wrap around the micelles. The long polymer chains are also able to bind several micelles and so span the region between micelles, filling this region more densely than in the case of SPEI. Thus in the LPEI/CTAB solutions, silicate species are less able to contact with the cationic surfactant directly, and no distinct silicate precipitation was seen in the solution. The strong interaction with the PEI also brings more silica into the films, as evidenced by the TGA measurements. Because of the higher molecular weight and hydrophobicity of the LPEI, the migration of the aggregates to the surface will be promoted, which results in a rapid phase separation and formation of the film.

Phase separation, mesophase ordering, silica polymerisation and drying within the film is competitive.[3] For high MW PEI, the ordered structures take some time to form and ordering improves with time, thus fast phase separation limits the self-ordering process of the micelles. Also the higher viscosity of the LPEI/CTAB layer, due to the high polymer MW, prevents rearrangement of the mesostructure into a more ordered form. On the contrary, for silica films synthesized with SPEI, the film takes a longer time to form and has a highly ordered structure. The shorter PEI polymer is barely long enough to span the gap between two micelles, given the measured d-spacings from the films, so each polymer binds to at most two micelles, leading to a lower density hydrogel between and around the micelles. The negatively charged silicate species will interact both with the nitrogen containing polymer and directly with the cationic surfactant, where this electrostatic interaction results in precipitation of composite silicate species in the solution. We have investigated the precipitate and it also has a 2D hexagonally ordered mesostructure. Because SPEI polymer chains are

less hydrophobic and bind fewer micelles, the migration of aggregates to the surface is slower, thus the phase separation to form the films takes a longer time. However, as a result of the low polymer molecular weight, the film itself is less viscous and contains less silica, which enables the ordering process, allowing the formation of highly ordered films. The addition of cross-linker does not change the silica film structure, but the cross-linking reaction occurs in tandem with the film formation and silica condensation processes. Essentially the cross-linking process makes short PEI longer and more hydrophobic, which speeds up the formation of films.

The addition of silica to PEI/CTAB solutions reduces the concentration range over which ordered films are observed to form at the air/water interface but also stabilizes and thickens non-ordered films. Such non-ordered films are observed in the CTAB/PEI only phase diagram but are unstable and can not be removed from the interface where they formed.[3, 4] Similarly the presence of PEI in these silica/surfactant/polymer films reduced the region of concentration over which ordering is observed compared to films formed from acidic silica/surfactant solutions (with no polymer)[44] but allows film formation to occur at high pH where normally only precipitates are found. The addition of polymer results in greatly enhanced film thickness and thus improved thermal stability and the retention of film geometry after template removal which is seldom seen in surfactant/silica films.

3.3.9.2 Evolution of the CTAB/PEI/Silica Film Forming Solutions and Film Formation Mechanism

The subphase solution of these silica film forming systems was investigated by time-resolved SAXS. Overall, the SAXS data indicate three stages for the evolution of the micelles in the bulk solution: the induction period, the formation of particle with a disordered close packed micellar structure, followed by the evolution of the mesostructure into an ordered phase.

Prior to TMOS addition, no particles were observed in the CTAB/PEI mixed solutions, which is similar to previous reports on formation of CTAB/PEI only films from similar solutions.[3] During the induction period, after TMOS addition but before

formation of particles, CTAB micelles remain dispersed in the polymeric aqueous solution. Just after the addition of TMOS, at the very beginning of mixing, these micelles are nearly spherical in the CTAB/SPEI/silica film forming solutions. Nearly one minute after the silicate precursor was added, the solution becomes opaque and we observe formation of particles with a certain degree of liquid crystalline ordering evident from a peak appearing in the time-resolved SAXS data. The solution has thus entered the second stage marked by the formation of liquid crystalline particles composed of disordered silica-coated micelles in a more concentrated silica/PEI/solvent matrix. The particle formation time in the PEI/CTAB solution is much shorter than that observed for acidic CTAB/silica film forming solutions (reported as 800 minutes),[29] but is close to nucleation times reported in alkaline CTAB-templated silica syntheses which do not form films.[20, 45] Thus the silicate hydrolysis and condensation process is not greatly affected by the presence of PEI despite the significant effect of this polymer on the morphology of the final material. In these solutions PEI takes the place of other basic species (NaOH, NH_3) added in the previous works on alkaline systems and recent findings provide insight to a simple biomimetic route for silica formation using this polymer.[46] Like CTAB itself, linear and branched PEI has the ability to form silica directly from TMOS almost instantly in aqueous solution. Linear PEI aggregates have been shown to induce hydrolytic condensation of TMOS, creating silicas with different morphologies.[46] Silicate/polymer hybrid fibers have also been synthesized via catalysis with PEI.[47] It is accepted that the polyamines catalyze silica formation due to the alternating presence of protonated and nonprotonated amine groups in the polyamine chains, which allows hydrogen bond formation with the oxygen adjacent to silicon in the precursor and this facilitates -Si-O-Si- bond formation.[48] Here, the polyamine groups in PEI therefore work synergistically with the quaternary amines in the CTAB surfactant template to hydrolyse and condense the silica precursors. Since there are no mesophase particles observed in the subphase of CTAB/PEI solutions without added silica, the hydrolyzed silicate precursor acts to electrostatically screen charges between micelles, as well as hydrogen bonding with PEI amine groups, under the basic conditions. All these

interactions will facilitate the formation of silica/PEI particles with the micelles trapped inside.

The third stage is the evolution of mesostructure within the disordered particles, which proceeds in a similar manner to that observed for surfactant/silica syntheses without added polymer, however now the influence of the polymer becomes more apparent. The particle mesostructure observed by SAXS is less ordered for very high or very low PEI concentrations. Low local PEI concentrations within the surfactant, polymer and silica particles and the influence of micelle charge density may be responsible for a less ordered mesostructure. The mesophase particles are believed to form due to the formation of a coacervate where an aqueous solution separates into two immiscible liquid phases, one is more concentrated while the other is more dilute. The formation of a coacervate depends on the concentration, charge density and molecular weight of polyelectrolyte.[49] Increased concentrations may therefore promote phase separation (coacervation) while a low polyelectrolyte concentration would limit the phase separation, resulting in smaller, less concentrated particles which thus have a less ordered mesostructure. The low polymer concentration could also result in incomplete wrapping of polymer around the micelles, allowing a kind of bridging flocculation to occur during the charge neutralization step, resulting in a less ordered material after TMOS is added. Formation of the coacervate phase in the surfactant solution is clearly primarily driven by the addition of TMOS (in the presence or absence of PEI). The silica ions are thus responsible for the total charge screening of the micelles which allows this phase separation to occur. At lower PEI concentrations, the micelles will initially be less shielded from each other thus having a relatively higher charge density which would be expected to promote ordering as is seen in the CTAB/PEI systems without silica.[1] However, since a less ordered phase is formed as the polymer concentration is decreased this suggests that if the polymer cannot uniformly coat each micelle, then the balance between silica interactions with the PEI and with the CTAB are disrupted.

When the PEI concentration is too high, coacervation is favored, but the silicate hydrolysis and condensation occur at much the same rate as for the lower polymer

concentrations. At higher concentration within the particles the polymer and the condensing silica network is more viscous, and greater charge screening of the micelles (by both the PEI and the silica) occurs, so the micelles find it difficult to rearrange into an ordered phase before silica condensation freezes the system in a disordered state. The ordered structure therefore could only be observed for particles at an intermediate PEI concentration, where the micelle charge density, silicate hydrolysis and condensation are balanced. Comparison of these results for time-resolved measurements on films grown on the surface of equivalent solutions suggests that charge screening is the an important factor driving ordering in these systems.

SAXS data, time-resolved neutron reflectivity data (**Figure 3.14**) and GIXD patterns (**Figure 3.15 and Figure 3.16**) for CTAB/TMOS solutions with LPEI or SPEI, all indicate that the mesostructure type and the degree of mesostructural ordering of the particles in the bulk solutions are identical to those found in the film structures.[42] As shown in **Figure 3.14**, for a CTAB concentration of 0.037M, and 40g/l SPEI a 2D dimensional hexagonal structure will be finally observed in the films. Notably, however, according to the time-resolved neutron reflectivity data for films grown at the air/water interface from this solution, a cubic intermediate structure was formed within 10 minutes and finally transformed into the 2D hexagonal mesostructure over one hour (**Figure 3.14**). From the SAXS data of the subphase solution with the same composite concentration (**Figure 3.19 C**), a highly ordered 2D hexagonal mesostructure has already formed about 5 minutes after the addition of TMOS. Assuming the film grown at the air/water interface is formed because particles aggregate from the bulk solution to this interface, this film should have a 2D hexagonal structure around 10 minutes rather than the observed cubic structure. Therefore we suggest that although the route of mesostructure evolution of the film is the same as that of the particles in the solution, the liquid crystalline phase at the interface is not directly formed by the particles which develop below the interface.

Instead our results support the work of Åberg et al[7] who suggest that evaporation from the solution surface promotes the formation of a phase separated layer at the

solution surface. This layer, similar to a coacervated liquid particle in the subphase is more concentrated than the subphase solution, and continues to dry from the top surface, making it much more viscous than the subphase coacervate particles. Thus although the same route to mesostructure formation is observed it is retarded in the films relative to the self-assembly in the subphase. The ordering in these films proceeds much more slowly due to their highly viscous nature, but for the same reagent concentrations the same final mesostructure results. Thus the ordering in the films is not cut short or trapped by silica polymerization prior to the completion of ordering, and the structure formed must reflect only the electrostatic or ion-dipole interactions at the relative concentrations of the CTAB, PEI and TMOS.

With all the previous data and SAXS data reported in the current study, we attempt to summarise the micellar evolution of the CTAB/PEI/silica film forming solution and develop the film formation mechanism, in **Scheme 3.1**.

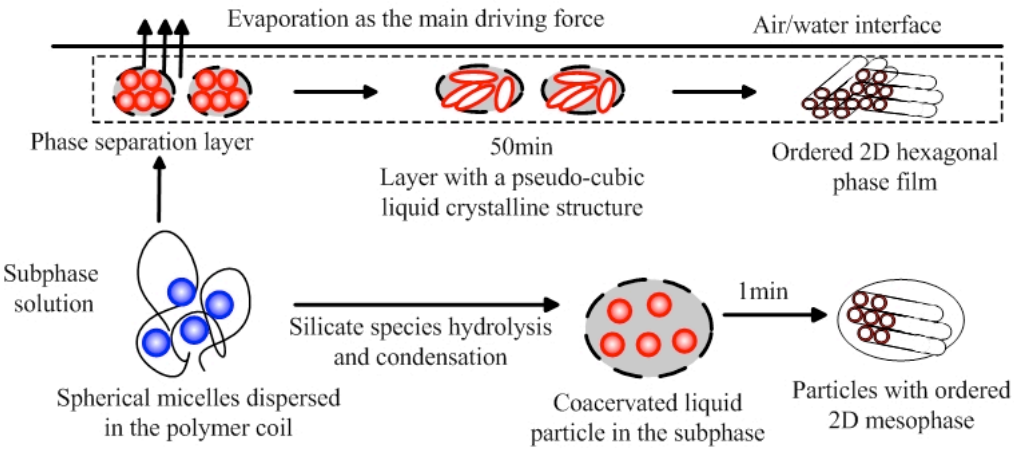

Scheme 3.1 *The interfacial CTAB/PEI/silica film formation mechanism.*

Initially, in solution the micelles have a spherical or ellipsoidal structure in the CTAB/PEI mixture, and addition of the silicate precursor drives formation of particles with a low degree of ordering. The mesostructure of the particles finally rearranges into a 2D hexagonal mesostructure for some intermediate polymer concentrations. The silicate precursor TMOS added to the mixture of CTAB and PEI, will infiltrate into the polymer networks and interact not only with polymer due to the hydrogen

bond formation with amine groups along the polymer chain, but also with the surfactant due to the electrostatic interaction between the negatively charged silica oligomers generated under basic conditions and the positively charged surfactant. Thus hydrolyzed and condensed silicate precursors as well as the polyelectrolyte will become a network which incorporates the spheroidal micelles to form CTAB/PEI/silica particles with a pseudo-cubic liquid crystalline structure. These particles show some degree of order at the beginning which increases and continuously rearranges into a 2D hexagonal mesostructure. Although it is difficult to catch the moment of the phase transformation within the CTAB/PEI/silica particles in the subphase, this same transformation was observed within the silica films at the air/water interface. In the viscous PEI/TMOS networks of the film at the solution interface, less water is present within the surfactant/polymer/silica phase, so the micelle transformation and rearrangement within the film will be much more difficult and the whole process needs a longer time. It is possible that during the film re-organization period, as evaporation continues from the solution surface, the level of the solution decreases and particles from the subphase become embedded in the bottom of the film which may assist in nucleating the final 2D hexagonal phase. Given the results from the films it is clear that the subphase particles must continue to be fluid for some time after the final 2D hexagonal phase is formed even if no further evolution in the phase is noted once an equilibrium structure has been reached. However upon merging with the film further rearrangement could still occur, leading to the ordered single-mesophase films observed.

3.4 Silica Monoliths Templated by Surfactant and Polyelectrolytes

3.4.1 Preparation of Silica Monoliths

The ordered 2D hexagonal mesoporous silica films were successfully synthesized with surfactant and polyelectrolytes, it was also possible to synthesize a silica monolith using surfactant and polyelectrolyte in similar solutions.

Sol-gel synthesis of silica in a bulk lyotropic liquid-crystalline phase allows the inorganic precursors to precipitate in the synthesis solution into the gaps between micelles. Complete removal of the residual solvent in the mesostructured silica gel allows fabrication of large monolith of the desired size and shape.[50-54] Transparent mesostructured silica monoliths are an ideal host for dyes for use in devices, such as lenses or laser devices.[55] In addition, mesoporous monoliths can be used as promising substrates for macromolecular separations.

Until now, many methods have been used to prepare monolithic mesoporous silicas based on an understanding of sol-gel process. Mesoporous monoliths have been mainly synthesized through mineralization of high concentration solutions of amphiphilic block copolymers,[51 56] microemulsions[53, 57] and cationic surfactants such as CTAB.[58] Hexagonal and cubic silica with 30 Å channel-like pores were synthesized with alkyl poly(ethylene oxide) oligomers as a template under acidic conditions.[59] Important developments in the direct templating method were achieved by using liquid crystalline phases of surfactants in bulk lyotropic and microemulsion systems.[56] Various dimensional structures with large mesoscopically ordered domains were synthesized using Brij 56 ($C_{16}EO_{10}$) and Pluronic copolymer as templates in aqueous acidic solutions.[53, 57, 60] However, instant preparation of lyotropic liquid crystal templated silica gel have not yet been reported.

There are two main problems that have to be overcome in the preparation of mesoporous monoliths: the first one is that the reaction conditions are too demanding and processing period is too long, since the reaction solution needs to be aged for at least 6 weeks and dried for several days to obtain the monolith.[56] The other problem is micro-cracks through drying due to the shrinkage which occurs when the solvent is removed from the gel. These two problems limit the practical application of monolithic mesostructured silica. So far, several drying and extraction methods have been used to prepare crack-free silica monoliths with highly ordered mesostructures, such as critical point extraction,[59] sealed vessel evaporation,[56] vacuum drying[61] as well as liquid paraffin-medium protected solvent evaporation.[62]

Here, we employed surfactant/polyelectrolyte mixtures to develop a method to prepare surfactant-templated monoliths, which not only gives fast reaction enabling a rapid synthesis process (the silica gel monolith formed within one minute), but also assists in solve the micro-crack problem during the drying process.

A photograph (**Figure 3.31 A**) shows a typical cylindrical silica monolith templated by Zonyl FSO–100/LPEI (synthesis procedure given in the **Section 2.3.5**), which has fully copied the shape of the reaction vessel. The diameter and the height of the silica monolith are 2cm and 0.5cm respectively. Using vessels with different shapes, the monolith shapes can be varied. Silica monoliths can only be prepared with LPEI at concentrations less than 20 g/l. If more LPEI is present, the time for the formation of monolithic gel becomes longer and the gel monolith is less solid. When the LPEI concentration was 10 g/l, a monolithic silica gel forms less than one minute after the silica precursor TMOS was added. The sample was dried in a 40°C oven uncovered for two days before the large crack free silica monolith shown in **Figure 3.31** was obtained. Colorful mesostructured silica monoliths doped with dyes can also be synthesized by simply soaking the monolithic gel in dye solutions after initial preparation. The gels do not crack upon exposure to the dye solutions despite the difference in osmotic pressure inside the gel and in the dye solution. As-synthesized CTAB/LPEI/silica monoliths show various colors in accordance with the corresponding dye colors. Take two dyes as examples; the dye structures are show in **Figure 3.32**. The silica monolith shows a pink color when the monolithic gel was doped with red rhodamine B dye, as shown in **Figure 3.31 B** while the monolith displays a blue color when the monolithic gel was doped with methylene blue dye (**Figure 3.31 C**). The diameter of this monolithic gel is nearly 4 cm. After drying, the macroscopic shapes are almost retained but some cracking is observed, the diameter of the blue monolith shrank to 1.6 cm.

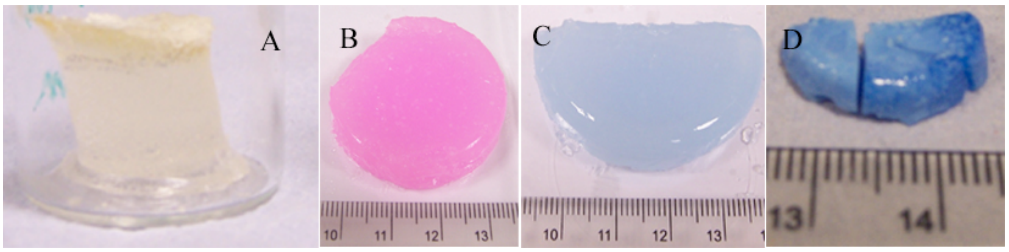

Figure 3.31 *Silica monoliths synthesized with surfactant and polyelectrolytes. (A) Dry monolith synthesized with a Zonyl FSO–100/LPEI complex (the radius and the height of the silica monolith are 1 cm and 0.5 cm). (B) Silica monolith gel synthesized with CTAB/LPEI and incorporating red Rhodamine B dye. (C) Silica monolith gel synthesized with CTAB/LPEI incorporating methylene blue dye. (D) Dry silica monolith of the sample in picture C. The ruler scale is in cm.*

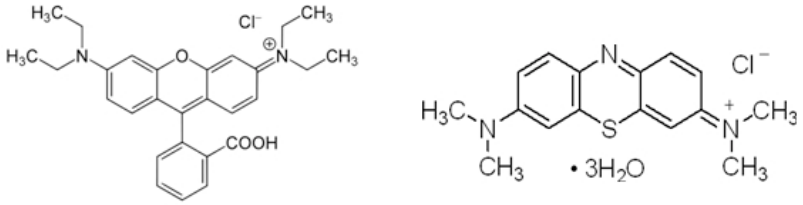

Figure 3.32 *Molecular structure of two dyes used here.*

Several surfactants with different concentrations were used to template the monolith, including Zonyl FSO-100, CTAB, Pluronic F-127 and Pluronic P-123, while the LPEI concentration was kept at 10g/l and TMOS concentration was constant at 0.169 M. SAXS data revealed the periodicity and ordering of the prepared mesostructured silica monoliths, shown in **Figure 3.33**. For Zonyl FSO-100 gels a broad peak around 0.14Å appeared only when the FSO concentration was increased to 0.15 M, indicating that the ordering of the monolithic gel improved with an increase of FSO concentration. When the LPEI concentration was kept at 5 g/l, the broad peak appeared when the FSO concentration was increased to 0.1M, as shown in **Figure 3.33 A**. Polyelectrolyte and silica precursor concentration do not show much effect on silica monolith structures prepared with Zonyl FSO–100/LPEI mixtures (**Figure 3.34**). Zonyl FSO-100 is a fluorinated surfactant with high levels of polydispersity in both

the ethylene oxide headgroup and the fluorocarbon tail so it is not very surprising that ordered mesostructures were not observed for this template, despite the expected strong segregation of fluorocarbon tails away from the aqueous gel phase.

For the dry monolith samples prepared with CTAB/LPEI mixtures for CTAB concentrations lower than 0.05 M (**Figure 3.33 B**), a broad peak around 0.22 $Å^{-1}$ was observed, indicating a low degree of long-range order. However, when the CTAB concentration was increased to more than 0.05 M, two sharp peaks at 0.24 $Å^{-1}$ and 0.48 $Å^{-1}$ appeared, which could be assigned to a lamellar mesophase with d-spacing of 26 Å possibly from crystalline CTAB within the gel. When the CTAB concentration was further increased to 0.1 M, the SAXS pattern shows three sharp diffraction peaks at 0.18 $Å^{-1}$, 0.21 $Å^{-1}$ and 0.23 $Å^{-1}$, which could be indexed as the (200), (210), (211) reflections of a cubic $Pm\bar{3}n$ mesophase structure with d-spacing of 34 Å. SAXS patterns also indicate that the regularity of the mesostructured ordering for CTAB/LPEI templated monoliths can be improved by doping with dye (as shown in **Figure 3.33 B red line**). These two dyes are positively charged when they are dissolved in the water (see their molecular structure in **Figure 3.32**), in the basic CTAB/PEI silica monolith forming solution, dye molecules are likely to get involved inside the micelle, with their hydrophobic part inside the micelle and their hydrophilic head group outside the micelle,[63] therefore it will not only improve the interaction between the positively charged CTAB micelles and negatively charged silica species, but also increase the micelle surface charge, assisting the repelling between micelles and then leading to a more ordered structure.

SAXS patterns of the monolith templated by Pluronic F-127/LPEI mixtures indicate an ordered lamellar structure formed only when the surfactant concentration is higher than 0.015 M, Two diffraction peaks at 0.03 $Å^{-1}$ and 0.06 $Å^{-1}$ were indexed as the (001) and (002) reflections, giving a d-spacing around 209 Å, as shown in **Figure 3.33 C**. When Pluronic P-123 was used, no diffraction peaks were observed for P-123 concentrations from 0.001 M to 0.015 M, indicating no ordered mesostructure forms in this range of surfactant concentrations.

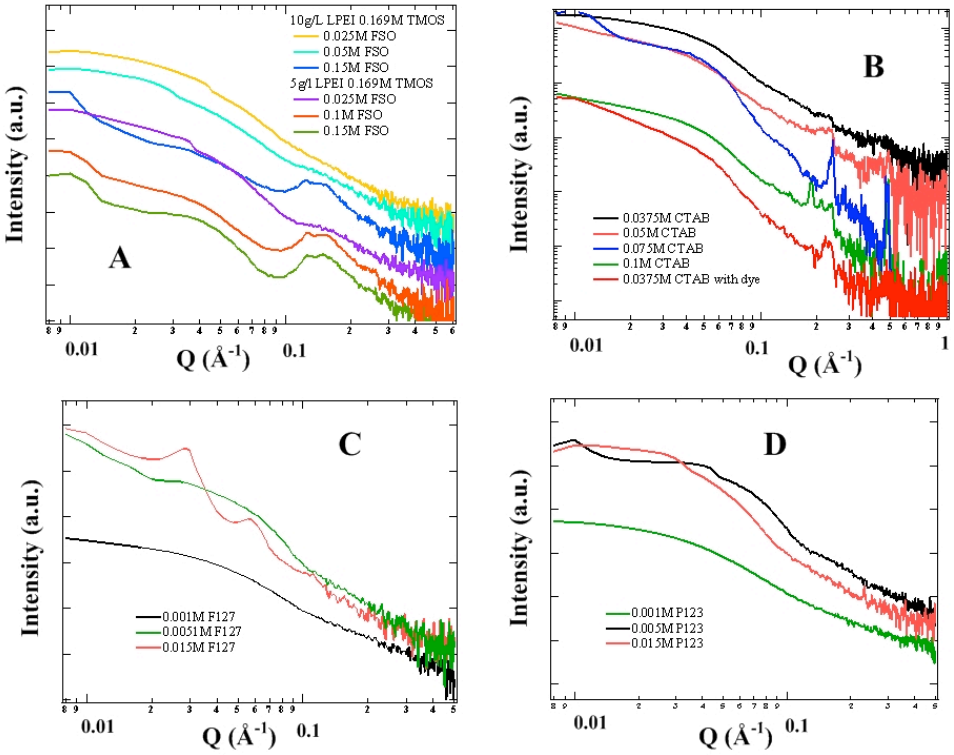

Figure 3.33 *SAXS patterns of silica monoliths synthesized with different surfactant/LPEI mixtures: (A) Zonyl FSO–100 two LPEI concentrations 10 g/l and 5 g/l were studied (B) CTAB (C) F-127 (D) P-123, the LPEI concentration was kept at 10 g/l. The TMOS concentration was constant for all cases at 0.169 M.*

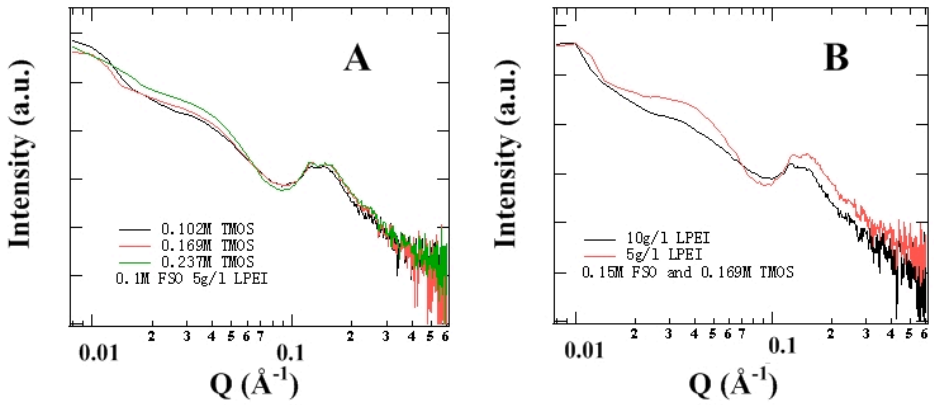

Figure 3.34 *Polyelectrolytes (A) and silica precursor concentration (B) effects on silica monolith structures prepared with Zonyl FSO–100/LPEI mixtures.*

3.4.2 Discussion - Monolith formation

Fabrication of silica monoliths based on the sol-gel process is a time consuming process. Generally, aging the reaction solution takes several days or even several weeks before an ordered mesostructured monolith gel is formed since insufficient aging time yields a weak network that does not possess the dimensional stability to withstand the increase in compressive stress during the evaporation process.[64] It is believed that the rigid silica network formed after enough aging time is an important factor to keep the highly ordered mesostructure. In this work, rigid silica monolith gels were formed in less than one minute with the addition of the polyelectrolyte PEI to the templating surfactant solution. The presence of PEI greatly affected the silicate hydrolysis and condensation process because the polyamines catalyze silica formation as noted above (**Section § 3.3.4**).[48] However, the fast hydrolysis and condensation also do not allow sufficient time for the surfactant micelles to rearrange themselves into an ordered mesostructure, so ordered mesostructures in the gels can only be obtained at high surfactant concentrations.

The nonionic surfactants, Zonyl FSO 100, Pluronic F-127 and Pluronic P-123 show less ordering than observed for the cationic surfactant CTAB suggesting that electrostatic interactions are the most efficient at promoting ordering of the mesostructure. For the nonionic surfactants the amount of ordering roughly corresponds to the hydrophobicity of the template molecule used. Fluorocarbons are the most hydrophobic, and the Zonyl FSO100 gels had some evidence of order, while the Pluronics have a relatively less hydrophobic polypropylene oxide block as the micelle core, so showed less evidence of aggregation in the gels. F-127 has a larger hydrophilic block than P-123, and at the highest concentrations used here is already in a two phase region close to the lamellar phase in its 2-component phase diagram.[65]Addition of PEI may assist assembly of this surfactant into the lamellar phase via depletion interactions. The presence of polymer also reinforces the gel blocks and they do not even crack after the take-up of dye molecules. These monoliths with dye can more or less remain whole without micro-cracks, although macroscopic cracking was observed.

3.5 Conclusion

In this work, surfactant/polyelectrolyte (CTAB/PEI and DDAB/PEI) films were investigated by GIXD and SAXS. Solid surfactant/polyelectrolyte films were able to be removed from the air/water surface, and the nanostructure found in the *in situ* films was shown to be retained in these polymer/surfactant films. The extent of structural ordering was affected by the concentration of cross-linker, but it mainly depends on the surfactant type, the concentration and molecular weight of the polymer.

When silica precursors are added, the CTAB/PEI/TMOS system presents different phases. Depending on concentration, the complexes will form gels, precipitates or films. Some of the CTAB/PEI/silicate films had no ordered repeat layers when they formed *in situ* at the solution surface, which results in disordered films when they are dried. However, at the air/water interface, most films show cubic phase ordering at the beginning of the film formation process and transform into a 2D hexagonal phase with time. This 2D hexagonal structure was retained when the films were dried. These silica films are strong and resist cracking, particularly for LPEI and have a high thermal stability since the ordered structure is maintained even after the removal of the template, which suggests potential applications in a variety of practical applications, such as catalysis and molecular sieving.

The electrostatic interactions between the silicate species and CTAB/PEI as well as the dipole-cationic interaction between silica or CTAB and PEI, allow their co-assembly and result in the homogenous dispersion of the polymer and silicate species around the CTAB micelles. SAXS was used to investigate the evolution of micelles in the subphase solutions of CTAB/PEI/TMOS which form films at the air/water interface. Simple models have been employed to quantify the size and shape of the micelles formed in solution. For film forming solutions with PEI, the micelles have a spherical or elliptical structure dispersed in the polymer solution immediately after mixing. There is no liquid crystalline ordering of the surfactant micelles occurring in the bulk solution prior to silica precursor addition. For all the film forming solutions, addition of silicate species does not initially change the micellar

size and structure. The hydrogen bond formation between the amine groups in the polyamine chains and the surfactant head groups with the oxygen adjacent to silicon in the precursor facilitate the silicate hydrolysis and condensation resulting in formation of phase separated particles with a disordered mesostructure. The mesophase within the CTAB/PEI/silica particles finally rearranges into a 2D hexagonal ordered structure. The mesostructure evolution process in the film is similar to the mesostructure evolution in the particles in the subphase, except that the whole process within the particles of the films takes a much longer time than that in the subphase solutions because of the relative dryness and viscosity of the PEI/silica networks at the solution surface.

An important implication of this work is that it is possible to balance the interaction between the surfactant, polymer and silica precursor, to achieve efficient co-assembly into a highly ordered mesostructured material. This work provides not only a straightforward way to introduce an polymer as part of the inorganic wall structure to make it more robust and mechanically strong, but also incorporates organic species into the silicate wall to make it more functional which could have great advantage towards practical applications. This is the first report of the synthesis of inorganic ordered mesoporous films templated by surfactant/polyelectrolyte complexes at the air/water interface. By altering the polyelectrolyte, inorganic precursor or the surfactant template, a wide range of free-standing organic/inorganic hybrid films could be generated at the air/water interface.

Silica monoliths with a certain degree of mesostructural ordering have also been prepared with the surfactant and polyelectrolyte system. By accelerating the gelation process of silica with addition of polyelectrolytes, the reaction solution gelling time is shortened to less than one minute. The incorporated polymer improves the crack resistance of the monoliths on drying. In addition, dyes can be easily doped into the silica/polymer monolith, which is expected to have positive implications for their applications in separation and optics.

3.6 References

(1) B. M. D. O'Driscoll, E. Milsom, C. Fernandez-Martin, L. White, S. J. Roser, and K. J. Edler, *Macromolecules* **38**(21), 8785 (2005).

(2) B. M. D. O'Driscoll, C. Fernandez-Martin, R. D. Wilson, S. J. Roser, and K. J. Edler, *Journal of Physical Chemistry B* **110**(11), 5330 (2006).

(3) B. M. D. O'Driscoll, C. Fernandez-Martin, R. D. Wilson, J. Knott, S. J. Roser, and K. J. Edler, *Langmuir* **23**(8), 4589 (2007).

(4) H. Comas-Rojas, E. Aluicio-Sarduy, S. Rodriguez-Calvo, A. Perez-Gramatges, S. J. Roser, and K. J. Edler, *Soft Matter* **3**(6), 747 (2007).

(5) E. Kokufuta, H. Suzuki, R. Yoshida, K. Yamada, M. Hirata, and F. Kaneko, *Langmuir* **14**(4), 788 (1998).

(6) F. Caboi, and M. Monduzzi, *Langmuir* **12**(15), 3548 (1996).

(7) C. Aberg, E. Sparr, K. J. Edler, and H. Wennerstrom, *Langmuir* **25**(20), 12177 (2009).

(8) K. J. Edler, A. Goldar, A. V. Hughes, S. J. Roser, and S. Mann, *Microporous and Mesoporous Materials* **44**, 661 (2001).

(9) K. J. Edler, T. Brennan, S. J. Roser, S. Mann, and R. M. Richardson, *Microporous and Mesoporous Materials* **62**(3), 165 (2003).

(10) S. J. R. C. Fernandez-Martin, K.J. Edler, *Langmuir* **20**(24), 10679 (2004).

(11) B. Platschek, R. Kohn, M. Doblinger, and T. Bein, *Chemphyschem* **9**(14), 2059 (2008).

(12) S. Sadasivan, C. E. Fowler, D. Khushalani, and S. Mann, *Angewandte Chemie-International Edition* **41**(12), 2151 (2002).

(13) C. Z. Yu, J. Fan, B. Z. Tian, and D. Y. Zhao, *Chemistry of Materials* **16**(5), 889 (2004).

(14) H. B. S. Chan, P. M. Budd, and T. D. Naylor, *Journal of Materials Chemistry* **11**(3), 951 (2001).

(15) J. Y. Zhang, Z. Luz, H. Zimmermann, and D. Goldfarb, *Journal of Physical Chemistry B* **104**(2), 279 (2000).

(16) S. Ruthstein, V. Frydman, and D. Goldfarb, *Journal of Physical Chemistry B* **108**(26), 9016 (2004).

(17) D. Baute, V. Frydman, H. Zimmermann, S. Kababya, and D. Goldfarb, *Journal of Physical Chemistry B* **109**(16), 7807 (2005).

(18) C. C. Egger, M. W. Anderson, G. J. T. Tiddy, and J. L. Casci, *Physical Chemistry Chemical*

Physics **7**(8), 1845 (2005).

(19) C. Egger, M. W. Anderson, G. J. T. Tiddy, and J. L. Casci, *Recent Advances in the Science and Technology of Zeolites and Related Materials, Pts a - C* **154**, 489 (2004).

(20) I. Beurroies, P. Agren, G. Buchel, J. B. Rosenholm, H. Amenitsch, R. Denoyel, and M. Linden, *Journal of Physical Chemistry B* **110**(33), 16254 (2006).

(21) D. Grosso, F. Babonneau, P. A. Albouy, R. Balkenende, and H. Amenitsch, *Abstracts of Papers of the American Chemical Society* **221**, U475 (2001).

(22) K. J. Edler, P. A. Reynolds, and J. W. White, *Journal of Physical Chemistry B* **102**(19), 3676 (1998).

(23) V. L. Zholobenko, A. Y. Khodakov, M. Imperor-Clerc, D. Durand, and I. Grillo, *Advances in Colloid and Interface Science* **142**(1-2), 67 (2008).

(24) K. J. Edler, J. Dougherty, R. Durand, L. Iton, G. Kirton, G. Lockhart, Z. Wang, R. Withers, and J. W. White, *Colloids and Surfaces a-Physicochemical and Engineering Aspects* **102**, 213 (1995).

(25) K. Flodstrom, C. V. Teixeira, H. Amenitsch, V. Alfredsson, and M. Linden, *Langmuir* **20**(12), 4885 (2004).

(26) K. Flodstrom, H. Wennerstrom, C. V. Teixeira, H. Amenitsch, M. Linden, and V. Alfredsson, *Langmuir* **20**(23), 10311 (2004).

(27) D. Grosso, F. Babonneau, P. A. Albouy, H. Amenitsch, A. R. Balkenende, A. Brunet-Bruneau, and J. Rivory, *Chemistry of Materials* **14**(2), 931 (2002).

(28) K. J. Edler, T. Brennan, and S. J. Roser, *Thin Solid Films* **495**(1-2), 2 (2006).

(29) T. Brennan, S. J. Roser, S. Mann, and K. J. Edler, *Chemistry of Materials* **14**(10), 4292 (2002).

(30) A. Nelson, *Journal of Applied Crystallography* **39**, 273 (2006).

(31) J. P. Hansen, and J. B. Hayter, *Molecular Physics* **46**(3), 651 (1982).

(32) J. B. Hayter, and J. Penfold, *Molecular Physics* **42**(1), 109 (1981).

(33) R.-J. Roe, *Methods of X-ray and Neutron Scattering in Polymer Science, Oxford University Press. Inc*, (2000).

(34) M. Kotlarchyk, and S. H. Chen, *Journal of Chemical Physics* **79**(5), 2461 (1983).

(35) S. S. Berr, *Journal of Physical Chemistry* **91**(18), 4760 (1987).

(36) G. G. Warr, R. Sen, D. F. Evans, and J. E. Trend, *Journal of Physical Chemistry* **92**(3), 774 (1988).

(37) C. Boissiere, A. Larbot, C. Bourgaux, E. Prouzet, and C. A. Bunton, *Chemistry of Materials* **13**(10), 3580 (2001).

(38) P. Linton, A. R. Rennie, M. Zackrisson, and V. Alfredsson, *Langmuir* **25**(8), 4685 (2009).

(39) J. Teixeira, *Journal of Applied Crystallography* **21**, 781 (1988).

(40) Q. S. Huo, D. I. Margolese, U. Ciesla, D. G. Demuth, P. Y. Feng, T. E. Gier, P. Sieger, A. Firouzi, B. F. Chmelka, F. Schuth, and G. D. Stucky, *Chemistry of Materials* **6**(8), 1176 (1994).

(41) D. Y. Zhao, J. Y. Sun, Q. Z. Li, and G. D. Stucky, *Chemistry of Materials* **12**(2), 275 (2000).

(42) B. Yang, and K. J. Edler, *Chemistry of Materials* **21**(7), 1221 (2009).

(43) J. N. Cha, K. Shimizu, Y. Zhou, S. C. Christiansen, B. F. Chmelka, G. D. Stucky, and D. E. Morse, *Proceedings of the National Academy of Sciences* **96**(2), 361 (1999).

(44) T. Brennan, A. V. Hughes, S. J. Roser, S. Mann, and K. J. Edler, *Langmuir* **18**(25), 9838 (2002).

(45) M. Linden, J. Blanchard, S. Schacht, S. A. Schunk, and F. Schuth, *Chemistry of Materials* **11**(10), 3002 (1999).

(46) J. J. Yuan, and R. H. Jin, *Advanced Materials* **17**(7), 885 (2005).

(47) P. A. Patel, J. Eckart, M. C. Advincula, A. J. Goldberg, and P. T. Mather, *Polymer* **50**(5), 1214 (2009).

(48) G. Pohnert, *Angewandte Chemie-International Edition* **41**(17), 3167 (2002).

(49) Y. J. Li, J. L. Xia, and P. L. Dubin, *Macromolecules* **27**(24), 7049 (1994).

(50) K. M. McGrath, D. M. Dabbs, N. Yao, I. A. Aksay, and S. M. Gruner, *Science* **277**(5325), 552 (1997).

(51) M. C. Weissenberger, C. G. Goltner, and M. Antonietti, *Berichte Der Bunsen-Gesellschaft-Physical Chemistry Chemical Physics* **101**(11), 1679 (1997).

(52) A. W. Xu, Y. P. Cai, L. Z. Zhang, and J. C. Yu, *Advanced Materials* **14**(15), 1064 (2002).

(53) S. A. El-Safty, and T. Hanaoka, *Advanced Materials* **15**(22), 1893 (2003).

(54) S. A. El-Safty, *Journal of Porous Materials* **15**(4), 369 (2008).

(55) B. J. Scott, G. Wirnsberger, and G. D. Stucky, *Chemistry of Materials* **13**(10), 3140 (2001).

(56) N. A. Melosh, P. Lipic, F. S. Bates, F. Wudl, G. D. Stucky, G. H. Fredrickson, and B. F. Chmelka, *Macromolecules* **32**(13), 4332 (1999).

(57) S. A. El-Safty, and T. Hanaoka, *Chemistry of Materials* **15**(15), 2892 (2003).

(58) Y. F. Lu, R. Ganguli, C. A. Drewien, M. T. Anderson, C. J. Brinker, W. L. Gong, Y. X. Guo, H. Soyez, B. Dunn, M. H. Huang, and J. I. Zink, *Nature* **389**(6649), 364 (1997).

(59) C. G. Goltner, S. Henke, M. C. Weissenberger, and M. Antonietti, *Angewandte Chemie-International Edition* **37**(5), 613 (1998).

(60) S. A. El-Safty, and T. Hanaoka, *Chemistry of Materials* **16**(3), 384 (2004).

(61) P. Y. Feng, X. H. Bu, G. D. Stucky, and D. J. Pine, *Journal of the American Chemical Society* **122**(5), 994 (2000).

(62) H. F. Yang, Q. H. Shi, B. Z. Tian, S. H. Xie, F. Q. Zhang, Y. Yan, B. Tu, and D. Y. Zhao, *Chemistry of Materials* **15**(2), 536 (2003).

(63) K. Hou, Q. H. Song, D. B. Nie, F. Y. Li, Z. Q. Bian, L. Y. Liu, L. Xu, and C. H. Huang, *Chemistry of Materials* **20**(12), 3814 (2008).

(64) C. J. Brinker, and G. W. Scherer, *Sol-gel science : the physics and chemistry of sol-gel processing*. Academic Press: Boston, 1990.

(65) G. Wanka, H. Hoffmann, and W. Ulbricht, *Macromolecules* **27**(15), 4145 (1994).

Chapter 4 Cat-anionic Surfactant/Polymer Complex Templated Silica Films at the Air/water Interface

4.1 Introduction

Mesoporous materials with a film geometry are of great interest because of their wide potential applications in chemical sensors, separation and catalysis. In the previous chapter, hydrothermally stable mesoporous films with a well ordered 2D hexagonal mesostructure, templated using CTAB/PEI complexes at high pH were discussed.[1] Employing polyelectrolytes as part of the surfactant template for inorganic mesostructured wall can not only make the thick inorganic films resist cracking but also introduce polymer functionality into the inorganic wall which will be advantageous for potential applications in a variety of fields such as catalysis, molecular separation and drug delivery. The pore orientation in these 2D hexagonal films is however thought to be largely parallel to the interface, preventing diffusion through the membrane, thus robust films with a cubic phase are more attractive in their potential applications, such as molecular separation, diffusion and absorption.

Mixing cationic surfactant and anionic surfactant results in cat-anionic surfactant solutions, in which two oppositely charged groups are distributed within mixed micelles. The micellar properties can be tailored by adjusting the competition of various molecular interactions (Van der waals, hydrophobic, electrostatic force etc), resulting in a variety of structures, such as cat-anionic vesicles, salts and micelles.[2-5] Cat-anionic complexes are reported to interact with hydrophobically modified biocompatible polymers,[6] DNA or charged polymers [7] and salts. Other work in the group has reported polymer films with highly ordered mesophases including cubic mesophases, at the air/water interface using water soluble polymers and cat-anionic surfactant mixtures.[8-10]

In this chapter, I have first extended the work on the thick robust cat-anionic surfactant-polyelectrolyte films, and then used polymers to alter the surface charge

and hydrophobicity of the cat-anionic surfactant micelles in order to controllably synthesize robust polymer/silica hybrid films with a variety of ordered mesostructures at the air/solution interface. The molar ratio of cationic surfactant to anionic surfactant, the polymer and reaction component total concentration are critical for the control of film mesostructure. By varying these factors phase transitions were induced from lamellar, to 2D-hexagonal, to bicontinuous cubic and to micellar cubic. These mesoporous silica films have improved mechanical strength; moreover, this film preparation method provides a simple way to impart polymer functionality into the mesostructured silica walls, which means these films have potential applications in a variety of fields such as catalysis, molecular separation and drug delivery.

4.2 Cat-anionic Surfactant/Polymer Films

Our group observed that thick robust films are formed when cat-anionic surfactant of CTAB and SDS are mixed with the water soluble polymer PEI as well as with polyacrylamide (PAAm).[10] Later, we also found that cat-anionic surfactant mixtures can spontaneously form robust films with a wide range of other polymers. Different polymer concentrations, and CTAB: SDS molar ratios result in films with different mesostructures.[9] The strength of the interaction between the polymer and surfactant appears to determine the final phase.

This chapter begins with the investigations of the mesostructure of interfacial cat-anionic surfactant/polyelectrolyte films and dry free-standing polymer films. Then descriptions of silica films prepared with these cat-anionic surfactant-polyelectrolyte complexes will follow.

4.2.1 CTAB/SDS/LPEI

Films were prepared as described in **Section § 2.3.2**. CTAB: SDS molar ratios were varied from 2:1 to 8:1 (For all the ratios used, CTAB final concentration is 0.037 M). The PEI concentrations used ranged from 10 g/l to 40 g/l. The results of these concentration variations will be detailed in the experiments results.

To investigate the mesophase of the interfacial CTAB/SDS/LPEI films, GIXD patterns were collected on ID10B, ESRF at two angles, a small angle of 0.045° above the critical angle of these solutions probing only the top ~100Å of the solution (**Figure 4.1 A & Ca** line profile at 0.007 $Å^{-1}$) and at the angle of the first diffraction peak (**Figure 4.1 B & Cb**). Line profiles for the top layers of film only display one peak at Q_z = 0.12 $Å^{-1}$, indicating that few repeat units of the film are visible at this angle due to the low penetration depth and suggesting a lack of in-plane ordering on this length scale. However, in the GIXD patterns taken with a higher penetration depth in the film, one sharp peak at 0.16 $Å^{-1}$ was observed and three broad features occur in the positions of 0.32 $Å^{-1}$, 0.48 $Å^{-1}$ and 0.64 $Å^{-1}$ where other orders of a lamellar phase should be expected. The d-spacing calculated from the first order diffraction peak is 39 Å.

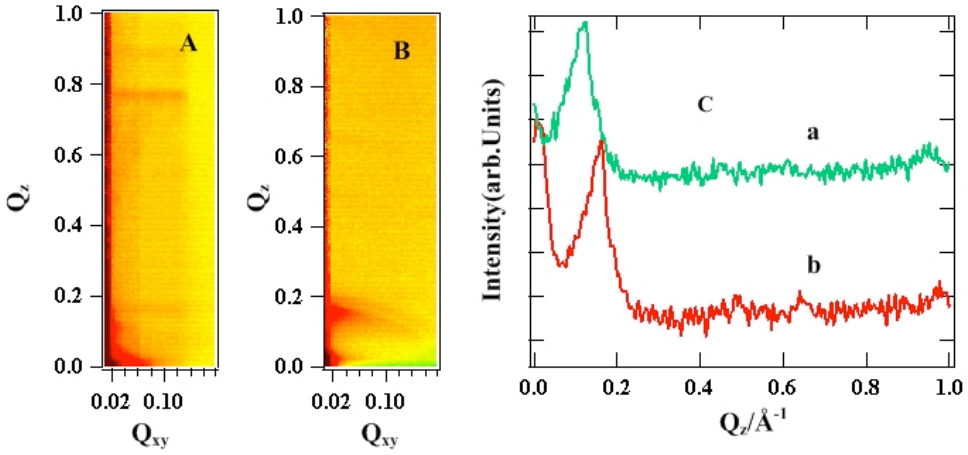

Figure 4.1 *GIXD patterns of interfacial films templated by complexes of cat-anionic surfactant mixtures (CTAB: SDS = 4) and 40 g/l LPEI. Structure of (A) top layers and (B) relatively deeper layers of interfacial films. (C) Line profiles at* Q_{xy} *= 0.007* $Å^{-1}$ *from GIXD patterns A (a) and B (b).*

Almost all the CTAB/SDS/LPEI solutions formed thick solid coherent films that could be recovered from the solution surface using an open mesh, SAXS patterns were collected on dried films synthesized with different CTAB: SDS molar ratio and LPEI concentrations, shown in **Figure 4.2**. The variation of LPEI concentration did not appear to greatly affect the mesophase of dry CTAB/SDS/LPEI films. For films

with a CTAB: SDS molar ratio of 6 (represented as CTAB:SDS = 6) and LPEI concentrations from 20 g/l to 50 g/l (**Figure 4.2 A**) three peaks at 0.17 $Å^{-1}$, 0.24 $Å^{-1}$ and 0.48 $Å^{-1}$ appear in all patterns, which may be assigned as (110), (200) and (400) peaks corresponding to $Im\bar{3}m$ symmetry with a repeating unit cell of 52 Å. Comparing the GIXD patterns and SAXS patterns of cat-anionic surfactant/LPEI films prepared with the same CTAB: SDS molar ratio and LPEI concentration, for example, a molar ratio of CTAB: SDS = 4 and a LPEI concentration of 40 g/l, it appears that the drying process drives a mesophase transformation from the lamellar phase to the cubic $Im\bar{3}m$ phase.

However, the impact of changing the CTAB:SDS molar ratio seems more straightforward than the effects of LPEI concentration (**Figure 4.2 D**). When the LPEI concentration was kept at 30 g/l and CTAB: SDS molar ratio varied from 2 to 8, three peaks at 0.17 $Å^{-1}$, 0.24 $Å^{-1}$ and 0.48 $Å^{-1}$ still could be observed and the peak positions did not move, however, the peak intensity of the first peak decreases while the peak intensity of the second peak increases. The Garstecki and Holyst model for calculating the intensity of peaks in bicontinuous cubic phases, which is based on the assumption of a bilayer membrane of surfactant with constant scattering length density across the membrane surrounded by aqueous solution, can be used here. In our case, the aqueous solution can be assumed to be polymer layer.[11, 12] When more SDS is present in the surfactant bilayer the average membrane thickness will decrease, altering the relative intensities of the diffraction peaks. Also increasing the SDS will strengthen the interaction with the opposite charges of CTAB and thus the surfactant headgroups are likely to sit closer together, and also the hydrophobicity of the surfactant bilayer will also be improved as the overall charge is neutralized. All of these reasons may be responsible for the variation of the thickness and volume fraction of the surfactant bilayer, leading to variation of peak intensities.

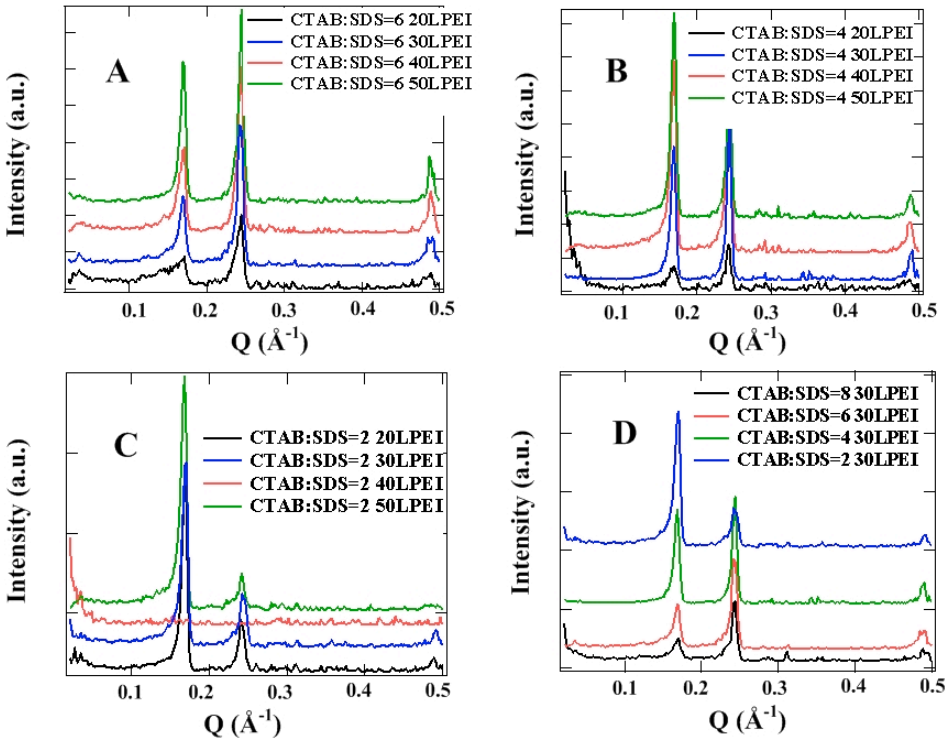

Figure 4.2 *SAXS patterns of the dry cat-anionic surfactant/LPEI films. (A) CTAB: SDS = 6 and LPEI concentration from 20 g/l to 50 g/l (B) CTAB: SDS = 4 and LPEI concentration from 20 g/l to 50 g/l (C) CTAB: SDS = 2 LPEI concentration from 20 g/l to 50 g/l (D) CTAB: SDS molar ratios vary from 2 to 8 and LPEI concentration is 30 g/l.*

4.2.2 CTAB/SDS/SPEI

The polymer molecular weight appears to have more effect on CTAB/SDS/PEI films. The mesophase of the films prepared using lower molecular weight SPEI are much more complex than films prepared with high molecular weight LPEI, as shown in **Figure 4.3**. In this case, for films synthesized with CTAB: SDS = 4 40 g/l SPEI, the mesostructure of the top layer of the film seems to be the same as the structure deeper in the film from GIXD patterns (**Figure 4.3 C**). Four distinct peaks at 0.12 $Å^{-1}$, 0.17 $Å^{-1}$ and 0.24 $Å^{-1}$ were observed. Taking all the peaks into consideration, the GIXD patterns of CTAB/SDS/SPEI films appear to correspond to an $Im\bar{3}m$ phase

with these three peaks assigned as the (110), (200), (220) reflections, and a repeating unit cell of 74 Å.

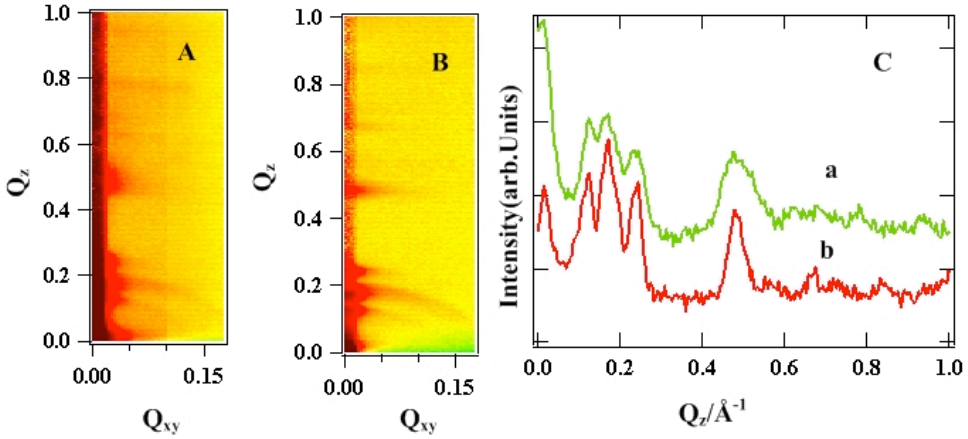

Figure 4.3 *GIXD patterns of interfacial films templated by cat-anionic surfactant (CTAB: SDS = 4) and 40 g/l SPEI complexes. Structure of (A) top layers and. (B) deeper layers of the interfacial film. (C) Line profiles at Q_{xy}=0.007 $Å^{-1}$ from GIXD patterns A (a) and B (b).*

However, only certain CTAB: SDS molar ratios and SPEI concentrations result in films, which are thick enough to be removed from the air/water interface. SAXS patterns of the dry films were also collected. Peak positions at 0.17 $Å^{-1}$ and 0.24 $Å^{-1}$ are similar to those found in the CTAB/SDS/LPEI dry films (**Figure 4.4**), which also can be indexed as $Im\bar{3}m$ with a repeating unit cell of 52 Å, however, the drying process caused the unit cell shrink by about 22 Å than that of the interfacial films.

When the CTAB: SDS molar ratio was 4:1, 40 g/l SPEI seems to be the optimum SPEI concentration to retain the dry film ordering since at this concentration the two diffraction peaks are more sharp. Films prepared with SPEI concentrations higher or lower than 40 g/l appear to be less ordered, as shown in **Figure 4.4 B**.

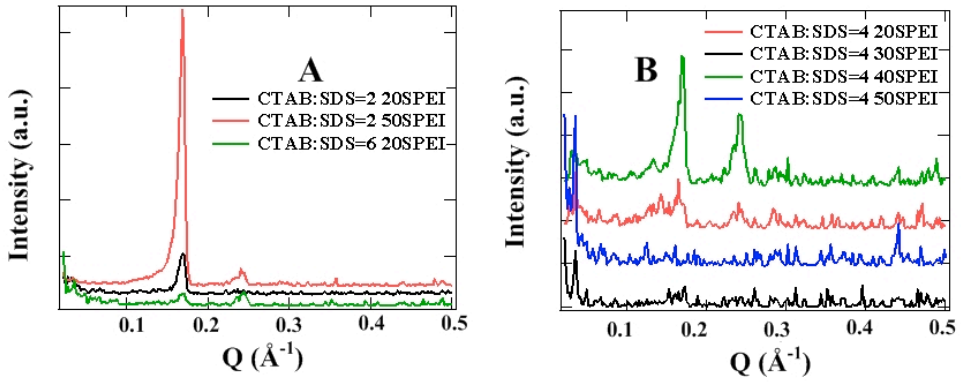

Figure 4.4 *SAXS patterns of the dry cat-anionic surfactant/SPEI films.*

4.2.3 CTAB/SDS/PAAm

In order to investigate the effect of the polymer used in this cat-anionic surfactant-polyelectrolyte film forming system, other polyelectrolytes have also been used in addition to PEI, such as PAAm and PEO.

Films were prepared with a molar ratio of CTAB: SDS = 4 and 25 g/l PAAm. GIXD patterns and their line profiles show two distinct peaks at 0.07 $Å^{-1}$ and 0.14 $Å^{-1}$, indicating the film structure is a lamellar mesophase with d-spacing of 90 $Å^{-1}$ (**Figure 4.5**).

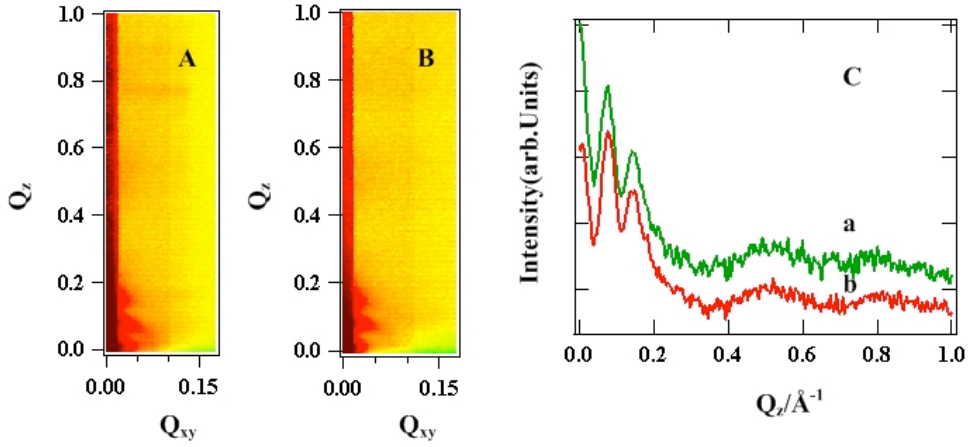

Figure 4.5 *GIXD patterns of interfacial films templated by cat-anionic surfactant (CTAB: SDS = 4) and 25 g/l PAAm complexes. Structure of (A) top layers and (B) deeper layers of interfacial films. (C) Line profiles at* Q_{xy} *= 0.007* $Å^{-1}$ *from GIXD patterns A (a) and B (b).*

The CTAB/SDS/PAAm films were opaque and thick, almost all the films were able to be recovered from the air/water interface. The CTAB: SDS molar ratios were changed from 2 to 8 and the PAAm concentrations were also varied from 12.5 g/l to 37.5 g/l. SAXS data indicate the mesophase in the dry films is not altered by varying either the CTAB: SDS molar ratio or the PAAm concentration. As shown in **Figure 4.6**, only a big broad peak around 0.07 $Å^{-1}$ could be observed, indicating a lack of long range ordering.

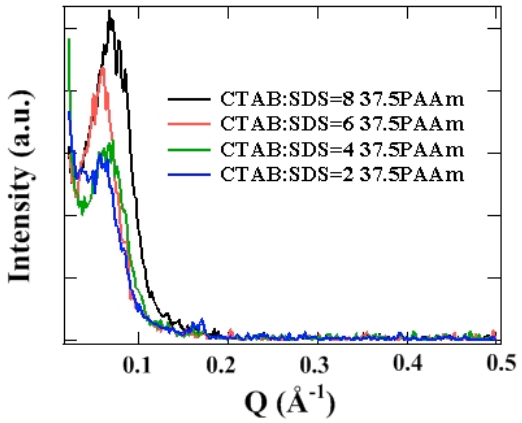

Figure 4.6 *SAXS patterns of the dry cat-anionic surfactant/PAAm films.*

4.2.4 CTAB/SDS/PEO

In the case of PEO (**Figure 4.7 and Figure 4.8**), the mesophases in the films are more complex than for the PAAm films. GIXD patterns taken at the two angles are different to each other suggesting the top and deeper layers of the film have different structures. For the low angle GIXD pattern (**Figure 4.7 A**) and its line profile (**Figure 4.7 Ca**) probing the top of the film, three sharp peaks at 0.20 $Å^{-1}$, 0.23 $Å^{-1}$, 0.31 $Å^{-1}$ can be indexed as the (211), (220), (321) reflections of an $Ia\bar{3}d$ cubic phase with a unit cell of 77 Å. Another spot was observed on both of the GIXD patterns, it may be artifact or detector problem, or it may be from the crystalline structure in the film. For the mesostructure of the film measured at higher incident angle, three peaks at 0.15$Å^{-1}$, 0.18 $Å^{-1}$ and 0.23 $Å^{-1}$ could also be observed but these three peaks belong to an $Ia\bar{3}d$ cubic phase, with a unit cell dimension calculated from the first diffraction peak of

102 Å, which is bigger than the unit cell of top layer. This could be due to drying of the top layer relative to the deeper layers in the film which are thicker as more water is present.

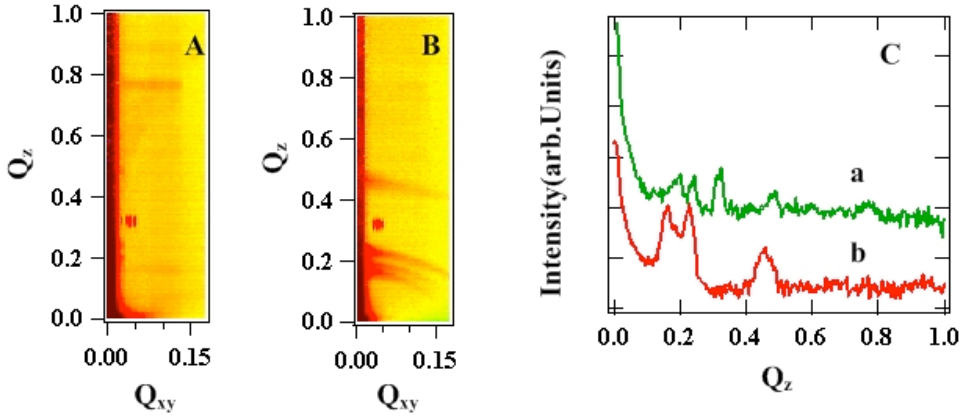

Figure 4.7 *GIXD patterns of interfacial films templated by cat-anionic surfactant (CTAB: SDS = 4) and 25 g/l PEO complexes. Structure of (A) top layers and. (B) relatively deeper layers of interfacial films. (C) Line profiles at* Q_{xy} *= 0.007* $Å^{-1}$ *from GIXD patterns A (a) and B (b).*

CTAB/SDS/PEO films are robust and thick enough to be removed from the solution interface. The SAXS patterns collected on the dry CTAB/SDS/PEO films were shown in **Figure 4.8**. Although the CTAB: SDS molar ratio varied from 2 to 8 and PEO concentrations changed from 25 g/l to 75 g/l, the SAXS patterns consistently display three peaks at 0.17 $Å^{-1}$, 0.24 $Å^{-1}$ and 0.48 $Å^{-1}$, which are very similar to those observed for CTAB/SDS/PEI films. Thus it may be assigned as $Im\bar{3}m$ with a d-spacing of 53 Å as well. When the CTAB: SDS molar ratio were constant at 2, 4 or 6, increasing the PEO concentration improves the mesostructural ordering since the peaks observed have higher intensities in all cases. Similar to the SAXS pattern of the CTAB/SDS/LPEI films, the intensity for the first two peaks varies according to the variation of CTAB: SDS molar ratio. The intensity for the first peak is higher than the second peak when more SDS is present in the cat-anionic surfactant solution, which

may also be due to the variation of the thickness and volume fraction of the surfactant bilayer described in a simple Garstecki and Holyst model (**refer to Section 4.2.1**).[11, 12]

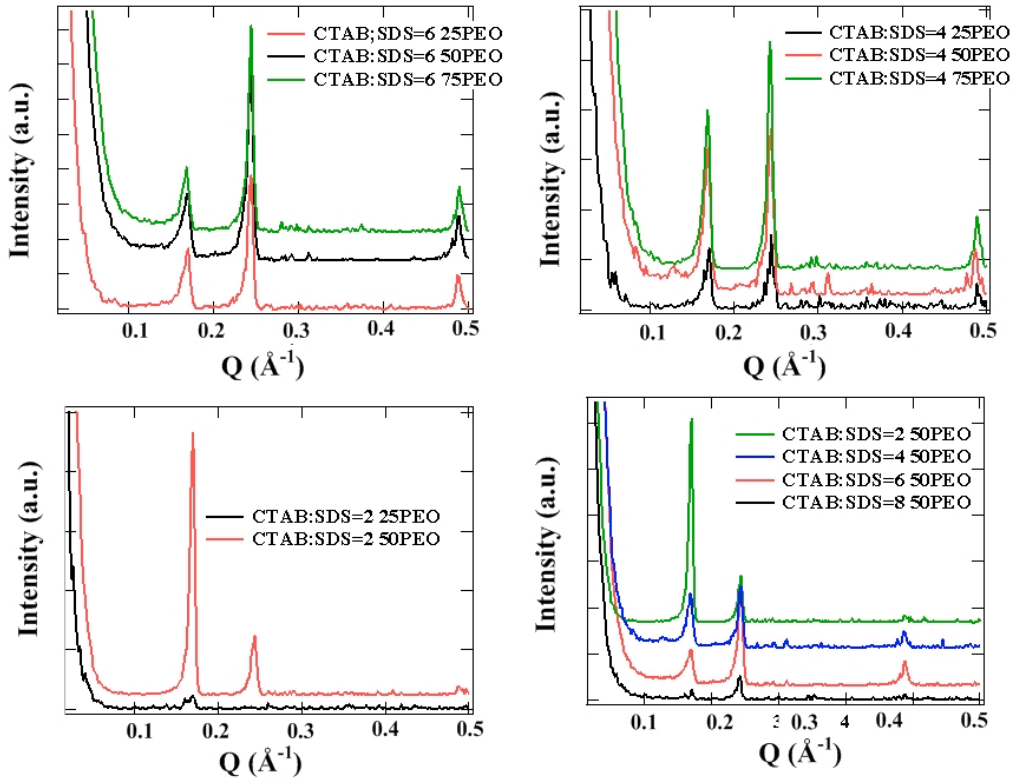

Figure 4.8 *SAXS patterns of the dry cat-anionic surfactant/PEO films.*

4.2.5 Discussion - Cat-anionic Surfactant/Polymer Films

The results outlined above indicate that the chemical nature of the polymer, the solution concentration of the polymer and the cat-anionic molar ratio have strong effects on the phase behavior in the films. Generally, mixture of cationic and anionic surfactants with an excess of either surfactant will form mixed cat-anionic micelles, which have larger aggregation numbers than those of micelles containing a uniform charged species. An excess of cationic surfactant (in this case CTAB) results in larger size, less compact and more polar mixed cat-anionic micelles.[8]

When polyelectrolytes (LPEI and SPEI) are introduced to the mixed surfactant solution, the interaction between the polyelectrolytes and cat-anionic surfactant induces a rich mesophase self-assembly behaviour. PEI is almost neutral in the pH

range used for this experiment (>3% charged between 9-10).[13, 14] Earlier work in the group suggested that the dominant interaction between the PEI and surfactant CTAB is a dipole-cation interaction, where the polymer amine groups interact with the charged CTAB quaternary ammonium group.[14] There is also a strong affinity between anionic surfactant SDS and PEI. The DS^- anion can interact electrostatically with the remaining positively charged amino groups of the polymer. Under basic conditions however, PEI is essentially a neutral polymer, so the ethylene group in PEI also gives the polymer a hydrophobic character. SDS binds to linear PEI at high pH because the hydrophobic interaction is much larger than electrostatic interaction and this will also occur in the hyper-branched PEI/SDS complexes used here.[13] Thus the complex interaction between the polymer, PEI, and cat-anionic surfactant mixture causes the formation of interfacial films with varied mesostructures.

Similar to cationic surfactant templated polymer films, high molecular weight LPEI form structures with relatively low internal ordering comparing to SPEI in the cationic surfactant templated film system.[15] Since LPEI has more branches and has a higher hydrophobicity, the phase separation to the interface during film formation is accelerated and the self-ordering process in the viscous high concentration surface layer is slow. In addition, since the bulky polymer molecules, which are larger than the preferred size of the gaps between the micelles in their ordered phase, must change their configuration, preventing the rearrangement of the micelles in the polyelectrolyte network, leading to less ordered structures. Dry films kept their mesostructure; however, the unit cell dimension shrank 19 Å upon drying.

When the polymer/silica hybrid films were prepared with PAAm, no matter what the polyelectrolyte concentration and the cat-ionic surfactant molar ratio are, the final mesophase of the interfacial films are always lamellar structures. Compared with PEI, PAAm is thought to have little interaction with either CTAB or SDS in solution or towards co-adsorption at the interface, thus the lamellar phase probably occurs via depletion interactions between the polymer and cat-anionic surfactant micelles concentrating the surfactant in solution into the lamellar phase.[9]

The PEO used here is 10,000 Da, which is smaller then LPEI (750,000 Da) and higher than SPEI (2000 Da) and it has a linear polymer structure. PEO is known to have a strong interaction with SDS in solution. A variety of explanations have been given for the forces underlying the binding, such as hydrophobic interactions, electrostatic interactions, and ion-dipole interactions between the surfactant headgroup and polymer.[16-21] PEO is also found to interact with CTAB. CTAB micelles become absorbed onto the polymer chain due to hydrophobic interactions, causing the polymer chain configuration to change and ultimately forming a bead necklace structure in solution as more micelles are absorbed. Increase of the polymer concentration and decrease of the temperature lead to the decrease of CMC of the mixture of polymer and surfactant.[22] However, interfacial films do not form with PEO and either of the pure surfactants indicating that a careful balance between these interactions is required for film formation.

From the above analysis, it appears that polymers with strong interactions with at least one of the surfactants have a greater effect on the structures in the film. When the cat-anionic surfactant molar ratio was constant at 4, solutions with SPEI form an $Im\bar{3}m$ structure while solutions with PEO forms $Ia\bar{3}d$ structures with a smaller micellar curvature. In these solutions with an excess of CTAB, the CTAB and SDS form cat-anionic micelles with a positively charged headgroup protruding on the outside of the micelles, as shown in **Scheme 4.1**. Since PEI is a branched polymer, the steric bulk of the polymer might drive the headgroups to become bigger and so further apart if the polymer binds to the CTAB (or SDS), thus leading to a bigger micelle packing parameter and smaller curvature reflected in the phases observed in these films.

4.3 Silica Templated by Cat-anionic Surfactant/Polymer Films

Mixed surfactants have many advantages over a single surfactant, such as changing critical micelle temperature (CMT) and critical micelle concentration (CMC) values, adjusting the interaction with inorganic silicate species, tuning pore sizes, preparing

hierarchical pore structures, and causing phase transitions.

Usually, mixing solutions of compatible surfactants results in mixed micelles which are very important to control the micelle surface curvature.[23, 24] Tian found that addition of oligomeric non-ionic surfactants, such as Brij 35, into Pluronic surfactant P-123 strengthens the hydrophobic volume of the micelle core, which can result in the formation of highly ordered cubic mesostructures.[25] Mesoporous silica vesicles with hierarchical structure were developed using co-surfactant of SDS and P-103 in the presence of sodium fluoride, variation of particle size and cavity diameter can be achieved by adjusting the anionic and non-ionic surfactant molar ratio.[26]

Cat-anionic surfactant and polyelectrolytes were used in this work to fabricate silica films. Robust free-standing silica films were formed by mixing the cationic and anionic surfactants and polyelectrolyte solutions of either PEI or PAAm with the inorganic precursor TMOS as described in **Section § 2.3.3**. PEO was also used but as the structure formed are identical to those formed with PEI, thus they will not be discussed in detail here.

The film forming solution was poured into a dish to allow film formation. When the CTAB: SDS molar ratio was 2 or below, and the LPEI concentration was higher than 30 g/l or the SPEI concentration was between 10 g/l to 40 g/l, only precipitation was observed and no film formation occurred. At all other concentrations tested, films formed at the air/solution interface within a few minutes. As shown in **Figure 4.9**, these free-standing films were white and smooth, robust enough to be removed from the water interface on an open mesh, and became transparent when dry. The dry film thickness ranged from 0.058 mm to 0.336 mm (with an error of ± 0.005 mm), which will be describe in **Section § 4.3.7**.

Films remained continuous, without cracking even after calcination at 600°C for 6 hours, suggesting the cat-anionic surfactant/polymer template improved the film thickness and strength compared to silica films templated using surfactant alone, which are usually fragile and tend to fracture into powders after calcination.

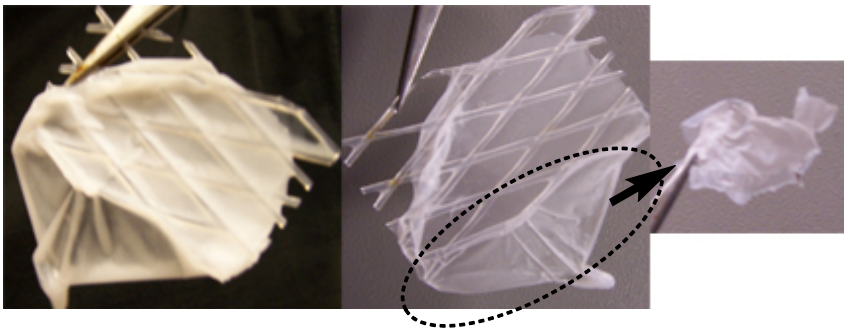

Figure 4.9 *Robust free standing cat-anionic surfactant/polyelectrolyte/silica films. The side of each cell in the mesh is 1 cm. (From left to right: wet film just after removal from the solution interface, dry film and calcined silica film)*

4.3.1 CTAB/SDS/SPEI/silica films

4.3.1.1 Interfacial Film Formation Process

In order to study the film formation process, time-resolved neutron reflectivity data were first collected on SURF (15 minute resolution) and later some samples were investigated again using INTER (1.5 minute resolution) to obtain data with better resolution in shorter time. Neutron reflectivity measurements on INTER and SURF on films prepared with a CTAB: SDS molar ratio of 4 with 30 g/l SPEI (**Figure 4.10 A & B**), or with a CTAB: SDS molar ratio of 8 and 40 g/l SPEI (**Figure 4.10 C & D**) are shown below, the peak position readings have an error about ± 0.01 $Å^{-1}$.

For films prepared with a CTAB: SDS molar ratio of 4 with 30 g/l SPEI, two sharp diffraction peaks at 0.09 $Å^{-1}$and 0.18 $Å^{-1}$ appeared within the first four minutes, and these two peaks become less intense, and another diffraction peak around 0.12 $Å^{-1}$ grew up with time (**Figure 4.10 A**). However, these three peaks are difficult to index as a purely cubic structure. Neutron data of this film formation process were also followed on SURF (**Figure 4.10 B**), however, the peaks at 0.09 $Å^{-1}$and 0.18 $Å^{-1}$ were not observed. Only a peak around 0.12 $Å^{-1}$ appears in the first 15min scan and it does not change within three hours. These peak assignments and film structure will be discussed below in **Section § 4.3.8.1**

For films prepared with a CTAB: SDS molar ratio of 8 with 40 g/l SPEI, neutron reflectivity data collected on SURF (**Figure 4.10 D**) shows one peak at Q = 0.13 $Å^{-1}$

appearing in the first scan which also does not seem to change with time. The final pattern at 207 min was collected for a longer time to obtain better signal to noise ratio, and two small peaks at Q = 0.13 $Å^{-1}$ and 0.17 $Å^{-1}$ are visible. Neutron data were also collected on INTER (**Figure 4.10 C**). One sharp peak at Q = 0.13 $Å^{-1}$ was apparent in the first scan, and this peak intensity decreased with time while a second sharp peak at Q = 0.16 $Å^{-1}$ appeared at about one hour. These two peaks may be indexed as two reflections (110), (111) of a primitive cubic $Pn\bar{3}m$ mesophase with d-spacing of 68Å. However, both diffraction peaks became broad and the second peak position moved gradually to 0.18 $Å^{-1}$ in the last measurement (at about 90 minute), which is similar to what was observed on SURF. In this case, these two peaks can be related as (110) (200) reflections of a primitive cubic or body-centered cubic $Im\bar{3}m$ phase. INTER data indicates the mesophase transformation between two different cubic mesophase occurs upon continuous evaporation and film drying with time. Water is thought to have distinct effects that combine to favor a highly curved mesophase.[27] The presence of water at the micelle interface promotes intercalation of water between the headgroups, pushing them apart by steric hindrance, which results in higher effective headgroup area, decreasing the packing parameter and increasing micellar curvature. Here losing water around micellar headgroup inside the interfacial film leads to smaller effective headgroup areas and a decrease in micellar curvature, resulting in the mesophase transformation. This observation confirms the dramastic role of the water content on the final interfacial film mesophase.

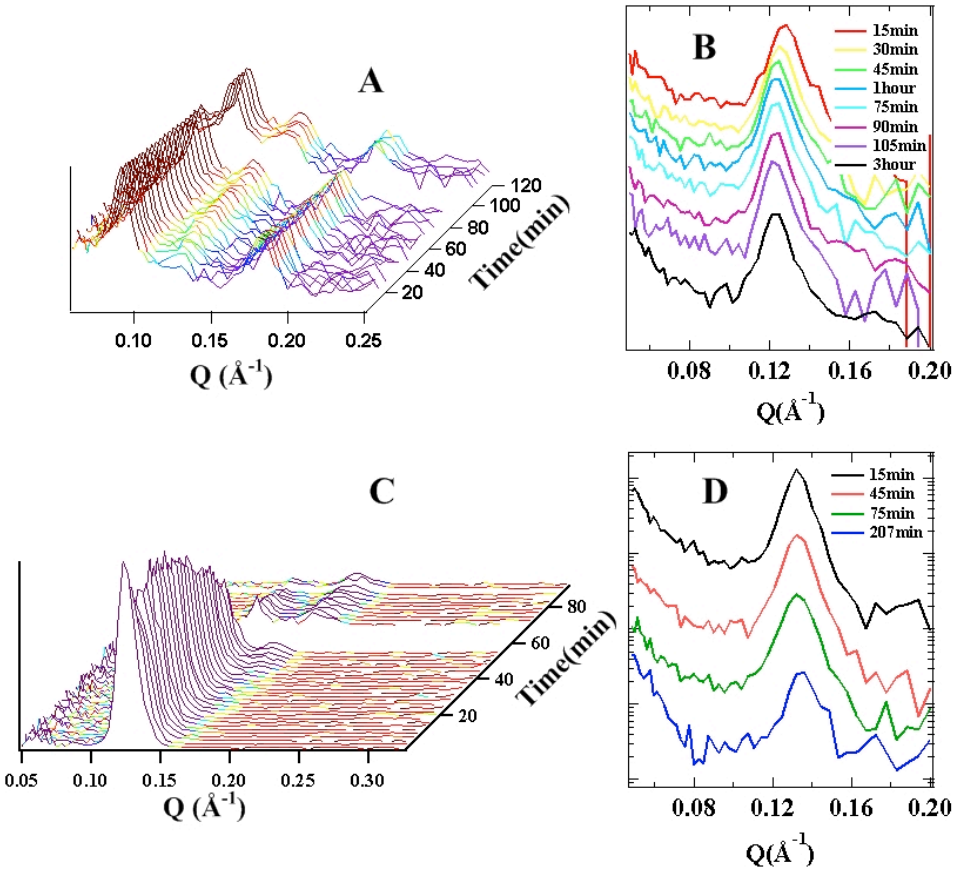

Figure 4.10 *Neutron reflectivity patterns of silica films grown at the air/water interface synthesized with CTAB/SDS/SPEI complexes collected on INTER and SURF instruments. (A and B) CTAB: SDS = 4 30 g/l SPEI and (C and D) CTAB: SDS = 8 40 g/l SPEI.*

4.3.1.2 Interfacial Film Structures

The formation of surfactant/polyelectrolyte/silica films depends on the interaction between inorganic and organic species, as well as the effect of water, discussed above; phase transitions can be achieved by the variation of cationic and anionic surfactant molar ratios and the polyelectrolyte concentration.

When films were prepared with a CTAB: SDS molar ratio of 8 and 20 g/l SPEI (**Figure 4.11 A and Da**), the GIXD patterns showed well resolved peaks at Q_{xy} = 0.14 $Å^{-1}$, 0.24 $Å^{-1}$, 0.28 $Å^{-1}$ which can be indexed as reflections (100), (110), (200), corresponding to a 2D hexagonal structure with unit cell dimension of 52 Å. This is

smaller than that observed for PEI/CTAB templated silica films at similar polymer and surfactant concentration (60 Å).[1] This difference may be due to the small amount of SDS reducing the charge on the cat-anionic micelles allowing closer packing of the cylindrical micelles in the cat-anionic surfactant templated films, as well as the shorter average tail length in the CTAB/SDS mixture reducing the micelle diameter.

When films were prepared at either high relative CTAB: SDS molar ratio of 4 or 10 g/l SPEI (**Figure 4.11 B and Db**), a bicontinuous cubic structure $Pn\bar{3}m$ was the dominant phase formed in the films. The GIXD pattern shows four distinct peaks at Q_{xy} = 0.14 Å^{-1}, 0.17 Å^{-1}, 0.20 Å^{-1}, 0.24 Å^{-1}, which are indexed as the (110), (111), (200), (211) reflections, respectively. The first order indicates a unit cell of 63Å, which does not change with concentration.

However, when the SPEI concentration is increased to more then 25 g/l (**Figure 4.11 C and Dc**), the GIXD pattern of the film showed seven strong reflections at 0.12 Å^{-1}, 0.14 Å^{-1}, 0.17 Å^{-1}, 0.20 Å^{-1}, 0.24 Å^{-1},0.34 Å^{-1}, 0.51 Å^{-1}, which can be described as a $Fm\bar{3}m$ cubic phase (reflections 0.12 Å^{-1} (111), 0.14 Å^{-1} (200), 0.20 Å^{-1} (220), 0.24 Å^{-1} (311)) with a unit cell dimension of 91 Å, combined with a lamellar phase (0.17 Å^{-1} (001), 0.34 Å^{-1} (002), 0.51 Å^{-1} (003)), having a unit cell dimension of 37 Å. This lamellar mesophase was previously reported as occurring at the surface of cat-anionic surfactant only solutions at a molar ratio of CTAB: SDS = 6: 4 with no polymer.[9, 10] An equivalent lamellar phase was also observed in the time-resolved synchrotron SAXS data of a mixed surfactant solution for molar ratio CTAB: SDS = 4, which will be discussed in the section on the subphase solution **Section § 4.3.1.3** below. This suggests that as well as regions of the film where polymer, the co-surfactants and silica all participate in formation of the composite phase, other regions of the film contain only the co-polymer mixture, perhaps due to incorporation of CTAB/SDS precipitate particles into the film. Since the d-spacing is identical to that observed for solutions of only the two surfactants (with no polymer or silica added) the CTAB/SDS particles giving this signal must not contain either polymer or

surfactant intercalated into the lamellae as this would be expected to increase the d-spacing of the lamellar phase.

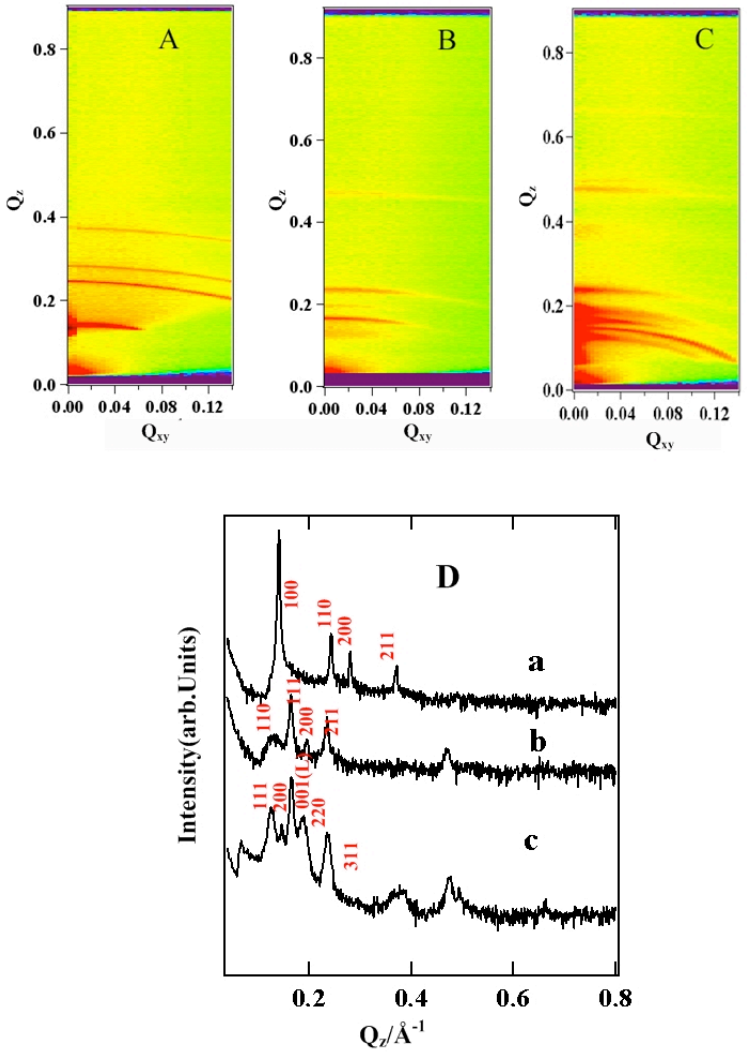

Figure 4.11 *GIXD patterns and line profiles at Q_{xy} = 0.007Å^{-1} from GIXD patterns collected from interfacial cat-anionic surfactant/SPEI/silica films in situ at the solution interface, showing typical mesophases. (A: CTAB: SDS = 8 20 g/l SPEI, B: CTAB: SDS = 4 10 g/l SPEI, C: CTAB: SDS = 4 40 g/l SPEI)*

Table 4.1 *Summary of structure assignments and unit cell parameters from GIXD patterns for cat-anionic surfactant/SPEI/silica films with typical mesophases measured in situ at the solution interface.*

CTAB: SDS molar ratio	Polyelectrolyte (g/l)	First peak Q_z (Å^{-1})	peak assignment	Phase assigned	Unit cell dimension (Å)
8	20	0.14	(100)	$p6mm$	52
4	10	0.14	(110)	$Pn\bar{3}m$	63
4	40	0.12	(111)	$Fm\bar{3}m$ & L	91 & L1(37)

The error in unit cell dimension is ±1Å

4.3.1.3 Investigation of the Subphase Solution by Time-resolved SAXS

Fast time-resolved SAXS at Diamond was used to investigate the evolution of micelles in the subphase solution of CTAB/PEI/silica films in the previous chapter (**Section 3.3.4**). It is believed that phase separation occurs at the solution surface partially driven by evaporation but also due to the hydrophobicity of the polymer/surfactant complex causing formation of a more concentrated layer which is similar to a coacervated liquid particle formed in the subphase. This layer is enriched in surfactant, polymer and inorganic precursor compared to the subphase solution, and becomes more concentrated due to drying, so the mesophase ordering transformation in the film is slower due to its viscous nature.

Cat-anionic surfactant/polyelectrolyte/silica film forming solutions were therefore also studied by time-resolved SAXS to probe the mechanism of formation for these solutions. The experiments were conducted in several steps. First the mixed surfactant solution was circulated for 4 min, then polyelectrolyte solution was added and solution was kept circulating for another 10 min. The silicate precursor TMOS then was introduced and the data was collected for 10 min (30 frames at 20 s per frame); finally, the collection time for each frame was changed to 100s and another 10 frames of data were collected before it was stopped.

Figure 4.12 shows the time-resolved SAXS patterns for a film forming solution with CTAB: SDS = 8 30 g/l SPEI. Precipitation was observed immediately after the mixing of the two surfactants, due to the formation of macroscopic size surfactant aggregates. The SAXS pattern of the mixed surfactant solution with different CTAB: SDS molar ratios is shown in **Figure 4.12 A**. It has one strong diffraction peak at 0.17 $Å^{-1}$, and the molar ratio has little effect on the mesophase of the mixed surfactant particles because the peak position does not change as this is varied. The d-spacing calculated from the peak position is around 37 Å, which is similar to the d-spacing observed at the surface of mixed surfactant solutions, suggesting that CTAB/SDS solution is forming solid crystalline particles, which in some cases can then be incorporated into the films (see **Table 4.1** above).[9, 10] SPEI was then introduced into the solution and the time-resolved SAXS pattern did not change (**Figure 4.12 B**). Silicate precursor TMOS was added at the third frame. Two sharp peaks at 0.14 $Å^{-1}$ and 0.17 $Å^{-1}$ then appear at the sixth frame (**Figure 4.12 C**), which may be related to the (110), (111) reflections of a $Pn\bar{3}m$ primitive cubic mesostructure with a unit cell of 63 Å or the (111), (200) reflections of a $Fm\bar{3}m$ face-centered cubic mesostructure with a unit cell of 78 Å, it may also related to the (211), (220) reflection of a $Ia\bar{3}d$ body-centered cubic mesophase with a unit cell of 109 Å. In other words, CTAB/SDS/SPEI/TMOS liquid crystalline particles with cubic mesostructures were formed 40 second after the introduction of the silicate precursor, however with only two peaks visible it is impossible to unambiguously assign this to a specific cubic phase. All of these phases are however cubic phases formed by the twisting of lamellar sheets, so could be formed through perturbation of the initial lamellar phase CTAB/SDS particles as SPEI and TMOS infiltrate into the particles.

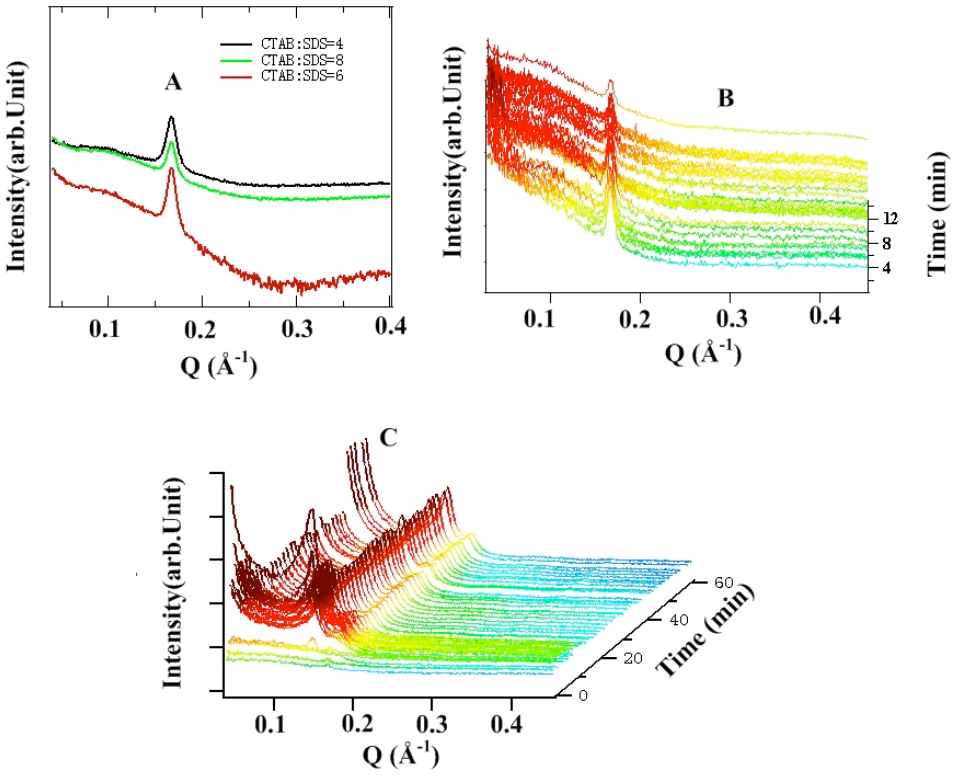

Figure 4.12 *Time-resolved SAXS pattern of silica film forming solutions CTAB: SDS = 8 30 g/l SPEI TMOS. (A) CTAB and SDS mixed surfactant solution. (B) CTAB/SDS/SPEI mixed solution (C) CTAB/SDS/SPEI/TMOS mixed solution; TMOS was added at the third frame (1minute after circulation began).*

Another film forming solution with CTAB: SDS = 4, 30 g/l SPEI was also studied by time-resolved SAXS (**Figure 4.13**). Variations of the CTAB: SDS molar ratio alters the final mesostructure of the liquid crystal particles. Before TMOS was introduced, the time-resolved SAXS patterns are similar to those observed for CTAB: SDS = 8, 30 g/l SPEI solution (**Figure 4.12 B**) showing the surfactant lamellar phase. TMOS was also introduced at the third frame, and three distinct peaks at 0.12 $Å^{-1}$, 0.14 $Å^{-1}$ and 0.16 $Å^{-1}$ appeared about 13 minutes after the addition of silicate species, corresponding to the (110), (111), (200) reflections of a $Pn\bar{3}m$ cubic phase with a unit cell of 74 Å. The retardation of mesostructure formation is probably due to higher viscosity of the solution induced by the addition of SDS.

Comparing these final mesostructures with two different CTAB: SDS molar ratios, more SDS present within the cat-anionic surfactant micelle neutralises the CTAB headgroup charge and allows the surfactant headgroups to sit closer together, resulting in smaller effective headgroup, and thus a bigger surfactant packing parameter and mesophase with a smaller micellar curvature. In the case of the subphase solution composed of CTAB: SDS =8 30 g/l LPEI, the face-centered cubic phase of $Fm\bar{3}m$ is therefore more likely to be correct. Otherwise, if the liquid particle micellar phase did not change and both solutions had a $Pn\bar{3}m$ cubic structure neutralizing the CTAB charge by increasing the SDS concentration should reduce the charge of the cat-anionic surfactant micelles, leading to a closer packing, thus the d-spacing should be smaller rather than bigger, which is opposite to the observed experiment results.

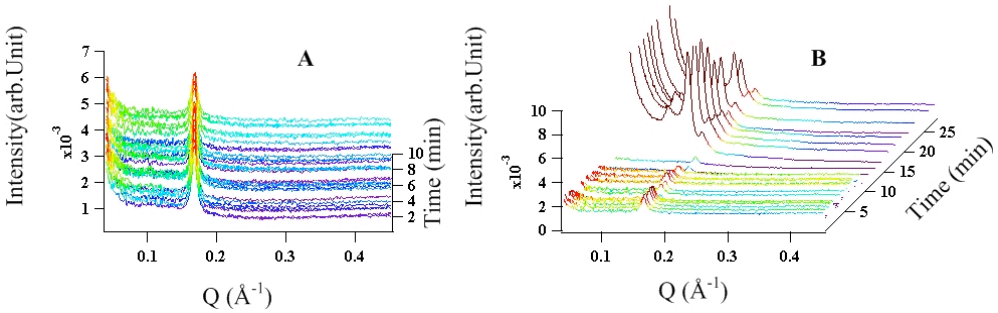

Figure 4.13 *Time-resolved SAXS patterns for silica film forming solutions (CTAB: SDS = 4 30 g/l SPEI TMOS). (A) CTAB/SDS/SPEI mixed solution (B) CTAB/SDS/SPEI/TMOS mixed solution. TMOS was added at the third frame (one minute after circulation began)*

4.3.1.4 Dry CTAB/SDS/SPEI/Silica Films

The cat-anionic surfactant/polyelectrolyte templated silica films are sufficiently robust to be removed from the air/water interface to form free-standing films. SAXS patterns of CTAB/SDS/SPEI/silica films showing typical mesophases are given in **Figure 4.14** (structure assignment and unit cell dimensions are in **Table 4.2**). Most of the as-synthesized film mesostructures were retained after drying, although the unit

cell dimension became smaller due to the removal of the water causing compaction of the unit cell. At the CTAB: SDS = 16 surfactant molar ratio, four peaks appear at 0.15 $Å^{-1}$, 0.24 $Å^{-1}$, 0.26 $Å^{-1}$, 0.30 $Å^{-1}$ which are exactly the same peak positions observed for CTAB/SPEI/silica films,[1] suggesting that the SDS in this film does not significantly perturb the structure away from the 2D hexagonally close-packed cylindrical phase found in the CTAB/SPEI/silica films. When more SDS is present and the CTAB: SDS molar ratio decreases to 8, a 2D hexagonal mesostructure is retained for most of these films, although the mesostructure is difficult to assign for film synthesized with high concentration of SPEI since only one diffraction peak at 0.15 $Å^{-1}$ could be clearly observed. When the surfactant molar ratio decreases to 4, the films mesostructures are dominated by a cubic phase. For dry films synthesized with the cat-anionic surfactants at a molar ratio of 4 and 20 g/l LPEI, taking the two peaks at 0.12 $Å^{-1}$ and 0.15 $Å^{-1}$ into account, the SAXS pattern appears to belong to a $Pn\bar{3}m$ structure with a unit cell of 72 Å. However for a film synthesized with a higher SPEI concentration of 30 g/l, three peaks at 0.15 $Å^{-1}$, 0.17 $Å^{-1}$, 0.24 $Å^{-1}$ can be indexed as the (111), (200), (220) reflections of a $Fm\bar{3}m$ phase with a unit cell of 72 Å. Increasing the SPEI concentration leads to the film mesophase transformation from $Pn\bar{3}m$ to the higher curvature phase $Fm\bar{3}m$ as also observed in the subphase solutions discussed in the previous section.

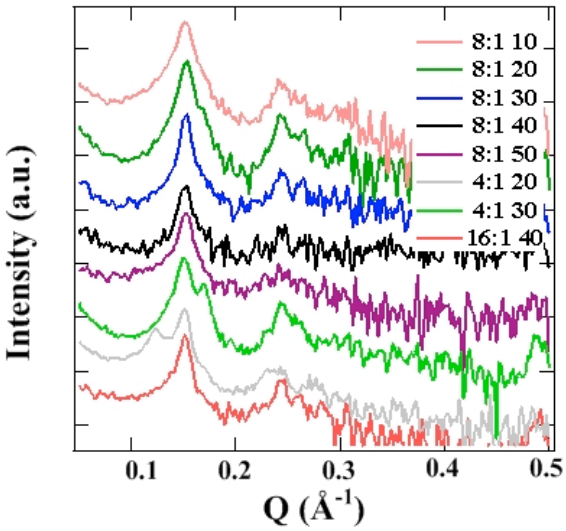

Figure 4.14 *SAXS pattern of dry silica films synthesized with CTAB/SDS/SPEI. The legend states the molar ratio of CTAB: SDS followed by the concentration of SPEI (g/l).*

Table 4.2 *Structure assignments and unit cell parameters from SAXS patterns for dry cat-anionic surfactant/SPEI/silica films with typical mesophases.*

CTAB: SDS molar ratio	Polyelectrolyte (g/l)	First peak Q (Å-1)	Peak assignment	Phase assigned	Unit cell dimension (Å)
16	40	0.15	(100)	*p6mm*	48
8	10-30	0.15	(100)	*p6mm*	48
8	40	0.15	-	-	7
4	20	0.12	(110)	$Pn\bar{3}m$	72
4	40	0.15	(111)	$Fm\bar{3}m$	72

– means the structure is impossible to identify since peak positions higher than 0.2 $Å^{-1}$ are not distinct. Error for the peak position is ± 0.01 Å and for the unit cell dimension is ±1 Å.

4.3.2 CTAB/SDS/LPEI/silica films

4.3.2.1 Interfacial Film Formation Process

Silica films templated by CTAB/SDS/LPEI take a much shorter time to grow on the interface than those prepared with CTAB/SDS/SPEI, especially for films

synthesized with high CTAB: SDS molar ratio or LPEI concentration. For some cases with 30 g/l or 40 g/l LPEI, no diffraction peaks could be observed as these films exhibited macroscopic roughening of the surface when the films were grown in the Teflon troughs.

Fast time-resolved neutron reflectivity data with 1.5 minute resolution was collected for films prepared with CTAB: SDS molar ratio 4:1 with 10 g/l LPEI (**Figure 4.15**) on INTER. For films prepared with LPEI, no obvious peaks were observed at the beginning, but peaks started to appear at Q = 0.13 $Å^{-1}$ after about 42 min and continued to grow in intensity, up to the last measurement (at 120 min). It means the film mesostructure appears around 42 min and continues to develop to be more ordered as the film matures. From this data, showing only one peak, the exact structure cannot be determined.

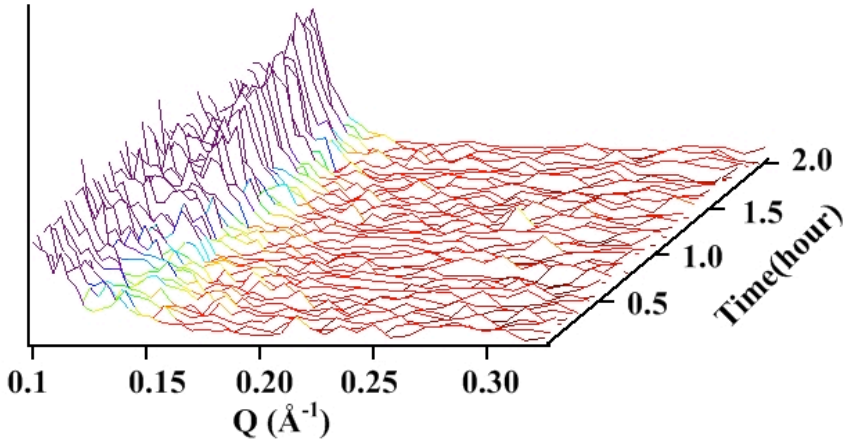

Figure 4.15 *Neutron reflectivity patterns of silica films grown at the air/water interface synthesized with CTAB/SDS/LPEI complex, CTAB: SDS = 4 10 g/l LPEI.*

4.3.2.2 Interfacial Films Structure

Figure 4.16 A and B shows grazing incidence X-ray diffraction (GIXD) patterns collected on air/water interfacial films for typical mesophases, found in silica films

synthesized with CTAB/SDS mixtures and LPEI. All these patterns showed strong diffraction rings spanning of the entire Q_{xy} range measured. For comparison, a line profile of the data along Q_{xy} = 0.007 Å^{-1} is shown in **Figure 4.16**, Structure assignments and unit cell dimensions for all the line profiles are given **Table 4.3**.

For films synthesized with a cat-anionic molar ratio of 4 and 10 g/l LPEI, a $Pn\bar{3}m$ phase was also typically obtained (**Figure 4.16 A and Ca**), with a unit cell dimension similar to that of films synthesized with low SPEI concentration at a similar molar ratio of CTAB: SDS. When the cat-anionic surfactant molar ratio is as low as 2 and LPEI concentration is 20 g/l (**Figure 4.16 B and Cb**), three distinct peaks at 0.17 Å^{-1}, 0.24 Å^{-1}, 0.33 Å^{-1} were observed. These three peaks were assigned to the (110), (200), (220) reflections of an $Im\bar{3}m$ phase with a unit cell dimension of 52 Å. One diffraction reflection (211) of this mesostructure is missing; it is probably due to different drying in the vertical direction compared to the in-plane direction.[28]

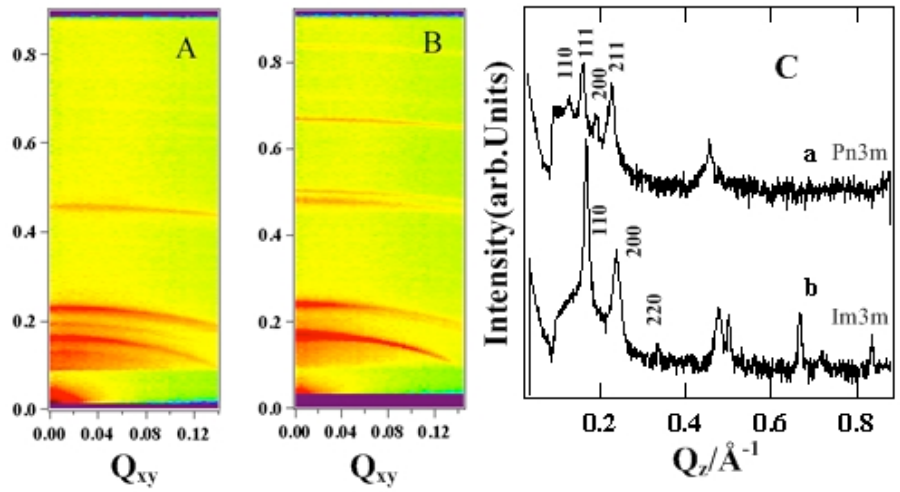

Figure 4.16 *GIXD patterns and corresponding line profiles at Q_{xy} = 0.007Å^{-1} collected from cat-anionic surfactant/LPEI/silica films in situ at the solution interface, showing typical mesophases. (A and C a: CTAB: SDS = 4 10 g/l LPEI, B and C b: CTAB: SDS = 2 20 g/l LPEI)*

Table 4.3 *Structure assignments and unit cell parameters from GIXD patterns for interfacial cat-anionic surfactant/LPEI/silica films with typical mesophases.*

CTAB: SDS molar ratio	Polyelectrolyte (g/l)	First peak Q (Å^{-1})	Peak assignment	Phase assigned	Unit cell dimension (Å)
4	10	0.14	(110)	$Pn\bar{3}m$	63
2	20	0.17	(001)	$Im\bar{3}m$	52

Error for the peak position is ± 0.01 Å and for the unit cell dimension is ± 1 Å.

4.3.2.3 Investigation of the Subphase Solution by Time-resolved SAXS

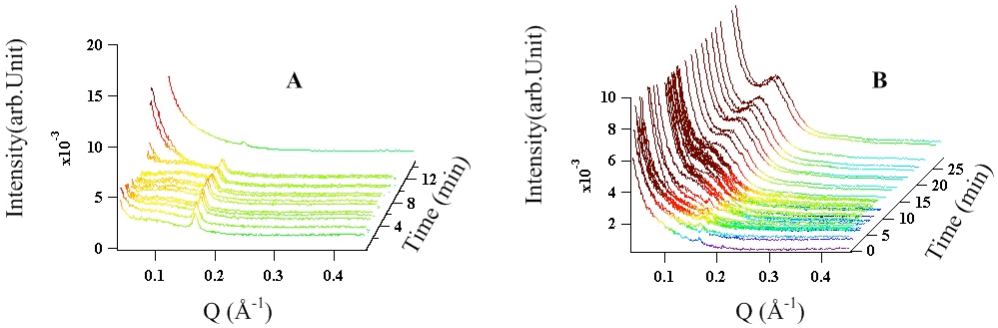

Figure 4.17 *Time-resolved SAXS pattern of silica film forming solutions (CTAB: SDS = 8 30 g/l LPEI TMOS) (A) CTAB/SDS/LPEI mixed solution (B) CTAB/SDS/LPEI/TMOS mixed solution. TMOS was added at the third frame (one minute after circulation began)*

For most concentrations of the CTAB/SDS/LPEI silica film forming solutions, the solution was too viscous to be circulated so it was impossible to conduct a time-resolved experiment. Time-resolved SAXS patterns of one silica film forming solutions with cat-anionic surfactant and LPEI which was sufficiently fluid to measure (CTAB: SDS = 8 30 g/l LPEI TMOS) are shown in **Figure 4.17**. Similarly to the time-resolved SAXS patterns of CTAB/SDS with SPEI, the CTAB/SDS solution formed solid crystalline particles immediately after the two solutions were mixed (**Figure 4.17 A**). After about 12 min, the increasing intensity in the low Q range

(before Q = 0.1 $Å^{-1}$) indicates the formation of a larger-scale structure, probably formation of disordered silica/surfactant/polymer particles that are too big to resolve in the Q range used. A bump appears at 0.14 $Å^{-1}$ around 10 minutes after adding TMOS (**Figure 4.17 B**). This bump grew in intensity with time, indicating a less organized mesophase forms in the solution probably within silica/surfactant/polymer particles. In this case, the appearance of the peak in the subphase scattering occurs later than mesostructure formation measured for the CTAB/SDS/SPEI subphase solution (**Figure 4.12**). LPEI are more branched and high molecular weight, thus the polyelectrolyte/silica network is too rigid around the micelles and makes their re-arrangement more difficult and more time consuming. However, this appearance of the diffraction peak is still earlier than the peak appearance shown in the interfacial film (**Figure 4.15**), probably because of the more rigid network in the film induced by evaporation, which leads to less water present than in the liquid crystalline particles in the subphase solution.

4.3.2.4 Dry CTAB/SDS/LPEI/Silica Films

SAXS patterns of dried CTAB/SDS/LPEI/silica films synthesized with CTAB: SDS molar ratios ranging from 8 to 1 and LPEI concentrations from 10 g/l to 40 g/l are shown in **Figure 4.18** (structure assignment and unit cell dimensions are in **Table 4.4**). Most of the as-synthesized film mesostructures were retained after drying, and the unit cell dimension became smaller due to the removal of the water causing compaction of the unit cell.

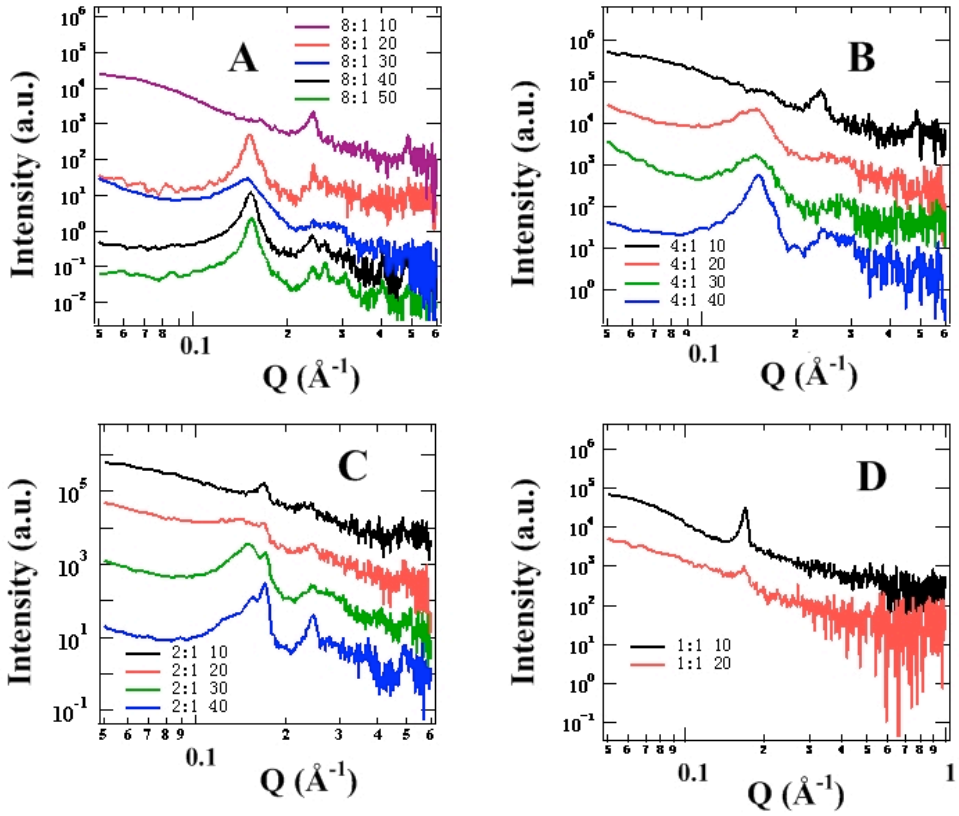

Figure 4.18 *LPEI concentration effects on dry silica film synthesized with CTAB/SDS/LPEI. LPEI concentrations were between 10 g/l and 40 g/l and CTAB: SDS molar ratio was varied between 8 and 2 separately.*

When the CTAB: SDS molar ratio is 8 (**Figure 4.18 A**), and the LPEI concentration is varied from 10 g/l to 50 g/l, the first peak at 0.24 $Å^{-1}$ shifts to a higher Q value of 0.15 $Å^{-1}$, which suggests more PEI was absorbed around the micelles leading to a bigger d-spacing. The peak position of 0.15 $Å^{-1}$ is similar to the peak position in dry silica films synthesized with CTAB/PEI complexes. The ordering was observed to improve for increased LPEI concentrations. When LPEI concentration increases over 40 g/l, four distinct peaks at 0.15 $Å^{-1}$, 0.24 $Å^{-1}$, 0.26 $Å^{-1}$, 0.30 $Å^{-1}$ could be observed. The peak at 0.24 $Å^{-1}$ is from excess crystalline CTAB which is assumed to be formed on the film surface where droplets of the subphase have dried, the other three peaks are indexed as an ordered 2D hexagonal structure. The results suggest that

the amount of SDS in this film does not significantly perturb the structure away from 2D hexagonally close-packed cylindrical phase found in those membranes.

Table 4.4 *Peak position and d-spacings taken from the SAXS patterns of the dry films synthesized with CTAB/SDS/ LPEI.*

Surfactant molar ratio	**LPEI (g/l)**	**Q[a] (Å^{-1})**				**d-spacing[a] (Å)**	**mesophase**
8:1	10	0.24	—	—	—	26	Disordered
8:1	20	0.15	0.24	—	—	41	Disordered
8:1	30	0.15	0.24	—	—	41	Disordered
8:1	40	0.15	0.24	0.26	—	41	$p6mm$
8:1	50	0.15	0.24	0.26	0.30	41	$p6mm$
4:1	10	0.24	—	—	—	26	Disordered
4:1	20	0.15	—	—	—	41	Disordered
4:1	30	0.15	—	—	—	41	Disordered
4:1	40	0.15	0.24	—	—	41	Disordered
2:1	10	0.17	0.24	—	—	37	Distorted $Im\bar{3}m$
2:1	20	0.14	0.17	0.25	—	43	Distorted $Im\bar{3}m$
2:1	30	0.13	0.15	0.17	0.248	50	$Pn\bar{3}m$
2:1	40	0.13	0.15	0.17	0.247	50	$Pn\bar{3}m$
1:1	10	0.17	—	—	—	37	Lamellar
1:1	20	0.17	—	—	—	37	Lamellar

a – error in the Q values is ±0.01 Å^{-1}, error in the d-spacing is ± 1 Å.

When the CTAB: SDS molar ratio is equal to 4:1 (**Figure 4.18 B**), the same peak shift was seen with an increase of the LPEI concentration. However, the first peak is

broader indicating either the structure is not as ordered as that of films synthesized with a CTAB: SDS molar ratio of 8 or that the mesophase is on the boundary of this phase region and was transforming to another structure when drying froze the transition.

When the CTAB: SDS molar ratio was equal to 2 (**Figure 4.18 C**), the peak intensity increases with increasing LPEI concentration indicating again that the increase of the LPEI concentration improves the mesostructure ordering. When the LPEI concentration is as low as 10 g/l, small peaks at 0.17 $Å^{-1}$ and 0.24 $Å^{-1}$ might relate to a distorted body-centered cubic mesophase. When the LPEI concentration is 30 g/l, three low angle Bragg peaks at 0.13 $Å^{-1}$, 0.16 $Å^{-1}$, 0.18 $Å^{-1}$ indexed as the (110), (111), (200), reflections corresponding to an ordered $Pn\bar{3}m$ cubic space group, with a unit cell around 68 Å. Further increase of the LPEI concentration to 40 g/l results in a more highly ordered cubic structure. However, the intensity of the peak at 0.16 $Å^{-1}$ decreases while the intensity of peak at 0.17 $Å^{-1}$ increases. The changing of the peak intensities probably also relates to the thickness variation of the surfactant bilayers in Garstecki and Holyst model discussed previously,[12] although in this case, the polymer/silica network is also expected to intercalate between the surfactant micelle headgroups further altering the density profile of the surfactant bilayer membrane.

When the CTAB: SDS molar ratio was equal to 1 (**Figure 4.18 D**), if the LPEI concentration was higher than 20 g/l, the solution precipitated and no film could be removed from the solution surface. However, if the LPEI concentration was lower than 20 g/l, one sharp peak at 0.17 $Å^{-1}$ can be seen in the SAXS pattern. The peak position is similar to the first peak position in the SAXS pattern of the film forming subphase solution, suggesting that the peak is related to the solid crystalline CTAB/SDS surfactant particles in the subphase solution (**Figure 4.13 and Figure 4.17**).

An increase of the SDS concentration for constant polymer concentration also induced a phase transformation, for example, when LPEI concentration was fixed at

40 g/l, and the CTAB: SDS molar ratio varied from 8 to 1, the film structure changes from 2D hexagonal to cubic, which is a similar trend to that observed for the CTAB/SDS/SPEI/silica films.

Based on all the above experiment results, phase diagrams for the CTAB/SDS with SPEI or LPEI film forming systems can be broadly sketched, as shown as below (**Figure 4.19**). The interactions responsible for the phase transitions observed are discussed in **Section § 4.3.9** below.

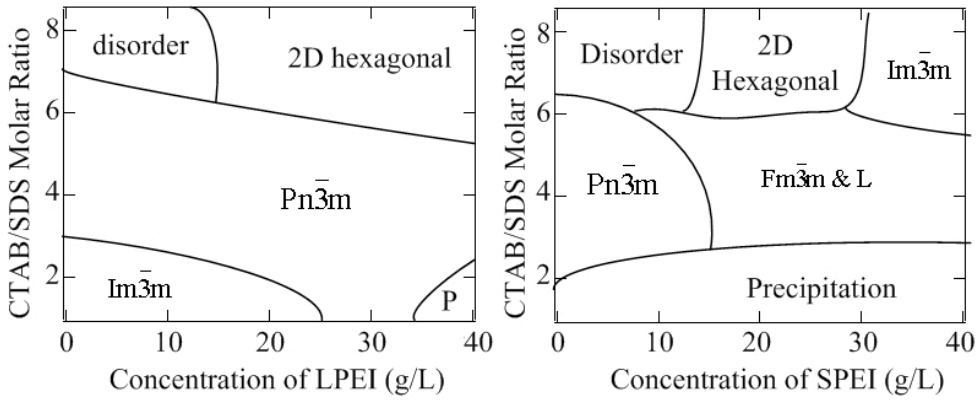

Figure 4.19 *Phase diagram of interfacial cat-anionic surfactant/polyelectrolyte/silica films (From left to right: LPEI, SPEI).*

4.3.3 CTAB/SDS/PAAm/Silica films

Thick films was also formed when PAAm was used as the polymer component. Slower time-resolved neutron reflectivity patterns with 15 minute resolution were collected for films formed with CTAB: SDS molar ratio 2 and 30 g/l PAAm (**Figure 4.20**) on SURF. For films prepared with PAAm, diffraction peaks were not visible in the first 30min, but had started to appear at Q = 0.08 $Å^{-1}$ in the 45 min scan. Two diffraction peaks at 0.08 $Å^{-1}$ and 0.16 $Å^{-1}$ were observed at about 1 hour and continued to grow in intensity with time. These two peaks indicate a lamellar mesophase with a d-spacing of 78 Å suggesting that in this case the polymer and silica are intercalated between the CTAB/SDS bilayers unlike the 37 Å lamellar phase observed in the PEI films where the d-spacing was equivalent to that found in precipitates containing only the two surfactants.

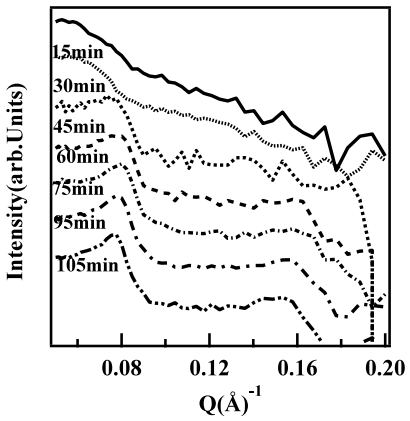

Figure 4.20 *Time-resolved neutron reflectivity data with 15 minute time resolution collected for films formed with CTAB: SDS molar ratio 2:1, 30 g/l PAAm on SURF.*

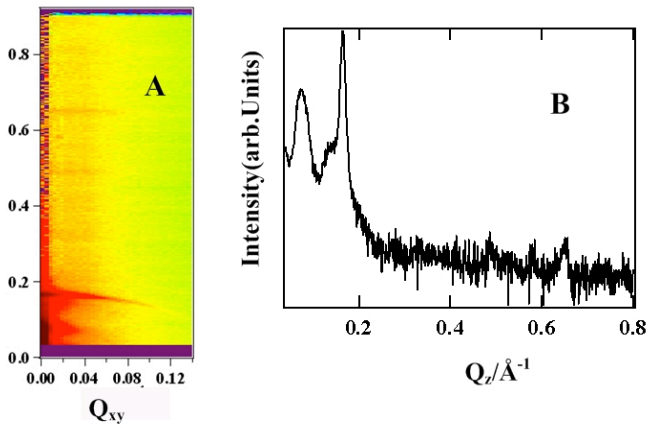

Figure 4.21 *GIXD patterns and corresponding line profiles at Qxy = 0.007Å^{-1} collected from cat-anionic surfactant/PAAm/silica films in situ at the solution interface (A, B: CTAB: SDS = 2 30 g/l PAAm), showing the typical lamellar mesophases.*

A typical GIXD pattern of the interfacial cat-anionic surfactant/PAAm/silica films (A: CTAB: SDS = 2 30 g/l PAAm) is shown in **Figure 4.21**. A sharp peak at 0.17 Å^{-1} may relate to the solid crystalline CTAB/SDS particles which are included inside the film as observed previously at the surface of CTAB/SDS surfactant solutions and in

the CTAB/SDS/PEI films. Apart from that sharp peak, two broad peaks at 0.08 $Å^{-1}$ and 0.16 $Å^{-1}$ were observed at all CTAB: SDS molar ratios, suggesting a lamellar phase with a unit cell dimension of 78 Å, which corresponds well with the neutron reflectivity data above.

The SAXS pattern of the subphase solution of a mixture of CTAB/SDS and PAAm solution indicates there is no long range ordering in the particles in the subphase solution as no peaks were observed, only an increase in intensity at the lowest angles due to particle formation and a broad bump which developed with time. Self-assembly into the lamellar phase in this system therefore only occurs in the films at the interface.

SAXS patterns of the dry CTAB/SDS/PAAm films indicate that the lamellar film mesostructure is partially retained **(Figure 4.23)**. One broad peak around 0.1 $Å^{-1}$ was observed indicating a less ordered mesostructure with a repeat unit of 63 Å. CTAB: SDS molar ratio and different PAAm concentrations had no big effect on structure or d-spacing in these films.

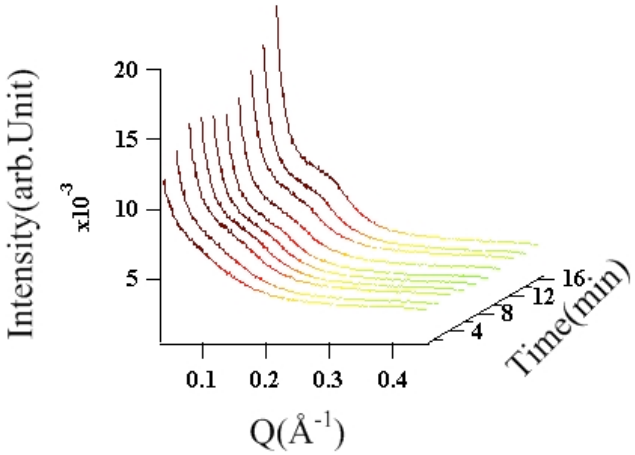

Figure 4.22 *Time-resolved SAXS pattern of silica film formation solution (CTAB: SDS = 8 25 g/l PAAm TMOS).*

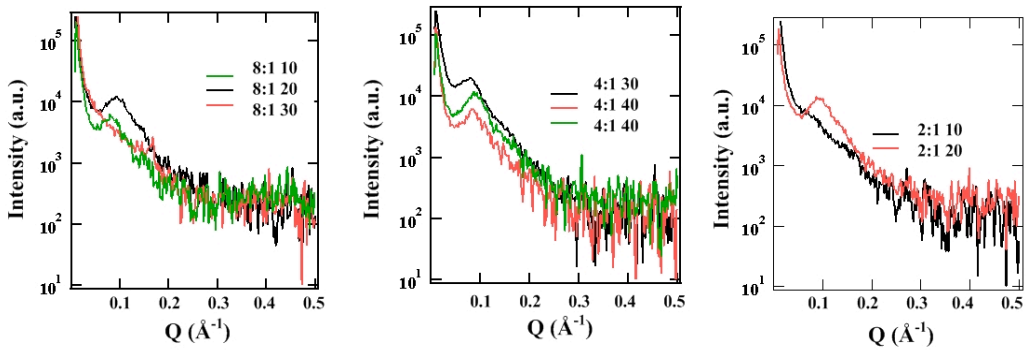

Figure 4.23 *SAXS pattern of dry silica films synthesized with CTAB/SDS/PAAm.*

4.3.4 Thermogravimetric Analysis

Some examples of TGA patterns from the silicate films synthesized with cat-anionic surfactant and polyelectrolyte are given in **Figure 4.24.** For silica films prepared with CTAB/SDS/LPEI complexes, the TGA patterns (**Figure24 A**) indicate a decomposition process consisting of three degradation weight-loss steps. The first drop is about 20wt% (up to 100 °C) due to water loss. The next step, 60wt% weight loss (at range of 100 °C - 350 °C), is the polymer and surfactant degradation by combustion. Weight loss between 350 °C - 600 °C is due to the further condensation of silicate.[29] From these measurements the as-synthesised films have a composition of about 20% silica.

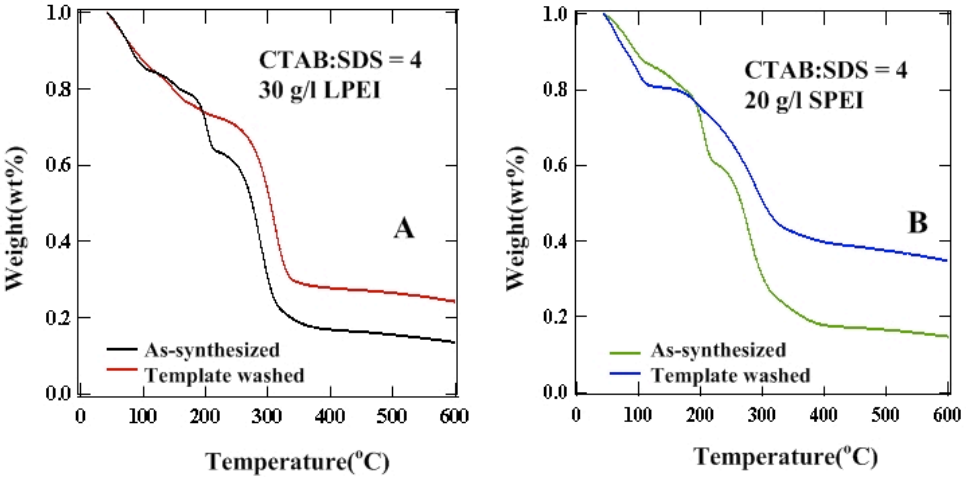

Figure 4.24 *Weight change curve for silica films synthesized with (A) CTAB: SDS = 4 30 g/l LPEI, (B) CTAB: SDS = 4 20 g/l SPEI.*

TGA data collected on the same LPEI sample after the surfactant part of the template was removed by washing with ethanol, shows a much smaller weight loss between 100 °C - 200 °C. This weight loss is decreased to less than 5wt% suggesting there is still about 5wt% of the surfactant present in the washed film. The weight loss between 250 °C – 350 °C due to the polymer combustion, is not greatly changed since only the surfactant was removed by ethanol, leaving PEI in the silica wall. Comparing both two patterns, the main weight loss range for the surfactant is 150 °C - 250 °C and most of the PEI was lost between 250 °C - 350 °C.

For sample synthesized with cat-anionic surfactant and SPEI, similar weight loss steps were observed, however, when this sample was washed with ethanol, very little weight was lost between 100 °C - 200 °C, indicating that the surfactant was almost entirely removed by ethanol washing.

4.3.5 Nitrogen Adsorption and Desorption

Shown in **Figure 4.25** are nitrogen adsorption isotherm for silica films templated by cat-anionic surfactant (CTAB: SDS = 4) and 30 g/l LPEI. In the calcined sample (**Figure 4.25A**), at low relative pressures, significant absorption occurs, which is usually considered as adsorption in micropores or monolayer adsorption. The hysteresis loop is characteristic of a typical type IV mesoporous material. The isotherm does not level off at relative pressures close to saturation vapor pressure indicating the presence of secondary, presumably interparticular, pores in these materials, of the size on the borderline between the mesopore and macropore ranges. The material exhibited a BET specific surface area of about 483.4 m^2/g, with a pore volume 113.6 cm^3/g, and the average pore diameter is about 50 Å. However, these estimates may be quite inaccurate due to the lack of the limiting amount adsorbed as the saturation vapor pressure was approached.

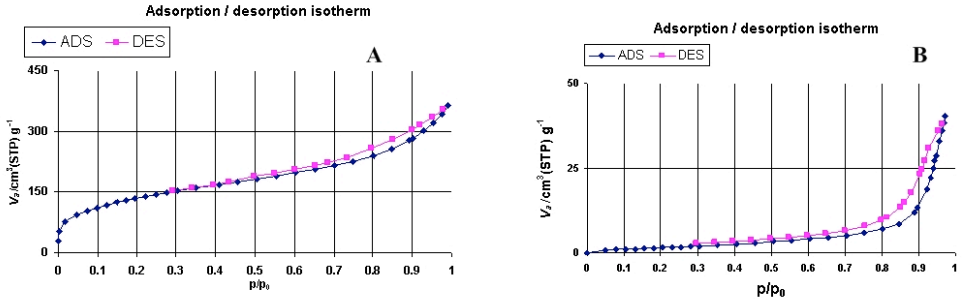

Figure 4.25 *Nitrogen adsorption isotherms for silica films templated by cat-anionic surfactant (CTAB: SDS = 4 and 30 g/l LPEI) (A) Sample with template removed by calcination. (B) Sample with template removed by ethanol wash.*

N_2 adsorption and desorption was also studied on the same sample whose template was removed by washing with ethanol, as presented in **Figure 4.25 B**. The absorption isotherm shows very little absorption at a low relative pressure and did not feature steps as observed in the calcined film sample. The calculated BET surface area exhibits a value as low as 7.8 m^2/g. This may demonstrates the inaccessibility of the primary micropores in the washed materials, which were still filled with hydrophilic polymers and thus inaccessible to the nitrogen adsorbate. It also indicates weak nitrogen-surface interactions due to the polymer coverage of the external surface of silica materials.[29] The hysteresis loops on the adsorption isotherm did not close at relative pressure of about 0.3-0.4, which is a common behavior observed for surface modified silica materials.[30] In this case, it is probably due to the mobility of the flexible polymer chain near or on the material surface. The presence of hysteresis loops due to the capillary condensation indicates the presence of mesopores in the materials.

4.3.6 Temperature Effects

Aging temperature is thought to play an important role in formation of the mesoporous material morphology and porosity by increasing the degree of silica wall condensation, and changing the surfactant aggregation properties as template in the synthesis.[31-33] When the CTAB and SDS stock solution were mixed together, white

precipitation can be observed in the immediate mixture. If the mixture was put in the oven and aged for a period of time this white precipitate disappeared and the solution appears clear, suggesting a better mixture of these two surfactants. Aging temperature has also been reported to induce a phase transition in cat-anionic surfactant mixtures.[34, 35] Thus effects of the aging temperature on the formation of the final mesostructures in the CTAB/SDS/polymer films is interesting.

Here, four temperatures from 30 to 60 *°C* were used to age the reaction solution prior to TMOS addition and before it was poured into a trough to form a film at room temperature. Two cat-anionic surfactant molar ratios (CTAB: SDS = 4 and 2), two PEI molecular weights and four polymer concentrations were investigated, as shown in **Figure 4.26 – 4.28.**

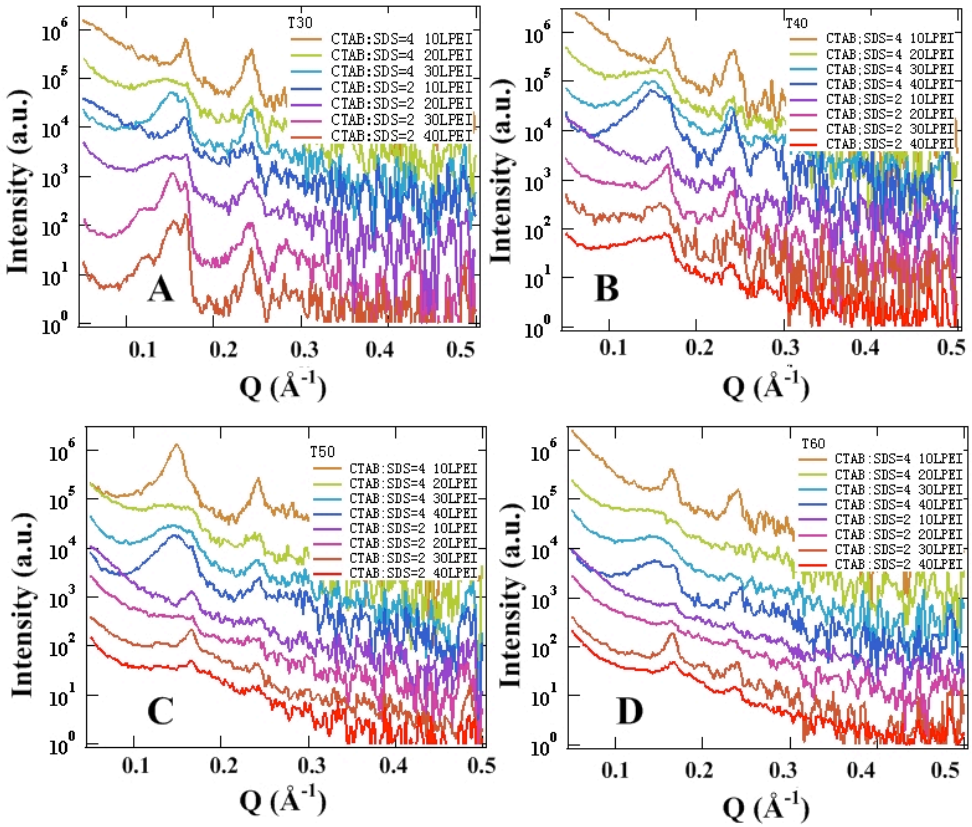

Figure 4.26 *Aging temperature effects on silica films synthesized with CTAB-SDS-LPEI at various CTAB: SDS molar ratios and LPEI concentrations. The temperatures were (A) 30 °C (B) 40 °C (C) 50 °C and (D) 60 °C.*

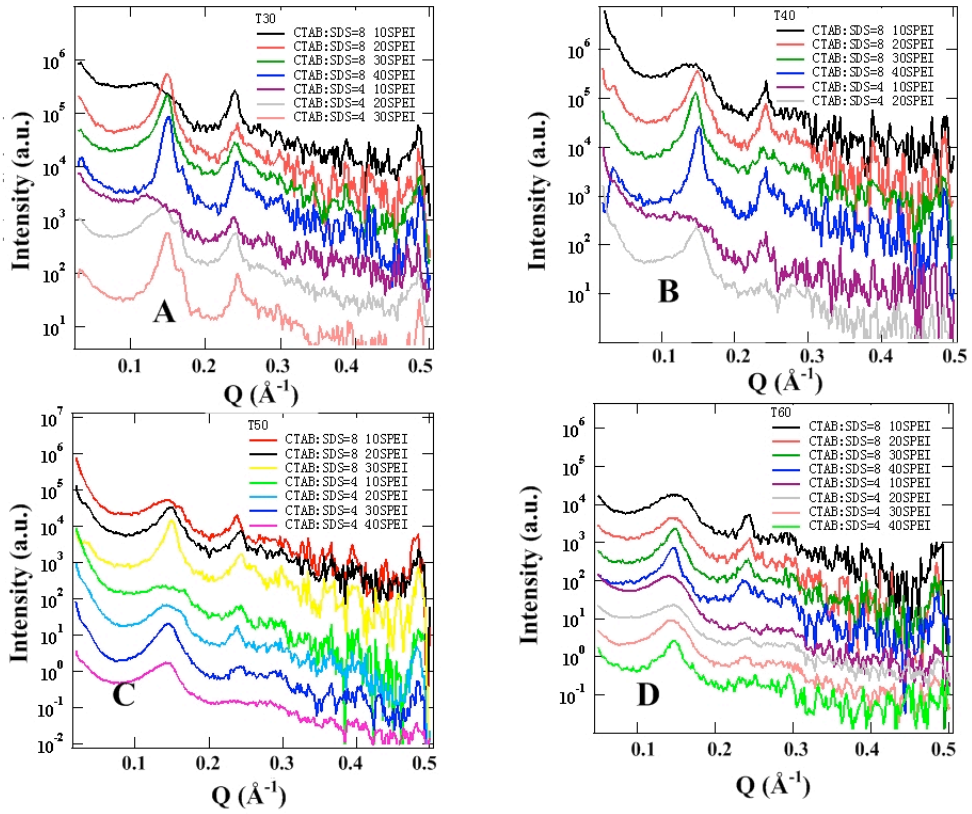

Figure 4.27 *Aging temperature effects on silica film synthesized with CTAB-SDS-SPEI, at various CTAB: SDS molar ratios and SPEI concentrations. The temperatures were (A) 30 °C (B) 40 °C (C) 50 °C and (D) 60 °C.*

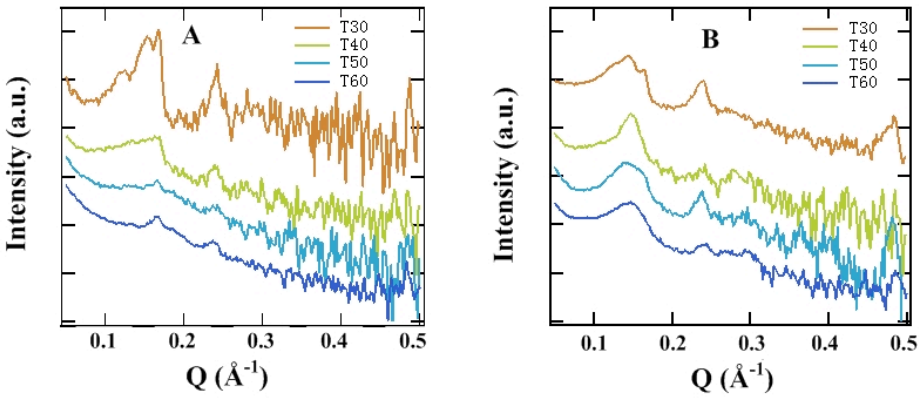

Figure 4.28 *Aging temperature effects on films synthesized with (A) CTAB: SDS = 2 30 g/l LPEI. (B) CTAB: SDS = 4 20 g/l SPEI.*

For films synthesized with the higher CTAB: SDS molar ratio of 4 and polymer LPEI concentration ranging from 10 g/l to 40 g/l as well as films synthesized with CTAB: SDS molar ratio of 2 and polymer LPEI concentration range of 10 g/l - 20 g/l, SAXS data on the dry films indicate the structure does not change with temperature. However, for films synthesized with CTAB: SDS molar ratio of 2 and polymer LPEI concentration of 30 g/l or 40 g/l, increasing the surfactant/polymer solution aging temperature results in a less ordered mesostructure because the intensity of these diffraction peaks fade out. Similar behaviours happened on films synthesized with CTAB: SDS molar ratio of 4 and 20 g/l SPEI. The surfactant/polymer mixture solution normally looks less viscous and transparent after it is left in the high temperature oven. Therefore, it might be due to the fact that the micelles in the solution at high temperature have high mobility and break up the surfactant/polymer particles which normally form immediately after mixing at room temperature, leading to the formation of a dilute lamellar phase in CTAB/SDS/polymer solution. This loose lamellar phase without much order is metastable when it is cooling down. When the TMOS is added, the bilayers can not compact together fast enough before the polymerization sets in the disordered structure.

4.3.7 Film Thickness

The thickness of hybrid surfactant/polyelectrolytes/silica films was measured by a micrometer (0 - 25mm) with an error of ± 0.005 mm. The effect of aging temperature, cat-anionic surfactant molar ratio, two PEI molecular weights and PEI concentrations on the thickness of the hybrid cat-anionic surfactant and polyelectrolyte silica films were investigated and shown in **Figure 4.29**.

The film thickness ranges from 50 μm to 350 μm with an error of 5 μm. The role of the aging temperature does not appear to have a straightforward effect on the film thickness. Films synthesized with a low CTAB: SDS molar ratio are thicker, for example in **Figure 4.29 C**, more SDS present in the film forming solution results in thicker films. This trend is especially clear when the polyelectrolyte concentration is at a high value of 40 g/l. Generally, compared to low molecular weight SPEI, LPEI

appear to improve the film thickness for a certain cat-anionic surfactant molar ratio and aging temperature. There is a strong affinity between anionic surfactant SDS and PEI. The DS^- anion can interact electrostatically with the remaining positively charged amino groups of the polymer. SDS also binds to PEI at high pH because of the hydrophobic interaction under basic environment,[13] thus increasing SDS concentration promotes this hydrophobic interaction, resulting in a thick hybrid cat-anionic surfactant/polyelectrolytes/silica film. It also neutralizes the charge on the mixed cat-anionic micelles allowing more micelles to aggregate together into the films.

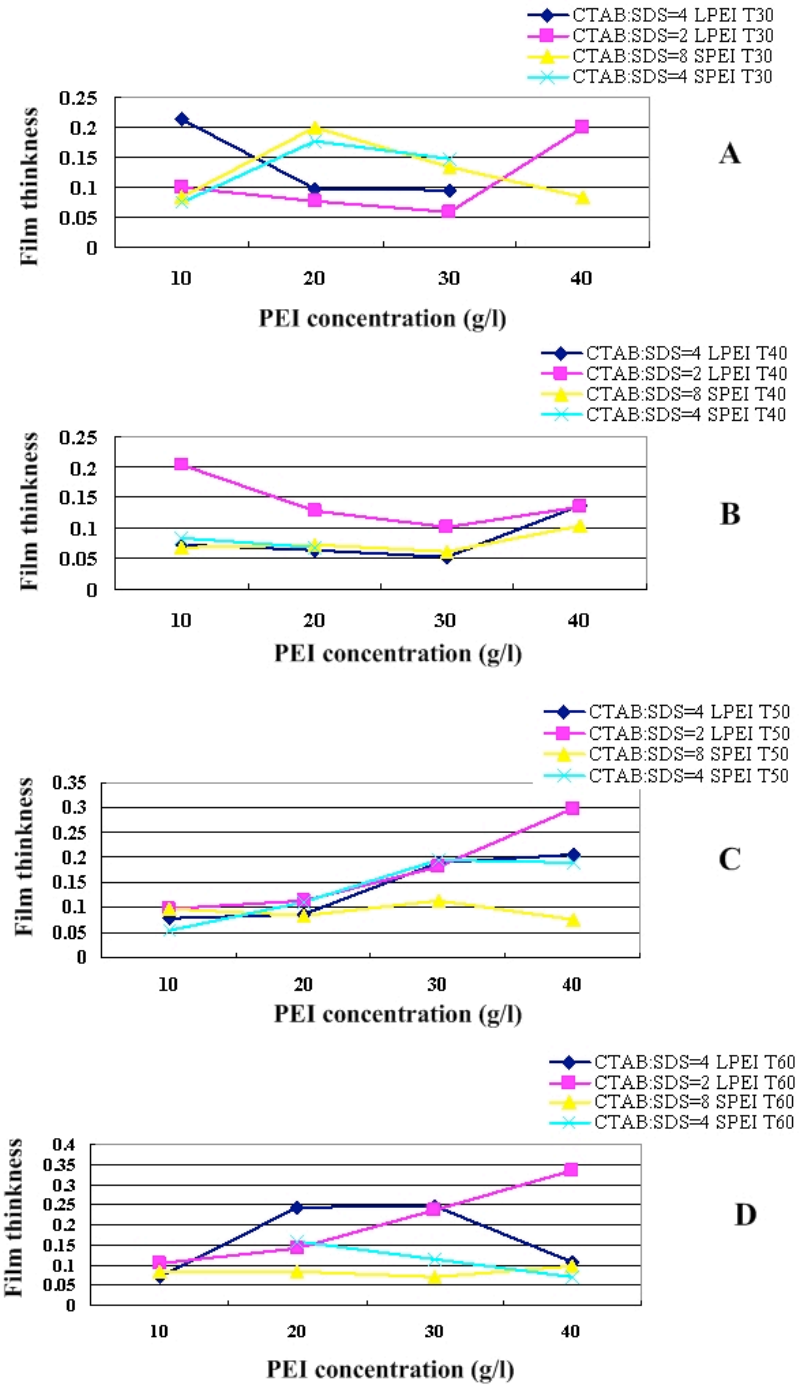

Figure 4.29 *Film thicknesses of the surfactant/polyelectrolytes/silica films aged at different temperature. Error for the measurements is ± 0.005mm, which is within the markers shown on the graphs.*

4.3.8 Low Template Concentration Investigations on Silica Films Templated by CTAB/SDS/SPEI

Robust silica films with ordered mesostructure could also be prepared from very dilute solutions. An interesting interfacial film mesophase transition was observed by varying the total concentration but keeping the molar ratio of all the composites constant. Time-resolved neutron reflectivity was used to follow the mesophase transition in the interfacial films, while time-resolved small angle X-ray scattering was used to investigate the bulk film forming solutions in order to help to understand the transition mechanism. Interactions between the cat-anionic surfactant, soluble polymer and inorganic precursors are thought to be responsible for a change in micelle curvature, leading to the phase transition.

4.3.8.1 Film Formation Process and Interfacial Film Structure

Templated by the cat-anionic surfactants and polyelectrolytes, films form under a wide range of polyelectrolyte concentrations and surfactant molar ratios. Here, the molar ratios of CTAB/SDS/SPEI/TMOS was held constant, while the total surfactant concentration was decreased from 0.046 M to as low as 0.012 M. However, robust films could still be observed and removed from interface with the total surfactant concentration as low as 0.005 M. At high total surfactant concentrations, the subphase solution was very viscous and had a tendency to gel as the films formed, but when the total concentration was decreased, the subphase solutions containing CTAB and SDS are cloudy but less viscous.

The formation process and evolution of mesostructure in the films was followed by time-resolved neutron reflectivity with three minute resolution. Neutron reflectivity patterns of the films formed with total surfactant concentrations of 0.046 M, 0.023 M and 0.012 M are shown in **Figure 30 A, a**, **Figure 30 B, b,** and **Figure 30 C, c** respectively. For films formed with a total surfactant concentration of 0.046 M, as described above, two sharp diffraction peaks at 0.09 $Å^{-1}$and 0.18 $Å^{-1}$ appeared within the first 4 min, and these two peaks become less intense, and another diffraction peak

around 0.12 $Å^{-1}$ grew up with time. At the beginning, the first two peaks were related as a lamellar structure with a d-spacing of 70 Å. However, the three peaks observed at 0.09$Å^{-1}$, 0.12 $Å^{-1}$, 0.18 $Å^{-1}$ are difficult to index to a purely cubic structure. Thus in order to clarify this mesostructure, a time-resolved neutron reflectivity experiment with 15 minute resolution (**Figure 4.10 B**) as well as GIXD experiments on well developed films were also conducted, and a line profile of the GIXD pattern was taken along Q_{xy} = 0.007 $Å^{-1}$. These are shown in **Figure 4.11 C and D**.

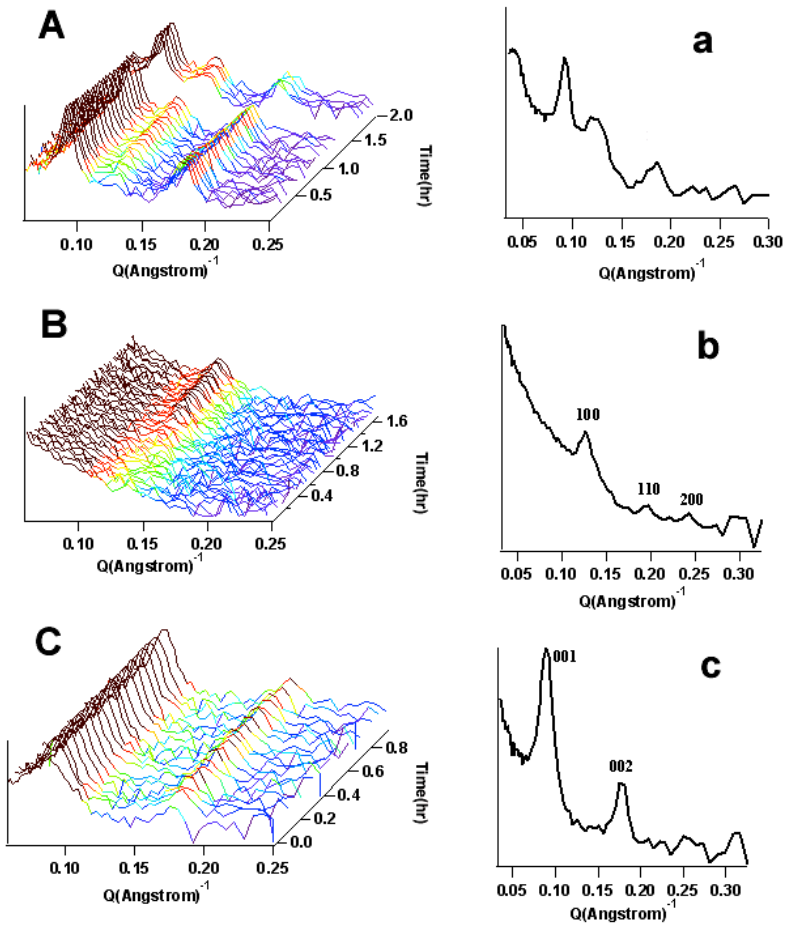

Figure 4.30 *Time-resolved neutron reflectivity patterns of films formed with a total surfactant concentration of 0.046 M (A, a), 0.023 M (B, b) and 0.012 M (C, c). (a,b,c) are the final pattern with more than 10 minute resolution graphed separately for clarity.*

The GIXD patterns confirmed a $Fm\bar{3}m$ cubic phase combined with a lamellar phase, the first peak position is 0.12 $Å^{-1}$. The time-resolved neutron reflectivity data with 15 minute resolution collected on SURF shows only one diffraction peak at 0.12 $Å^{-1}$ as well, which is different to the neutron reflectivity data with 3 minute time resolution collected on INTER. This may be because the experimental conditions, such as humidity and temperature, were not well controlled since the experiments were conducted in different seasons and locations.

When the films were prepared with total concentration of 0.023 M, solutions were evenly white and no lumps were observed. Time-resolved neutron reflectivity patterns are presented in **Figure 4.30 B**. No diffraction peaks were seen during the beginning 40 minutes, but a peak at around 0.12 $Å^{-1}$ grew with time, Neutron reflectivity patterns (8 min resolution) of the well developed films reveal three diffraction peaks at 0.12 $Å^{-1}$, 0.20 $Å^{-1}$ and 0.24 $Å^{-1}$, which correspond to (100), (110), (200) reflections (**Figure 4.30 b**), indicating an ordered 2D hexagonal mesostructure with a unit cell dimension of 70 Å.

Films still grew when the total surfactant concentration was decreased to 0.012 M. These solutions were also opaque with no visible lumps. Time-resolved neutron reflectivity patterns were collected as shown in **Figure 4.28 C and c,** only two diffraction peaks at 0.09 $Å^{-1}$ and 0.18 $Å^{-1}$ were observed during the first run and became sharper with time. This corresponds to a lamellar phase with a unit cell of 70Å, which is similar to that observed in the earlier stage of neutron reflectivity patterns of films prepared with 0.046 M total concentration.

4.3.8.2 Investigation of the Subphase Solution by Time-resolved SAXS

Time-resolved small angle X-ray scattering was used as a very powerful kinetic means to give detailed information and structure features of the phase transformation even after the precipitates were formed. In the current study, time-resolved SAXS experiments with 30 second resolution were conducted on the subphase solutions at different total concentrations, as shown in **Figure 4.31 A**.

TMOS was added after about 1minute to the mixed polymer and surfactant solutions had began to circulate along the flow cell. When the total surfactant concentration was 0.046 M (**Figure 4.31 A**), the mesophase structure has already been discussed in **Section § 4.3.1** Time-resolved SAXS indicates the particles in the subphase evolve into an ordered $Pn\bar{3}m$ mesostructure in around 15 minutes.

When the total surfactant concentration was decreased to 0.023 M or lower, the solution was white and less viscous and time-resolved SAXS patterns are shown in **Figure 4.31 B**. At the beginning, only a lamellar structure of the mixed surfactant solutions were observed, but 80 second after the TMOS was added, two strong reflections with a spacing of 0.14 Å and 0.17 Å, which can be an indicative of (211), (220) reflections respectively of the cubic double gyroid cubic $Ia\bar{3}d$ phase with a unit cell of 110 Å, or it may be related to the (110) (111) reflection of a $Pn\bar{3}m$ primitive cubic mesostructure with a unit cell of 63 Å, it also may be assigned as (111) (200) reflection of a $Fm\bar{3}m$ face-centered cubic mesostructure with a unit cell of 78 Å. Moreover, the $Ia\bar{3}d$ phase seems to be the most preferable phase, the reasons will be discussed in the **Section 4.3.9**.

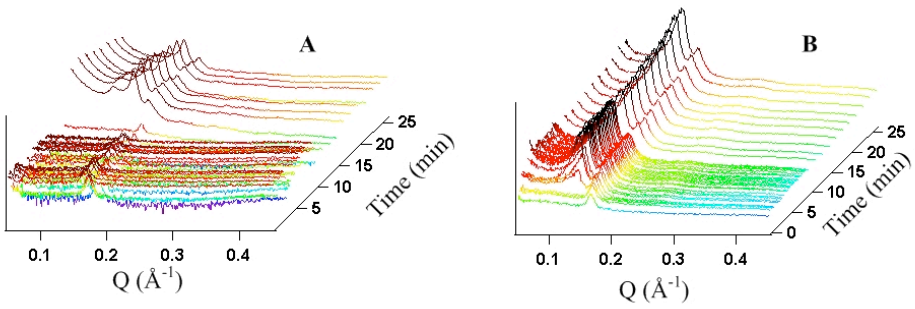

Figure 4.31 *Time-resolved X-ray scattering patterns (30 s resolution) of film forming solutions with total surfactant concentrations of 0.046 M (A) and 0.023 M (B).*

4.3.8.3 SAXS Investigation on Dry Films

These films are white and smooth, and still robust enough to be removed from air/water interface onto an open mesh, although the dry film thickness decreases with

a decrease of total composite concentration in solution. These free-standing films remain continuous without cracks even after calcination at 600 °C.

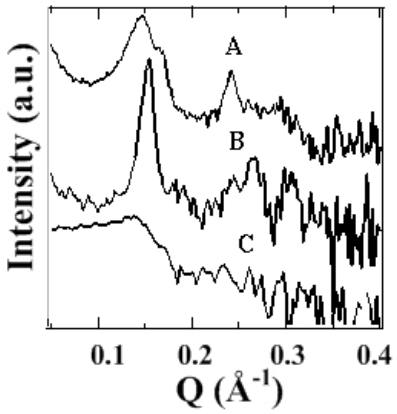

Figure 4.32 *SAXS patterns of dried films formed with total surfactant concentrations of (A) 0.046 M (B) 0.023 M and (C) 0.012 M.*

SAXS data from the dried films are shown in **Figure 4.32**. When the film was prepared with a total surfactant concentrations of 0.046M (**Figure 4.32 A**), three distinct peaks at 0.15 $Å^{-1}$, 0.17 $Å^{-1}$ and 0.24 $Å^{-1}$ were indexed as (111) (200) (220) reflections, corresponding to a $Fm\bar{3}m$ structure with a unit cell of 72 Å. For dry films prepared with a total surfactant concentration of 0.023M (**Figure 4.32 B**), SAXS data shows three diffraction peaks at 0.15 $Å^{-1}$, 0.27 $Å^{-1}$ and 0.30 $Å^{-1}$, which index as the (100) (110) and (200) reflections of an ordered 2D hexagonal structure with a unit cell of 47 Å. Only a broad peak at 0.14 $Å^{-1}$ was obtained for the dry films prepared with a total surfactant concentrations of 0.012 M, suggesting a less ordered mesophase as shown in **Figure 4.32 C**. Both the GIXD of the wet interfacial film and the SAXS data on the dry films, suggesting the film structures were retained even after drying.

4.3.9 Discussion – Silica Films Templated by Cat-anionic Surfactant/Polymer Complexes at the Air/water Interface

This cat-anionic surfactant and polyelectrolyte system was employed successfully to synthesize silica films at the air/water interface. In the previous chapter, the formation mechanism of the films synthesized with surfactant and polyelectrolyte at the air/water interface was studied. Evaporation and hydrophobicity cause interfacial phase separation and induced the formation of the layer with organic micelles trapped inside at the interface, which will finally evolve into the ordered mesostructure. The evolution process from disorder to order happened both in the particles formed in the subphase solution and in the phase separated layer at the air/water interface. Here, at the early stage, only mixed CTAB/SDS particles were formed before the silicate precursor was added, but silicate particles with different liquid crystalline ordering formed afterwards, which is similar to the CTAB/polyelectrolyte templated films. However, the mesophase of the particles and film in the subphase was enriched in this case because of the relatively more complicated interactions between the various polyelectrolytes and the two surfactants.

From the previous investigations of the CTAB/PEI templated silica films, silica films formed with LPEI are known to take a longer time to develop into a relatively less ordered structure. Here again, when time-resolved SAXS was used to investigate the solution below the film, the mesostructure of the particles in the CTAB/SDS/LPEI mixture takes a much longer time to appear compared to the mesostructured particles in the solution with SPEI. Particles in the film forming solutions with LPEI display a less ordered mesostructure while the particles in the film forming solution with SPEI mainly display a $Pn\bar{3}m$ structure over a range of polyelectrolyte concentrations and surfactant molar ratios. Similar behavior happens for the mesostructure of the film formed from interfacial phase separation. Film synthesized with LPEI take more than 1hr to show diffraction peaks while the film prepared with SPEI show the mesostructure in 15 minute and this ordering continues to develop until a highly ordered structure is formed in less than 2 hours.

Polyelectrolyte molecular weight, and chemical nature as well as the cationic-anionic surfactant molar ratio can be used to control the mesophase geometry of the cat-anionic surfactant/polymer templated films. Free standing thick silica films with lamellar, 2D hexagonal and several cubic mesostructures were obtained. The mesophase generated in the film can be described by the surfactant packing parameter, $g = V / a_o L$ where V is the chain volume, a_o is the effective hydrophobic to hydrophilic interfacial area, and L is the chain length. This packing parameter was used to describe the surface curvature of the micelles and the micelle shape.[36, 37] A high packing parameter yields a low interfacial curvature. Surface curvature of the phase assembly in microemulsions has been observed to increase in the following order for mesophases: l*amellar - cubic* $Ia\bar{3}d$ *- hexagonal* $p6mm$ *- 3d hexagonal - cubic* $Im\bar{3}m$ *– cubic* $Pn\bar{3}m$ *– cubic* $Pm\bar{3}n$ *- face-centered cubic* $Fm\bar{3}m$ (Refer to **Section § 7.1 and Section 1.3.2.1** for mesoporous structure).[38]

The interaction between cat-anionic surfactant mixtures and PEI can lead to a significant change in the micelle interfacial curvature, which is responsible for the observed transitions in the polymer/silica film mesophase. Adding SDS causes the cat-anionic micelles to become more compact and more hydrophobic due to charge neutralization of the CTAB,[8] which will improve the hydrophobic interactions between both surfactants and PEI, thus PEI can pack more closely around the head group of the micelle. A bigger head group area leads to a smaller packing parameter and higher micelle curvature, resulting in a phase transition from 2D hexagonal, to bicontinuous cubic $Pn\bar{3}m$ or $Im\bar{3}m$ to micellar cubic $Fm\bar{3}m$ as more SDS is added to the system. Also an increase of the polymer concentration has the same trend for constant cat-anionic surfactant molar ratios. As PEI concentration increases, more polyelectrolyte chains will pack around the cat-anionic micelle head groups to make it bigger, which also leads to a high micelle curvature, resulting in phase transitions from 2D hexagonal to a cubic $Im\bar{3}m$ mesophase or cubic $Pn\bar{3}m$ mesophases to micellar cubic $Fm\bar{3}m$ at different cat-anionic surfactant molar ratios. This trend in

phase transitions and the surface curvature of the micellar assembly are consistent with previous reports for surfactant templated silicas.[37-39]

The overall amount of the component concentrations are found to also have a great effect on the mesostructures both in the subphase solution and in the films. When the film was prepared with a total surfactant concentration of 0.046 M and poured into the trough, small lumps dispersed in the opaque initial film forming solution were observed, which means a local inhomogeneity. Additionally, particle with lamellar phases of 37 Å were observed both at the interface and the earlier stage (about 30 minute learnt from the SAXS data of the subphase solution, see **Section 4.3.8.3 Figure 4.31 A**) after mixing the subphase film forming solution. In other words, these small lumps in the solution are lumps of CTAB/SDS observed at earlier neutron reflectivity experiment, these lumps can be got incorporated inside the film while the interfacial film is growing. After about 30 minute, these CTAB/SDS particles transformed into $Pn\bar{3}m$ mesophase with the first diffraction peak 0.12 $Å^{-1}$ in the subphase solution SAXS patterns. In addition, it also takes about an hour for the neutron reflectivity facility to observe the appearance of the diffraction peak at 0.12 $Å^{-1}$, indicating the lamellar phase of the CTAB/SDS particles captured inside the films start to transform to a cubic phase, although this transformation is later than that observed in the solution. The delay may be because of the factor that the interfical film is more dry and the network is more rigid. The final film structure which is observed by the GIXD is $Fm\bar{3}m$, indicating a possible phase transformation from $lamellar$ to $Fm\bar{3}m$ with particles involved and transformed inside the interficial film. However, some of the particles in the film do not transform because the evaporation causes the top layer of the film dry and the film network is more rigid, thus these CTAB/SDS particles with 37 Å lamellar phase can be observed by the GIXD.

However; when the films were synthesized with a total surfactant concentration of 0.023 M, films formed with an initial cubic mesophase transferred to 2D hexagonal mesophase upon drying, which has also been observed by Cagnol

previously.[40] As phase separation occurs in these solutions causing film formation, micelles are trapped in the concentrated layer at the interface along with the polymer. The silicate hydrolised and condensed around the cat-anionic surfactant micelle headgroup, resulting in a increase in the effective headgroup area of the surfactant, therefore decrease the g value. Thus it is reasonable that the mesostructure changed to a higher curvature mesophase while the film is growing and drying. Based on this discussion, the cubic phase $Ia\bar{3}d$ is expected to be the most probable mesophase for the subphase particle when the total surfactant concentration is 0.023 M. However, when the film forming solution concentration is too dilute, only multilayers formed at the interface, and particles with a bicontinuous cubic mesostructure formed in the subphase. Soft particles from the subphase incorporated into the films will stretch along the interface and organise to form a lamellar structure.

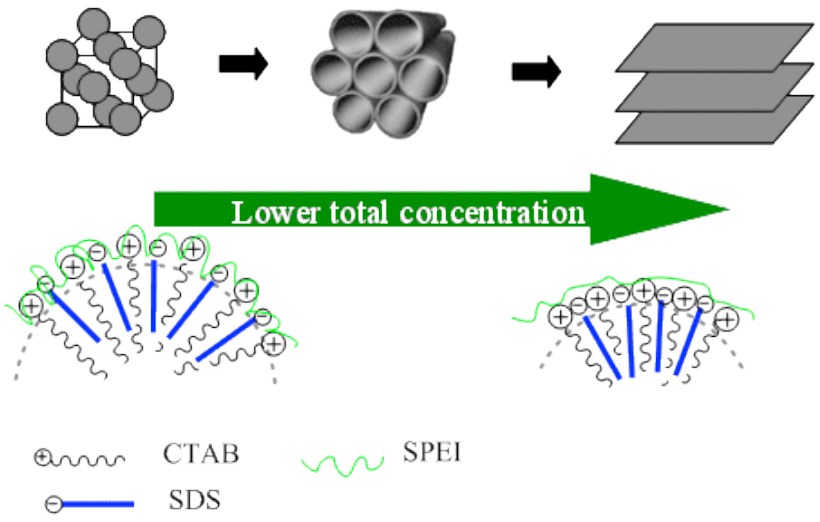

Scheme 4.1 *Total component concentration drives the film mesophase transition at the air/water interface*

While films with various mesostructures have been studied previously, the introduction of polymer into the reaction system makes it feasible to form electro-static, and hydrophobic interactions between cat-anionic surfactants,

polyelectrolyte and the inorganic precursors to control the packing parameter, and these are key factors in the formation and transition of the highly ordered mesophases.

Here, it has been shown that an interfacial mesophase transferred from a micellar cubic $Fm\bar{3}m$ to a 2D hexagonal and a lamellar structure with the continuous dilution of the film formation solution. Earlier work in the group suggested that the dominant interaction between the CTAB and PEI is the dipole-cation interaction; SDS shows strong affinity to PEI due to the electrostatic and the hydrophobic interactions. Polyelectrolytes were thought to wrap around the micelles, but PEI is more likely to move into the solution and become less packed around the micelle head group when the total surfactant and polymer concentration decreases, thus the electrostatic interaction between the CTAB and SDS will bring them closer which is attributed to less steric hindrance from PEI (shown in **Scheme 4.1**). It results in a smaller effective headgroup, bigger g value and a decrease of the curvature, thus diluting the film forming solution causes the film structure transition to 2D hexagonal and a lamellar phase at the interface.

4.4 Conclusion

Thick free standing mesostructured films of cat-anionic surfactant and polyelectrolytes spontaneously self-assemble at the air/water interface. The mesostructure of the interfacial polymer film and dry polymer films were examined.

These surfactant and polymer systems were also mineralized to synthesize robust silica films. This method provides an easy way to synthesize mesoporous silica films with a variety of mesostructures grown at the air/water interface. Interfacial film formation processes were probed by neutron reflectivity and well developed film mesostructures were clarified by GIXD. The subphase was also studied by time-resolved SAXS. Polyelectrolyte molecular weight, and chemical nature as well as the cationic-anionic surfactant molar ratio can be used to control the mesophase geometry of the cat-anionic surfactant/polymer templated films. Lamellar, 2D hexagonal and several cubic mesostructures were obtained and a phase diagram in

terms of the cat-anionic molar ratio and polyelectrolyte concentration was drawn. These films are thick and robust enough to be easily removed from interface and the film morphology is retained even after calcination.

Silica films can also be prepared from very dilute solutions using cat-anionic surfactant and polyelectrolyte at the air/water interface. With the assistance of the time-resolved X-ray scattering characterisation techniques, particles with cubic mesostructure were found in the subphase but this structure was altered in the film due to the silicate hydrolysis and condensation. Neutron reflectivity suggests the mesophase transition from $Fm\bar{3}m$ to lamellar observed in the films when the film formation solutions were diluted. This mesophase transition was attributed to the interactions between the cat-anionic surfactant, polymer and inorganic precursors.

These films with different mesostructure are strong, robust and have good thermal stability. By washing out the template, robust polymer–silica hybrid films can be obtained straightforwardly. They retain the polymer functionality in the pore wall of the silica materials, which could allow binding of specific species in the pore or allow synergistic interactions between the organic functionality from the polymer and the inorganic species in the walls for various applications. We are currently investigating these aspects of the films to develop them into useful membranes for future applications, such as heavy ion removal, or CO_2 absorption.

4.5 References

(1) B. Yang, and K. J. Edler, *Chemistry of Materials* **21**(7), 1221 (2009).

(2) E. W. Kaler, A. K. Murthy, B. E. Rodriguez, and J. A. N. Zasadzinski, *Science* **245**(4924), 1371 (1989).

(3) E. W. Kaler, K. L. Herrington, A. K. Murthy, and J. A. N. Zasadzinski, *Journal of Physical Chemistry* **96**(16), 6698 (1992).

(4) L. L. Brasher, K. L. Herrington, and E. W. Kaler, *Langmuir* **11**(11), 4267 (1995).

(5) L. L. Brasher, and E. W. Kaler, *Langmuir* **12**(26), 6270 (1996).

(6) J. H. Lee, J. P. Gustin, T. H. Chen, G. F. Payne, and S. R. Raghavan, *Langmuir* **21**(1), 26 (2005).

(7) F. E. Antunes, E. F. Marques, R. Gomes, K. Thuresson, B. Lindman, and M. G. Miguel, *Langmuir* **20**(11), 4647 (2004).

(8) H. Chakraborty, and M. Sarkar, *Langmuir* **20**(9), 3551 (2004).

(9) K. J. Edler, M. J. Wasbrough, J. A. Holdaway, and B. M. D. O'Driscoll, *Langmuir* **25**(7), 4047 (2009).

(10) B. M. D. O'Driscoll, E. A. Nickels, and K. J. Edler, *Chemical Communications* (10), 1068 (2007).

(11) P. Garstecki, and R. Holyst, *Langmuir* **18**(7), 2529 (2002).

(12) P. Garstecki, and R. Holyst, *Langmuir* **18**(7), 2519 (2002).

(13) M. A. Winnik, S. M. Bystryak, C. Chassenieux, V. Strashko, P. M. Macdonald, and J. Siddiqui, *Langmuir* **16**(10), 4495 (2000).

(14) B. M. D. O'Driscoll, E. Milsom, C. Fernandez-Martin, L. White, S. J. Roser, and K. J. Edler, *Macromolecules* **38**(21), 8785 (2005).

(15) B. M. D. O'Driscoll, C. Fernandez-Martin, R. D. Wilson, J. Knott, S. J. Roser, and K. J. Edler, *Langmuir* **23**(8), 4589 (2007).

(16) Z. S. Gao, R. E. Wasylishen, and J. C. T. Kwak, *Journal of Physical Chemistry* **95**(1), 462 (1991).

(17) M. I. Gjerde, W. Nerdal, and H. Hoiland, *Journal of Colloid and Interface Science* **197**(2), 191 (1998).

(18) E. D. Goddard, *Colloids and Surfaces* **19**(2-3), 301 (1986).

(19) E. D. Goddard, *Colloids and Surfaces* **19**(2-3), 255 (1986).

(20) E. Pettersson, D. Topgaard, P. Stilbs, and O. Soderman, *Langmuir* **20**(4), 1138 (2004).

(21) Z. S. Hou, Z. P. Li, and H. Q. Wang, *Journal of Dispersion Science and Technology* **20**(5), 1507 (1999).

(22) M. K. Baloch, A. Rauf, F. Ahmad, G. F. Durani, and G. Hameed, *Journal of Applied Polymer Science* **116**(4), 2133 (2010).

(23) F. Kleitz, J. Blanchard, B. Zibrowius, F. Schuth, P. Agren, and M. Linden, *Langmuir* **18**(12), 4963 (2002).

(24) A. Lind, J. Andersson, S. Karlsson, P. Agren, P. Bussian, H. Amenitsch, and M. Linden, *Langmuir* **18**(4), 1380 (2002).

(25) B. Z. Tian, X. Y. Liu, Z. D. Zhang, B. Tu, and D. Y. Zhao, *Journal of Solid State Chemistry* **167**(2), 324 (2002).

(26) B. Yang, K. Edler, C. Guo, and H. Z. Liu, *Microporous and Mesoporous Materials* **131**(1-3), 21 (2010).

(27) D. Grosso, F. Cagnol, G. J. D. A. Soler-Illia, E. L. Crepaldi, H. Amenitsch, A. Brunet-Bruneau, A. Bourgeois, and C. Sanchez, *Advanced Functional Materials* **14**(4), 309 (2004).

(28) G. E. S. Toombes, A. C. Finnefrock, M. W. Tate, R. Ulrich, U. Wiesner, and S. M. Gruner, *Macromolecules* **40**(25), 8974 (2007).

(29) M. Kruk, M. Jaroniec, R. Ryoo, and S. H. Joo, *Chemistry of Materials* **12**(5), 1414 (2000).

(30) C. P. Jaroniec, M. Kruk, M. Jaroniec, and A. Sayari, *Journal of Physical Chemistry B* **102**(28), 5503 (1998).

(31) A. Galarneau, N. Cambon, F. Di Renzo, R. Ryoo, M. Choi, and F. Fajula, *New Journal of Chemistry* **27**(1), 73 (2003).

(32) M. Kruk, M. Jaroniec, C. H. Ko, and R. Ryoo, *Chemistry of Materials* **12**(7), 1961 (2000).

(33) A. Sousa, and E. M. B. Sousa, *Journal of Non-Crystalline Solids* **352**(32-35), 3451 (2006).

(34) H. G. Li, S. A. Wieczorek, X. Xin, T. Kalwarczyk, N. Ziebacz, T. Szymborski, R. Holyst, J. C. Hao, E. Gorecka, and D. Pociecha, *Langmuir* **26**(1), 34 (2010).

(35) H. Q. Yin, J. B. Huang, Y. Q. Gao, and H. L. Fu, *Langmuir* **21**(7), 2656 (2005).

(36) J. N. Israelachvili, D. J. Mitchell, and B. W. Ninham, *Journal of the Chemical Society-Faraday Transactions Ii* **72**, 1525 (1976).

(37) D. Y. Zhao, Q. S. Huo, J. L. Feng, B. F. Chmelka, and G. D. Stucky, *Journal of the American Chemical Society* **120**(24), 6024 (1998).

(38) S. A. El-Safty, and T. Hanaoka, *Chemistry of Materials* **16**(3), 384 (2004).

(39) S. A. El-Safty, and T. Hanaoka, *Advanced Materials* **15**(22), 1893 (2003).

(40) F. Cagnol, D. Grosso, G. J. D. A. S. Soler-Illia, E. L. Crepaldi, F. Babonneau, H. Amenitsch, and C. Sanchez, *Journal of Materials Chemistry* **13**(1), 61 (2003).

Chapter 5 Titania and Iron Oxide Mesostructured Film Templated by Cat-anionic Surfactant and Polyelectrolytes at the Air/water Interface

5.1 Introduction

Surfactant templated mesoporous materials experienced a major burst of research interests since they display a periodic array of mesopores, which are narrowly size distributed and can be tailored. However, the research field initially mainly focused on the synthesis of silica based solids, since most of the research groups working with mesoporous materials originally worked on the chemistry of zeolites, thus are more familiar with the chemistry of silicate and aluminum than with that of transition metals. The transition metal based systems are more difficult to master compared with the sol-gel chemistry of silicon since the precursors (1) present high reactivity towards hydrolysis and condensation; (2) present different oxidation states and coordination; (3) have oxides that tend to crystallize when heated. However, transition metal based mesoporous materials are still of great research interest due to their wide range of applications due to their electronic and magnetic properties. Especially, high surface area titanium oxide is a very promising material in the aspect of controlled delivery, photocatalysis, energy conversion and optical applications.

Many different strategies have been developed to synthesize transition metal oxide based mesoporous materials. Most of the strategies have targeted the control of the transition metal hydrolysis and condensation by adding complex molecules and strong acids. [1-3] Use of non-aqueous solvents were also explored to decrease the reactivity of transitional metals.[3] So far, most reports concern powder materials.[4-6] Stucky and co workers prepared mesoporous transitional metal powders, including TiO_2, ZrO_2, Al_2O_3, SnO_2 with 2D hexagonal or cubic structures by using nonionic block copolymers as the template in ethanolic solutions of MCl_n.[7, 8]

Moreover, processing in a controlled morphology is required because porous transition metal films, especially titania mesoporous films are of special interest as film sensors, for encapsulation of drugs for targeted or controlled release, catalysis, separation, optical sensors and photovoltaic application such as solar cells.[9, 10] However, reproducible production of mesoporous thin titania films which have linked high porosity, and mesoscopic organization with defined spatial orientation remains a challenge.

EISA is a widely used procedure for the synthesis of transition metal based materials because it utilizes very dilute initial solutions from which a liquid crystalline mesophase gradually formed upon solvent evaporation. Grosso et al first employed EISA method (dip coating) to prepare uniform crack free TiO_2 thin films that present a high regularity in the pore mesostructure and orientation using poly(ethylene oxide) based surfactant as structuring agents and $TiCl_4$ as the inorganic precursors in ethanol-water solution.[11] Controlled conditions in the deposition, post-synthesis, thermal treatment, such as controlled quantities of water, acidity, temperature, aging, were used to determine the time evolution of mesostructure.[12] Thermally stable nanocrystallised titania thin films with an organised cubic mesostructure and a high surface area were also fabricated.[13, 14] Mesoporous titania films with large pore diameter, narrow pore-size distribution, high surface area and nanocrystalline inorganic wall were prepared with a triblock copolymer template using butanol as an alternative solvent.[15]

The air/water interface also offers a useful platform to prepare metal oxide based thin films via a sol-gel process.[16-19] The rational design of hybrid metal oxide-organic composite films at the interface via a self assembly route uses surfactants to direct the nucleation, growth and morphology of the oxide. Tetradecyltrimethylammonium chloride (C_{14}TAC) and SDS templated mesostructured titania films were grown at the air/water interface. The formation of these films was attributed to the attraction between the surfactant headgroup and titania above and below the pH of the formal isoelectric point of titania.[20, 21] However, these films are thin which limits their application. Recently, our group has done a lot of work on the synthesis of ordered

titania films at the air/solution interface. The fluorinated surfactant FSO-100 and $PEPEG_{2250}$ were used as templates to form films on a high alcohol solvent system in the presence of a high concentration of acid.

In this work nanoporous iron oxides have also been studied because iron oxide has been widely used in many applications such as data recording and storage,[22] biomedical applications,[23] catalysis,[24] and rechargeable lithium batteries.[25] A soft-templating approach via supramolecular surfactant self assembly is a highly desirable strategy to the synthesis of ordered mesoporous iron oxide. Tolbert et al first reported the synthesis and magnetic properties of an ordered, lamellar iron oxide and surfactant composite.[26] Srivastava et al reported an amorphous mesoporous iron oxide made using a cationic surfactant;[27] while Jiao et al prepared two dimensional and three dimensional mesoporous iron oxide powders with high surface area using decylamine as the template.[28] Malik synthesized mesostructured iron oxide in the presence of carboxylate and amine surfactants.[29] Wirnsberger prepared iron oxyhydroxide-surfactant composites by oxidizing Fe(II) solution using H_2O_2 in the presence of anionic surfactant.[30, 31] A chelating triol surfactant was also found to be an ideal templating agent for the synthesis of mesoporous iron oxide since iron （III） prefers coordination to tris-chelating hard oxygen donors.[32] Most recently, mesoporous iron oxide with high surface area was prepared using SDS and SDS-benzyl alcohol systems.[33] However, to the best of our knowledge so far, most of the iron oxide materials are powders and there are no reports in the literature on successful synthesis of thick iron oxide films using soft templating at the air/water interface.

Inspired by bio-mineralization, many soluble polymers mimicking the organic matrix in natural organisms have been employed to control the morphology, phase and texture of TiO_2 particles.[34-36] Therefore, here we employed water soluble polymers with the cat-anionic surfactant system discussed in **Chapter 4** to spontaneously form mesostructured titania films at the air/water interface.

PAAm contains amino and carbonyl functional group and can interact with metal ions by chemical and physical adsorption, thus it plays an important role in the structure and stabilization of anatase phase titania.[34] Nonionic surfactants such as those containing PEO have been shown to yield materials with thick titania walls that are robust towards crystallization indicating a strong interaction with titania species.[11, 12, 37] Thus polyacrylamide (PAAm) and poly(ethylene oxide) (PEO) were chosen for investigation as the polymer component in our film forming system (refer to **Figure 1.2** for molecular structures), two types of inorganic precursors titanium butoxide (TiB) and titanium (IV) bis(ammonium lactato)dihydroxide (TiBALD) (see **Figure 1.9** for molecular structures) and different cat-anionic surfactant ratios were also investigated . In this work, we also attempted to use PEI with cat-anionic surfactants and the titania precursor TiBALD to synthesize titania films however, only very limited concentrations were observed to form films, and the dry film structure was similar to those observed for cat-anionic surfactant/PEO/titania film so these studies are not reported in detail here.

Structural arrangement at the air/water interface and film growth processes were followed by neutron reflectivity and GIXD. These polymer-titania hybrid films were thick enough to be removed from the interface and SAXS patterns on the dry films indicate the mesostructural ordering was retained in the dry films. In order to improve retention of mesostructure after removing the surfactant/polymer template, post synthesis treatments were conducted by either soaking the hybrid films in titania precursor or exposing the films under titania precursor vapor at very low pressure. Moreover, dry surfactant-polyelectrolytes film was also investigated as a dry template to prepare titania films, since by this method we can easily and quickly generate a mesostructured scaffold where the amount of water present can be controlled. This raises the possibility of synthesis of mesostructured inorganic films which can not be templated in aqueous systems due to their rapid reactivity with water.

Finally, thick iron oxide/surfactant films with lamellar mesostructured were successfully prepared using SDS and a high molecular PEI under alkaline conditions at the air/water interface.

5.2 Cat-anionic Surfactant and Polymer Templated Titania Films

5.2.1 Titania Films Templated by CTAB/SDS/PAAm

5.2.1.1 Film Formation Process

Solutions were prepared as described in **Section § 2.3.6** and poured into Teflon troughs for measurement of the developing structure. Neutron reflectivity experiments with 15 minute time resolution were conducted on the CRISP reflectometer at ISIS, in order to follow the development of cat-anionic surfactant/PAAm templated titania films at the air/water interface. Two dimensional neutron reflectivity profiles for cat-anionic surfactant/PAAm titania film forming solutions with different CTAB/SDS ratios, PAAm concentrations as a function of time, are shown in **Figure 5.1**.

When the CTAB:SDS molar ratio was 6 and PAAm concentration was 25 g/l (**Figure 5.1 A**), no diffraction peak was visible in the first 15 minute scan, but two broad diffraction peaks at 0.08 $Å^{-1}$ and 0.15 $Å^{-1}$ appeared in the second 15 minute scan after pouring the film forming solution. These peaks continued to grow in intensity up to the last measurement at 120 minute. When more SDS was present in the film forming solutions, as shown in **Figure 5.1 B and C**, diffraction peak at 0.08 $Å^{-1}$ was visible in the first scan and grew in intensity with time. This suggests that CTAB-SDS-PAAM-titania film structure formation proceeds much more quickly when more SDS is present in the film forming solution. In bench experiments, the film forming solution with more SDS appeared white and less viscous than film forming solution with less SDS, thus high solution viscosity may hinder the micelle mobility and structure appearance. Polymer PAAm concentration has also been investigated and the results are shown in **Figure 5.1 D, B, E**. When 12.5 g/l PAAm was used, one diffraction peak at 0.06 $Å^{-1}$ appeared at the first scan but it became more broad at about 45 minute. When the PAAm concentration was increased to 37.5 g/l, fringes were also observed in the first scan and one diffraction peak at 0.08 $Å^{-1}$ appeared and did not change over the whole process. The structure of these films will be discussed below.

A neutron reflectivity experiment on mixed CTAB/SDS/PAAm/TiB films using different neutron contrast (by substituting CTAB with d-CTAB) was also conducted. Two strong peaks around 0.08$Å^{-1}$ and 0.16 $Å^{-1}$ can be seen in both cases, indicating that SDS is present in the mesostructure, as shown in **Figure 5.1 F**. The neutron reflectivity data also suggests the presence of a small peak at 0.05 $Å^{-1}$ for the CTAB/SDS/PAAM/TiB film although it is largely within the error bars, and is not seen in the sample with dCTAB/SDS/PAAM/TiB. GIXD data (**Figure 5.2 A, B & C**) below also do not show this peak.

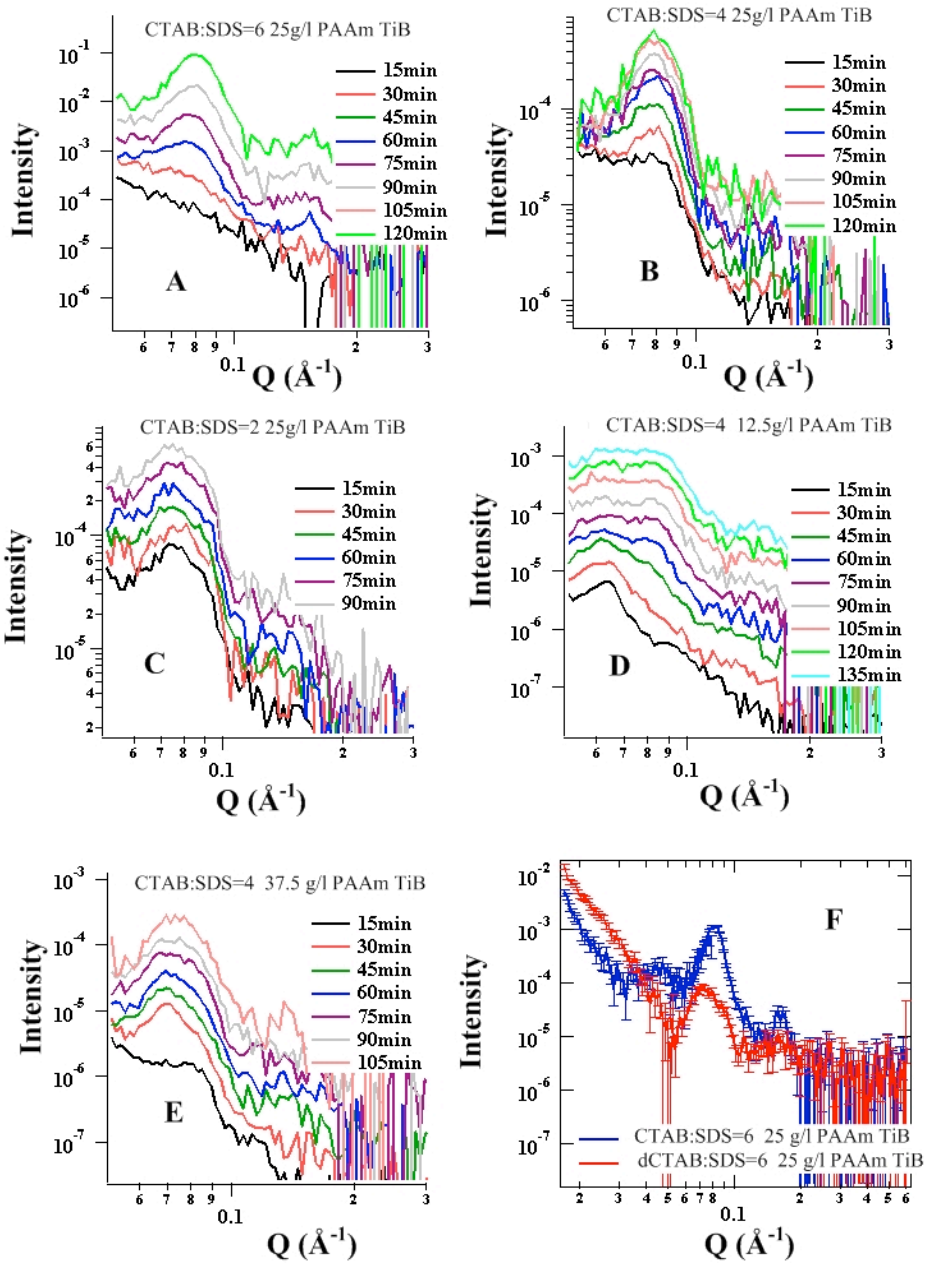

Figure 5.1 *Time-resolved neutron reflectivity of the interfacial cat-anionic surfactant/PAAm/titania films. The titania precursor TiB concentration is 0.037M for all the samples.*

5.2.1.2 Interfacial Film Structure

To clarify the cat-anionic surfactant/PAAm/titania film structure at the solution surface, GIXD patterns were collected and the Structure assignments and unit cell parameters are shown in **Table 5.1**.

GIXD patterns of the films grown with molar ratio CTAB: SDS = 6 25 g/l PAAm were shown in **Figure 5.2 A and B**. Line profiles at Q_{xy} = 0.007 $Å^{-1}$ from these patterns are also shown in **Figure 5.2 C**, two diffraction peaks at 0.08 $Å^{-1}$ and 0.16 $Å^{-1}$ are visible. The results correspond well to the neutron reflectivity data and indicate a lamellar phase with d-spacing of 78 Å. The same mesostructure was also observed for the top film layers suggesting that the lamellar phase is not aligned to the interface.

Different CTAB/SDS molar ratios also have great effects on the final interfacial film structure. When the CTAB: SDS ratio is 4 (**Figure 5.2 D**), three diffraction peaks at 0.07 $Å^{-1}$, 0.11 $Å^{-1}$ and 0.14 $Å^{-1}$ can be indexed as the (110), (200) and (220) reflections of an $Im\bar{3}m$ cubic phase with a repeating unit cell of 127 Å. At a low incident angle, probing only the top layer of the film, only one peak is seen at 0.14 $Å^{-1}$ which is the same position as that of (220) reflection mentioned above. It may be the case that there are not enough repeats of the other planes in the unit cell within the top 100 Å thickness of the film, leading to the lack of other diffraction peaks in the low angle pattern.

When the CTAB: SDS molar ratio is decreased to 2, three diffraction peaks at 0.1$Å^{-1}$, 0.14 $Å^{-1}$ and 0.2 $Å^{-1}$ might be related to the (110), (200) and (220) reflections of an $Im\bar{3}m$ cubic phase with a repeating unit cell of 89 Å. which is smaller than the d-spacing of mesostructured film prepared with a molar ratio of CTAB: SDS = 4. The line profiles of the low angle GIXD patterns show peaks at 0.06 $Å^{-1}$, 0.15 $Å^{-1}$ as well as some fringes between these two peaks. However, the mesostructure is difficult to define due to the lack of clearly defined peaks. From the above, we concluded that increasing the SDS concentration induced a phase transformation from lamellar structure to $Im\bar{3}m$ cubic phase since SDS plays an important role in determining the mesostructure in the cat-anionic surfactant/PAAm/titania system. SDS alone in water forms $Im\bar{3}m$ cubic structure,[38] and this phase was also observed in the CTAB/SDS/LPEI/silica films in **Chapter 4**, when the SDS concentration was high.

When the CTAB/SDS molar ratio decreased from 4 to 2, the cubic film structure does not change, but the d-spacing decreased by 28 Å, suggesting that the more presence of SDS in the cubic structure neutralizes the cat-anionic micelles allowing closer packing of the micelles, as well as reducing the average micelle size.

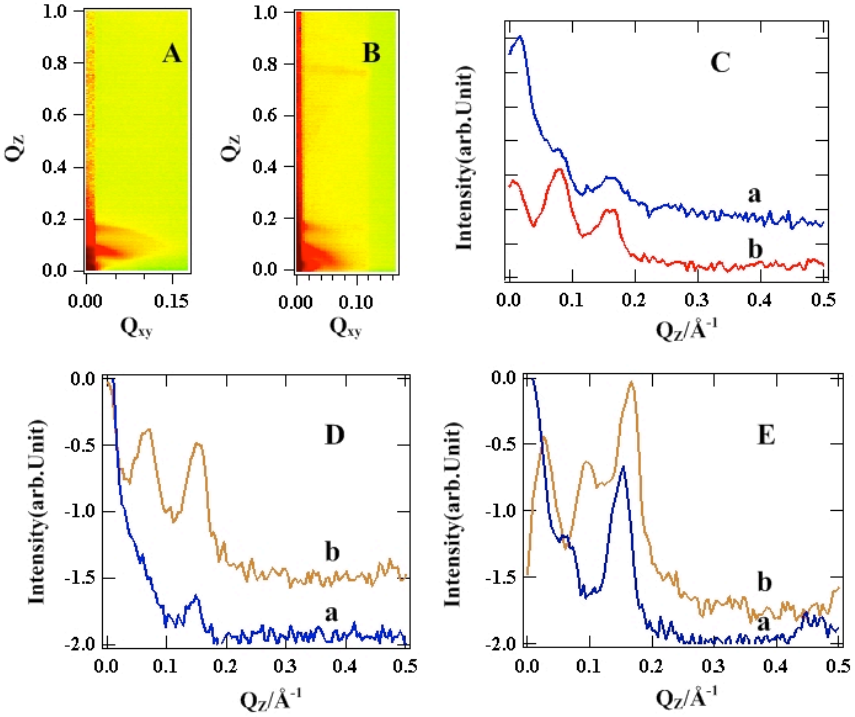

Figure 5.2 *GIXD patterns of the interfacial cat-anionic surfactant/PAAm/titania films prepared with CTAB:SDS = 6 25 g/l PAAm; (A) GIXD pattern of top thin layers of interfacial films; (B) GIXD pattern of relatively deeper layer of interfacial films; (C) Line profiles of (A) and (B) at* Q_{xy} *= 0.007* $Å^{-1}$*. (D), CTAB: SDS = 4 25 g/l PAAm; (E), CTAB: SDS = 2 25 g/l PAAm. For all the line profiles, a is for the low angle (0.045°) GIXD pattern and b is for the pattern taken at higher incident angle (0.204°, 0.11°, 0.42° for CTAB: SDS molar ratio of 6, 4 and 2 respectively).TiB concentration is 0.037M).*

PAAm concentration effects on the final film mesostructure were also investigated by GIXD (**Figure 5.3**). When the PAAm concentration is either a relatively low concentration 12.5 g/l or a relatively high concentration 37.5 g/l, two broad peaks at

0.08 $Å^{-1}$ and 0.16 $Å^{-1}$ could be observed, indicating a lamellar mesophase. The cubic $Im\bar{3}m$ phase only appears at an intermediate polymer concentration of 25 g/l. The curvature of the mixed cat-anionic micelles due to the packing parameter is in this case thought to be mainly determined by the effective surfactant headgroup area. PAAm is thought to have little interactions with either CTAB or SDS, as described in **Section § 4.2.5**. However, it has interaction with metal ions because of the amino and carbonyl functional groups,[34] and both CTAB and SDS were reported as templates to synthesize mesoporous titania materials,[39-41] thus PAAm and cat-anionic surfactant interactions maybe improved due to the presence of titania precursor. In this case, PAAm are able to physically pack around the surfactant headgroup to increase the headgroup size, inducing the appearance of cubic mesostructure, which was not observed for the CTAB/SDS/PAAm/silica films.

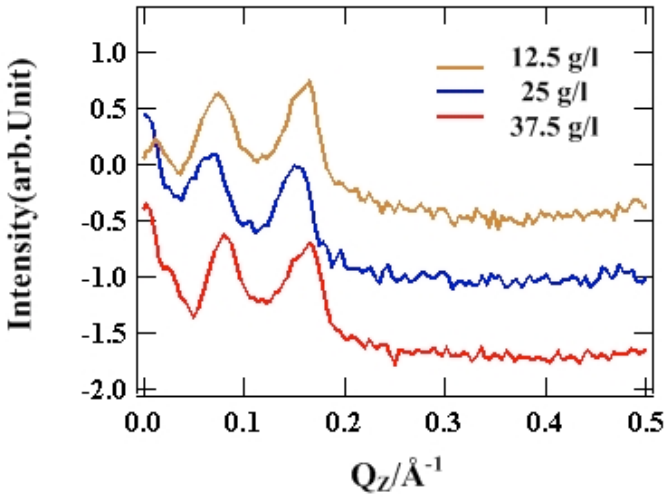

Figure 5.3 *Line profiles from higher incident angle (0.19°, 0.11°, 0.345°) GIXD patterns showing polyelectrolyte concentration effects on cat-anionic surfactant CTAB/SDS/PAAm/titania films, in which the molar ratio of CTAB: SDS = 4 and the TiB concentration is 0.037M.*

Titania(IV) Bis(Ammonium Lactato)-Dihydroxide (TiBALD) was also used to synthesize titania films at the air/water interface since it is stable at ambient temperature in neutral aqueous solution. Compared to the film forming solution with

TiB, the film forming solution with TiBALD is very viscous and gels much quicker. Neutron reflectivity patterns of the cat-anionic surfactant/PAAm/titania films made from this precursor show a less ordered mesostructure with a unit cell of 79 Å, as shown in **Figure 5.4 A**. The GIXD pattern (**Figure 5.4 B**) shows two peaks at 0.08Å^{-1} and 0.12 Å^{-1}, suggesting a $Im\bar{3}m$ mesostructure with a repeating unit cell of 111 Å. Increasing the titania precursor concentration only resulted in more precipitation and no films could be observed (refer to the phase diagram in **Section § *5.2.1.5).***

The difference in structure may be due to the small molecules released by hydrolysis of the titania precursors. TiBALD releases ammonium lactate after hydrolysis while TiB releases butanol. It is well documented that the addition of long chain alcohols like butanol can reduce the CMC of ionic and non-ionic surfactants in aqueous solution,[42-44] Butanol was used to achieve thermally stable, large surface area titania materials with anatase crystallites in the walls due to its hydrophobic properties which enhances the phase separation between water and the template. Butanol also helps to increase the pore diameter since the addition of long-alkyl-chain alcohol increases the volume of the hydrophobic core.[45] Thereby, compared to the titania precursor TiBALD, butanol released during the TiB hydrolysis process assists the phase separation between the water and surfactant so improving the film mesostructure. The surfactant hydrophobic volume was also increased by the presence of butanol inside the micelles; thus the mesophase transformed into a mesostructure with low curvature lamellar phase. In addition, the unit cell of films prepared with TiB is larger than that of film prepared with TiBALD due to the swelling of the surfactant phase by cooperation of the hydrophobic long-alkyl-chain of the butanol.

Comparing with the effects of butanol, ammonium lactate which is released from the hydrolysis of TiBALD, also has effects towards the micelle structure and the final film mesostructure. Brady et al reported that the CMC of C_{12}TAB increased when sodium propionate (ie lactate) was added, thus it was harder to form cationic micelles in the presence of this counterion.[46] However, Umlong et al reported the co-ion like acetate or lactate did not have much effect towards the micellization behavior of

SDS.[47] In addition, lactate is negatively charged at neutral pH (unlike butanol which is neutral), so it probably competes with the SDS to bind to the CTAB, and it hinders the formation of cat-anionic micelles, leading to a less organized mesophase.

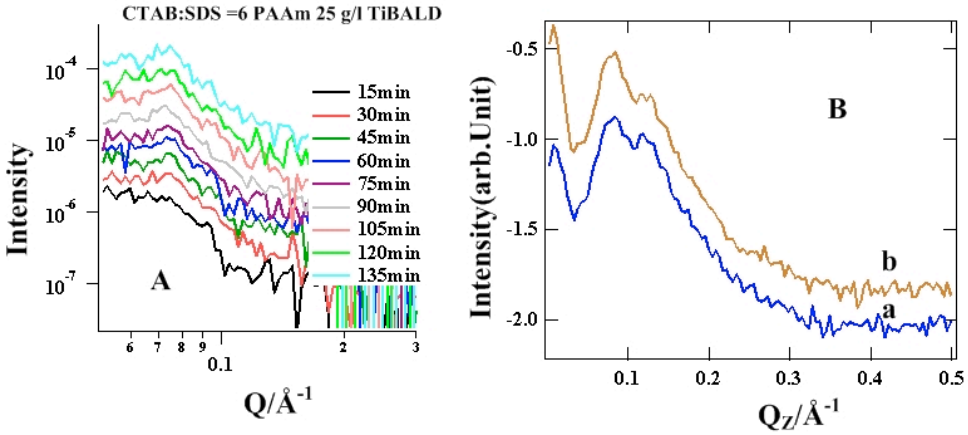

Figure 5.4 *(A)Time-resolved neutron reflectivity patterns and GIXD line profiles of the cat-anionic surfactant/PAAm/titania films (titania precursor TiBALD), in which CTAB: SDS = 6 25 g/lPAAm, TiBALD concentration is 0.026 M. (a) is for the low angle (0.045°) GIXD pattern and (b) is for the higher incident angle (0.173°).*

Table 5.1 *Structure assignments and unit cell parameters from GIXD patterns for interfacial cat-anionic surfactant/PAAm/Titania films with typical mesophases.*

Titania precursor	CTAB: SDS molar ratio	PAAm (g/l)	First peak Q (Å^{-1})	peak assignment	Phase assigned	Unit cell dimension (Å)
TiB (0.037 M)	6	25	0.08	(100)	*Lamellar*	78
	4	25	0.07	(110)	$Im\bar{3}m$	127
	2	25	0.10	(110)	$Im\bar{3}m$	89
	4	12.5	0.08	(001)	*Lamellar*	78
	4	37.5	0.08	(001)	*Lamellar*	78
TiBALD (0.017 M)	6	25	0.08	(110)	$Im\bar{3}m$	111

Error for the peak position is ± 0.01 Å and for the unit cell dimension is ± 1 Å.

5.2.1.3 Subphase Solution

The mixed solution of cat-anionic surfactant, PAAm and TiB is very viscous and gelled during the time-resolved SAXS data collection process, thus the SAXS patterns of film forming solutions with different CTAB/SDS molar ratios (from 6 to 2) were collected in a capillary (**Figure 5.5**). One peak at 0.17 $Å^{-1}$ (37 Å) was observed for all the SAXS patterns. This peak has also been observed for CTAB/SDS/polyelectrolyte solutions and in the earlier stages of the cat-anionic surfactant/polyelectrolyte/silica film forming solutions mentioned in **Section § 4.3.1.3**. It was assigned to the surfactant-only particles formed in these solutions. The intensity of the peak increases with an increase of the SDS concentration, in other words, SDS promotes the aggregation of surfactant micelles into particles. This is because increased SDS concentration decreases the micelle charge thus improving the aggregation and reducing the headgroup area, allowing lower curvature structures to form. The increasing intensity at the low Q range (before Q = 0.1 $Å^{-1}$) also indicates the formation of large-scale structures in the film forming solutions, ie the aggregated surfactant particles.

Comparing the silica film formation mechanism in **Section 3.3.4.3,** as well as the synchrotron SAXS patterns on CTAB/SDS/PAAM/silica film forming solutions, both the interfacial and sub-surface mesophases are quite different, suggesting a similar mechanism may apply, in which the film at the interface is independently formed and does not grow because of the collection of the subphase particles.

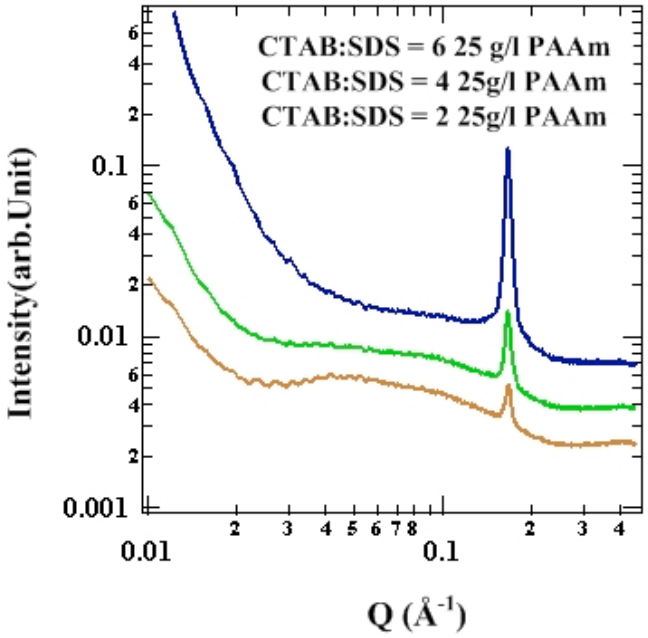

Figure 5.5 *Static SAXS patterns of the cat-anionic surfactant/PAAm/ titania film forming solutions, TiB concentration is 0.037M.*

5.2.1.4 Dry Film Structure

Films synthesized with cat-anionic surfactant/PAAm are flat and thick enough to be removed from the interface on mesh. SAXS patterns on the dry films prepared with different CTAB/SDS molar ratios (from 2-6) , polymer concentrations (from 12.5 g/l to 37.5g/l) ,TiB or TiBALD are shown in **Figure 5.6.**

One broad peak exists around 0.08 $Å^{-1}$ (78 Å) in all of the SAXS patterns, corresponding to the first order peak seen in the interfacial films (**Section § 5.2.1.1** and **Section § 5.2.1.2**), indicating that the film mesostructure was partially preserved. Two diffraction peaks at 0.17 $Å^{-1}$ and 0.24 $Å^{-1}$ were also observed in dried films formed at surfactant molar ratios of CTAB: SDS = 2 and the first diffraction peak intensity is higher than the intensity of the second peak. These two diffraction peaks were also observed for a CTAB: SDS molar ratio of 6 but with the second diffraction peak intensity higher than the first diffraction peak. These two peaks were assigned previously; the first peak comes from CTAB/SDS surfactant particles[48] while the second one is from the excess crystalline CTAB.[49] The intensity of these two peaks is

determined by the relative content of CTAB and SDS in the film forming solution. When the CTAB and SDS mixing ratio is 4, these two diffraction peaks were not visible and all of the mixed surfactant phase is incorporated into the film mesostructures. Theoretically, CTAB: SDS =1 seems the optimum concentration ratio if their charges match, in this case ,SDS concentration is much lower, this is probably because titania anions can fit in around CTAB headgroup and thus replace some SDS when they interact with CTAB/SDS template.

The SAXS patterns on the dry films prepared with different CTAB/SDS ratios, polymer concentrations and TiBALD are shown in **Figure 5.6**. The film structure was also partially retained as most of the SAXS patterns show the first diffraction peak at 0.13 $Å^{-1}$ (d-spacing is 48 Å) which was also seen in the *in situ* films; In addition, the diffraction peak at 0.24 $Å^{-1}$ due to crystalline excess CTAB, was also observed for the highest CTAB/SDS molar ratio of 6.

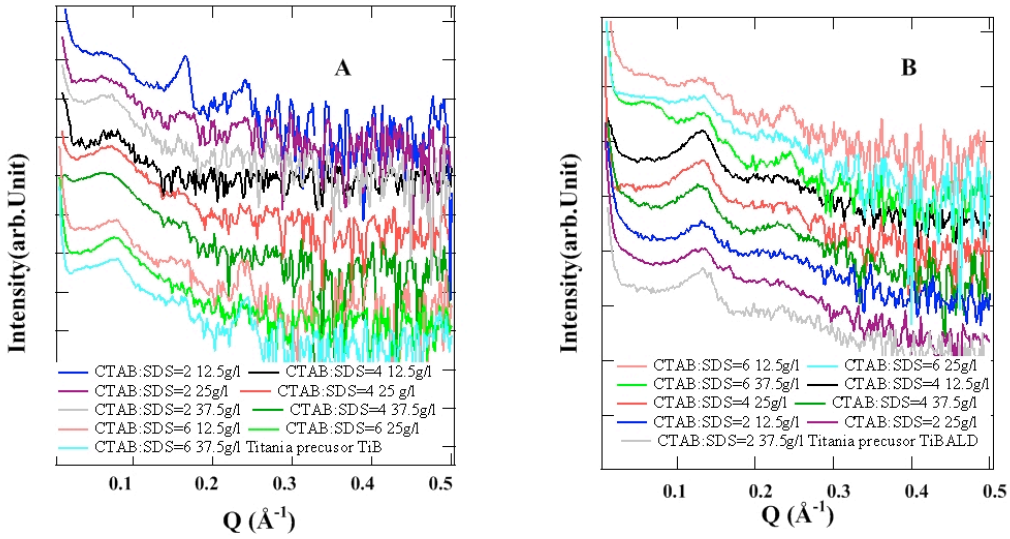

Figure 5.6 *SAXS patterns of the dry CTAB/SDS/PAAm/ titania films, (A)Titania precursor TiB concentration is 0.037 M (B)Titania precursor TiBALD concentration is 0.026 M.*

5.2.1.5 Phase Behaviour of the CTAB/SDS/PAAm/Titania System

Different cat-anionic surfactant molar ratio, PAAm concentration, and TiB concentrations effects towards the final CTAB/SDS/PAAm/titania interfacial films

were investigated and the phase behavior of these systems is depicted in **Scheme 5.1**. When the titania concentration (TiB) was kept low, almost every concentration can form robust flat films. But when the CTAB: SDS molar ratio is increased to 2 and PAAm concentration increased from 25 g/l to 37.5 g/l, then only precipitates rather than films can be observed.

One strategy to synthesize mesostructure materials is to generate an electrostatic interaction between the inorganic component (I^+) and the surfactant headgroup (S^-) either directly or by collection with a counter-charged ion. SDS is known to act as a template for the synthesis of mesostructured titania for some time,[50] and has even been used to prepare interfacial titania films at the air-water interface.[21] The experimental results here indicate that increasing concentration of the SDS and TiB might strengthen the electrostatic interaction between these two species, leading to the formation of precipitates rather than films.

For the CTAB/SDS/PAAM/TiBALD system, films only formed with relatively lower TiBALD concentration, such as 0.026 M. If higher TiBALD concentrations (0.052 M, 0.078 M).were used, no films formed but lumps and precipitates appeared in the solution. In addition, only precipitates were observed no matter what the cat-anionic surfactant molar ratio and PAAm concentration were.

The phase diagram also suggest that the molecules released upon titania precursor hydrolysis are important. When TiBALD is used, it releases the negatively charged amphiphilic lactate anion, film formation only occurs at low precursor concentration where the total charge on the surface of the micelles in the system remains positive. When too much lactate anion and SDS are present, the amount of negative charge outweighs the positive and the surfactant aggregates become negative, favoring precipitation of the titania rather than film formation. Film formation has previously been shown to require a positively charged micellar species.[48]

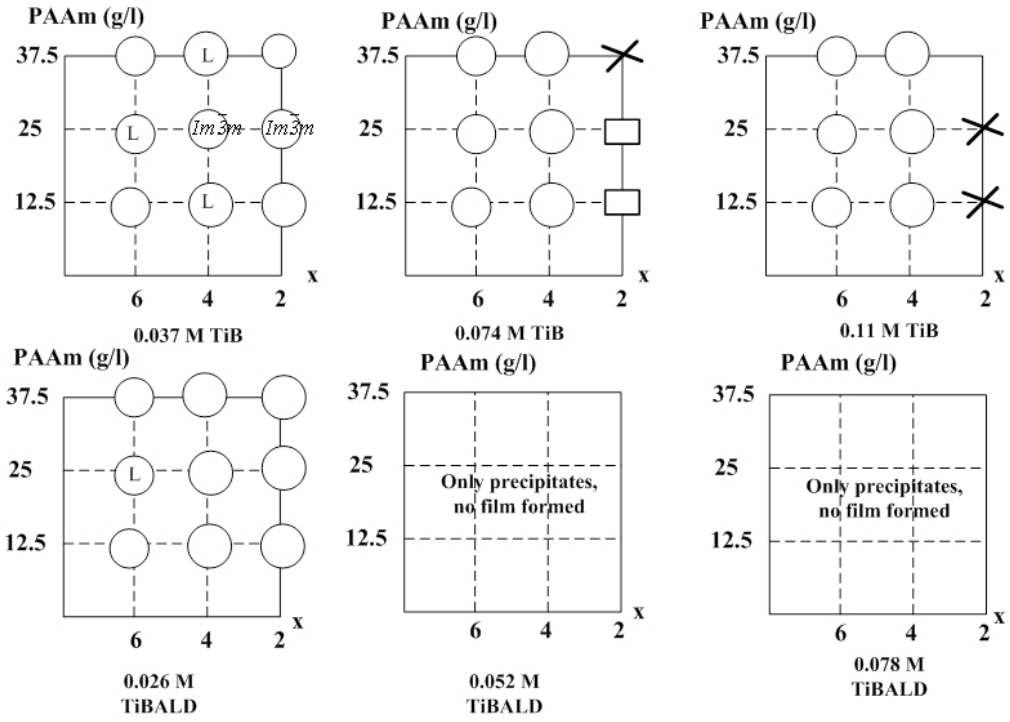

Scheme 5.1 *Phase behaviour of the CTAB/SDS/PAAm/Titania system. Circles mean formation of robust thick films while the solution is opaque, no obvious precipitate can be observed, in addition, the assigned phase and d-spacing is summarised in* ***Table 1****. A square means white precipitate can be seen but no continuous film. Cross mark means no film can be observed only the precipitates. x axis is the CTAB: SDS molar ratio.*

5.2.2 Titania Films Templated by CTAB/SDS/PEO

PEO based nonionic surfactants act as a promising template to yield thick titania walls that are robust towards crystalline, showing the affinity between titania and PEO species.[11, 12, 37] Additionally, PEO are able to stop the titania forming large crystals in the material walls so that the materials mesostructure can be improved and retained better upon calcination. Therefore, cat-anionic surfactant and PEO complex is used to generate titania films with ordered mesostructure.

5.2.2.1 Film Formation Process

Neutron reflectivity experiments with 15 minute resolution were also conducted to follow the development of CTAB/SDS/PEO templated titania films at the air/water interface. Two dimensional neutron reflectivity profiles for cat-anionic surfactant/PEO/titania film forming solutions with different CTAB/SDS molar ratios, as a function of time, are shown in **Figure 5.7 A and B**. When the film was prepared at a molar ratio of CTAB: SDS = 4 , and a PEO concentration of 15 g/l, (**Figure 5.7A)**, three sharp diffraction peaks at 0.05 $Å^{-1}$, 0.07 $Å^{-1}$ and 0.10 $Å^{-1}$ were visible in the first 15 minute scan. These peaks can be related to the (110), (200), (220) reflections of an $Im\bar{3}m$ cubic structure with a d-spacing of 126 Å. However, these three peaks disappeared in the second scan and new peaks began to grow 1hr after mixing. Two peaks at 0.05 $Å^{-1}$ and 0.10 $Å^{-1}$ appeared at this point and grew in intensity over the remaining neutron data collection time. When the SDS concentration was decreased and CTAB: SDS molar ratio increased to 6, the same sharp peaks were observed in the first 15 minute scan and also were not visible at the second 15 minute scan. New peaks appeared around 75 minutes after mixing the solution, which was slower than for the film prepared with a CTAB: SDS molar ratio of 4, (**Figure 5.7 B)**. This suggests that increasing the amount of SDS increases the rate of formation of film structure. This is probably because SDS neutralizes the cat-anionic surfactant, improves the micellar aggregation and promotes the phase separation to the interface, thus it speeds up the mesostructure evolution in the interfacial surfactant/polymer/titania layer. At 75 minutes similarly, two peaks at 0.05 $Å^{-1}$ and 0.10 $Å^{-1}$ appeared and grew intensity with time, becoming stable around 2 hours after mixing the solution.

Titania precursor TiBALD also used to prepare titania films with the CTAB/SDS/PEO complex, as shown in **Figure 5.7 C**. No distinct diffraction peaks could be observed indicating disordered mesostructures formed in the interfacial surfactant/PEO/titania film, which is the similar trend to that seen above in the cat-anionic surfactant/PAAm/titania films.

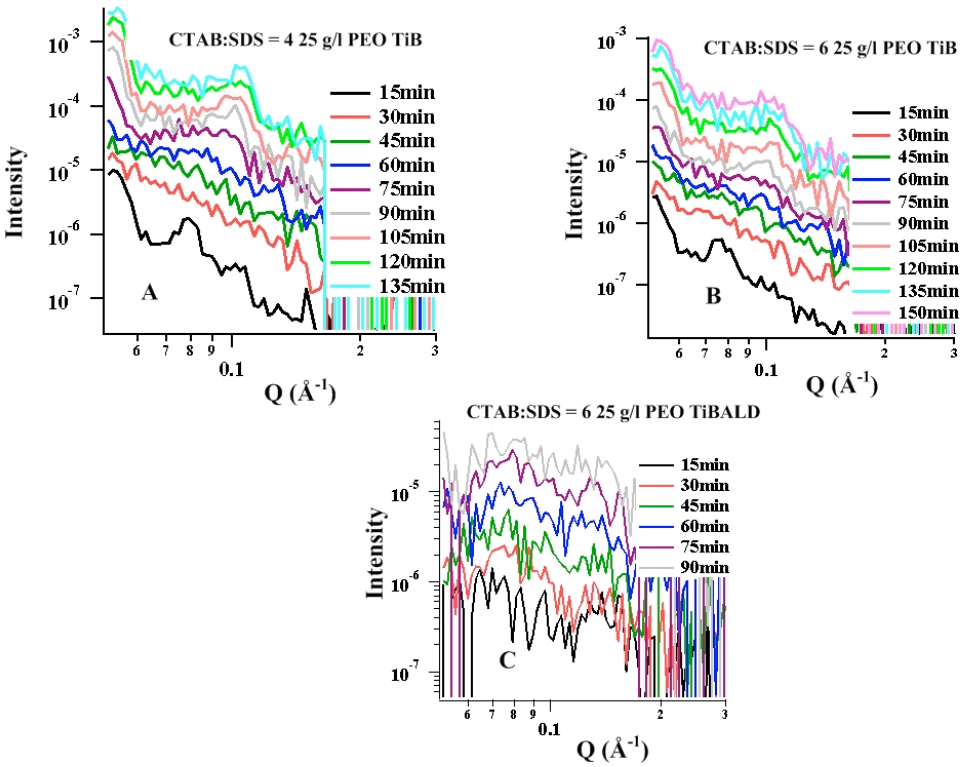

Figure 5.7 *Time-resolved neutron reflectivity of the interfacial cat-anionic surfactant/PEO/Titania films.*

5.2.2.2 Interfacial Film Structure

GIXD patterns were also collected on the cat-anionic surfactant/PEO/titania films at the air/water interface and the structure assignment and unit cell parameter were shown in **Table 5.2**. When films grown with a molar ratio of CTAB: SDS = 2 25 g/l PEO, GIXD of the interfacial film structure is shown in **Figure 5.8 A and B** and line profiles at Q_{xy} = 0.007 Å^{-1} are also shown in **Figure 5.2 C**. For the low incident angle, which is used to probe the top layers of film (**Figure 5.8 C a)**, there are three peaks at 0.15 Å^{-1}, 0.18 Å^{-1} and 0.21 Å^{-1} which may be indexed as the (110) (111) (200) reflections of a $Pn\bar{3}m$ structure with a repeating unit cell of 59 Å. For the higher incident angle, where deeper layers are probed (**Figure 5.8 C b**), three diffraction peaks at 0.17 Å^{-1}, 0.19 Å^{-1} and 0.23 Å^{-1} were visible, which could also be indexed as a $Pn\bar{3}m$ phase with a repeating unit cell of 52 Å, about 7 Å smaller than that of the top

layer film. This is unusual since the drying process normally makes the d-spacing of the top layer smaller than in deeper layers. One possible explanation is that we always collected the low angle GIXD data first, and then followed this by collecting the higher angle GIXD patterns. Since GIXD takes about 45 minute to collect one pattern at one angle, the film was older when the GIXD was taken at the high incident angle, and continuing titania condensation during data collection may result in the apparent shrinkage of the unit cell dimensions. Specular X-ray reflectivity results taken about three hours after pouring the film forming solution confirmed the same diffraction peak positions and mesostructure, as shown in **Figure 5.8 D**. Neutron reflectivity data (**Figure 5.8 E**) however shows much larger structures at very low angles, four peaks around 0.04 $Å^{-1}$, 0.06 $Å^{-1}$, 0.08 $Å^{-1}$, 0.12 $Å^{-1}$ can be indexed to a $Pn\bar{3}m$ structure but with a much bigger d-spacing of 161 Å. The relationship between neutron reflectivity data and x-ray reflectivity data is not clear. But the neutron reflectivity pattern was collected about one hour after pouring the solution and the GIXD patterns were much "older" and taken about five hours after pouring, the decrease of the d-spacing may be due to drying effects.

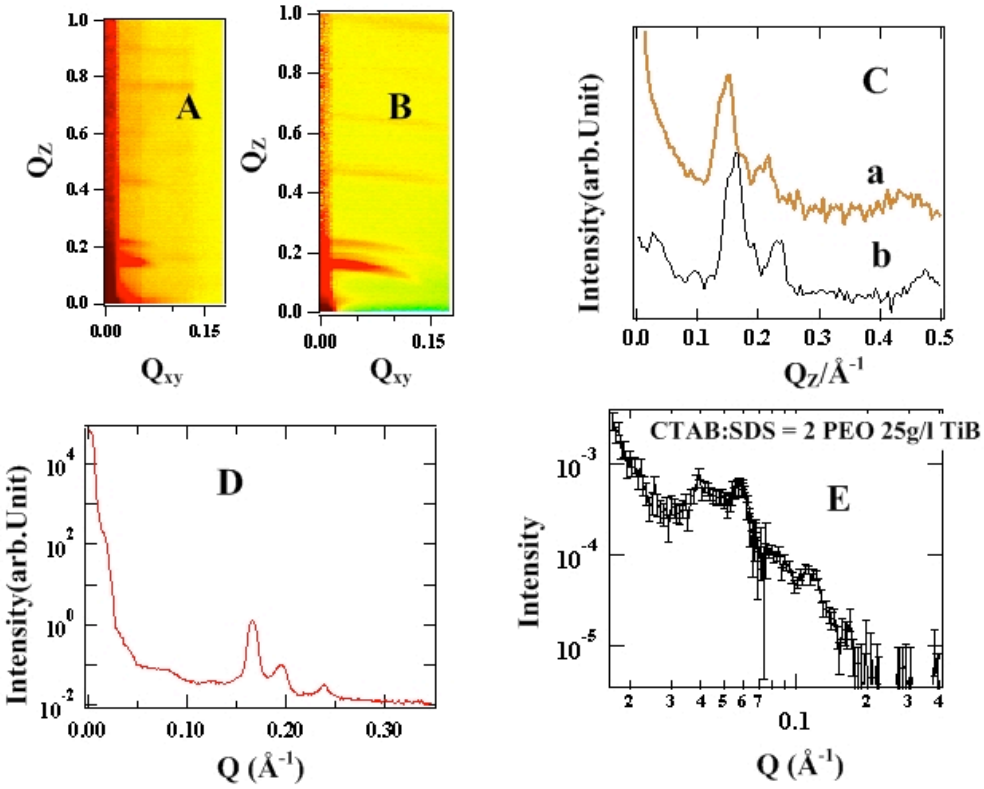

Figure 5.8 *(A and B) GIXD patterns, (C) line profiles at Q_{xy} = 0.007 Å^{-1} (a is top layer and b is deeper layer), (D) Specular X-ray reflectivity pattern, (E) neutron reflectivity pattern of interfacial cat-anionic surfactant/PEO/titania films (all the samples were prepared with a molar ratio of CTAB: SDS = 2, 25 g/l PEO and a TiB concentration of 0.037 M).*

The film mesostructure is sensitive to the cationic-anionic surfactant molar ratios, as shown in **Figure 5.9**. When the CTAB: SDS = 8, the GIXD line profile of titania films synthesized with 25 g/l PEO displays a cubic structure. Peaks at 0.10 Å^{-1}, 0.15Å^{-1} and 0.18Å^{-1} were observed and could be assigned as the (110), (200), (211) reflections of an $Im\bar{3}m$ space group, with a repeating unit cell of 88 Å (as shown in **Figure 5.9 A blue line**). When the molar ratio of CTAB: SDS = 6 (**Figure 5.9 red line**), the GIXD line profile shows two diffraction peaks 0.19 Å^{-1} and 0.24 Å^{-1}, which may be indexed as a distorted $Pn\bar{3}m$ mesophase or alternatively may be assigned as

an intermediate mesophase between $Im\bar{3}m$ and $Pn\bar{3}m$. When the molar ratio of CTAB: SDS = 4 (**Figure 5.9 green line**), three diffraction peaks at 0.17Å^{-1}, 0.19Å^{-1}, and 0.24 Å^{-1} indicate a $Pn\bar{3}m$ phase with a repeating unit cell of 52 Å. When CTAB: SDS = 2, as described above, the mesostructure was assigned to $Pn\bar{3}m$ with a repeating unit cell of 52 Å as well. However, the intensity of the diffraction peaks varies, it is probably due to the different thickness or volume fraction of the surfactant bilayer in the cubic phase.[51, 52] Or this structure may relate to a mixture of two lamellar phases, 0.17 Å^{-1} may relate to one lamellar phase containing CTAB and SDS,[48] and 0.24 Å^{-1} can be assigned to the lamellar phase that only contains CTAB.[49] However, the assignment of the cubic phase is more preferable, first because these two peaks positions are related to $\sqrt{2}$, and the second reason is that when the CTAB: SDS concentration is around 8, positively charged CTAB in the cat-anionic surfactant plays the main role to determine the final mesostructure; however, when negatively charged SDS concentration increases, the interaction between these two oppositely charged surfactant should be stronger, therefore CTAB should be more likely to stay inside the cat-anionic micelles rather than get out to template titania by itself. The above result indicates that increasing the SDS content induces mesophases with higher surfactant micelle curvature, which is similar to the trends observed for the cat-anionic surfactant/PAAm/titania films discussed above.

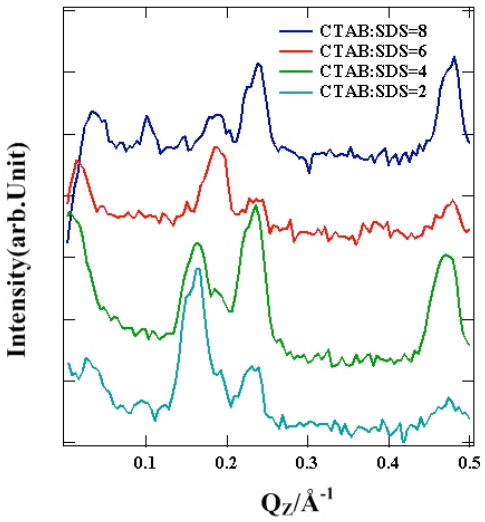

Figure 5.9 *Cat-anionic surfactant molar ratio effects on the CTAB/SDS/PEO/titania films, in which PEO concentration is 25 g/l and the TiB concentration is 0.037M.*

The role of polymer concentration in the determination of the final film mesostructure was also investigated. The GIXD pattern line profiles for titania films prepared with cat-anionic surfactant (at a molar ratio of CTAB: SDS = 4) and different PEO concentrations (12.5 g/l to 37.5 g/l) are shown in **Figure 5.10**. Films prepared with 12.5 g/l PEO, had three diffraction peaks at 0.17 $Å^{-1}$, 0.20 $Å^{-1}$and 0.24 $Å^{-1}$ which could be assigned as a $Pn\bar{3}m$ structure with a repeating unit cell of 52 Å; The mesostructure of films prepared with 25 g/l PEO was previously described as $Pn\bar{3}m$ phase with a repeating unit cell of 52 Å. When the polymer concentration increased to 37.5 g/l, the first diffraction peak is at 0.16 $Å^{-1}$, another two diffraction peaks exist, also assigned as a $Pn\bar{3}m$ phase. The fist diffraction peak suggests a d-spacing of 55 Å. The above results suggest PEO does not change the film mesophase but the size of the repeating unit cell increases slightly as more polymer is added to solution.

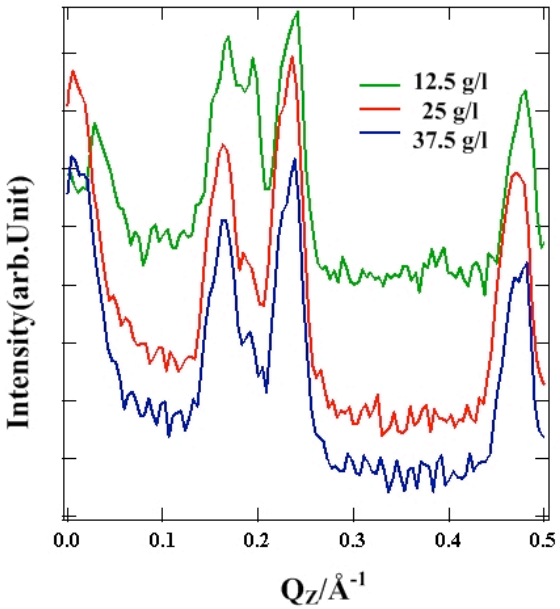

Figure 5.10 *Polymer concentration effects on the cat-anionic surfactant/PEO/titania films, in which the molar ratio of CTAB: SDS = 4 and TiB concentration is 0.037 M.*

Time-resolved neutron reflectivity indicated that PEO films prepared with titania precursor TiBALD are again less ordered than films prepared with TiB. The GIXD line profiles show the mesostructure for the top layer and deeper layer of the interfacial films are similar, having two relatively broad diffraction peaks around 0.12Å^{-1} and 0.17 Å^{-1} which might relate to a distorted $Im\bar{3}m$ structure with a repeating unit cell of 74 Å.

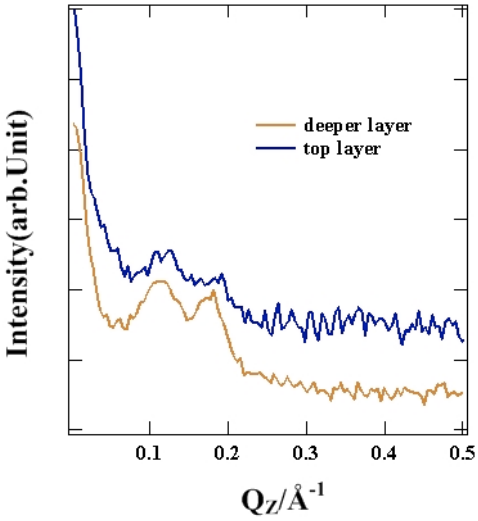

Figure 5.11 *Line profiles from GIXD patterns of the cat-anionic surfactant/PEO/titania films (titania precursor TiBALD), in which the molar ratio of CTAB: SDS = 6, 25 g/l PAAm, and TiBALD concentration was 0.017M.*

Table 5.2 *Structure assignments and unit cell parameters from GIXD patterns for interfacial cat-anionic surfactant/PEO/Titania films with typical mesophases.*

Titania precursor	CTAB: SDS molar ratio	PAAm(g/l)	First peak Q ($Å^{-1}$)	peak assignment	Phase assigned	Unit cell Dimension (Å)
TiB (0.037 M)	8	25	0.10	(110)	$Im\bar{3}m$	88
	6	25	0.19	(110)	-	-
	4	25	0.17	(110)	$Pn\bar{3}m$	52
	2	25	0.17	(110)	$Pn\bar{3}m$	52
	4	12.5	0.17	(110)	$Pn\bar{3}m$	52
	4	37.5	0.16	(110)	$Pn\bar{3}m$	55
TiBALD (0.017 M)	6	25	0.12	(110)	$Im\bar{3}m$	74

- means difficult to determine the phase and cell parameter; Error for the peak position is ± 0.01 Å and for the unit cell dimension is ± 1 Å.

5.2.2.3 Dry Film Structure

SAXS patterns of the dry cat-anionic surfactant/PEO/Titania films were shown in **Figure 5.12**. The CTAB: SDS molar ratios were decreased from 8 to 2 using the titania precursor is TiB (**Figure 5.12 A)**, but two distinct peaks at 0.17 $Å^{-1}$ and 0.24 $Å^{-1}$ could be observed in all the SAXS patterns except that again the relative peak intensities are different. These two peaks were assigned to an $Im\bar{3}m$ mesostructure with a repeating unit cell of 52 Å. When CTAB/SDS molar ratios from 6 to 2 and the titania precursor TiBALD was used (**Figure 5.12 B**), similar two distinct peaks at 0.17 $Å^{-1}$ and 0.24 $Å^{-1}$ can be observed in all the SAXS patterns. The relative peak intensities are different according to the CTAB: SDS molar ratios and higher polymer concentrations induce a less ordered mesostructure, which is similar to what has observed with the dry films prepared with TiB. If the polymer concentration is high, PEO can interact with titania strongly and can also interact with SDS by hydrophobic interactions, but does not strongly interact with CTAB/SDS complexes since the CTAB component is higher than SDS component in this complex and micelles are positively charged. Therefore, the film formed at high polymer concentration maybe only contains PEO and titania with less cat-anionic surfactants, which results in a less ordered mesostructure.

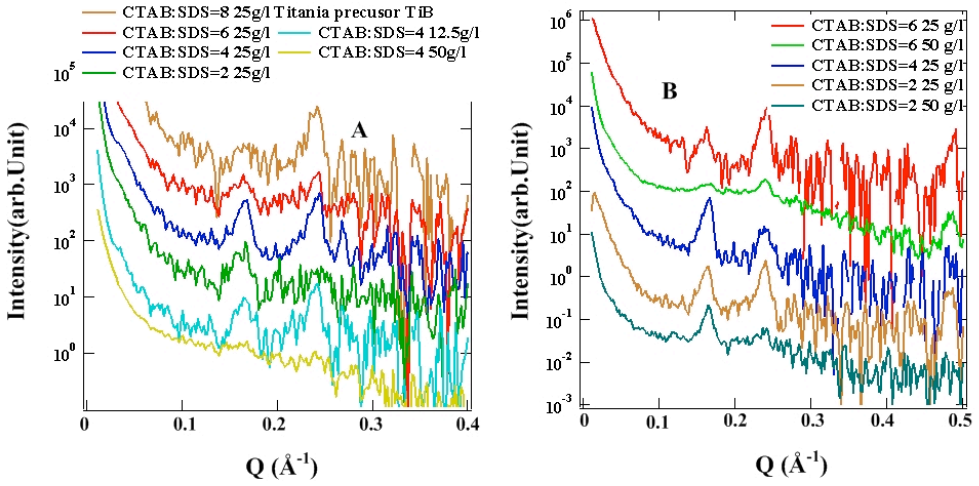

Figure 5.12 *SAXS patterns of the dry cat-anionic surfactant-PEO- titania films, (A) titania precursor TiB concentration is 0.037 M. (B) titania precursor TiBALD concentration is 0.017 M.*

5.2.2.4 Phase Behaviour of the CTAB/SDS/PEO/Titania System

Different cat-anionic surfactant molar ratio, PEO concentration, and Titanium precursor concentration effects towards the final CTAB/SDS/PAAm/Titania (TiB) interfacial films were investigated and the phase behavior of these systems was summarized in **Scheme 5.2**.

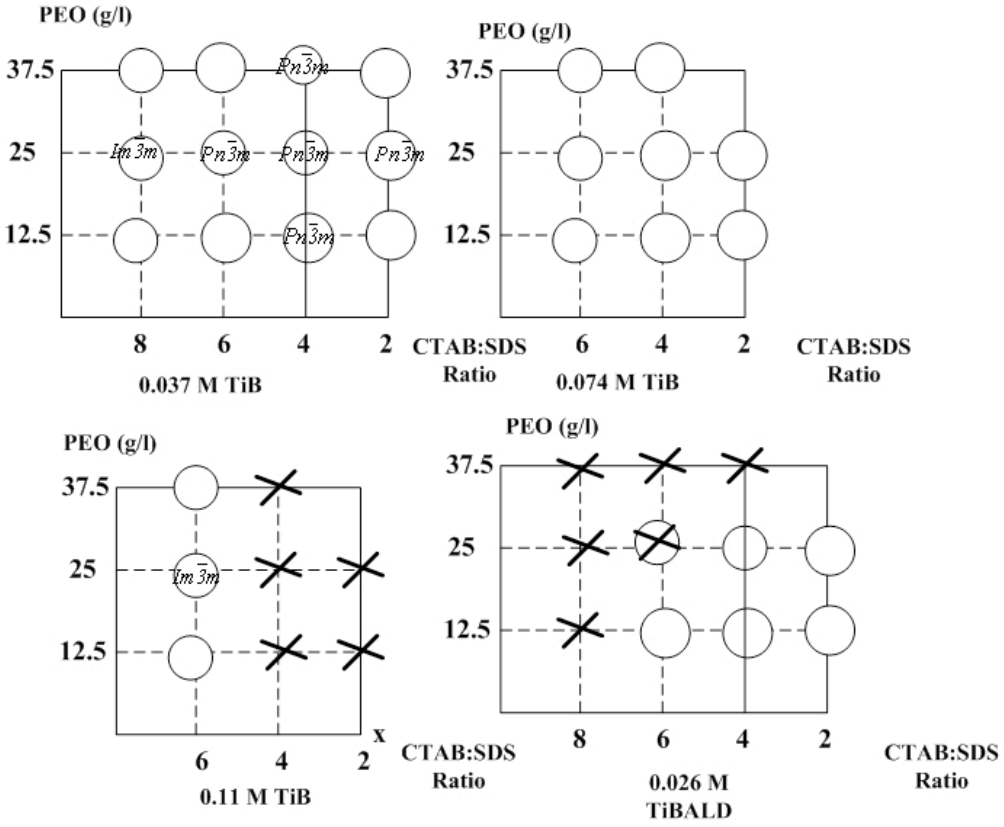

Scheme 5.2 *Phase behaviour of the CTAB/SDS/PEO/titania system. Circles indicate formation of robust thick films and film structures which have been investigated are shown inside the circle. Crosses mean no film was observed, only precipitates.*

5.2.3 Post Synthesis Treatment

Titania has three crystalline polymorphs: anatase, rutile and brookite and can also form an amorphous phase. Rutile is thermodynamically stable compared to anatase and brookite, although thermodynamic stability also depends on particle-size and

rutile is typically only formed at very high temperatures.[53] Rutile can be used in electronics industry applications such as capacitors, power circuits due to its high dielectric constant and high electrical resistance. Anatase has a large band gap energy and suitable redox potentials for practical use in photo-catalysis and photo-electronics and forms at lower temperatures. Various methods have been attempted to increase titania crystallinity since it is initially amorphous in most surfactant-templated materials, without losing the mesophase structure. These include incremental heat treatments, delayed rapid crystallization and substrate-assisted crystallization and have achieved some progress in improving crystallinity. However, the destruction of mesoporous structure in these methods as the crystallites grow still leads to a decrease of porosity and surface area.[14, 54]

Until now, thin walls in titania mesostructured materials resulting in low thermal stability is a serious limitation to their performance. Here, the titanium oxide films prepared at the air/water interface are initially amorphous titania, since no crystalline diffraction peaks were observed at high angles in the dried films. These films so far are also not thermally strong since they fell apart after calcination at 450°C, probably due to a lack of sufficient titania inside the film. Thus the cat-anionic surfactant/polymer/titania films were soaked in the titania precursor TiB to improve the titania loading. The TiBALD precursor was also tried but as it is supplied in a solution containing 50wt% water the precursor solution dissolved the hybrid film. SAXS patterns of the as-synthesized, TiB soaked samples and the same samples with template removed by acidic ethanol wash, or by calcination are shown in **Figure 5.13**.

Only one broad peak exists in all patterns after soaking in TiB, indicating that the micelles in the film probably rearranged themselves into a less ordered structure when the films were soaked in the TiB precursor, and may also have been swollen by butanol generated by the precursor hydrolysis since this peak moves to lower angles in the scattering pattern. However, the increased intensity of the peak indicates the titania content did increase within these films. This altered mesostructure was retained when the surfactant was removed by washing. Although the film physical strength

was improved by the soaking procedure, since film did not crack even after calcination, the mesostructure was completely lost when they were calcined.

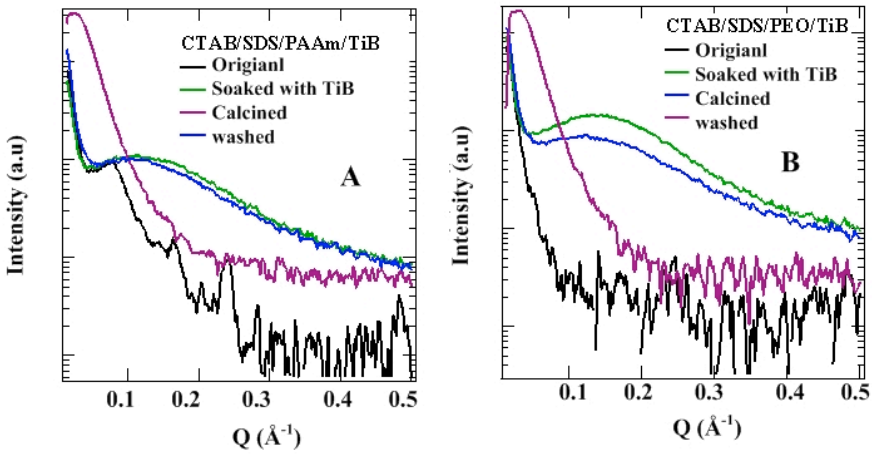

Figure 5.13 *Titania films prepared by soaking dry CTAB/SDS/polymer/titania free standing films in TiB precursor. Film was prepared with (A) CTAB: SDS = 6 12.5 g/l PAAm, TiB 0.037M; (B) CTAB: SDS = 6 25 g/l PEO, TiB 0.037M.*

The hybrid titania films were also exposed under titania precursor vapor after drying in the air as an alternate means to increase titania content in the films. Five titania precursors were used: TiB, TiBALD, titanium(IV) ethoxide, titanium propoxide, and titanium tetrachloride. However, only titanium tetrachloride was possibly to evaporate into the films as the vapour pressure of the other precursors was too high. Cat-anionic surfactant/polymer (PEO, and PAAm)/titania films were used as dry templates for titanium precursor evaporation but their SAXS patterns did not show much difference before and after vapour treatment.

CTAB/SDS/PAAm/titania films were put under $TiCl_4$ vapor at a very low pressure of 9 mbar (the vapor pressure for $TiCl_4$ is 66 mbar). SAXS patterns of the films which were exposed to the $TiCl_4$ vapor for 1 day, 2 day and calcined samples after 2 day evaporation, as shown in **Figure 5.14**. However, the mesostructure was lost after calcination and the calcined film fell apart probably because titanium tetrachloride hydrolyses very fast and was only deposited in a thin layer on top of the dry template, stopping the continuous accumulation into the deeper layers of the dry template films.

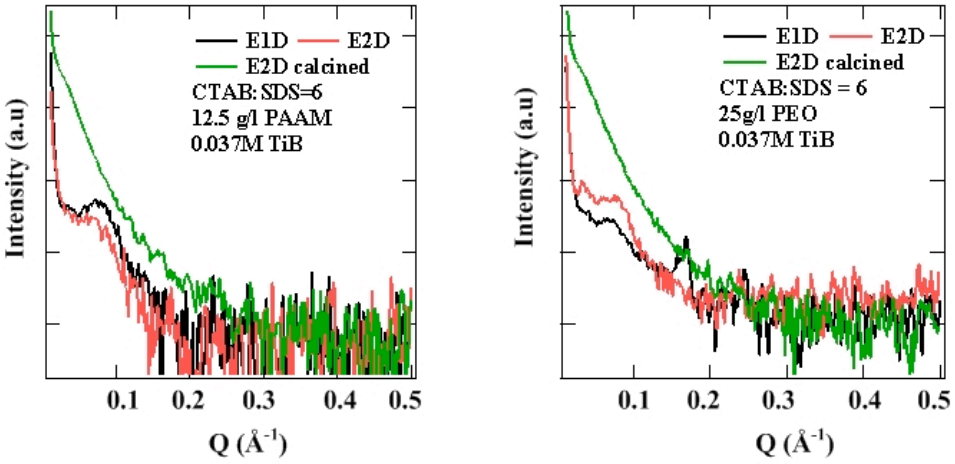

Figure 5.14 *Titania films prepared by evaporating dry CTAB/SDS/polymer/titania free standing films under $TiCl_4$ vapor at low pressure of 9 mbar.*

5.2.4 Titania Films Prepared with Cross-linked Dry Polymer/surfactant Film

Water content and humidity play important roles to control the speed of the titania precursor hydrolysis, thus dry surfactant/polymer films with very limited water content were tried as a potential soft template to prepare titania films. Cross-linked thin block copolymer films sitting on a substrate have previously been successfully used to templated mesoporous silica and titania films.[55] Our mesostructured polymer/surfactant films are easier to prepare, since they do not require complicated synthesis of block copolymers, and use only readily available components.

Soaking dry the CTAB/PEI films and CTAB/SDS/polymer (PEI, PEO, and PAAm) films sitting on an open mesh directly in TiB precursor, resulted in breaking of the polymer film and an intact film was difficult to recover. The cross-linker EGDGE contains two epoxides that are susceptible to nucleophilic addition reactions involving the amine groups on the polymer, so it was used to reinforce the CTAB/PEI film and its effects on the mesostructure were investigated in **Section § 3.2.1**. Therefore, a first trial was conducted by soaking cross-linked CTAB/PEI dry films into the TiB precursor solution. Because of the cross-linker, polymer films were still continuous even after soaking in the titania species. The titania precursors were effectively

incorporated inside the polymer films and subsequently condensed, leading to a significant increase in film thickness and volume. Film physical strength was improved since the film morphology was retained even after calcination. The SAXS pattern (**Figure 5.15**) indicates the micelles inside the original polymer films reorganized and the soaking technique disorganizes the initial polymer/surfactant structure. Unfortunately, film mesostructure in these materials was also lost after calcination. Further efforts are underway to optimize the soaking conditions and calcination conditions such as the calcination temperature to get robust ordered porous titania films. A suitable calcination temperature will not only remove the surfactant template and keep the film mesostructure, but also will able to generate a high degree of crystallinity. In addition, the film wall crystallinity needs further investigation. Cross-linker effects on PAAm/CTAB/SDS films should also be studied in future investigations, and cross-linking of PEO containing films using a different cross-linking method could also be studied.

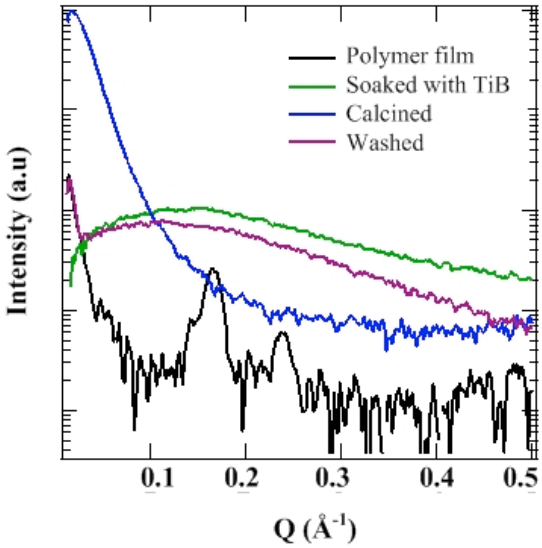

Figure 5.15 *Titania films prepared by soaking dry cross-linked CTAB/SDS/SPEI free standing films into TiB precursor. Film was prepared with CTAB: SDS = 2, 50g/l SPEI, 0.04 M EGDGE.*

5.3 Surfactant and Polyelectrolyte Templated Iron Oxide Films

In recent work by others, when mixing high molecular weight PEI solution with precursor $FeCl_2$, thick red iron oxide films were observed at the air/water interface, so this could also be a potential system to synthesize mesostructured iron oxide film via use of surfactant micelles as a structure directing agent. Here, we employed CTAB and SDS as separate templates and also the CTAB/SDS co-surfactant, to template iron oxide films at the air/water interface. **Figure 5.16** is an example of a dry free-standing iron oxide film on a mesh; the film is red and thick. The ferric precursor $FeCl_4.H_2O$ was first dissolved in water and the pH value was about 2.15, since the hexaaquairon(II) ion $[Fe(H_2O_6]^{2+}$ is acidic as a result of the reaction

$$[Fe(H_2O_6]^{2+} + H_2O \rightarrow [Fe(H_2O)_5(OH)]^{+} + H_3O^{+} \qquad \textbf{(5.1)}$$

When LPEI was mixed with ferric chloride solution a dark green color solution with some precipitates was observed, due to the reaction of iron ions with LPEI chain amine group resulting in precipitation of $[Fe(H_2O)_4(OH)_2]$ which is dark green in color. Red orange iron oxide film formed across the surface within one hour.

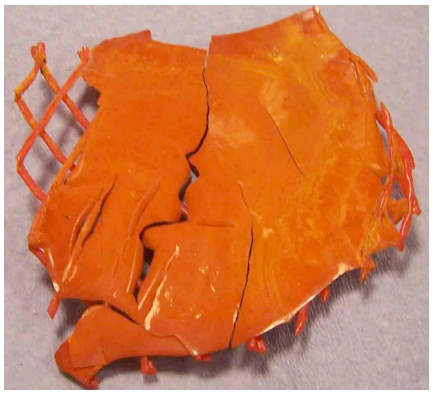

Figure 5.16 *Photo of a typical free-standing iron oxide films prepared using PEI and CTAB at the air/water interface. The side of each mesh square is 1cm.*

5.3.1 Interfacial Film Structure

A range of different surfactant and polymer concentrations were used to prepare iron oxide films. However, a mesostructured film was only observed with 0.02 M

SDS, 20 g/l LPEI at pH 12. GIXD patterns were collected on the SDS/LPEI/iron oxide films at the air/water interface and shown in **Figure 5.17 A and B**. For the high angle GIXD probing the deeper layers, two broad diffraction peaks at 0.08 $Å^{-1}$ and 0.16 $Å^{-1}$ in the line profiles can be indexed as a lamellar phase with a d-spacing of 82 Å (as shown in **Figure 5.17 C b**). For the top layer of the film, measured at low incident angle, no distinct diffraction could be observed. This is not surprising if the film has a lamellar structure, since at this angle only about the top 100 Å of the film is probed, and if the lamellar repeat is 82 Å very few repeating layers will be included in the scattering volume, so no diffraction peaks will be observed.

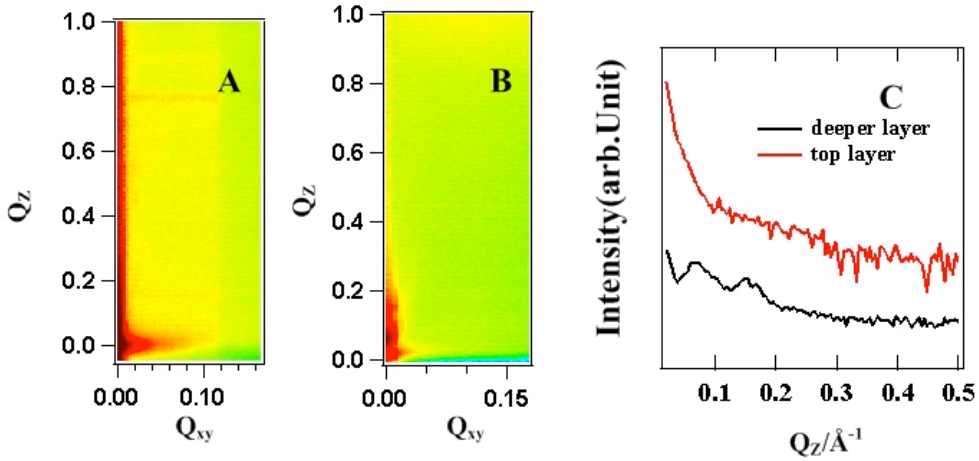

Figure 5.17 *GIXD patterns (A and B) and line profiles at Q_{xy} = 0.007 $Å^{-1}$ (C) of the interfacial iron oxide films templated by SDS (0.02M) and LPEI 20g/l at pH = 12.*

5.3.2 Dry Film Structure

SAXS patterns of the dry as-synthesized SDS/LPEI/iron oxide film and films where the template was removed by ethanol wash and calcination at 450 °C are shown in **Figure 5.18**. An ordered lamellar phase was retained after film drying (a), but the lamellar phase collapsed when the template was removed either by washing or calcination. This is also not very surprising since once the surfactant and polymer is removed, the iron oxide layers will collapse as there is no three dimensional connectivity to keep them apart. Four different temperatures of 200 °C, 300 °C, 400°C and 500 °C[56] were also used to get rid of the template and the wall crystallinity

was also checked by wide angle X-ray diffraction patterns, however, none of them show any crystallinity in the pore walls.

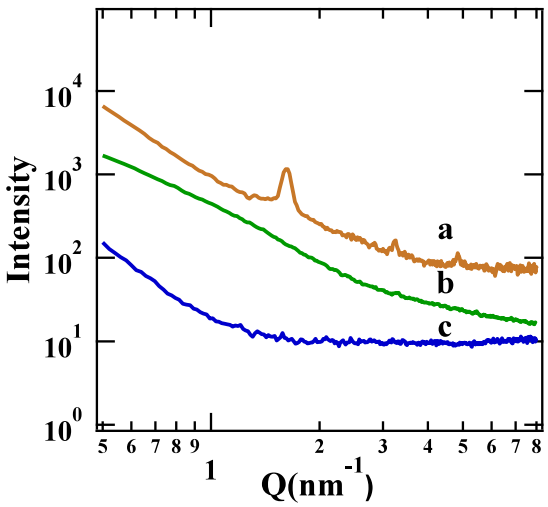

Figure 5.18 *SAXS patterns of (a) as synthesized dry free-standing iron oxide films templated by SDS (0.02M) LPEI 20g/l at pH = 12; (b) sample with templated washed out by ethanol and (c) calcined sample.*

SDS/LPEI/Iron oxide films were successfully synthesized under an alkaline condition of pH = 12. Cationic surfactant was previously reported to form a less organized mesoporous structure because of the weaker electrostatic interaction between surfactant and inorganic species for iron oxides.[27] For our mesoporous iron oxide films, when the film formation solution is highly alkaline, the iron oxide framework is essentially cationic and thus the formation of a mesophase could be explained through a strong interaction between the surfactant and inorganic species in a S^-I^+ pathway, where S^- is the anionic surfactant SDS and I^+ is the inorganic species. Recently, lamellar mesostructured iron oxide powder materials were also reported.[33] In future, other anionic surfactant with bigger head group or longer hydrophobic tail may be able to be used to fabricate iron oxide films with various mesophases, by considerating the micelle packing parameter and curvature.

5.4 Conclusion

In summary, thick titania films were prepared with cat-anionic surfactant and polymers (PAAm and PEO) at the air/water interface. Time-resolved neutron reflectivity was used to follow the film formation process and the GIXD technique was used to clarify the interfacial mesostructure. Cat-anionic surfactant ratios, the chemical nature of the polymer, polymer concentration, and the chemical nature of titania precursors were used to govern the mesophase geometry of the polymer/titania hybrid films. Phase diagrams for the titania forming systems were drawn, illustrating the lamellar and different cubic phases ($Im\bar{3}m$, $Pn\bar{3}m$) that were obtained.

Those films were robust enough to be removed from the interface and the mesostructures were partially retained on drying. However, these titania films have a low thermal stability due to a relatively low titania content in the film and fell apart after calcination. Thus two post-synthesis strategies were employed: either soaking the dry polymer/titania hybrid film in the neat titania precursor or exposing the film under titania precursor vapor. The film physical strength was improved but unfortunately, the mesopores were still not able to be retained after calcination.

Dry cross-linked surfactant/polymer films were also used to attempt to directly template titania films. Titania precursor was able to effectively be incorporated in the polymer/surfactant matrix, but it disorganized the initial film structure. Further efforts are underway to optimize the soaking conditions to get robust ordered titania films via dry polymer templates.

Under highly alkaline conditions, robust SDS/LPEI/iron oxide films with an ordered lamellar mesostructure were also spontaneously formed at the air/water interface. The mesostructure could be retained in the dry iron oxide films. The lamellar mesophase collapsed when the template is removed either by calcination or washing. To our knowledge, this is the first time thick iron oxide films were formed at the air/water interface, which might be useful in exploring their potential applications in future.

5.5 References

(1) N. Husing, B. Launay, D. Doshi, and G. Kickelbick, *Chemistry of Materials* **14**(6), 2429 (2002).

(2) J. Blanchard, S. Barbouxdoeuff, J. Maquet, and C. Sanchez, *New Journal of Chemistry* **19**(8-9), 929 (1995).

(3) P. C. A. Alberius, K. L. Frindell, R. C. Hayward, E. J. Kramer, G. D. Stucky, and B. F. Chmelka, *Chemistry of Materials* **14**(8), 3284 (2002).

(4) G. J. D. A. Soler-Illia, and C. Sanchez, *New Journal of Chemistry* **24**(7), 493 (2000).

(5) G. J. D. A. Soler-Illia, E. Scolan, A. Louis, P. A. Albouy, and C. Sanchez, *New Journal of Chemistry* **25**(1), 156 (2001).

(6) G. J. D. A. Soler-Illia, A. Louis, and C. Sanchez, *Chemistry of Materials* **14**(2), 750 (2002).

(7) P. D. Yang, D. Y. Zhao, D. I. Margolese, B. F. Chmelka, and G. D. Stucky, *Chemistry of Materials* **11**(10), 2813 (1999).

(8) P. D. Yang, D. Y. Zhao, D. I. Margolese, B. F. Chmelka, and G. D. Stucky, *Nature* **396**(6707), 152 (1998).

(9) L. Kavan, J. Rathousky, M. Gratzel, V. Shklover, and A. Zukal, *Microporous and Mesoporous Materials* **44**, 653 (2001).

(10) M. Gratzel, *Nature* **414**(6861), 338 (2001).

(11) D. Grosso, G. J. D. A. A. Soler-Illia, F. Babonneau, C. Sanchez, P. A. Albouy, A. Brunet-Bruneau, and A. R. Balkenende, *Advanced Materials* **13**(14), 1085 (2001).

(12) E. L. Crepaldi, G. J. D. A. Soler-Illia, D. Grosso, F. Cagnol, F. Ribot, and C. Sanchez, *Journal of the American Chemical Society* **125**(32), 9770 (2003).

(13) E. L. Crepaldi, G. J. D. A. Soler-Illia, D. Grosso, and M. Sanchez, *New Journal of Chemistry* **27**(1), 9 (2003).

(14) D. Grosso, G. J. D. A. Soler-Illia, E. L. Crepaldi, F. Cagnol, C. Sinturel, A. Bourgeois, A. Brunet-Bruneau, H. Amenitsch, P. A. Albouy, and C. Sanchez, *Chemistry of Materials* **15**(24), 4562 (2003).

(15) S. Y. Choi, M. Mamak, N. Coombs, N. Chopra, and G. A. Ozin, *Advanced Functional Materials* **14**(4), 335 (2004).

(16) I. Moriguchi, H. Maeda, Y. Teraoka, and S. Kagawa, *Journal of the American Chemical Society* **117**(3), 1139 (1995).

(17) I. Moriguchi, K. Sonoda, K. Matsuo, S. Kagawa, and Y. Teraoka, *Chemical Communications* (15), 1344 (2001).

(18) M. Oswald, V. Hessel, and R. Riedel, *Thin Solid Films* **339**(1-2), 284 (1999).

(19) F. Facca, G. Puccetti, and R. M. Leblanc, *Colloids and Surfaces a-Physicochemical and Engineering Aspects* **149**(1-3), 89 (1999).

(20) M. J. Henderson, D. King, and J. W. White, *Australian Journal of Chemistry* **56**(9), 933 (2003).

(21) M. J. Henderson, D. King, and J. W. White, *Langmuir* **20**(6), 2305 (2004).

(22) B. Martinez, X. Obradors, L. Balcells, A. Rouanet, and C. Monty, *Physical Review Letters* **80**(1), 181 (1998).

(23) A. Kumar, B. Sahoo, A. Montpetit, S. Behera, R. F. Lockey, and S. S. Mohapatra, *Nanomedicine-Nanotechnology Biology and Medicine* **3**(2), 132 (2007).

(24) R. J. G. Lopes, A. M. T. Silva, and R. M. Quinta-Ferreira, *Applied Catalysis B-Environmental* **73**(1-2), 193 (2007).

(25) M. V. Reddy, T. Yu, C. H. Sow, Z. X. Shen, C. T. Lim, G. V. S. Rao, and B. V. R. Chowdari, *Advanced Functional Materials* **17**(15), 2792 (2007).

(26) S. H. Tolbert, P. Sieger, G. D. Stucky, S. M. J. Aubin, C. C. Wu, and D. N. Hendrickson, *Journal of the American Chemical Society* **119**(37), 8652 (1997).

(27) D. N. Srivastava, N. Perkas, A. Gedanken, and I. Felner, *Journal of Physical Chemistry B* **106**(8), 1878 (2002).

(28) F. Jiao, and P. G. Bruce, *Angewandte Chemie-International Edition* **43**(44), 5958 (2004).

(29) A. S. Malik, M. J. Duncan, and P. G. Bruce, *Journal of Materials Chemistry* **13**(9), 2123 (2003).

(30) G. Wirnsberger, K. Gatterer, and P. Behrens, *Journal of Materials Chemistry* **8**(7), 1509 (1998).

(31) G. Wirnsberger, K. Gatterer, H. P. Fritzer, W. Grogger, B. Pillep, P. Behrens, M. F. Hansen, and C. B. Koch, *Chemistry of Materials* **13**(5), 1453 (2001).

(32) A. Lezau, M. Trudeau, G. M. Tsoi, L. E. Wenger, and D. Antonelli, *Journal of Physical Chemistry B* **108**(17), 5211 (2004).

(33) A. Mitra, C. Vazquez-Vazquez, M. A. Lopez-Quintela, B. K. Paul, and A. Bhaumik, *Microporous and Mesoporous Materials* **131**(1-3), 373 (2010).

(34) X. L. Liu, Y. F. Gao, C. X. Cao, H. J. Luo, and W. Z. Wang, *Langmuir* **26**(11), 7671 (2010).

(35) M. B. Dickerson, K. H. Sandhage, and R. R. Naik, *Chemical Reviews* **108**(11), 4935 (2008).

(36) N. Kroger, and K. H. Sandhage, *Mrs Bulletin* **35**(2), 122 (2010).

(37) B. Ma, J. Ma, and G. K. L. Goh, *Journal of Materials Science* **43**(12), 4297 (2008).

(38) X. Auvray, T. Perche, R. Anthore, C. Petipas, I. Rico, and A. Lattes, *Langmuir* **7**(10), 2385 (1991).

(39) T. Y. Peng, D. Zhao, K. Dai, W. Shi, and K. Hirao, *Journal of Physical Chemistry B* **109**(11), 4947 (2005).

(40) V. Luca, J. N. Watson, M. Ruschena, and R. B. Knott, *Chemistry of Materials* **18**(5), 1156 (2006).

(41) N. Agoudjil, and T. Benkacem, *Desalination* **206**(1-3), 531 (2007).

(42) R. Zana, *Advances in Colloid and Interface Science* **57**, 1 (1995).

(43) J. Armstrong, B. Chowdhry, J. Mitchell, A. Beezer, and S. Leharne, *Journal of Physical Chemistry* **100**(5), 1738 (1996).

(44) K. W. Kwon, M. J. Park, J. Hwang, and K. Char, *Polymer Journal* **33**(5), 404 (2001).

(45) H. Choi, E. Stathatos, and D. D. Dionysiou, *Thin Solid Films* **510**(1-2), 107 (2006).

(46) J. E. Brady, D. F. Evans, G. G. Warr, F. Grieser, and B. W. Ninham, *Journal of Physical Chemistry* **90**(9), 1853 (1986).

(47) I. M. Umlong, and K. Ismail, *Colloids and Surfaces a-Physicochemical and Engineering Aspects* **299**(1-3), 8 (2007).

(48) B. M. D. O'Driscoll, E. A. Nickels, and K. J. Edler, *Chemical Communications* (10), 1068 (2007).

(49) B. M. D. O'Driscoll, C. Fernandez-Martin, R. D. Wilson, J. Knott, S. J. Roser, and K. J. Edler, *Langmuir* **23**(8), 4589 (2007).

(50) S. Nagamine, and E. Sasaoka, *Journal of Porous Materials* **9**(3), 167 (2002).

(51) P. Garstecki, and R. Holyst, *Langmuir* **18**(7), 2519 (2002).

(52) P. Garstecki, and R. Holyst, *Langmuir* **18**(7), 2529 (2002).

(53) H. Z. Zhang, and J. F. Banfield, *Journal of Materials Chemistry* **8**(9), 2073 (1998).

(54) Y. Sakatani, D. Grosso, L. Nicole, C. Boissiere, G. J. D. A. Soler-Illia, and C. Sanchez, *Journal of Materials Chemistry* **16**(1), 77 (2006).

(55) R. C. Hayward, B. F. Chmelka, and E. J. Kramer, *Advanced Materials* **17**(21), 2591 (2005).

(56) X. H. Liu, Y. Guo, Y. G. Wang, J. W. Ren, Y. Q. Wang, Y. L. Guo, Y. Guo, G. Z. Lu, Y. S. Wang, and Z. G. Zhang, *Journal of Materials Science* **45**(4), 906 (2010).

Chapter 6 Conclusion and Future work

Robust silica films with ordered 2D hexagonal and cubic mesostructure have been synthesized using cationic surfactant and cat-anionic surfactant with a range of water soluble polymers. The film formation process was investigated using Brewster angle microscopy and time-resolved reflectivity, while the interfacial film structure was clarified by using grazing incidence diffraction. Film forming subphase solution evolution was examined by time-resolved small angle x-ray scattering and data modeling of the scattering profiles was undertaken to provide further detail on the micelles. A film formation mechanism was thus proposed. Dry film textural properties were studied by small angle x-ray scattering, nitrogen adsorption and TGA. Additionally, this surfactant/polyelectrolyte mineralization was also extended to titania and iron oxide based mesostructured films.

6.1 Cationic Surfactant/polyelectrolytes Templated Silica Materials

Initially formation of polyethylenimine films with different cationic surfactants was investigated. Evaporation drives the surfactant micelle/polymer complex phase separation and formation of mesostructured solid film across the solution interface. With the assistance of cross-linker, solid CTAB/PEI and DDAB/PEI films were possible to remove from the air/water surface. SAXS indicates that nanostructure was preserved in these dry polymer-surfactant films. The extent of structural ordering mainly depends on the chemical properties of the surfactant, concentration and molecular weight of the polymer. The concentration of cross-linker also plays an important role on the structural ordering.

We then explored synthesis of the mesostructured silica films by combining our research on surfactant-templated inorganic materials with our recently developed polyelectrolyte-surfactant films. In other words, we aimed to synthesize inorganic

materials using these ordered mesostructured polymer surfactant materials as secondary templates. This was done by introducing silica precursors into the solution along with the soluble polymer and surfactant. The electrostatic interactions between the silicate species and CTAB/PEI as well as the dipole-cationic interaction between silica or CTAB and PEI, allow their co-assembly and result in the homogenous dispersion of the polymer and silicate species around CTAB micelles.

Some of the CTAB/PEI/silicate films had no ordered repeat layers when they formed in situ at the solution surface, which resulted in disordered films when they are dried. However, under a certain surfactant and polyelectrolyte concentrations, robust highly 2D hexagonal ordered silica films were obtained. Neutron reflectivity results indicate that most films have cubic phase ordering at the beginning of the film formation process and transform into a 2D hexagonal phase with time at the air/water interface. This 2D hexagonal structure was retained when the films were dried. These silica films are strong and resist cracking, have a high thermal stability since the ordered structure is maintained even after the removal of the template. This work provides an easy way to introduce a polymeric organic species as part of the inorganic film pore structure to make it robust and mechanically strong, but also to incorporate polymer into silicate wall to enhance its functionality which could have advantages in practical applications in catalysis and sensing. In addition, when silica precursors are introduced the CTAB/PEI system presents different phases. The phase diagram shows gels or precipitates were also observed depending on concentration the complexes.

Time-resolved SAXS with 20s resolution was used to investigate the evolution of micelles in the subphase solutions of CTAB-PEI-silica which form films at the air/water interface. Simple models were employed to quantify the size and shape of the micelles formed in solution at the induction period. For film forming solutions with PEI, the micelles have a prolate morphology dispersed in the polymer matrix immediately after mixing. No liquid crystalline ordering was observed for the surfactant micelles occurring in the bulk solution prior to silica precursor addition. For all the film forming solutions, addition of silicate species does not initially change the micellar size and structure. Hydrogen bond formation between the amine groups

in the polyamine chains and the surfactant head groups with the oxygen adjacent to silicon in the precursor facilitate the silicate hydrolysis and condensation resulting in formation of phase separated particles with a disordered mesostructure. The mesophase within the CTAB-PEI-silica particles finally rearranges into a 2D hexagonal ordered structure. Evaporation-induced rapid phase separation to the interface results in an initially amorphous layer at the interface at the same time as or even before the first disordered particles form in the subphase, but it is independent of particle formation in the subphase. The mesostructure evolution process in the film is similar to the mesostructure evolution in the particles in the subphase, except that the whole process within the particles of the films takes a much longer time than that in the subphase solutions because of the relative dryness and viscosity of the PEI-silica networks at the solution surface.

Upon the understanding of the interaction between the surfactant, polymer and silica precursor, an efficient co-assembly into a highly ordered mesostructured material was obtained. This work provides not only a straightforward way to introduce an polymer as part of the inorganic wall structure to make it more robust and mechanically strong, but also incorporates organic species into the silicate wall to make it more functional which could have great advantage towards practical applications. To our knowledge, this is the first report of the synthesis of inorganic ordered mesoporous films templated by surfactant-polyelectrolyte complexes at the air/water interface. By altering the polyelectrolyte or the surfactant, a wide range of free-standing organic-inorganic hybrid films could be generated at the air/water interface.

Silica monoliths have also been prepared with a range of surfactant and LPEI system. By accelerating the gelation process of silica with addition of polyelectrolytes, the reaction solution gelling time is shortened to less than one minute. SAXS data indicates that the mesostructure is dependent on the surfactant chemical properties and surface charge. The incorporated polymer improves the crack resistance of the monoliths on drying. In addition, dyes can be easily doped into the silica/polymer monolith, which is expected to have positive implications for their applications in separation and optics.

6.2 Cat-anionic Surfactant/polyelectrolyte Templated Silica Films

If mixed cationic and anionic surfactants are used, thick, opaque films form with a wide range of polymers at the solution surface, making this a more versatile film forming system. Cat-anionic surfactant micelles and four types of polyelectrolytes (LPEI, SPEI, PAAm and PEO) were employed to form solid mesostructured surfactant and polyelectrolyte films at the air/water interface. Film nanostructure and ordering were determined by the interaction between the surfactant head group and polyelectrolyte, polyelectrolyte concentration and cat-anionic surfactant molar ratios. PEI and PEO have been well documented to have strong interaction with either CTAB or SDS in terms of electrostatic forces or hydrophobic interactions, leading to formation of cubic phases such as $Im\bar{3}m$ and $Ia\bar{3}d$. Mainly lamellar phase films were observed for films prepared with PAAm since PAAm is thought to have little interaction with either CTAB or SDS.

These surfactant and polyelectrolyte systems were also employed in a mineralization process to synthesize robust silica films. This provides an easy method to synthesize mesoporous silica films with a variety of mesostructures grown at the air/water interface.

A similar film formation mechanism as the CTAB/polyelectrolyte/TMOS could also be occurring here. Cat-anionic surfactant and polyelectrolyte form aggregates at an early stage immediately after mixing. Silicate particles with liquid crystalline ordering form after the introduction of silicate precursors, but the mesophase of the particles and interfacial films were enriched due to more complicated interactions between polyelectrolytes and two surfactants than in the case of the cationic surfactant/polymer systems.

Interfacial film formation processes were probed by neutron reflectivity and well developed film mesostructures were clarified by GIXD. The subphase was also studied by time-resolved SAXS. Polyelectrolyte molecular weight, and chemical nature as well as the cationic-anionic surfactant molar ratio can be used to control the

mesophase geometry of the cat-anionic surfactant-polymer templated silica films. Lamellar, 2D hexagonal and several cubic mesostructures were obtained and phase diagrams in terms of the cat-anionic ratios and polyelectrolyte concentration were drawn. These films are thick and robust enough to be easily removed from interface and the film morphology is retained even after calcination.

The cat-anionic surfactant/polyelectrolyte/silica films thickness ranges from 50 μm to 350 μm. Aging temperature of the initial surfactant/polymer solution disorders the final film mesostructure and has no obvious affects on the film thickness. High molecular weight PEI and high SDS concentration result in thicker hybrid interfacial film due to the increased hydrophobicity of the complexes formed with these species.

Silica films also can be prepared in dilute solutions (as low as 0.012 M) using cat-anionic surfactant and polyelectrolyte at the air/water interface. During a continuous dilution process, the time-resolved characterization technique shows transformation of the particles mesophase from $Pn\bar{3}m$ to $Ia\bar{3}d$ mesostructures. Neutron reflectivity suggests mesophase transitions in the interfacial films from $Fm\bar{3}m$ to 2D hexagonal to lamellar. This mesophase transition is attributed to the micelle packing parameter. The bigger the micelle packing parameter, the smaller the micellar curvature will be; and the interactions between the cat-anionic surfactant, polymer and inorganic precursors determines the micellar packing parameter in terms of the hydrophobic volume, effective micellar head group and micelle hydrophobic tail length.

Films with different mesostructures are strong, robust and have good thermal stability. By washing out the template, robust polymer–silica hybrid films can be obtained straightforwardly, they retain the polymer functionality in the pore wall of the silica materials, which could allow binding of specific species in the pore or allow synergistic interactions between the organic functionality from the polymer and the inorganic species in the walls for catalysis. We are currently investigating these aspects of the films to develop them into useful membrane for future applications, such as CO_2 absorption, heavy ion remove and dye separation.

6.3 Cat-anionic Surfactant/polymer Templated Titania Films and Iron Oxide Films

Thick titania films were prepared with cat-anionic surfactant and polyelectrolyte (PAAm and PEO) at the air/water interface. Time-resolved neutron reflectivity was used to follow the film formation process, showing that the film mesostructure appears faster for smaller CTAB: SDS molar ratios and that the film mesostructure ordering was improved with increase of polymer concentration. Films prepared with TiB show much better mesostructural ordering compared to films prepared with TiBALD. Butanol was released during the TiB hydrolysis process, and diffused into the micelle hydrophobic region and helps to improve the phase separation, transforms the mesostructure into a lower curvature phase by increasing the hydrophobic volume relative to the headgroup area.

The GIXD technique was used to clarify the interfacial mesostructure. Cat-anionic surfactant ratios, the chemical nature of the polymer, polymer concentration, and the chemical nature of the titania precursors could be used to govern the mesophase geometry of the polymer/titania hybrid films. Lamellar and different cubic phases were found.

Those films were robust enough to be removed from the interface and the mesostructures were partially retained on drying. However, these titania films have a weak thermal stability and fell apart after calcination. Thus two post-synthesis strategies were employed: either soaking the dry polymer/titania hybrid film in the titania precursor or exposing it under titania precursor vapor. The film physical strength could be improved but unfortunately, the mesopores were not kept after calcination.

Dry surfactant/polymer film was also tried to template titania films. Titania precursor could effectively be incorporated into the polymer matrix. But it disorganizes the initial polymer structure. Further efforts are underway to optimize the soaking conditions to get robust ordered titania films via dry polymer templates.

Under a highly alkaline condition, robust SDS/LPEI/Iron oxide films were spontaneously formed at the air/water interface. GIXD and SAXS indicate a lamellar structure present in the film. The mesostructure could be retained in the dry iron oxide films. But the lamellar mesophase collapsed when the template was removed either by calcination or washing. To our knowledge, this is the first time thick iron oxide films were formed at the air/water interface, which might be useful in exploring their potential applications in future.

6.4 Future work

Various inorganic materials with interesting mesostructures (lamellar, 2D hexagonal, cubic) and morphologies (film, monolith) have been fabricated using the surfactant and polyelectrolyte complexes as templates. Through the understanding of the evaporation system as well as the surfactant/polyelectrolyte template, film formation mechanism began to be elucidated. To a certain degree, controllable yield inorganic materials with mesostructure were achieved from aqueous conditions. However, many efforts listed as follows still need further investigation:

(1) Ordered cubic surfactant/polymer/silica hybrid films were obtained and their mesostructure were preserved in the dry film. These films lost some ordering when the template was removed either by washing and calcination. This is probably due to a low degree of the silica condensation or thin material wall. Hydrothermal treatment was applied to the fabrication of mesostructure silica powder (like MCM-41[1] and SBA-15[2]) but not on the silica film or surfactant/polymer/silica materials. This strategy could be employed to enforce the cubic structure, which will help to retain the pore ordering after removing template.

(2) Post-synthesis treatment to preserve the mesostructure and improve the wall crystallinity for titania and iron oxide films need to be explored, such as calcination temperature, or calcination of the sample under a protective gas such as nitrogen.

(3) Free-standing cross-linked dry surfactant/polymer films were investigated as templates to produce titania films by soaking in the titania precursor. Titania precursor could be effectively introduced into the polymer matrix, but it also cause a disorganization of the mesostructure of the original polymer/surfactant films; More experimental conditions, such as soaking time, soaking solution, calcination temperature and the cross-linking degree of the polymer films could be studied in future work.

(4) Inorganic silica, titania and iron oxide films generated at the air/water interface are thick and reproducible and it is possible to retain the polymer functional group inside the silica wall after washing away the template. Moreover, mesostructured silica gel monolith formed in a very short time and showed a good ability to absorb dye molecules by soaking in a dye solution without dissociation or cracking. Materials with the novel properties prepared in this work show good potential and it is interesting to explore these for practical future applications, such as catalysis, CO_2 absorption, delivery system as well as photovoltaic applications.

6.5 Overall Summary

In summary, surfactant and polyelectrolytes complexes have been used for the production of solid mesostructured polymer films, mesostructured inorganic films at the air/water interface as well as to prepare other materials such as monoliths. Cationic surfactant and PEI successfully templated thermally stable highly ordered 2D hexagonal silica films. Alternatively, cat-anionic surfactant mixtures of CTAB and SDS interact with a range of water soluble polymers (PEI, PEO, PAAm), which gave an opportunity to produced robust silica films with various cubic mesostructure. Cubic mesostructures facilitate diffusion inside the pore system which has a great potential in applications such as absorption, or separation. It was found possible to produce not only thick mesostructured titania films but also thick mesostructured iron oxide films using cat-ionic surfactant/polyelectrolytes complexes at the air/water

interface. Self assembly and spontaneous film formation at the air/solution interface is easy, less sensitive to environmental conditions and repeatable which show good potential for fabricating inorganic films suitable for practical applications as in catalysis, chemical sensing, and delivery systems.

6.6 References

(1) C. T. Kresge, M. E. Leonowicz, W. J. Roth, J. C. Vartuli, and J. S. Beck, *Nature* **359**(6397), 710 (1992).

(2) D. Y. Zhao, J. L. Feng, Q. S. Huo, N. Melosh, G. H. Fredrickson, B. F. Chmelka, and G. D. Stucky, *Science* **279**(5350), 548 (1998).

Chapter 7 Appendices

7.1 Summary of mesostructures

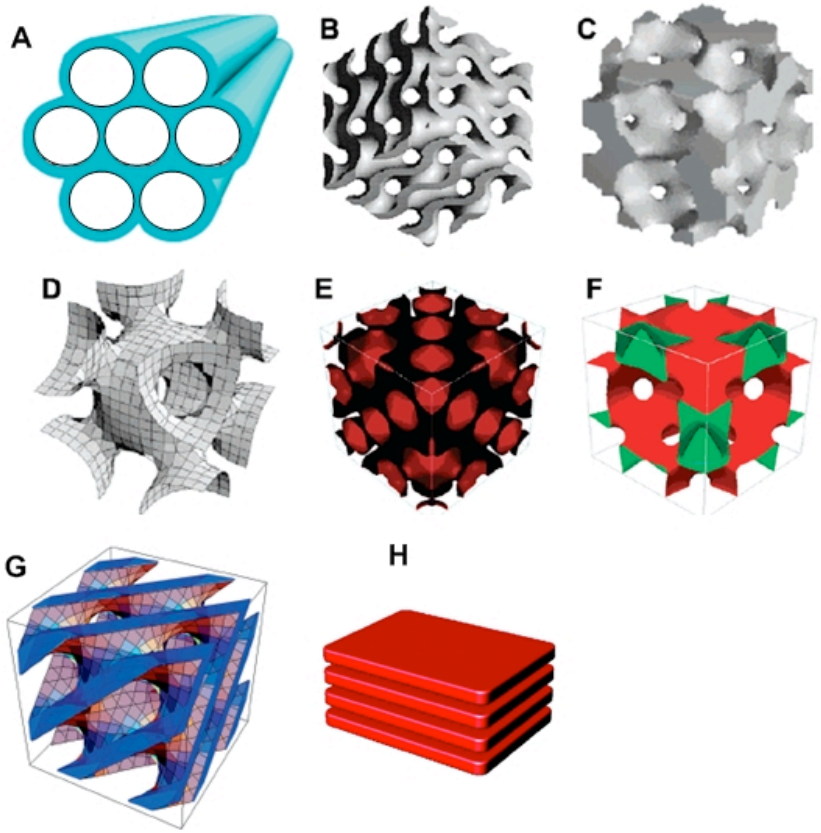

Figure 7.1 *Pore models of mesostructures with symmetric of (A) p6mm (B)* $Ia\bar{3}d$[1] *(C)* $Pm\bar{3}n$[2] *(D)* $Im\bar{3}m$[2] *(E)* $Fd\bar{3}m$[3] *(F)* $Fm\bar{3}m$[4] *(G)* $Pn\bar{3}m$[5] *(H) Lamellar*[6]*, Use with permission from the above cited references.*

7.2 Absorption in Polymer/Surfactant Templated Materials

7.2.1 Dye Absorption

In **Chapter 4**, robust silica films with various cubic structures have been synthesized with cat-anionic surfactant. The template can be washed out by ethanol, leaving amine functional groups on the material pore surfaces. These materials might

have a potential application in molecular absorption and separation. In this section, some work on silica film application to the absorption of dye and iron ions will be introduced.

Cubic silica films templated by CTAB:SDS = 8 40SPEI was prepared at the air/water interface, then they were exposed under TMOS vapor for a day and left in the 80 °C oven overnight to make sure silica condensation was complete. Templates were removed by ethanol wash carried out about 10 times and dried in the oven at 40°C.

Rhodamine B (molecular formula shown in **Figure 7.2**) has maximum absorption wavelength around 555 nm in UV-VIS spectroscopy. It is a basic dye with molecular size of 1.59 nm × 1.18 nm × 0.56 nm and molecular weight of 478 g/mol,

For a typical absorption measurement, Rhodamine B was dissolved in water and the initial concentration was 8×10^{-5} M. 10 mg of the dry silica/polymer hybrid film sitting on mesh was put into 10 ml Rhodamine B solution to soak and left for 3 days in order to reach adsorption equilibrium. The absorption was carried out at room temperature. Upon equilibrium, the film was taken out the solution and the remaining solution was tested with UV-VIS spectroscopy.

In addition, five standard Rhodamine B solutions with concentrations of 5×10^{-6} M, 8×10^{-6} M, 1×10^{-5} M, 2×10^{-5} M, 3×10^{-5} M were tested with UV-VIS spectroscopy and used to make a calibration graph. About 3.2×10^{-6} M Rhodamine B is absorbed by one mesh of our silica/polymer hybrid films in the initial 8×10^{-5} M Rhodamine B solution.

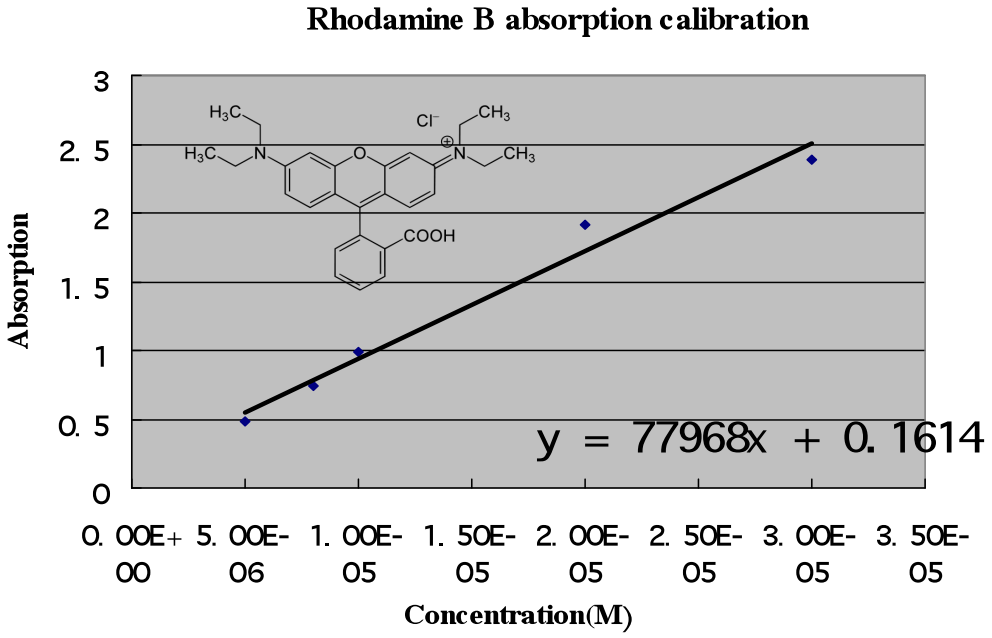

Figure 7.2 *Concentration calibration in which the UV-VIS absorption is plotted against different Rhodamine B concentrations; the rhodamine B molecular structure is shown in the insert.*

7.2.2 Iron Ion Absorption

Mesoporous films templated by CTAB: SDS=4 30g/l LPEI complexes have also been used to absorb iron ions, which may facilitate its application in the environmental industry for waste water cleaning.

Integrating organic functional group into the siliceous mesoporous materials has attracted a lot of attention recently. Typically the organic group was incorporated inside the silica mesoporous materials either by simple adsorption of an organic guest or by postsynthetic modification, such as grafting.[7] Here we use our one-step strategy to synthesize mesoporous materials with amine functional group and applied them to absorb iron ions due to the affinity between the iron ions and the amine group on the polymer (discussed previously in **Section 5.3**).

A routine way to prepare films which is similar to the films prepared for the dye absorption experiments was used, however about 30 meshes of CTAB/SDS/PEI/TMOS film needed to be prepared to supply enough material for these absorption experiments. A large batch of solution was prepared with the components mixed together and thick films were grown at the air/water interface in multiple 6 cm diameter plastic petrie dishes. Then the films were treated under TMOS vapor for a day and left in the 80° C oven for 12 hours. The films were divided into two parts after they were cut off the mesh, half of the films were calcined at 600°C for 6 hours to get the rid of the template while the other half were washed with ethanol 10 times to remove only the surfactant part of the template leaving the PEI in the walls of the material.

Calcined samples (28 mg) were suspended in 5 ml 3 mM solution of $FeCl_3$, this suspension was sonicated for 1 hour, after which the solid was filtered off. The washed sample (28 mg) was used in the same procedure to absorb iron ions. The iron ion uptake was monitored by measuring the UV absorption at 295 nm wavelength of the initial and final solution. The calculations indicated that the calcined sample absorbed amount can reach 96.6 % while for washed samples; only 40.4 % of iron ions were absorbed. The polymer containing samples did not show higher absorption as expected, probably because of three reasons: (1) Some polymer may be trapped inside the pore and reduce some of the pore volume and surface area, preventing diffusion of iron ions into the material. (2) The polymer as well as the iron ions attached has been washed into the iron ion solution during soaking. (3) The pH of the solution may also matters, since the pH of iron ions solution is about 2.15, when polymer is positively charged in the $FeCl_3$ solution, which will repel the positive charged iron ions. The experiment results suggest that the mesoporous materials we have prepared are promising as absorbents for iron ions but more work needs to be done in this area.

7.2.3 CO_2 Absorption

CO_2 is a major greenhouse gas causing global warming, thus there is growing interest in developing techniques for the efficient capture of large quantities of CO_2. Mesoporous silica materials, especially amine-grafted mesoporous silica materials have been found to be effective adsorbents for this gas. However to date these materials were prepared by post-synthesis grafting or backfilling calcined mesoporous silicas with amine species.[8-10]

Our absorption materials were prepared with the one-step strategy as described in the above sections. 0.0821 g calcined mesoporous silica were degassed at 300° C over night and 0.3062 mg amine group functionalized silica films were out-gassed at 75° C for 2 days. The CO_2 absorption experiments were also conducted on both the calcined samples and washed samples on ASAP instruments, however on this instrument, the relative pressure only can be increased up to 0.03 since the saturation pressure of CO_2 at this temperature is 26600mmHg and the maximum analytical pressure of the ASAP machine in the Chemical Engineering department is 800mmHg. Thus only the lower part of the CO_2 adsorption isotherm can be measured (**Figure 7.3**).

Experimental data showed that the calcined samples absorbed more than the amine-functionalized silica mesoporous material, which is opposite to our expectation, therefore, more experiments are probably required to optimize the materials and to ensure water adsorption on the hydrophilic PEI present in the washed samples does not affect the measured CO_2 adsorption.

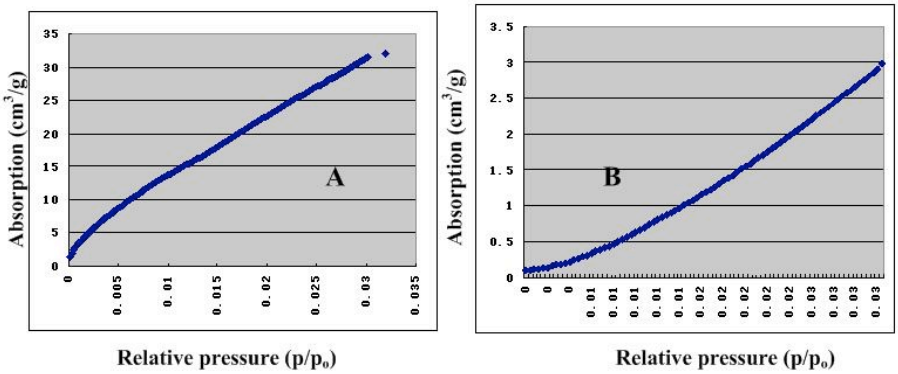

Figure 7.3 *Low pressure CO_2 absorption isotherm for calcined sample (A) and washed sample (B).*

7.3 Filtration System Designed to Use Polymer/surfactant/ Silica Films as a Molecular Filter

A filtration system was designed to use the polymer/surfactant/silica films as a molecular filter to separate dye molecules out of solution. The filtration systems can be assembled in two ways, as shown in **Figure 7.4**.

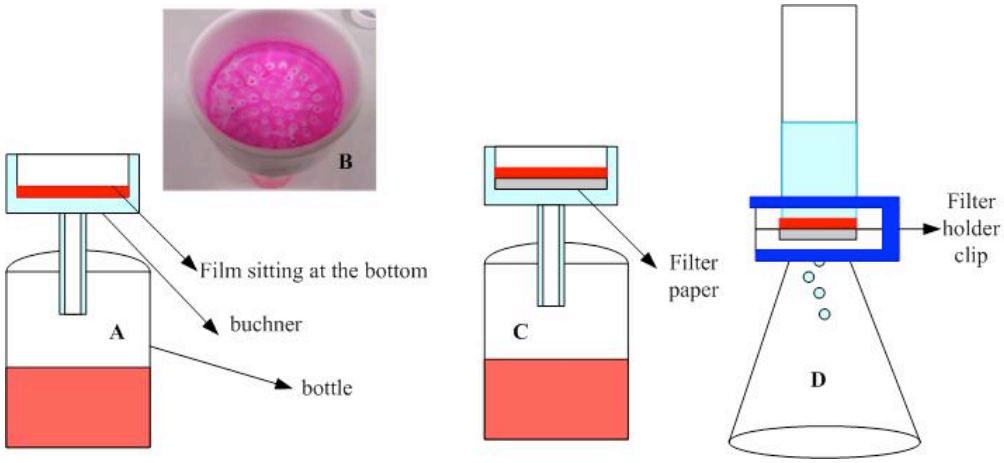

***Figure 7.4** Scheme of the designed filtration systems.*

The first way is to pour the film forming solution into a Büchner funnel with the outlet sealed with Parafilm, a thick film can be observed at the interface after a night. The outlet of the Büchner funnel was then unsealed letting the film forming solution drop out of the Büchner funnel. Then the thick film will sit on the bottom of the Büchner funnel, as shown in **Figure 7.4 A**. The film was dried at 40°C in an oven and washed with ethanol to open up the porosity. However, some parts of the film near the Büchner funnel pores were found to break, thus a second method using a piece of filter paper below the film was tried. The solution was prepared as before but with a filter paper on which the film sits after the other liquid is drained away. For very viscous film forming solutions (as show in **Figure 7.4 C**), a vacuum pump was employed to make sure all the film forming solution was removed. The films were again dried in an oven at 40°C in an oven and washed with ethanol to open up the

porosity. Dye solution was then poured into the Büchner and filtered with this apparatus. **Figure 7.4 B** is a picture of the dye filtration system, the red part in the bottom of the Büchner funnel is the synthesized film with dye absorbed.

However, during this process it was observed that the filter paper supporting the film can be warped in the drying process after washing with ethanol, therefore a second filter apparatus was designed, as shown in **Figure 7.4 D**. In this case the filter paper with the interfacial film was taken out of the Büchner funnel and mounted inside a solvent filtration bottle by a filter holder.

Unfortunately in all three systems we did not observe successful dye separation. Using methods A and B defects in the film (due to the cracking near the pores of the Büchner funnel in A, or the warping of the filter paper substrate in B) allowed dye solutions to pass freely through the membrane. In method D the membrane did not have defects but the static water pressure above the membrane was not sufficient to get measureable drainage of the solvent through the film probably due to the nanoscopic size of the pores in our membranes.

7.4 Solar Cells

Highly ordered mesoporous materials with properties such as the versatile framework nature (e.g. multioxide, crystalline, silicate, transitional metal), high surface area, and tailored pore structure, have enabled them to be used in a variety of applications like thin film sensors, encapsulation of drugs for targeted or controlled release, catalysis, separation, optical sensors and photovoltaic application like solar cells. However, based on the direction of my future research work, this part will mainly focus on application of such materials in solar cells.

Grätzel's cell, a nanocrystalline dye sensitized solar cells named after its inventor Michael Grätzel, is a remarkable innovation made in 1991.[11] In Grätzel's cell, electrons are injected by the photo-excitation of dye molecules, anchored to a mesoporous TiO_2 film, and are efficiently diffused to the back contact achieving solar energy conversion at efficiencies exceeding 10%.

Figure 7.5 shows how a dye-sensitized cell works. Attached to the surface of this film is a monolayer of the charge transfer dye. Photo excitation of the dye leads to an electron being passed into the conduction band of the oxide. The dye is returned to its original state by the donation of an electron from the electrolyte, typically an organic solvent containing a redox couple such as iodide/tri-iodide complex. The dye sensitizer is restored by an electron from iodide, and at the same time, iodide is regenerated by the reduction of tri-iodide at the front contact. The circuit is closed by the flow of electrons through an external circuit. The voltage produced corresponds to the difference between the Fermi level of the electron in the solid and the redox potential of the electrolyte. A solar cell's performance is measured by two factors: the incident photon-to-current conversion efficiency (IPCE) for monochromatic radiation and the overall white light-to-electrical conversion efficiency.

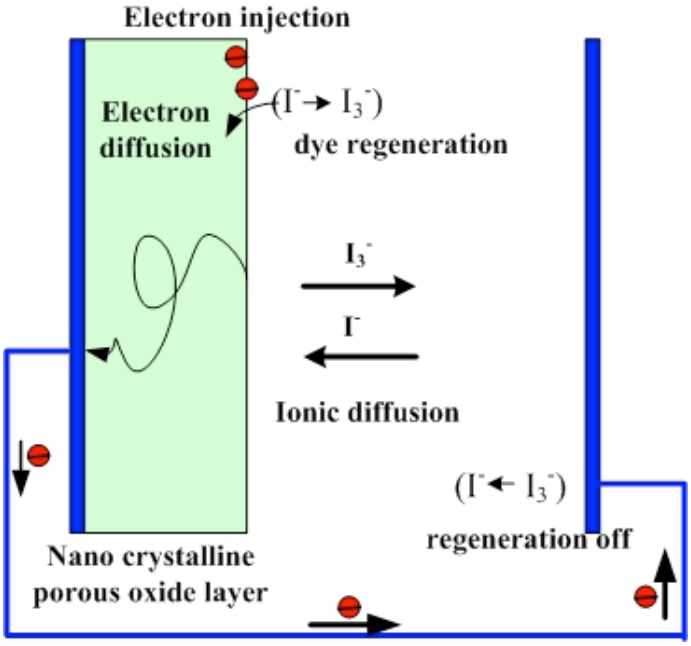

Figure 7.5 *How a Grätzel dye-sensitized cell works.*[12]

Assembly steps of typical solar cell are shown in **Figure 7.6**. This process starts with two sheets of glass coated with a transparent layer of fluorine-doped tin oxide. One plate is coated with a thin layer of colloidal TiO_2 paste consisting of particles

with sized in the 20-40nm range. The film is sintered in air at 400°C to produce a mesoporous layer (about 10μm) with a porosity about 50%. Generally this procedure will be repeated once again to get a thicker TiO_2 layer (**Figure 7.6 A).** A mixture of $TiCl_4$ and ice water is then sprayed onto the film surface, and the film then will be put into a 70°C oven for half an hour, and finally calcined at 500°C to produce porosity. The TiO_2 film is then sensitized by adsorption of a dye by immersing the film into a dye solution in ethanol over night (**Figure 7.6 B)**.

The second glass is coated with a thin layer of platinum by sputtering or by electrochemical deposition. These two glasses are sandwiched together with a hot melt polymer gasket (surlyn tape), as shown in **Figure 7.6 C**. The electrolyte consisting of the iodide/tri-iodide redox couple in a suitable solvent is filled through small holes in the platinum coated plate, which are then sealed using surlyn and another glass on top.

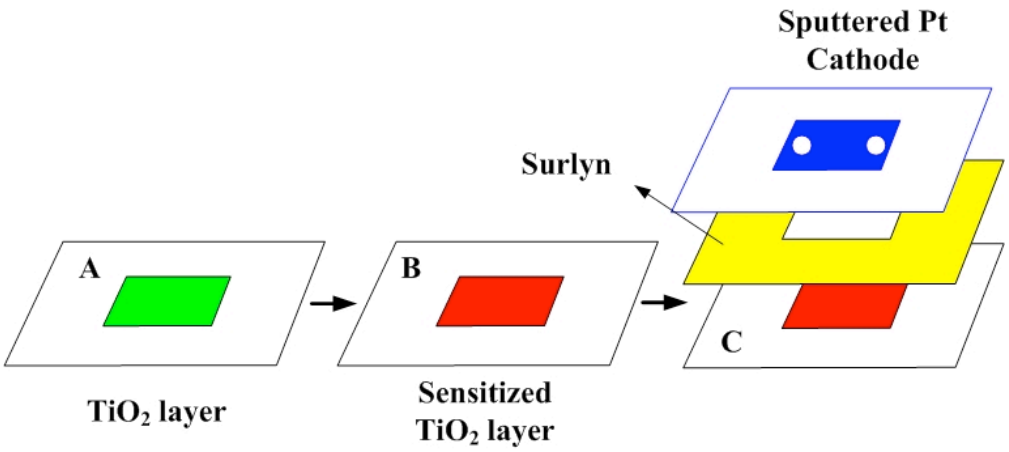

***Figure 7.6** Fabrication of a dye sensitized solar cell.*

To make an efficient solar cell, the electrolyte must be able to penetrate the pores and reach anywhere where dye is present, in order to rapidly regenerate the oxidised dye for the purposes of charge transport. So the porosity is very important for the whole cell efficiency. Until now, most of the mesopores in the films used come from the inter-crystalline voids rather than regular and integrated pores,[13] thus a major problem associated with the dye-sensitized solar cells is the electron percolation within the oxidized film and the filling of the porous film with the hole transporting

organic materials.[14] Synthesis of inorganic films with mesopores, which are templated by surfactants, gives a chance to meet this rigorous porosity requirement. The inorganic species polymerised around the surfactant micelles which can be removed by calcination, leaving an ordered porous network. Surfactant-based mesoporous films should have a good efficiency due to the ordered and continuous framework, high surface area and a smooth neck structure of nanocrystals along the framework.

Literature concerning the photovoltaic properties of mesoporous TiO_2 films is limited but consistent. Several experiments show that mesoporous anatase TiO_2 films exhibit a higher light-to-electricity conversion compared to that of nanocrystalline colloidal anatase TiO_2 films with the same thickness. Using poly (3-octylthiophene) as hole conductor and P123 as a pore structure directing agent, Lancelle-Beltran synthesized nanocrystalline mesostructure TiO_2 film which achieves a very promising energy conversion efficiency of about 0.52% for a thin film with thickness of 250nm.[15] Crack-free and transparent ordered TiO_2 films with thickness up to 7μm have been synthesized by combination of traditional doctor blade technique and a two step EISA method, a solar efficiency of 6.53% was obtained by employing this film.[16] Hou has also reported the importance of TiO_2 film thickness, multi-layered mesoporous TiO_2 films with thickness up to 4.0μm has exhibit a light-to-electricity conversion up to 5.31%.[17]

Crystallinity of the TiO_2 film is another important factor. Lancelle-Beltran reported that the best photovoltaic properties come from fully nanocrystalline TiO_2 films with the highest specific area, based on the investigation of the photovoltaic performance as a function of the mesostructure and crystallinity of the porous TiO_2 film in all solid state photovoltaic cells.[18] Crystallinity contributes to the facial electron transfer to the collector electrode, increment of electron-hole pair density generated at the hybrid interface, and improvement of impregnation of the hole-transporting organic materials.

However, thickness is still the biggest limitation for TiO_2 mesoporous films. Nowadays, most reported strategies are based on dip-coating strategy. In order to get thick films, self assembly and precalcination procedures had to be repeated many

times, moreover, the repeating dip-coating and precalcination procedures may lead to degradation of the film mesostructure to some extent. This disadvantage makes the previous strategy to be time consuming and inefficient for deposition of thick mesoporous film with good quality.

Growing films at the air/water surface normally reproducibly and rapidly results in thick films, which gives us a good chance to synthesize films with promising solar conversion efficiency. Titania films prepared by the methods described in this thesis should be tested in dye-sensitised solar cells to determine their efficiency in this application.

7.5 L_3 surfactant Phase Templated Inorganic Materials

The L_3 (sponge) surfactant phase is a promising template for inorganic materials since it is composed of large uniform water filled pores separated by a surfactant bilayer.[19, 20] If the bilayer is coated in inorganic material, the pores of the resulting composite can be adjusted simply by water swelling of the initial L_3 phase rather than by increasing surfactant content and no calcination is required to open up the major pore network. Previous work, using water soluble silica precursors, resulted in aerogel-like materials with poor reproducibility, due to a diffuse silica gel filling the water-regions rather than coating the surfactant bilayer. During this project I also carried out some initial investigations of the preparation of materials using the L_3 phase using hydrophobic inorganic precursors, which are naturally segregated into the bilayer. Hydrolysis occurs in the palisade region, leading to condensation reactions which occur in the immediate vicinity of the bilayer leading, we predicted the formation of a denser coating of inorganic oxide on the bilayer surface rather than filling the water pores.

In this experiment, we used a well established sponge phase system composed of cetylpyridinium chloride (CpCl)/hexanol/brine,[19, 20] where the brine component is replaced by HCl solution as an acid catalysis for the polymerisation of the inorganic precursor. The L_3 phase is found for CpCl: hexanol molar ratios between 1.1-1.2 and

for water contents from 40% to 95%. The pores in this relatively disordered material range from 60 to 350 Å, depending on the aqueous solvent content. Three hydrophobic inorganic precursors were used to replace a proportion of the hexanol in the sponge phase structure. As the inorganic precursors hydrolyse they produce butanol or propanol, which remains in the surfactant bilayer while the non-polar inorganic species condenses around the membrane.

In this experiment, we prepared mineralised sponge phases at four concentrations of water (60%，70%, 80% and 90%) , using three types of hydrophobic inorganic precursors (tetrabutylorthosilicate (SiB), titanium(IV) butoxide (TiB) and tetrapropoxysilane (TPS)). Detailed concentrations and phenomena observed are shown in **Table 7.1** to **Table 7.4** below. All the samples were kept for a month, but no very solid gel formed at any of these concentrations.

Samples were prepared ahead of beam time as well as during the beam time to allow "time-resolved" studies to be conducted, since the polymerisation reaction is slow in these solutions. Due to the sequestration of the inorganic precursor in the surfactant bilayers the hydrolysis reaction only occurs when the precursor contacts the acidic water phase, making the overall reaction slow. With these samples we hoped to gain an understanding the relationships between inorganic species hydrolysis/condensation and material structure variation.

Small angle X-ray scattering (Diamond) are shown in **Figure 7.7**. These samples were prepared a week before the SAXS experiments. Small angle neutron scattering (SANS2D) experiments were also conducted on these samples, all the samples were prepared either in D_2O or 70% D_2O & 30%H_2O.

SANS patterns of the L_3 phase samples synthesized with cetylpyridinium chloride (CpCl)/hexanol are shown in **Figure 7.8**, two solutions with different SLD variation were used. Relatively broad bumps are seen, which are typical for SANS patterns of the L_3 phase structure.[19] The bump moves to a smaller q with an increase of water concentration, as the size of the water-filled pores increases when more water is present in the L_3 phase.

Two sets of L_3 phase mineralization samples were prepared in order to gain a "time-resolved" understanding of these system. One was prepared about a week before the experiment (as shown in **Figure 7.9**). The other prepared on the same day of experiment (**Figure 7.10**). We also made use of contrast variation to assist in determining the detailed structure, by preparing samples in 100% or 70% D_2O to achieve variation in the scattering length densities in the different regions of the sponge phase materials

The appearance of sharp peaks in most of these patterns suggests that the polymerization of the inorganic precursor led to formation of a lamellar phase rather than the desired L_3 phase. The L_3 phase exists only in a narrow range of concentrations in the CpCl/hexanol/brine phase diagram[19, 20] so it is possible that the substitution of hexanol for smaller alcohols such as butanol and propanol released by the hydrolysis of the inorganic precursors did not adequately match the properties of hexanol to allow formation of the L_3 phase in the final mineralized systems. More work would need to be done to map the region of L_3 phase formation in the presence of shorter chain alcohols.

Table 7.1 *L_3 phase formed by CpCl/hexanol/0.2M HCl in water*

	CpCl (g)	hexanol (g)	0.2M HCl (g)	h/c wt ratio	a night after the mixing of standard solution
60wt%	0.589	0.6775	1.9	1.15	clear solution
70wt%	0.442	0.5085	2.217	1.15	clear solution
80wt%	0.2975	0.336	2.5325	1.13	clear solution
90wt%	0.1495	0.1675	2.85	1.12	light opaque solution

Table 7.2 *Mineralization of L_3 phase by adding titanium(IV) butoxide (TiB) in water.*

	CpCl (g)	hexanol (g)	0.2M HCl (g)	butanol generated from TiB hydrolysis (g)	TiB (g)	h/c ratio	but/(total alcohol)	a night after the mixing of standard solution	a night after precursor is added
60wt%	0.589	0.5375	1.9	0.14	0.1607	1.150	0.207	viscous clear solution	white solution, almost gel
70wt%	0.442	0.4035	2.217	0.105	0.1206	1.150	0.206	viscous clear solution	opaque solution, almost gel
80wt%	0.2975	0.2685	2.5325	0.0675	0.0775	1.129	0.201	viscous little opaque solution	little opaque solution, likely to gel
90wt%	0.1495	0.1325	2.85	0.035	0.0402	1.120	0.209	viscous opaque solution	opaque solution, less viscous, likely to gel

Table 7.3 *Mineralization of L_3 phase by adding tetrabutylorthosilicate (SiB) in water.*

	CpCl (g)	hexanol (g)	0.2M HCl (g)	butanol from SiB hydrolysis (g)	SiB (g)	h/c ratio	but/(total alcohol)	a night after the mixing of standard solution	a night after precursor is added
60wt%	0.589	0.5375	1.9	0.14	0.1514	1.150	0.207	viscous clear solution	clear solution likely to gel
70wt%	0.442	0.4035	2.217	0.105	0.1135	1.150	0.206	viscous clear solution	clear solution likely to gel
80wt%	0.2975	0.2685	2.5325	0.0675	0.0730	1.129	0.201	viscous little opaque solution	clear solution likely to gel
90wt%	0.1495	0.1325	2.85	0.035	0.0378	1.120	0.209	viscous opaque solution	opaque solution, likely to gel

Table 7.4 *Mineralization of L_3 phase by adding tetrapropoxysilane (TPS) in water.*

	CpCl (g)	hexanol (g)	0.2M HCl (g)	propanol from TPS hydrolysis (g)	TPS (g)	h/c ratio	prop/total alcohol	a night after the mixing of standard solution	a night after precursor is added
60wt%	0.589	0.5375	1.9	0.14	0.1540	1.150	0.207	viscous clear solution	clear solution, likely to gel
70wt%	0.442	0.4035	2.217	0.105	0.1155	1.150	0.206	viscous clear solution	clear solution, likely to gel
80wt%	0.2975	0.2685	2.5325	0.0675	0.0743	1.129	0.201	viscous little opaque solution	clear solution, likely to gel
90wt%	0.1495	0.1325	2.85	0.035	0.0385	1.120	0.209	viscous opaque solution	clear solution, likely to gel

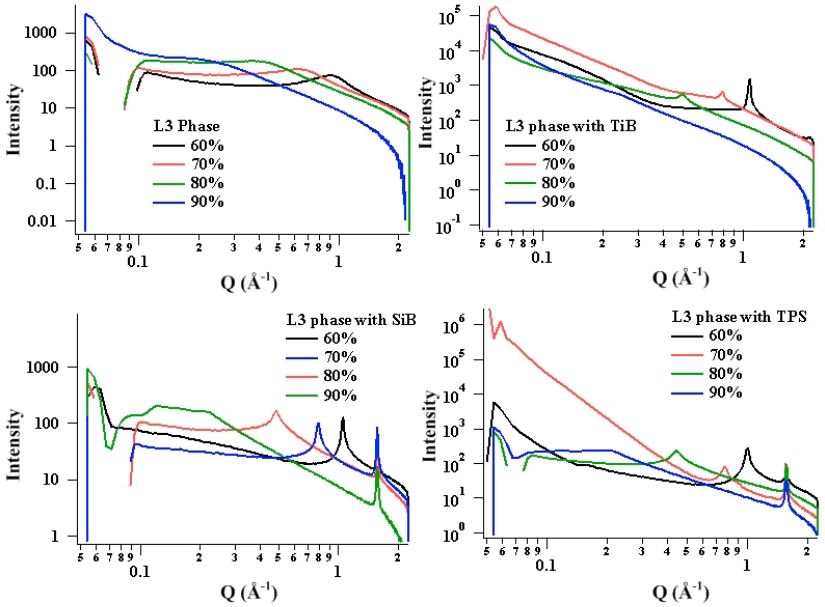

Figure 7.7 *Small angle X-ray scattering from the L_3 phase (top left) and mineralization of L_3 phase samples.*

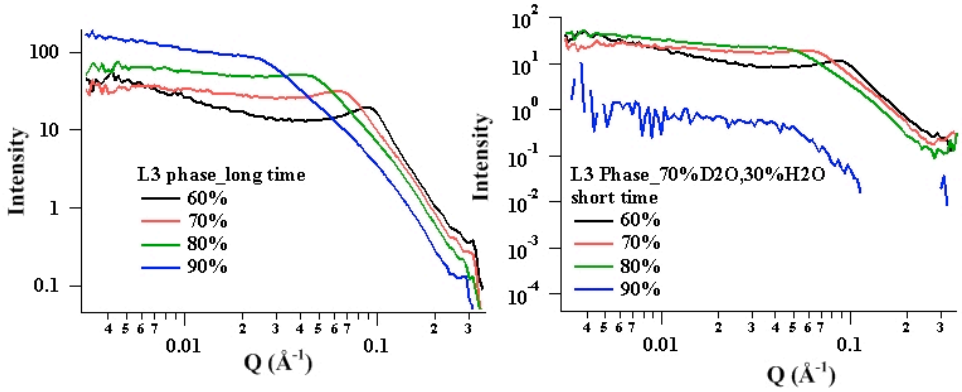

Figure 7.8 *Small angle neutron scattering patterns on the L_3 phase. 100% D_2O (left) and 70% D_2O/30% H_2O solution (right) was used to achieve variation in the scattering length densities in the different regions of the sponge phase materials.*

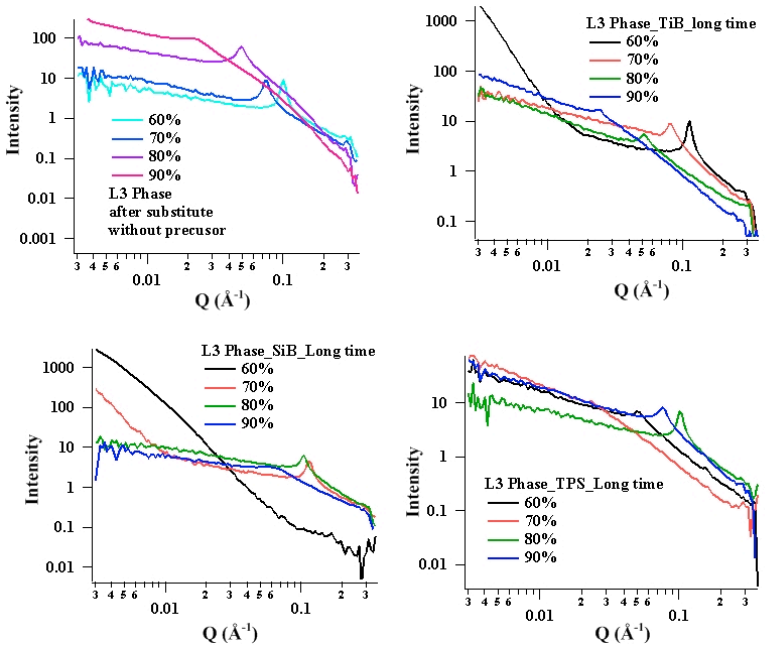

Figure 7.9 *Small angle neutron scattering patterns on the L_3 phase samples and L_3 phase mineralization samples which were prepared one week before data collection.*

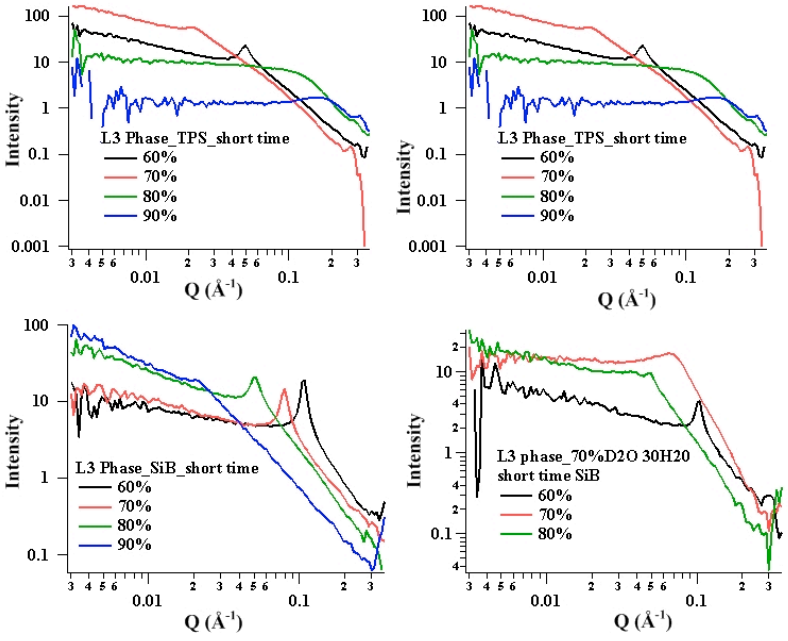

Figure 7.10 *Small angle neutron scattering patterns on the fresh L_3 phase mineralization samples which were prepared on the same day as data collection.*

7.6 References

(1) M. Kaneda, T. Tsubakiyama, A. Carlsson, Y. Sakamoto, T. Ohsuna, O. Terasaki, S. H. Joo, and R. Ryoo, *Journal of Physical Chemistry B* **106**(6), 1256 (2002).

(2) Y. Sakamoto, M. Kaneda, O. Terasaki, D. Y. Zhao, J. M. Kim, G. Stucky, H. J. Shim, and R. Ryoo, *Nature* **408**(6811), 449 (2000).

(3) A. E. Garcia-Bennett, K. Miyasaka, O. Terasaki, and S. N. Che, *Chemistry of Materials* **16**(19), 3597 (2004).

(4) T. Yu, H. Zhang, X. W. Yan, Z. X. Chen, X. D. Zou, P. Oleynikov, and D. Y. Zhao, *Journal of Physical Chemistry B* **110**(43), 21467 (2006).

(5) C. B. Gao, Y. Sakamoto, K. Sakamoto, O. Terasaki, and S. N. Che, *Angewandte Chemie-International Edition* **45**(26), 4295 (2006).

(6) B. K. Cho, A. Jain, S. M. Gruner, and U. Wiesner, *Science* **305**(5690), 1598 (2004).

(7) B. Hatton, K. Landskron, W. Whitnall, D. Perovic, and G. A. Ozin, *Accounts of Chemical Research* **38**(4), 305 (2005).

(8) W. J. Son, J. S. Choi, and W. S. Ahn, *Microporous and Mesoporous Materials* **113**(1-3), 31 (2008).

(9) H. Y. Huang, R. T. Yang, D. Chinn, and C. L. Munson, *Industrial & Engineering Chemistry Research* **42**(12), 2427 (2003).

(10) X. C. Xu, C. S. Song, J. M. Andresen, B. G. Miller, and A. W. Scaroni, *Energy & Fuels* **16**(6), 1463 (2002).

(11) B. Oregan, and M. Gratzel, *Nature* **353**(6346), 737 (1991).

(12) L. M. Peter, *Journal of Physical Chemistry C* **111**(18), 6601 (2007).

(13) K. Hara, H. Sugihara, Y. Tachibana, A. Islam, M. Yanagida, K. Sayama, H. Arakawa, G. Fujihashi, T. Horiguchi, and T. Kinoshita, *Langmuir* **17**(19), 5992 (2001).

(14) E. Palomares, J. N. Clifford, S. A. Haque, T. Lutz, and J. R. Durrant, *Journal of the American Chemical Society* **125**(2), 475 (2003).

(15) E. Lancelle-Beltran, P. Prene, C. Boscher, P. Belleville, P. Buvat, S. Lambert, F. Guillet, C. Boissiere, D. Grosso, and C. Sanchez, *Chemistry of Materials* **18**(26), 6152 (2006).

(16) W. Chen, X. D. Sun, Q. Cai, D. Weng, and H. D. Li, *Electrochemistry Communications* **9**(3), 382 (2007).

(17) K. Hou, B. Z. Tian, F. Y. Li, Z. Q. Bian, D. Y. Zhao, and C. H. Huang, *Journal of Materials Chemistry* **15**(24), 2414 (2005).

(18) E. Lancelle-Beltran, P. Prene, C. Boscher, P. Belleville, P. Buvat, S. Lambert, F. Guillet, C. Marcel, and C. Sanchez, *European Journal of Inorganic Chemistry* (6), 903 (2008).

(19) K. M. McGrath, D. M. Dabbs, N. Yao, K. J. Edler, I. A. Aksay, and S. M. Gruner, *Langmuir* **16**(2), 398 (2000).

(20) K. M. McGrath, D. M. Dabbs, N. Yao, I. A. Aksay, and S. M. Gruner, *Science* **277**(5325), 552 (1997).